Computational multiscale analysis and optimization of multiphase hierarchical structures within a continuum micromechanics framework

A THESIS
SUBMITTED TO THE FACULTY OF THE GRADUATE SCHOOL
OF THE UNIVERSITY OF MINNESOTA
BY

Tarun Gangwar

IN PARTIAL FULFILLMENT OF THE REQUIREMENTS
FOR THE DEGREE OF
DOCTOR OF PHILOSOPHY

Prof. Dominik Schillinger

August, 2021

Acknowledgments

The past five years have been very rich in experiences that hopefully will help me navigate the next steps in my life and career. I would like to express my gratitude to many people who helped and supported me in this journey.

First, I would like to acknowledge this excellent institution, The University of Minnesota, that has enriched me with a wholesome academic experience. I always felt that every part of this institution, from classes, seminars, administrators, student groups, resource centers to the Department of Civil, Environmental, and Geo-Engineering, has been with me in the pursuit of excellence. This environment has allowed me to work seamlessly in an interdisciplinary setting, which I have immensely enjoyed. I gratefully acknowledge the support from the National Science Foundation, the Minnesota Department of Agriculture, the Departmental Sommerfeld Fellowship, and the MnDRIVE Informatics Fellowship.

I would like to express my sincere gratitude to my advisor, Prof. Dominik Schillinger, for his guidance, support, and, most importantly, his time. A wise person from my undergraduate time told me that, in an academic setting, time is the most important resource, and anyone, who invests time in you, genuinely wants you to do good in life. Thanks to Dominik's time, openness, and belief, which encouraged me to work on a wide range of enjoyable topics that reflect in this thesis. Many of these learnings I would like to imbibe in my future academic endeavors. I vividly remember our first conversation during the Ph.D. admission process, when we talked for 3.5 hours about the possible research directions! Our first scientific discussion started over a cappuccino, examining whether it is solid or fluid from a continuum mechanics perspective. Many such long discussions followed over the last five years have provided me a perspective for academics or life in general and are the part of my fondest memories.

I would like to thank my committee members: Prof. Henryk K. Stolarski, Prof. Ryan Elliott, Prof. Jeff Calder, and Prof. Stefano Gonella, for generously taking their time out to read and provide feedback to this work. I am grateful to Dr. D. Jo Heuschele, Prof. Kevin P. Smith (Agronomy and Plant Genetics), Prof. Alex Fok (Minnesota Dental Research Center for Biomaterials and Biomechanics), and Prof. Michele Guala (Civil, Environmental, and

Geo-Engineering) for providing collaborative opportunities to work on an exciting inter-disciplinary project, which forms the central idea of this thesis. I especially appreciate D. Jo Heuschele's time to discuss the project in great detail and support in availing all the required resources for this project. I would also like to thank Alexander Q. Susko and Svetlana Baranova for the wind tunnel testing and modeling aspects of this project. I am also grateful to Prof. Jeff Calder (School of Mathematics) and Prof. Takashi Takahashi (Dept. of Radiology) for their guidance in developing a fully autonomous variational image segmentation approach during my first year of Ph.D. program, which instilled a belief in me to pursue collaborative research in a broader context of computational mechanics.

I also want to thank all the members of Schillinger's group at the UMN: Lam Nguyen, Stein Stoter, Qiming Zhu, Zhilin Han for many helpful and intense discussions. I would especially like to acknowledge the efforts of Lam and Stein in my initial years of Ph.D. in creating a very welcoming and supportive environment. I was also fortunate to visit the Institute of Mechanics and Computational Mechanics (IBNM), Leibniz University of Hannover. I thank the colleagues of IBNM with a special mention of René Hiemstra, Adnan Ebrahem, Etienne Jessen, Hoa Nguyen, Michal Mika, Vahid Badrkhani and Marco Eikelder for many fun discussions over coffee breaks.

My time in the U.S. would have been less easy in the absence of my excellent apartment-mate and friend Pramesh. He has been an ever-supporting person since our undergraduate time. Our long late-night discussions over tea, his positivity, and his enthusiasm for the research have kept me motivated. I would also like to thank my friends from Minneapolis: Alisha, Anuj, Shivam, Vivek, Resy, Deepak Ojha, Datta, Arvind, for creating a mini "hostel" life and especially for the memorable farewell. A big thanks to my friends, mentor, and siblings (often exchanging roles): Shashank, Vinitendra, Shubham, Sukhdarshan, Mitra, Geetika, Rashmi, Deepak for all their love, support, and life advice. Memories of Germany would be incomplete without mentioning Himanshu and Chandrakant. Our cooking sessions, cricket, and many graphs from our long discussions made this time memorable.

I am sending my deepest gratitude to my undergraduate institution, IIT Roorkee, and many important persons I interacted with. A big thank to Prof. Pradeep Bhargava and Prof. Anupam Chakrabarti for sowing the seeds for research during my undergraduate time. The most accidental, fortunate, and fulfilling event was to be a part of SOPAN at IIT Roorkee. My gratitude to its mentees and all the members with a special mention of Vishvendra, Jitin and Pranav, who continue to inspire me.

Finally, my greatest gratitude to my parents and grandfather for their unconditional love, support, and imparted values. Verbal language is yet to mature to convey my regard and love to them. I would especially like to mention my father, who also has been one of the most influential teachers that I have had in my academic life. His physics lessons from

school times continue to form a strong foundation to date. More importantly, I would like to imbibe his teaching ethos and outlook in my future academic life. This thesis is dedicated to my parents and grandfather.

Dedication

To my family.

Abstract

Hierarchical multiphase systems such as plant structures apply the concept of microheterogeneity repetitively across a hierarchy of well-separated length scales: composite microstructures at a smaller scale form the base materials for new microstructures at the next larger scale. Their complex multiphase hierarchical organization in conjunction with physiological, reproductive, and phylogenetic constraints pose significant challenges for understanding their mechanical behavior. A rational understanding of microstructure interdependencies across hierarchical scales is, therefore, essential to pave the way towards more efficient and sustained tailoring with improved properties, for instance in the context of the targeted breeding of agricultural crops.

This thesis aims to develop computationally feasible and accurate multiscale analysis and optimization methods that rationally predict the mechanical behavior and self-adapting mechanisms of multiphase hierarchical systems across multiple scales. We focus on three objectives to accomplish the outlined goal. First, we develop a multiscale modeling approach within the continuum micromechanics framework to predict the macroscale stiffness and strength of multiphase hierarchical materials focusing on a broad class of plant materials. Our approach is supported by microimages and chemical analysis data and extensively validated with the reported experiments in the literature and performed experiments by ourselves in the lab. Second, we integrate results from the continuum micromechanics and topology optimization frontiers to establish rigorous theoretical foundations for an efficient concurrent material and structure optimization framework for multiphase hierarchical systems. The framework accounts for the elastoplastic limit behavior across hierarchical scales, while its computational cost does not explode exponentially with the number of hierarchical scales. Finally, working with plant geneticists, we transfer these concepts to rationalize the biotailoring of cereals for improved lodging resistance. This thesis presents a unique opportunity and foundation concepts for the collaborative research efforts of computational mechanics and plant science in a broader context of the biomechanical tailoring of plants.

Table of contents

List of tables

List of figures

Chapter 1

Introduction and outline

Multiphase hierarchical materials apply the concept of microheterogeneity repetitively across a hierarchy of well-separated length scales: composite microstructures at a smaller scale form the base materials for new microstructures at the next larger scale. This principle constitutes the backbone of virtually all biological materials, enabling them to combine various functional properties at different length scales with favorable mechanical properties at the macroscale [25, 53, 59, 151, 188, 206].

Typical examples are plant materials, as illustrated in Fig. 1.1. They rely on cells with strong composite walls that accommodate various functions (e.g., photosynthesis, transport). Different types of cells and cell regions are hierarchically composed to optimize stiffness and strength at the macroscale. Although made up of just four basic building blocks (cellulose, hemicellulose, lignin, pectin), plant materials use their hierarchical arrangement to achieve a wide range of macroscale mechanical properties. For example, Young's modulus varies from 0.3 MPa in parenchyma (e.g., apple pulp) to 15 GPa in wood (oak, arborescent palms), while compressive strength varies from 0.3 MPa to over 300 MPa [72]. Other examples include wood, bone, rocks, and soil.

Recent advances in the biotechnology arena have paved the way forward to many engineering applications involving biological materials such as the genetic tailoring of crops [29, 127], bone remodeling [26, 153], and the fabrication of bioinspired engineering materials [95, 188]. However, attempting to improve one property by modifying single components leads to gains at one end but often implies serious losses at other ends. A classic example is the idea of reducing lignin in poplar plants to improve biomass processability for paper production [15]. Lignin reduction, however, initiates microstructure adaptation, which not only reduces

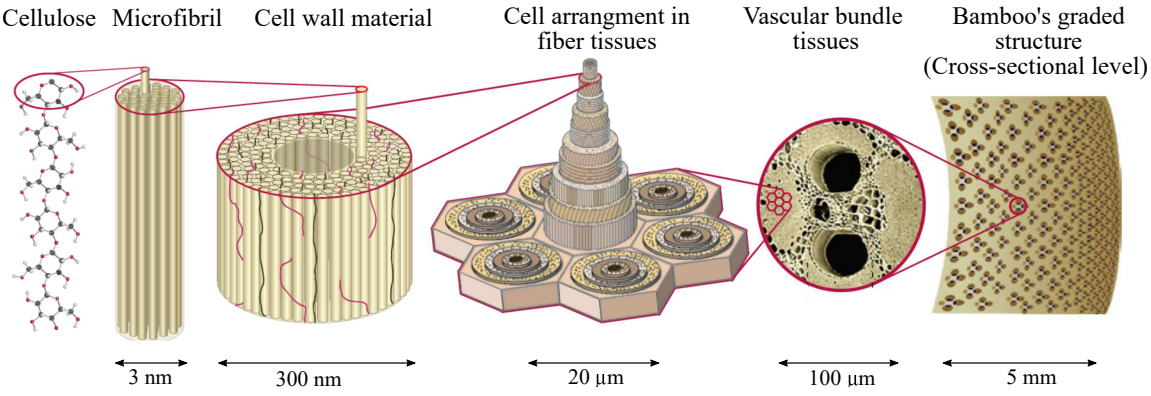

Fig. 1.1: *Hierarchical structure of plants with an example of bamboo culm material. Adapted from Wegst et al. [188] with kind permission from Nature Publishing Group.*

wood stiffness and strength but also impedes water transport, eventually lowering growth efficiency and plant survival rates [182]. A rational understanding of microstructure interdependencies across hierarchical scales is, therefore, an essential prerequisite for realizing these applications.

Biological materials have evolved to their sophisticated hierarchical organization after a very long evolutionary process. These materials dynamically respond to the biophysical stimuli of their environment and develop self-adapting mechanisms for improved performance [66, 72, 193]. In other words, biological systems adapt their "*form*" (or shape/structure) against the dynamic external environment and improve the "*microstructure architecture*," fulfilling the local needs imposed by physiological, phylogenetic, and reproductive constraints. This complex interplay between various factors poses significant challenges for the study of their comprehensive mechanical behavior.

Experimental methods constitute conventional approaches to study biological systems, including plants. One approach is to test the effects of various biological entities on the whole living system. These studies are called *in vivo*, a Latin word for "within the living," and animal testing and clinical trials are the major elements of *in vivo* research. Moreover, *in vitro* experiments, meaning "in glass," implying test tubes, are performed in a laboratory setting on small biological units such as cells or bio-molecules outside their natural biological environment. *In vitro* approach simplifies the studied unit compared to the whole living system. This simplification allows to understand biological functions and relevant mechanisms at small scales, which later inform the whole system behavior. It is evident that the time and resource costs of both *in vivo* and *in vitro* experiments are relatively high, and accounting for all the factors in an experimental study is prohibitive.

The overarching goal of this thesis is to develop computationally feasible modeling and simulation tools that enable us to study the mechanical behavior of multiphase hierar-

chical systems comprehensively and rationally. These tools will enable to conduct computational or *in silico* (meaning "in silicon" or on computer chips) experiments to quantify the microstructure interdependencies on the macroscopic functional response. In contrast to *in vivo* and *in vitro* experiments, computational experiments are cheap, fast, and free from any complications [59]. In addition, they are not restricted by natural laws and allow us to investigate the effects of mechanisms that are not found or implausible in nature. Thus, they could help us in understanding the origin of observed mechanical responses. We acknowledge that the *in silico* simulations can not entirely replace the *in vivo* and *in vitro* experiments. However, they can significantly help interpret the experimental results, design future experimental studies, and reduce labor and resource costs.

In this thesis, we work towards three objectives to accomplish the outlined goal. First, we develop a multiscale modeling approach within the continuum micromechanics framework to predict the macroscale stiffness and strength of multiphase hierarchical materials focusing on a broad class of plant materials. Second, we integrate results from the continuum micromechanics and topology optimization frontiers to establish rigorous theoretical foundations for an efficient concurrent material and structure optimization framework for multiphase hierarchical systems with elastoplastic constituents at microscales. Finally, working with plant geneticists, we transfer these concepts to demonstrate the advantages of simulations, for the example of rationalizing biotailoring of crops for improved lodging resistance. These objectives and motivation are elaborated in the following discussion.

Remark: The term *multiphase hierarchical system* is used for the combined representation of the multiphase hierarchical material and macrostructure domain that habitats it.

1.1 Thesis motivation

Analysis and design are two essential pillars of any engineering framework. Broadly speaking, analysis refers to examine any system's response for given external conditions at a desired level of accuracy for intended applications. Design algorithms, integrating insights from analysis, optimally allocate the limited resources to achieve the intended objectives, respecting the constraints imposed on the system. For example, in aerospace applications, composites are used to meet extreme thermomechanical demands that the system is anticipated to experience in its lifetime. Therefore, a highly accurate understanding of its mechanical behavior and rigorous optimization algorithms are imperative for efficient material use and cost savings. For multiphase hierarchical systems, the first step is to develop rigorous analysis and optimization methods balancing their predictive accuracy and computational feasibility.

From a multiscale analysis viewpoint, modeling the effective properties of microheterogeneous materials requires incorporating microstructure information. One approach is to use phenomenological models, for instance the framework of cellular solids, to estimate microstructure-function relationships from composition data such as apparent mass density [71, 73, 74]. The resulting models, however, require extensive empirical parameter tuning, which limits their use for applications involving multiphase hierarchical systems.

Full resolution of all relevant scales in the sense of direct numerical simulation is usually prohibitively expensive and only justified when high-fidelity solutions of problems with strongly localized phenomena are sought [78, 87, 120, 128]. Given the strong separation between the scales, computational homogenization in the context of the finite element (FE) method marks the starting point of efficient homogenization [58, 69, 211]. Bridging one scale is based on a series of fine-scale FE solutions computed numerically on a representative volume element (RVE) at each quadrature point of the coarse-scale FE mesh, motivating the widely used term FE^2 [57]. This approach often implies a prohibitive computational cost, limiting this approach to simple scenarios with no more than two scales [136, 137, 202].

In the context of design, topology optimization is an established framework for the optimal design of structures. Substantial progress has been made over the past few decades in topology optimization research [16, 17, 19, 163, 187]. These approaches are now industry standards for optimizing performances in a wide range of manufacturing, aerospace, marine, energy, and infrastructure applications [48, 97, 111, 118, 210]. Few recent studies have also focused on designing multiphase hierarchical systems in various contexts, including bone-remodeling, multi-functional materials, and bio-inspired functionally graded materials [33, 36, 67, 149, 186]. However, an exponential increase in design variables with each scale characterization in multiphase hierarchical systems restricts these approaches to scenarios where only the mesoscale is important.

It is evident that the existing computational approaches for analysis and optimization suffer the *curse of dimensionality* and the computational cost remains out of reach for multiphase hierarchical systems for practical engineering problems. Moreover, biological materials often exhibit a random microstructure with complex geometric characteristics of their constituents. Usually, only partial statistical information such as the volume fraction, the shape of constituents, and their interaction with other constituents is available. This *uncertainty and limited geometrical resolution* of scale poses theoretical limitations on the homogenized properties, and only adequate "estimates" can be derived.

Continuum micromechanics promises an excellent opportunity in tackling the outlined roadblocks [134, 167, 204]. Given the statistical description of an RVE, continuum micromechanics provides a rigorous foundation for deriving homogenized estimates for its mechanical properties. Due to its analytical nature, continuum micromechanics formulations are not

affected by the curse of dimensionality and are, therefore, able to rationally account for the hierarchical organization of multiscale materials in the sense of a multistep homogenization procedure without eluding feasible solution. Thus, continuum micromechanics can become a foundation for multiscale analysis and optimization methods that can balance the predictive accuracy and computational feasibility for multiphase hierarchical systems.

1.2 Research objectives

In this thesis, we mainly focus on the following three objectives to work towards our goal:

↪ **Objective 1:** Developing a continuum micromechanics-based approach of macroscopic strength and stiffness properties of a broad class of plant materials supported by microimages and chemical analysis data and extensively validating this approach with the reported experiments in the literature and performed experiments in the lab.

↪ **Objective 2:** Integrating results from the continuum micromechanics and topology optimization frontiers to establish rigorous theoretical foundations for an efficient concurrent material and structure optimization framework that can tackle the computing challenge of optimizing multiphase hierarchical systems, including elasto-plastic constituents at microscales.

↪ **Objective 3:** Showcasing the effectiveness of the developed multiscale analysis and optimization tools to gain insights into potential material and structure related traits that improve lodging resistance of cereals.

1.3 Thesis outline

This thesis is organized into three parts. Each part aims at the specific research objectives outlined in the previous section. Each part starts with an introduction section briefing the background literature and research questions that need to be addressed to accomplish the objective. Chapters 2, 3, and 4 constitute Part I. Chapters 5, 6, and 7 constitute Part II. Part III comprises of Chapters 8 and 9. These chapters are organized as follows:

↪ Chapter 2 reviews the foundational principles of multiscale analysis within the framework of continuum micromechanics. In particular, we summarize the essential schemes for estimating the homogenized elastic and inelastic properties of hierarchical systems with random microstructures. These schemes will constitute the central theme for subsequent chapters.

↪ In Chapter 3, we derive a multistep micromechanical approach for the macroscopic stiffness and strength properties of functionally-graded hierarchical culm materials with an example of bamboo. Model input data such as morphology and volume fractions of all heterogeneous components at each hierarchical level is retrieved from the imaging data (transmission electron microscopy, scanning electron microscopy, light microscopy, micro-CT scans) reported in the literature. The model is validated against the independent experiments reported by Dixon and Gibson for bamboo [49].

↪ Chapter 4 extends the micromechanical approach for material modeling of cereal stems with a configuration of an inner layer of foam-like parenchyma cells surrounded by a dense outer shell. From the application viewpoint of this thesis, we focus on oat stems. We experimentally profile using chemical analysis and microimaging, working with our collaborators in Plant Science and Genetics and Minnesota Dental Research Center for Biomaterials and Biomechanics at the University of Minnesota. We validate this model with a series of bending experiments that we conducted with oat stem samples.

↪ In Chapter 5, we formulate an end-compliance minimization (or stiffness maximization) based concurrent material and structure optimization approach for multiphase hierarchical systems that relies on homogenization estimates based on continuum micromechanics to account for material behavior across many different length scales. We establish that the computational cost does not explode exponentially with the number of hierarchical scales with our formulation. We illustrate this strength with the help of newly defined benchmark tests with several material scales that, for the first time, become computationally feasible via our framework.

↪ Chapter 6 establishes the opportunities provided by continuum micromechanics estimates in handling the path-dependent computationally prohibitive macroscale structure (topology) optimization problems with given elastoplastic multiphase hierarchical material definition. From an algorithmic implementation viewpoint, we also brief the finite element discretization of the initial boundary value problem, its linearization with the Newton-Raphson method, the closest point projection algorithm for integrating homogenized material constitutive relations, and path-dependent sensitivity analysis using the adjoint method.

↪ In Chapter 7, we, for the first time, establish the rigorous theoretical foundations of elastoplastic concurrent material and structure optimization, including suitable sub-problem formulations for elastoplastic material optimization based on the thermo-mechanical formulation of elastoplasticity. In particular, we develop an algorithmic procedure for the material optimization problem based on the maximum plastic dissipation principle in the format of a typical return mapping algorithm for elastoplastic

constitutive law. We verify the validity and efficiency of our formulation and associated algorithms with newly defined benchmark problems.

↪ Chapter 8 demonstrates the potential of our multiscale material model in understanding the multiscale origin of failure mechanisms of wheat and oat stems observed in a controlled wind tunnel experimental setting. These insights would not have been possible with a purely experimental approach. This chapter essentially explores the opportunities offered by the collaborative research efforts of computational mechanics and plant science in a broader context of breeding.

↪ In Chapter 9, we outline the potential of our optimization framework for engineering applications by reproducing naturally existing self-optimizing mechanisms in plants. We also reflect on the mechanistic perspective on the evolution of biological systems, indicating our framework's potential in the broader context of growth and self-adaption.

↪ Chapter 10 closes the discussion with broad conclusions and suggested future work.

PART I

Evidence-based multiscale material modeling of multiphase hierarchical systems

Introduction

From a multiscale analysis viewpoint, the cost for resolving hierarchical scales computationally, for instance through multiscale finite elements [52, 138, 139] or computational homogenization [24, 114, 119, 203], increases exponentially with each additional scale, making the computational treatment of multiphase hierarchical materials prohibitively expensive. The framework of analytical continuum micromechanics [134, 167, 204] constitutes an opportunity to derive microstructure-property relationships that rationally account for the multiscale levels of multiphase hierarchical materials in the sense of a multistep homogenization procedure. An important prerequisite for the applicability of continuum micromechanics is identifying hierarchical levels with a clear separation of length scales. In the context of plant biomaterials, this concept was used for the first time by Hofstetter and co-authors [92, 94] to predict stiffness and elastic limits of wood materials. In [11, 12], Bader and co-authors extended this model to incorporate poromechanical effects. We note that within the last decade, strength and stiffness models based on continuum micromechanics have been explored for many multiphase hierarchical materials, such as bone and cement [61, 62, 81, 84, 86, 132, 147].

In this first part, we establish a multistep homogenization approach in the continuum micromechanics framework for the macroscale stiffness and strength of multiphase hierarchical materials focusing on a broad class of plant materials. The hierarchical organization of plants is statistically characterized with the help of microimaging (micro-CT, scanning electron microscopy, light microscopy, transmission electron microscopy) and chemical analysis data. Our approach analytically transfers this statistical information of multiphase plant hierarchical materials, such as volume fraction, the shape of constituents, and interaction between constituents, into the estimates of associated macroscale properties. The approach is extensively validated against reported experiments in the literature and performed experiments in the lab.

This part is divided into three chapters. Chapter 2 briefs the foundational principles of continuum micromechanics with relevant schemes for estimating the homogenized stiffness and strength properties of microheterogeneous materials. These schemes will be used

frequently in the subsequent chapters. Chapter 3 derives a multistep micromechanical model for the macroscopic stiffness and strength properties of functionally-graded hierarchical culm materials for the example of bamboo. Due to its significance as an emerging sustainable building material, an extensive amount of data is available for bamboo in the recent literature, which we use to characterize the hierarchical organization of bamboo. We validate this approach against the independent experiments reported by Dixon and Gibson for bamboo [49]. In Chapter 4, we built upon the developed concepts for the micromechanical modeling of cereal stem materials, focusing on oats, which we experimentally characterize working with our collaborators in Plant Science and Genetics and Minnesota Dental Research Center for Biomaterials and Biomechanics at the University of Minnesota. We validate this model with a series of bending experiments that we conducted with oat stem samples.

Chapter 2

Multiscaling concepts in continuum micromechanics

In this chapter, we briefly review basic multiscale analysis principles with (semi-) analytical schemes for the homogenized stiffness and strength properties of microheterogeneous material. The chapter largely based on the excellent presentations given in [50, 51, 132, 166, 167, 176, 177, 204]. This chapter forms the basis of this thesis and frequent references will be made to this chapter throughout this work.

The chapter is organized as follows: Section 2.1 introduces the foundation principles of continuum micromechanics with an emphasis on the basic assumptions. Section 2.2 outlines the important schemes for the elastic homogenization, including cascade continuum micromechanics model for a broad class of matrix-inclusion problems. Finally, we discuss approaches for estimating homogenized elastoplastic properties focusing on the second order moment method and transformation field analysis (TFA) method.

2.1 Foundation principles

In this section, we describe key principles that form the foundation of continuum micromechanics. We specifically emphasize on the basic assumptions behind the concepts.

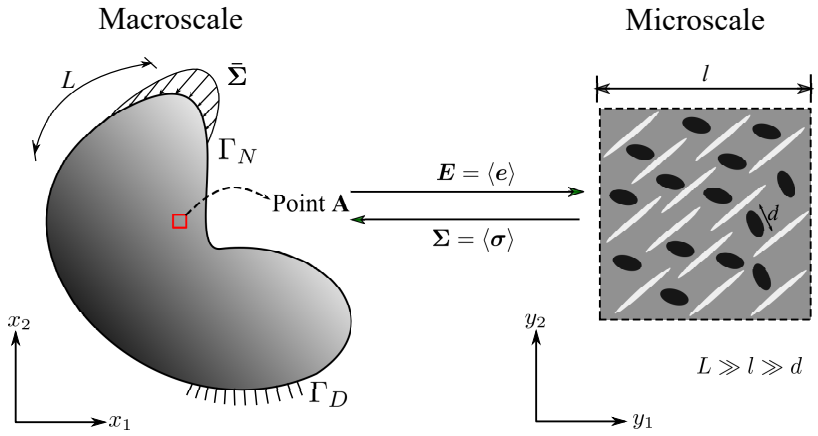

Fig. 2.1: *Homogenization and multiscale principles.*

2.1.1 Representative volume element (RVE) and scale separation

The goal of any homogenization method is to replace the actual complex heterogeneous medium with a fictitious homogeneous one that has equivalent global behavior. Figure 2.1 illustrates the key concepts. An important objective is to establish an "equivalent homogeneous element" whose mechanical response is equivalent to a representative volume element (RVE) of the microheterogeneous material. For the existence of such an RVE, a minimal requirement is that the characteristic length, d, of the considered inhomogeneities and deformation mechanisms is much smaller than the size, l, of the RVE. As a consequence, the RVE can be considered representative of the material in the macroscaleally homogeneous body (see Fig. 2.1). Moreover, l must be much smaller than the characteristic length scale of the variation in the loading on the macroscale structure, L. Therefore, proper scale separation implies that:

$$d \ll l \ll L. \tag{2.1}$$

We start with the variational form of the macroscale boundary value problem defined on a domain Ω as shown in Fig. 2.1. The domain is subjected to traction $\bar{\boldsymbol{\Sigma}}$ at the Neumann boundary Γ_N and prescribed displacements at the Dirichlet boundary Γ_D with a body force field $\boldsymbol{b}$. The weak form states: Find a macroscale displacement field $\bar{\boldsymbol{u}} \in U$ such that

$$\int_\Omega \boldsymbol{\Sigma}(\bar{\boldsymbol{u}}) : \boldsymbol{E}(\boldsymbol{v})\, d\Omega = \int_\Omega \boldsymbol{b} \cdot \boldsymbol{v}\, d\Omega + \int_{\Gamma_N} \bar{\boldsymbol{\Sigma}} \cdot \boldsymbol{v}\, ds, \quad \forall \boldsymbol{v} \in U, \tag{2.2}$$

where the space U of test and trial functions is kinematically admissible. A constitutive relation between the macroscale stress $\boldsymbol{\Sigma}$ and the macroscale strain $\boldsymbol{E}$ will close this

boundary value problem.

Figure 2.1 schematically illustrates the homogenization framework for establishing the relation between $\boldsymbol{\Sigma}$ and $\boldsymbol{E}$. The macroscale strain tensor $\boldsymbol{E}$ is calculated for each material point in the domain Ω. Next, $\boldsymbol{E}$ is utilized to formulate boundary conditions imposed on the microscale RVE. A numerical solution or an analytical estimate of the microscale boundary value problem will provide the macroscale stress tensor $\boldsymbol{\Sigma}$. The nature of boundary conditions on the microscale RVE is unknown, and that makes the microscale boundary value problem an "ill-posed" problem. Assumptions on the boundary conditions have to be made to define this boundary value problem.

2.1.2 Microscale problem and the choice of boundary conditions

According to the *homogeneous strain boundary conditions*, the RVE is subjected to the prescribed surface displacements $\boldsymbol{u}^g(\boldsymbol{x}, \bar{\boldsymbol{y}})$ at the boundary such that:

$$\boldsymbol{u}^g(\boldsymbol{x}, \bar{\boldsymbol{y}}) = \boldsymbol{E}(\boldsymbol{x}) \cdot \bar{\boldsymbol{y}}. \tag{2.3}$$

Here, any field $f(\boldsymbol{x}, \boldsymbol{y})$ denotes a microstructural field variation in the RVE domain Ω_y situated at a macroscale material point $\boldsymbol{x}$. The position vector at the boundary of the RVE is denoted by $\bar{\boldsymbol{y}}$. The corresponding kinematically compatible microscale trial strain field $\boldsymbol{e}(\boldsymbol{x}, \boldsymbol{y})$ inside the RVE fulfills an equivalent volume average as:

$$\langle \boldsymbol{e}(\boldsymbol{x}, \boldsymbol{y}) \rangle_{\Omega_y} = \frac{1}{|\Omega_y|} \int_{\Omega_y} \boldsymbol{e}(\boldsymbol{x}, \boldsymbol{y}) \, d\Omega_y = \boldsymbol{E}(\boldsymbol{x}). \tag{2.4}$$

Similarly, the *homogeneous stress boundary conditions* rely on the surface tractions $T^g(\boldsymbol{x}, \bar{\boldsymbol{y}})$ that are prescribed at the boundary and produce a constant stress $\boldsymbol{\Sigma}(\boldsymbol{x})$ in the fictitious homogeneous material at a point $\boldsymbol{x}$ as:

$$T^g(\boldsymbol{x}, \bar{\boldsymbol{y}}) = \boldsymbol{\Sigma}(\boldsymbol{x}) \cdot n, \tag{2.5}$$

where n is the unit outward normal at the boundary of the RVE. Any equilibrated trial stress field $\boldsymbol{\tau}(\boldsymbol{x}, \boldsymbol{y})$ in the RVE, that is, $\nabla_y \cdot \boldsymbol{\tau}(\boldsymbol{x}, \boldsymbol{y}) = 0$, obeys:

$$\langle \boldsymbol{\tau}(\boldsymbol{x}, \boldsymbol{y}) \rangle_{\Omega_y} = \frac{1}{|\Omega_y|} \int_{\Omega_y} \boldsymbol{\tau}(\boldsymbol{x}, \boldsymbol{y}) \, d\Omega_y = \boldsymbol{\Sigma}(\boldsymbol{x}). \tag{2.6}$$

We assume that all constituent phases in the RVE are linear elastic and perfectly bonded

with each other. This assumption allows us to define a strain-energy potential $\wp(\boldsymbol{y}, \boldsymbol{e})$ inside the RVE domain Ω_y as:

$$\wp(\boldsymbol{y}, \boldsymbol{e}) = \frac{1}{2}\boldsymbol{e}(\boldsymbol{x}, \boldsymbol{y}) : \mathbb{c}(\boldsymbol{x}, \boldsymbol{y}) : \boldsymbol{e}(\boldsymbol{x}, \boldsymbol{y}) \;\; \forall y \in \Omega_y, \tag{2.7}$$

where $\mathbb{c}(\boldsymbol{x}, \boldsymbol{y})$ defines the linear elastic tensor at the microscale RVE situated at the macroscale material point $\boldsymbol{x}$. The principle of minimum potential energy at the microscale RVE is based on the actual strain field $\boldsymbol{\varepsilon}$ in the RVE as:

$$\langle \frac{1}{2}\boldsymbol{\varepsilon} : \mathbb{c}(\boldsymbol{x}, \boldsymbol{y}) : \boldsymbol{\varepsilon} \rangle_{\Omega_y} = \min_{e \, \in \, \mathcal{K}(\boldsymbol{E}(\boldsymbol{x}))} \langle \frac{1}{2}\boldsymbol{e} : \mathbb{c}(\boldsymbol{x}, \boldsymbol{y}) : \boldsymbol{e} \rangle_{\Omega_y}, \tag{2.8}$$

where $\mathcal{K}$ is the set of kinematic admissible trial strain fields following the homogeneous strain boundary conditions defined in (2.3) and (2.4).

For the linear elastic constituent phases, the effective strain-energy potential $\mathcal{W}(\boldsymbol{x})$ at the macroscale is:

$$\mathcal{W}(\boldsymbol{x}) = \frac{1}{2}\boldsymbol{E}(\boldsymbol{x}) : \mathbb{C}(\boldsymbol{x}) : \boldsymbol{E}(\boldsymbol{x}), \tag{2.9}$$

where $\mathbb{C}(\boldsymbol{x})$ is the homogenized stiffness tensor at the macroscale material point $\boldsymbol{x}$. Following (2.8), (2.9), and Hill's Lemma, we conclude:

$$\boldsymbol{E}(\boldsymbol{x}) : \mathbb{C}(\boldsymbol{x}) : \boldsymbol{E}(\boldsymbol{x}) \;\; = \min_{\boldsymbol{e} \, \in \, \mathcal{K}(\boldsymbol{E}(\boldsymbol{x}))} \langle \boldsymbol{e} : \mathbb{c}(\boldsymbol{x}, \boldsymbol{y}) : \boldsymbol{e} \rangle_{\Omega_y}. \tag{2.10}$$

Essentially, relation (2.10) bridges the macro- and microscales. Given a complete material and geometric description of the RVE, (2.10) can be solved numerically. In the case of partial statistical information, however, only suitable estimates to $\mathbb{C}$ can be obtained, which we summarize in the following subsection. We can also derive an equivalent statement to (2.10) for the complementary stress potential with the statically admissible trial stress field set $\mathcal{T}$ as:

$$\boldsymbol{\Sigma}(\boldsymbol{x}) : [\mathbb{C}(\boldsymbol{x})]^{-1} : \boldsymbol{\Sigma}(\boldsymbol{x}) = \min_{\boldsymbol{\tau} \, \in \, \mathcal{T}(\boldsymbol{\Sigma}(\boldsymbol{x}))} \langle \boldsymbol{\tau} : [\mathbb{c}(\boldsymbol{x}, \boldsymbol{y})]^{-1} : \boldsymbol{\tau} \rangle_{\Omega_y}. \tag{2.11}$$

Remark: We would like to emphasize that the differences between the homogenized *estimates* originating from the choice of homogeneous boundary conditions (i.e., homogeneous stress or strain boundary conditions) decrease with decreasing d/l ratio in (2.1) and diminish with $d/l \to 0$. Therefore, given a strong separation of scale, a specific choice of

homogeneous stress or strain boundary condition does not affect the homogenization results. However, if (2.1) does not hold strongly, the choice of homogeneous boundary condition is very important. The homogeneous stress boundary conditions leads to a *lower bound*, while the homogeneous strain boundary conditions leads to an *upper bound* for the homogenized properties.

2.2 Estimation of homogenized elastic properties

In this section, we derive the homogenized elastic properties of the micro-heterogeneous material. First, we introduce the concept of strain and stress concentration tensors for a RVE with linear elastic base constituents. Then, we brief the Eshelby's matrix-inclusion solution based estimation of concentration tensors, and, hence, homogenized stiffness of the RVE [90, 109, 131, 185]. Finally, we focus on a broad class of matrix-inclusion problems introducing the cascade continuum micromechanics (CCM) model [176, 177].

2.2.1 Strain and stress concentration tensors

The linear constitutive relations for the constituent phases in the RVE imply that the trial strain and stress fields $(\boldsymbol{e}, \boldsymbol{\tau})$ must be linear and homogeneous with respect to $\boldsymbol{E}$ and $\boldsymbol{\Sigma}$. Therefore, $\boldsymbol{e}$ and $\boldsymbol{\tau}$ can be written in terms of the strain and stress concentration tensors $\mathbb{A}$ and $\mathbb{B}$ as:

$$\boldsymbol{e}(\boldsymbol{x}, \boldsymbol{y}) = \mathbb{A}(\boldsymbol{x}, \boldsymbol{y}) : \boldsymbol{E}(\boldsymbol{x}) \;\text{ and }\; \boldsymbol{\tau}(\boldsymbol{x}, \boldsymbol{y}) = \mathbb{B}(\boldsymbol{x}, \boldsymbol{y}) : \boldsymbol{\Sigma}(\boldsymbol{x}). \tag{2.12}$$

Using these relations in (2.10) and (2.11), we arrive at the following bounds:

$$\boldsymbol{E} : (\langle \mathbb{A}^T : \mathbb{c} : \mathbb{A} \rangle - \mathbb{C}) : \boldsymbol{E} \geq 0 \;\text{ and }\; \boldsymbol{\Sigma} : (\langle \mathbb{B}^T : [\mathbb{c}]^{-1} : \mathbb{B} \rangle - [\mathbb{C}]^{-1}) : \boldsymbol{\Sigma} \geq 0. \tag{2.13}$$

It is clear from (2.13) that the estimation of the concentration tensors $\mathbb{A}$ and $\mathbb{B}$ will result in the upper and lower bound for the homogenized stiffness $\mathbb{C}$. The simplest choice for $\mathbb{A}$ and $\mathbb{B}$ is to assume a uniform strain or stress state throughout the RVE. Mathematically, it means that $\mathbb{A} = \mathbb{I}$ or $\mathbb{B} = \mathbb{I}$, where $\mathbb{I}$ is a fourth-order symmetric unit tensor. This choice leads to the famous Voigt and Reuss estimates for the homogenized stiffness. However, the Voigt-Reuss bounds do not consider any other statistical information beyond the volume fraction of phases.

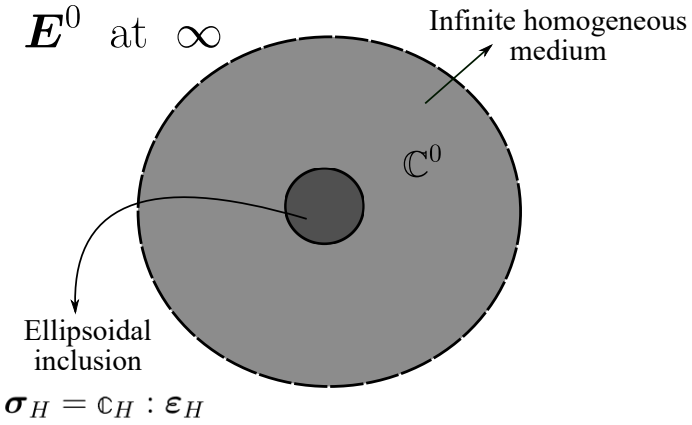

Fig. 2.2: *Eshelby matrix inclusion problem.*

2.2.2 Elastic homogenization based on Eshelby's analytical solution

Homogenization schemes based on Eshelby's matrix-inclusion solutions can incorporate the volume fraction, the shape of phases, and their interaction with each other. Eshelby's matrix-inclusion problem relates strains in an ellipsoidal inclusion perfectly bonded with the surrounded homogeneous infinite elastic matrix to the applied homogeneous strains at infinity (see Fig. 2.2). We denote the elastic moduli of the ellipsoidal inclusion and the matrix as $\mathbb{c}_H$ and $\mathbb{C}^0$, respectively. The strains in the inclusion in response to the homogeneous strain $\boldsymbol{E}^0$ at infinity are found to be uniform. The uniform strain field $\boldsymbol{\varepsilon}_H$ in the inclusion is:

$$\boldsymbol{\varepsilon}_H = [\mathbb{I} + \mathbb{P}^0_H : (\mathbb{c}_H - \mathbb{C}^0)]^{-1} : \boldsymbol{E}^0. \tag{2.14}$$

The Hill tensor $\mathbb{P}^0_H$ characterizes the morphology of the inclusion and its interaction with the surrounding matrix. $\mathbb{P}^0_H$ depends on the morphology, that is, the shape and orientation of the inclusion as well as the stiffness tensor of the reference matrix $\mathbb{C}^0$. Hill tensor can be computed as:

$$\mathbb{P}^0_{H,ijkl} = -\Big(\partial^2\Big(\int_H G^0_{ik}(x - x')dV'\Big)/\partial x_j \partial x_l\Big)_{(ij)(kl)}. \tag{2.15}$$

$G^0(x-x')$ is a Green's function that relates the displacement at point x in an infinite medium of stiffness $\mathbb{C}^0$ with a unit force applied at x'. The indices $(ij)(kl)$ refer to symmetrization with respect to (ij) and (kj). Analytical expressions for $\mathbb{P}^0_H$ can be found in [112, 113, 124].

An important conclusion from Eshelby's analytical solution is that the strain field in the inclusion is uniform. Given the uniform stiffness moduli of the phases in the RVE, we can

replace the stress and strain fields in the phases with the average stress and strain values $\boldsymbol{\sigma}_r$ and $\boldsymbol{\varepsilon}_r$, respectively. Following (2.4) and (2.6), we write $\boldsymbol{E}$ and $\boldsymbol{\Sigma}$ in terms of $\boldsymbol{\varepsilon}_r$ and $\boldsymbol{\sigma}_r$ as:

$$\boldsymbol{E} = \sum_r \phi_r \boldsymbol{\varepsilon}_r \quad \text{and} \quad \boldsymbol{\Sigma} = \sum_r \phi_r \boldsymbol{\sigma}_r, \tag{2.16}$$

where ϕ_r is the volume fraction of the phase r. Following (2.4), we can relate the micro-strain average $\boldsymbol{\varepsilon}_r$ in the phase r and the macroscale strain $\boldsymbol{E}$ with the help of an average concentration strain tensor $\mathbb{A}_r$:

$$\boldsymbol{\varepsilon}_r = \mathbb{A}_r : \boldsymbol{E}. \tag{2.17}$$

We combine (2.16) and (2.17) with the phase constitutive relation $\boldsymbol{\sigma}_r = \mathbb{c}_r : \boldsymbol{\varepsilon}_r$. Comparison with the macroscale constitutive relation $\boldsymbol{\Sigma} = \mathbb{C} : \boldsymbol{E}$ yields the homogenized estimate of stiffness in terms of the volume fraction, stiffness, and localization tensor of constituent phases as:

$$\mathbb{C} = \sum_r \phi_r \mathbb{c}_r : \mathbb{A}_r. \tag{2.18}$$

For the estimation of $\mathbb{A}_r$, we approximate the average strains in each phase r by the inclusion strains $\boldsymbol{\varepsilon}_H$ in (2.14), i.e., $\boldsymbol{\varepsilon}_r = \boldsymbol{\varepsilon}_H$. It implies that the average strains $\boldsymbol{\varepsilon}_r$ in each phase of the RVE are considered equal to those of an ellipsoidal inhomogeneity with the phase stiffness $\mathbb{c}_r$, embedded in a fictitious infinite matrix with stiffness $\mathbb{C}^0$, subjected to some homogeneous strain $\boldsymbol{E}^0$ applied at infinity. Using the strain average rule in (2.16), we find a relation between the homogenized macroscale strain $\boldsymbol{E}$ and the homogeneous strain $\boldsymbol{E}^0$ at infinity in the fictitious matrix as:

$$\boldsymbol{E}^0 = \Big\{ \sum_r \phi_r [\mathbb{I} + \mathbb{P}_r^0 : (\mathbb{c}_r - \mathbb{C}^0)]^{-1} \Big\}^{-1} : \boldsymbol{E}. \tag{2.19}$$

With $\boldsymbol{\varepsilon}_r = \boldsymbol{\varepsilon}_H$, the substitution of $\boldsymbol{E}^0$ in (2.14) and the comparison with (2.17) yields the following estimate of the concentration strain tensor $\mathbb{A}_r$:

$$\mathbb{A}_r = [\mathbb{I} + \mathbb{P}_r^0 :(\mathbb{c}_r - \mathbb{C}^0)]^{-1} : \Big\{ \sum_r \phi_r [\mathbb{I} + \mathbb{P}_r^0 : (\mathbb{c}_r - \mathbb{C}^0)]^{-1} \Big\}^{-1}. \tag{2.20}$$

The expression for the homogenized stiffness $\mathbb{C}$ follows from (2.18) as:

$$\mathbb{C} = \sum_r \phi_r \mathbb{c}_r : [\mathbb{I} + \mathbb{P}_r^0 : (\mathbb{c}_r - \mathbb{C}^0)]^{-1} : \Big[\sum_s \phi_s [\mathbb{I} + \mathbb{P}_s^0 : (\mathbb{c}_s - \mathbb{C}^0)]^{-1} \Big]^{-1} . \tag{2.21}$$

In (2.20) and (2.21), $\mathbb{C}^0$ accounts for the influence that inclusions have on each other in the RVE. If one of the phases assumes the role of the matrix for other phases, that is, $\mathbb{C}^0 = \mathbb{c}_M$, where $\mathbb{c}_M$ represents the stiffness of the matrix phase, the homogenization method is called the **Mori-Tanaka** scheme [131, 185]. Another way to capture this influence is averaging the response of all phases in the sense of a virtual matrix material, that is, $\mathbb{C}^0 = \mathbb{C}$. This homogenization method is known as the **self-consistent scheme** [90, 109]. It is particularly useful in the morphologically disordered case, for instance, when several phases are present that interpenetrate each other such that a clear distinction between matrix and inclusions is impossible.

2.2.3 Cascade continuum micromechanics model for a broad class of matrix-inclusion problems

Many pore morphologies specifically at higher porosities can not be suitably represented by either the Mori-Tanaka scheme or the self-consistent scheme. On the one hand, the Mori-Tanaka scheme assumes inclusions to be completely isolated with a continuous matrix, and this completely connected matrix contributes to the overall stiffness even at a very high volume fraction of the inclusions. Therefore, it largely overestimates the elastic properties at higher inclusion volume fractions. On the other hand, the self-consistent scheme assumes phases to be perfectly in contact with each other. Beyond a certain volume fraction of inclusions, however, the matrix does not have a sufficient volume fraction to form a connected matrix to resist material failure. Therefore, the self-consistent scheme leads to physically meaningless homogenization estimates above a particular inclusion volume fraction [191].

Timothy and Meschke proposed the cascade continuum micromechanics (CCM) model to estimate elastic properties for a broad range of inclusion volume fractions [176, 177]. In the CCM model (see Fig. 2.3), a set of matrix-inclusion problems are obtained through recursion. The CCM model is inspired by the self-consistent scheme. Instead of the virtual "average" matrix phase, the stiffness of the matrix phase at cascade level n is recursively updated and set equal to the previously homogenized stiffness (see Fig. 2.3). At all cascade levels, inclusion properties are assumed to remain the same.

We assume that there are two phases in a RVE, namely inclusion and matrix, with volume fractions ϕ_{ic} and ϕ_m, respectively, and $\phi_{ic}+\phi_m = 1$. We denote inclusion and matrix stiffness

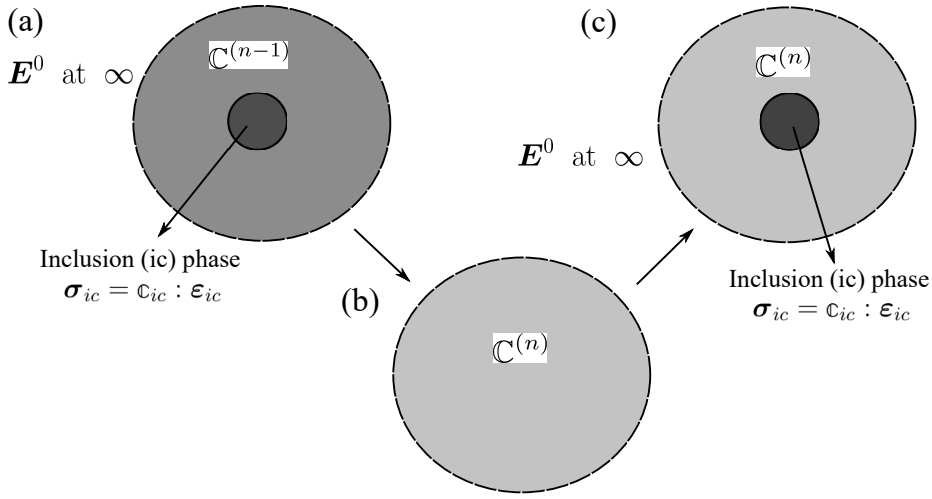

Fig. 2.3: *Outline of the cascade continuum micromechanics scheme: (a) matrix-inclusion problem with matrix stiffness $\mathbb{C}^{(n-1)}$, (b) homogenized composite with stiffness $\mathbb{C}^{(n)}$, (c) matrix-inclusion problem with updated matrix stiffness $\mathbb{C}^{(n)}$ obtained from step (b) (for more details see [176]).*

properties with $\mathbb{c}_{ic}$ and $\mathbb{c}_m$, respectively. Following (2.20) and (2.21), we can write the homogenized stiffness $\mathbb{C}^{(n)}$ at cascade level n after setting the matrix stiffness equal to the homogenized stiffness obtained from the previous homogenization step ($\mathbb{C}^0 = \mathbb{c}_m = \mathbb{C}^{(n-1)}$) as:

$$\begin{aligned}\mathbb{C}^{(n)} =& \Big[\phi_m\, \mathbb{C}^{(n-1)} + \phi_{ic}\, \mathbb{c}_{ic} : [\mathbb{I} + \mathbb{P}_{ic}^{(n-1)} : (\mathbb{c}_{ic} - \mathbb{C}^{(n-1)})]^{-1}\Big] : \\ & \Big[\phi_m\, \mathbb{I} + \phi_{ic}\, [\mathbb{I}\ + \mathbb{P}_{ic}^{(n-1)} : (\mathbb{c}_{ic} - \mathbb{C}^{(n-1)})]^{-1}\Big]^{-1}.\end{aligned} \tag{2.22}$$

The Hill tensor $\mathbb{P}_{ic}^{(n-1)}$ describes the morphological description of the inclusion in the matrix with elastic stiffness $\mathbb{C}^{(n-1)}$.

Equation (2.22) represents the recursive equation for the homogenized stiffness of the RVE. The initial configuration at $n = 1$ is assumed to be a continuous matrix with a disconnected distribution of the inclusions. The homogenized elastic properties for $n = 1$ is provided by the Mori-Tanaka scheme ($\mathbb{C}^{(1)} = \mathbb{C}^{MT}$). The Mori-Tanaka estimate C^{MT} of the configuration at $n = 1$ can be obtained from (2.21) with $\mathbb{C}^0 = \mathbb{c}_m$ and $r \in \{ic, m\}$. We summarize the algorithm for cascade levels $n = 1$ and $n = 2$:

$$\begin{aligned}\text{n = 1:}\quad & \mathbb{C}^{(n-1)} = \mathbb{c}_m \\ & \mathbb{C}^{(1)} = \mathbb{C}^{MT} = \Big[\phi_m\, \mathbb{c}_m + \phi_{ic}\, \mathbb{c}_{ic} : [\mathbb{I} + \mathbb{P}_{ic}^{m} : (\mathbb{c}_{ic} - \mathbb{c}_m)]^{-1}\Big] : \\ & \Big[\phi_m\, \mathbb{I} + \phi_{ic}[\mathbb{I} + \mathbb{P}_{ic}^{m} : (\mathbb{c}_{ic} - \mathbb{c}_m)]^{-1}\Big]^{-1},\end{aligned} \tag{2.23a}$$

$$
\begin{aligned}
\text{n = 2:} \quad & \mathbb{C}^{(n-1)} = \mathbb{C}^{(1)} \\
& \mathbb{C}^{(2)} = \Big[\phi_m\ \mathbb{C}^{(1)} + \phi_{ic}\ \mathbb{c}_{ic} : [\mathbb{I} + \mathbb{P}_{ic}^{(1)} : (\mathbb{c}_{ic} - \mathbb{C}^{(1)})]^{-1}\Big] : \\
& \Big[\phi_m\ \mathbb{I} + \phi_{ic}[\mathbb{I} + \mathbb{P}_{ic}^{(1)} : (\mathbb{c}_{ic} - \mathbb{C}^{(1)})]^{-1}\Big]^{-1}.
\end{aligned}
\tag{2.23b}
$$

The cascade level n can be thought of as a reflection of the connectivity of the inclusion phase. $n = 1$ represents the isolated inclusions in a continuous matrix (the Mori-Tanaka estimate). $n \to \infty$ represents a completely intermixed inclusion phase (the self-consistent estimate). This feature enables CCM to predict homogenization estimates for a large range of volume fractions of the inclusion phase with different microstructure quality.

2.3 Estimation of homogenized inelastic properties

In this section, we briefly review classical homogenization methods to predict the inelastic behavior of the RVE from the constitutive behavior of their base constituents and geometric information about their microstructure. First, we discuss the second order moment of strain field based homogenization of the elastic limit strength [165, 166]. Later, we brief a general approach based on transformation field analysis for the homogenization of inelastic properties [50, 51, 132].

2.3.1 Homogenization of the elastic limit strength

A macroscale RVE reaches the elastic limit state when any one of the constituents in the RVE yields. Let us focus on the weakest constituent phase, denoted by index $r = w$. We assume that its elastic limit behavior is described by the folllowing failure criterion

$$
\mathfrak{f}_w(\boldsymbol{\sigma}_w) \leq 0, \tag{2.24}
$$

where $\boldsymbol{\sigma}_w$ is the stress distribution in the weak phase w. We write $\boldsymbol{\sigma}_w$ in terms of the effective strain $\boldsymbol{\varepsilon}_w^*$ with the help of the elasticity tensor $\mathbb{c}_w$ as:

$$
\boldsymbol{\sigma}_w = \mathbb{c}_w : \boldsymbol{\varepsilon}_w^* \,. \tag{2.25}
$$

A natural choice for the effective strain tensor $\boldsymbol{\varepsilon}_w^*$ would be the average phase strain introduced in (2.17). However, microscopic failure is governed by "peak strains" rather than by "average strains." The strain peaks in phase w can be estimated with the second-order moment of the strain field in this phase, which is the quadratic strain average $\overline{\overline{\boldsymbol{\varepsilon}}}_w$ over the phase volume V_w expressed as:

$$\boldsymbol{\varepsilon}_w^* = \overline{\overline{\boldsymbol{\varepsilon}}}_w = \langle \boldsymbol{\varepsilon} : \boldsymbol{\varepsilon} \rangle_w^{1/2} = \Big(\frac{1}{V_w} \int_{V_w} \frac{1}{2} \boldsymbol{\varepsilon} : \boldsymbol{\varepsilon} \, dV \Big)^{1/2} . \tag{2.26}$$

The stress tensor $\boldsymbol{\sigma}_w$ can be computed in the weak phase with the effective strain $\boldsymbol{\varepsilon}_w^*$, which allows us to evaluate the failure criterion for the weak phase from (2.24). $\mathbb{C}$ represents the overall stiffness of the RVE as a function of the elastic stiffness coefficients of the individual constituent phases. The elastic coefficients, the bulk modulus and the shear modulus, of the weak phase with the volume fraction $\overline{\phi}_w$ are denoted by k_w and μ_w, respectively. Following [166], the von Mises equivalent strain $\varepsilon_{eq(w)}$ of the quadratic strain average $\overline{\overline{\boldsymbol{\varepsilon}}}_w$ can be related to the macroscopic strains $\boldsymbol{E}$ imposed on the boundary of the RVE as:

$$\langle \varepsilon_{eq(w)}^2 \rangle = \frac{1}{3\overline{\phi}_w} \boldsymbol{E} : \frac{\partial \mathbb{C}}{\partial \mu_w} : \boldsymbol{E} . \tag{2.27}$$

If $\mathfrak{f}_w$ is a scalar deviatoric stress-based failure criterion such as the von Mises criterion, then it can be expressed in terms of the macroscopic strains $\boldsymbol{E}$ with the help of (2.27). With $\boldsymbol{E} = [\mathbb{C}]^{-1} : \boldsymbol{\Sigma}$, the weak phase criterion $\mathfrak{f}_w$ translates to the macroscopic failure criterion $\mathfrak{F}$ as:

$$\mathfrak{F}(\boldsymbol{\Sigma}) \ = \leq 0 . \tag{2.28}$$

We note that the limiting stress level $\boldsymbol{\Sigma}$ in (2.28) is the elastic limit strength of the RVE.

2.3.2 Transformation field analysis (TFA) based upscaling of plastic strains

The previous approach is limited to cases with relatively simple morphology of RVEs with scalar deviatoric stress-based failure criterion for constituent phases. Dvorak and Benveniste [50, 51] proposed a fundamental approach called "Transformation field analysis" for the homogenization of more complex morphologies with generic elastoplastic constitutive behavior for the constituent phases in the RVE. The approach basically exploits the kinematically incompatible nature of plastic microtrains and treats them as free strains

or eigenstrains. We revisit these concepts briefly in this section.

We, first, assume a general elastoplastic behavior for the constituent phases. In each phase r, the average microscopic stress $\boldsymbol{\sigma}_r$, the average microscopic strain $\boldsymbol{\varepsilon}_r$, the average plastic strain $\boldsymbol{\varepsilon}_r^p$ and the phase stiffness $\mathbb{c}_r$ are related as:

$$\boldsymbol{\sigma}_r = \mathbb{c}_r : (\boldsymbol{\varepsilon}_r - \boldsymbol{\varepsilon}_r^p). \tag{2.29}$$

For phase r, we assume a suitable yield criterion $\mathfrak{f}_r(\boldsymbol{\sigma}_r)$ and an ideal associated flow rule,

$$d\boldsymbol{\varepsilon}_r^p = d\lambda_r \frac{\partial \mathfrak{f}_r}{\partial \boldsymbol{\sigma}_r}, \tag{2.30}$$

where λ_r denotes the plastic multiplier. The flow rule is accompanied by loading-unloading conditions,

$$d\lambda_r \mathfrak{f}_r(\boldsymbol{\sigma}_r) = 0, \quad d\lambda_r \geq 0, \quad \mathfrak{f}_r(\boldsymbol{\sigma}_r) \leq 0. \tag{2.31}$$

Next, kinematically incompatible plastic micro-strains $\boldsymbol{\varepsilon}_r^p$ are considered as free strains [50, 51]. Therefore, the phase strains $\boldsymbol{\varepsilon}_r$ can be related linearly to the macroscopic strains $\boldsymbol{E}$ and the free strains $\boldsymbol{\varepsilon}_r^p$ through a concentration tensor $\mathbb{A}_r$ and the influence tensors $\mathbb{D}_{rs}$:

$$\boldsymbol{\varepsilon}_r = \mathbb{A}_r : \boldsymbol{E} + \sum_s \mathbb{D}_{rs} : \boldsymbol{\varepsilon}_s^p \tag{2.32}$$

Here, the plastic strains $\boldsymbol{\varepsilon}_s^p$ are uniform in each phase s. Hence, they cannot represent complex plastic flow patterns that result from the morphology or the anisotropy of the phases. One can, however, divide the RVE into many sub-volumes such that complex plastic flow patterns in each phase can be approximated by varying uniform plastic strains in each sub-volume [62, 132].

The homogenized macroscopic stress and strains, $\boldsymbol{\Sigma}$ and $\boldsymbol{E}$, are related with the homogenized macroscopic stiffness tensor $\mathbb{C}$ and macroscopic plastic strain tensor $\boldsymbol{E}^p$ as:

$$\boldsymbol{\Sigma} = \mathbb{C} : (\boldsymbol{E} - \boldsymbol{E}^p). \tag{2.33}$$

Using (2.29), (2.16) and (2.33), the macroscopic plastic strain $\boldsymbol{E}^p$ can be expressed as:

$$\boldsymbol{E}^p = -[\mathbb{C}]^{-1} : \left\{ \sum_r \phi_r \mathbb{c}_r : \left(\left[\mathbb{A}_r : \boldsymbol{E} + \sum_s \mathbb{D}_{rs} : \boldsymbol{\varepsilon}_s^p \right] - \boldsymbol{\varepsilon}_r^p \right) \right\} + \boldsymbol{E}. \tag{2.34}$$

The estimation of concentration and influence tensors, $\mathbb{A}_r$ and $\mathbb{D}_{rs}$, in (2.34) leads us to the sought homogenized elastoplastic constitutive law (2.33). We depart from our discussion in Section 2.2.2 for the estimation.

Following Kröner [110], we assume that the plastic strains in each phase can be interpreted as a "stress-free strain." In this case, $\boldsymbol{\varepsilon}_r^p$ can be treated as an independent loading parameter. We refer to (2.14) for the estimation of strain field $\boldsymbol{\varepsilon}_H$ in the inclusion. With $\boldsymbol{\varepsilon}_H^p$ and $\boldsymbol{E}^{0,p}$ as the plastic free-strains in the inclusion and surrounding infinite matrix, $\boldsymbol{\varepsilon}_H$ can be estimated by augmenting (2.14) following [204] as:

$$\boldsymbol{\varepsilon}_H = [\mathbb{I} + \mathbb{P}_H^0 : (\mathbb{c}_H - \mathbb{C}^0)]^{-1} : [\boldsymbol{E}^0 + \mathbb{P}_H^0 : (\mathbb{c}_H : \boldsymbol{\varepsilon}_H^p - \mathbb{C}^0 : \boldsymbol{E}^{0,p})]. \tag{2.35}$$

Similar to (2.19), the relation between the macroscopic strain $\boldsymbol{E}$ and the uniform strain $\boldsymbol{E}^0$ applied at infinity reads as:

$$\begin{aligned} \boldsymbol{E}^0 =& \Big\{ \sum_r \phi_r [\mathbb{I} + \mathbb{P}_r^0 : (\mathbb{c}_r - \mathbb{C}^0)]^{-1} \Big\}^{-1} : \\ & \Big\{ \boldsymbol{E} - \sum_s \phi_s [\mathbb{I} + \mathbb{P}_s^0 : (\mathbb{c}_s - \mathbb{C}^0)]^{-1} : [\mathbb{P}_s^0 : (\mathbb{c}_s : \boldsymbol{\varepsilon}_s^p - \mathbb{C}^0 : \boldsymbol{E}^{0,p})] \Big\}. \end{aligned} \tag{2.36}$$

With $\boldsymbol{\varepsilon}_r = \boldsymbol{\varepsilon}_H$, substitution of $\boldsymbol{E}^0$ in (2.35) yields:

$$\begin{aligned} \boldsymbol{\varepsilon}_r =& [\mathbb{I} + \mathbb{P}_r^0 : (\mathbb{c}_r - \mathbb{C}^0)]^{-1} : \Big\{ \Big\{ \sum_i \phi_i [\mathbb{I} + \mathbb{P}_i^0 : (\mathbb{c}_i - \mathbb{C}^0)]^{-1} \Big\}^{-1} : \\ & \Big\{ \boldsymbol{E} - \sum_s \phi_s [\mathbb{I} + \mathbb{P}_s^0 : (\mathbb{c}_s - \mathbb{C}^0)]^{-1} : [\mathbb{P}_s^0 : (\mathbb{c}_s : \boldsymbol{\varepsilon}_s^p - \mathbb{C}^0 : \boldsymbol{E}^{0,p})] \Big\} + \\ & \mathbb{P}_r^0 : (\mathbb{c}_r : \boldsymbol{\varepsilon}_r^p - \mathbb{C}^0 : \boldsymbol{E}^{0,p}) \Big\}. \end{aligned} \tag{2.37}$$

When the RVE is in a fully elastic state, all plastic strain components in (2.37) vanish.

The estimation of plastic free strain $\boldsymbol{E}^{0,p}$ remains to be discussed. In the Mori-Tanaka scheme, we assume the plastic free strain $\boldsymbol{E}^{0,p}$ as a free strain in the matrix phase denoted as $\boldsymbol{\varepsilon}_M^p$. Applying the **Mori-Tanaka** assumptions in (2.37), the average microscopic strain $\boldsymbol{\varepsilon}_r$ in phase r becomes:

$$\begin{aligned} \boldsymbol{\varepsilon}_r =& [\mathbb{I} + \mathbb{P}_r^0 : (\mathbb{c}_r - \mathbb{c}_M)]^{-1} : \Big\{ \Big\{ \sum_i \phi_i [\mathbb{I} + \mathbb{P}_i^0 : (\mathbb{c}_i - \mathbb{c}_M)]^{-1} \Big\}^{-1} : \\ & \Big\{ \boldsymbol{E} - \sum_s \phi_s [\mathbb{I} + \mathbb{P}_s^0 : (\mathbb{c}_s - \mathbb{c}_M)]^{-1} : [\mathbb{P}_s^0 : (\mathbb{c}_s : \boldsymbol{\varepsilon}_s^p - \mathbb{c}_M : \boldsymbol{\varepsilon}_M^p)] \Big\} + \\ & \mathbb{P}_r^0 : (\mathbb{c}_r : \boldsymbol{\varepsilon}_r^p - \mathbb{c}_M : \boldsymbol{\varepsilon}_M^p) \Big\}. \end{aligned} \tag{2.38}$$

where $\mathbb{C}^0 = \mathbb{c}_M$ represents the stiffness of the matrix phase that incorporates the perturbed far-field strain state.

In the **self-consistent scheme**, the fictitious matrix does not have any volume fraction. Hence, it cannot accumulate any free strain. A natural choice is therefore to assume $\boldsymbol{E}^{0,p}$ equal to zero [62]. Applying these assumptions in (2.37), the average microscopic strain of the self-consistent scheme becomes:

$$\begin{aligned}\boldsymbol{\varepsilon}_r =&[\mathbb{I} + \mathbb{P}_r^0 : (\mathbb{c}_r - \mathbb{C})]^{-1} : \Big\{ \Big\{ \sum_i \phi_i [\mathbb{I} + \mathbb{P}_i^0 : (\mathbb{c}_i - \mathbb{C})]^{-1} \Big\}^{-1} : \\ &\Big\{ \boldsymbol{E} - \sum_s \phi_s [\mathbb{I} + \mathbb{P}_s^0 : (\mathbb{c}_s - \mathbb{C})]^{-1} : \mathbb{P}_s^0 : \mathbb{c}_s : \boldsymbol{\varepsilon}_s^p \Big\} + \mathbb{P}_r^0 : \mathbb{c}_r : \boldsymbol{\varepsilon}_r^p \Big\}.\end{aligned} \tag{2.39}$$

Comparing (2.38) and (2.39) with (2.32), we can identify the concentration and influence tensors $\mathbb{A}_r$ and $\mathbb{D}_{rs}$. This eventually estimates the homogenized macroscopic elastoplastic law (2.33).

Chapter 3

Multiscale modeling of stiffness and strength of hierarchical culm materials

In this chapter, we present a micromechanics approach that derives a hierarchical microstructure driven model of the macroscopic stiffness and strength properties of functionally-graded hierarchical culm materials. As model input, it requires mechanical properties of the base constituents such as cellulose and lignin as well as morphology and volume fractions of all heterogeneous components at each hierarchical level. The latter can be retrieved from imaging data at different length scales, obtained from scanning electron and transmission electron microscopy. We illustrate our modeling approach for the example of bamboo that has gained increasing attention in the last decade due to its role as a sustainable building material. Validating its predictions of macroscopic stiffness moduli and ultimate strength with corresponding experimental measurements, we demonstrate that the micromechanics model provides excellent accuracy without any further phenomenological calibration. We also show that the multiscale modeling approach enables a better physics-based understanding of the origins of bamboo stiffness and strength across different scales.

The chapter is organized as follows: In Section 3.1, we discuss the multiscale nature of culm materials for the example of bamboo, using microimaging results from the literature to illustrate properties of bamboo microstructure at different length scales. In Section 3.2, we transfer the identified hierarchical scales into a multistep micromechanical representation. Section 3.3 explains the multistep procedure for the elastic stiffness coefficients based on the concepts developed in the previous chapter. Section 3.4 describes the estimation of

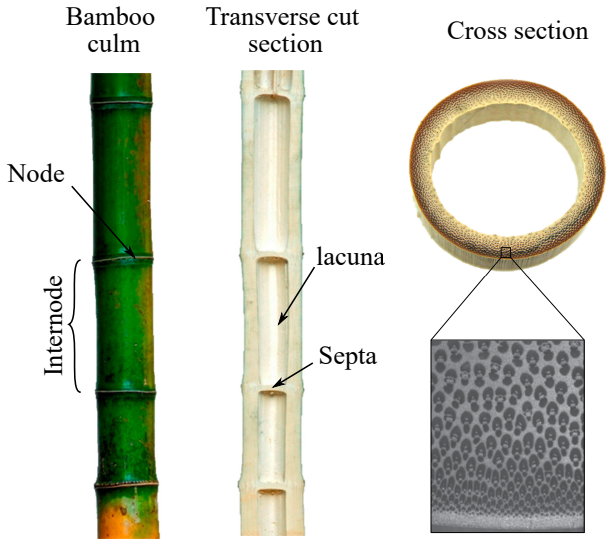

Fig. 3.1: *Macroscale anatomy of a bamboo culm.*

macroscopic strength properties outlining the essential modeling assumptions and their motivation from a plant mechanics viewpoint. Focusing on bamboo in Section 3.5, we discuss the identification of model parameters, compare stiffness and strength results obtained from our model with experimental data reported in the literature and show that they can contribute to a better physics-based understanding of the origins of stiffness and strength of bamboo across different scales.

3.1 Multiscale characterization through microimaging

Bamboo is a prominent member of the grass family *Poaceae*. Its culm (or stem) as illustrated in Fig. 3.1 is cylindrical, hollow, and divided into nodes and internodes. At the nodes, a diaphragm (septa) is formed which divides the culm in transverse direction. The main mechanical function of the septa is to prevent Brazier buckling initiated by ovalization of the cross section during bending [159]. In contrast to wood, bamboo does not show secondary growth, which restricts geometric adaption and increases the need for structural optimization at the material level [7, 116].

For a physics-based prediction of the mechanical behavior of bamboo material, its characterization in terms of its multiscale hierarchical composition is a key prerequisite for micromechanics modeling. Figure 1.1 illustrates the typical hierarchical organization of bamboo culm material. Each hierarchical scale can be characterized by suitable microimaging technologies. The corresponding images are essential to derive key parameters required by our modeling approach. In the following, we briefly describe the heterogeneous microstruc-

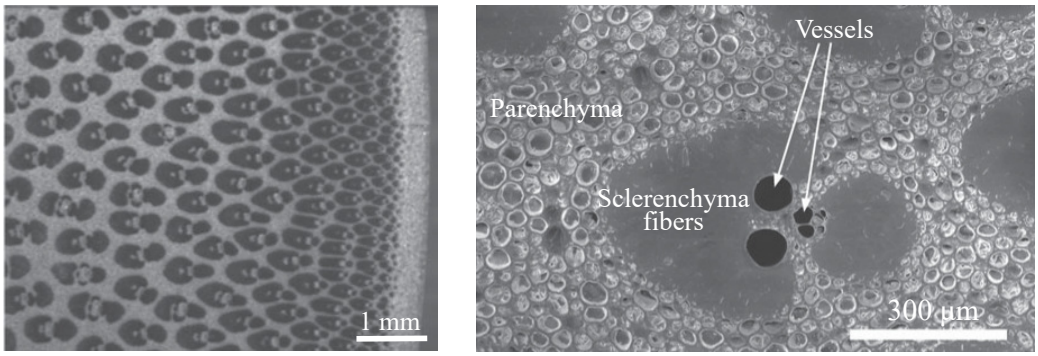

(a) Graded density of vascular bundles.

(b) Microstructure of an individual vascular bundle.

Fig. 3.2: *SEM images depicting the radial gradation within the bamboo cross section and the typical structure of a vascular bundle. The images are reported by* Mannan, Knox *and* Basu *[121] and* Gibson *and* Dixon *[49] and reproduced with kind permission from Royal Society Publishing.*

tures that are found at each hierarchical scale and illustrate them with corresponding imaging data taken from the literature. We also provide a brief account on how we choose the elastic and failure properties of the base materials cellulose, hemicellulose and lignin that stem from mechanisms at the nano- and atomic scale.

3.1.1 Macroscale: cross section

The macroscopic observation level corresponds to a length scale of several millimeters to centimeters. At this scale, the bamboo *cross section* is characterized by vascular bundle tissues whose main axis is parallel to the longitudinal direction of the stem. They are embedded in a matrix made up of parenchyma tissue. As illustrated in Fig. 3.1, the density of vascular bundles increases in radial direction of the circular cross section. This distribution of bundles can be quantified with the help of scanning electron microscopy (SEM). Figure 3.2a shows an example microimage that illustrates the grading of vascular bundles in radial direction, given by Mannan, Knox and Basu [121].

3.1.2 Mesoscale: functional regions

A *vascular bundle* has a diameter of the order of 100μm. It consists of xylem and phloem tissues surrounded by sclerenchyma fiber sheath. Xylems and phloems are responsible for transportation of nutrients and water into the plant. Sclerenchyma fibers provide support to the xylem and phloem vessels. The volumetric contribution and morphology of fibers and

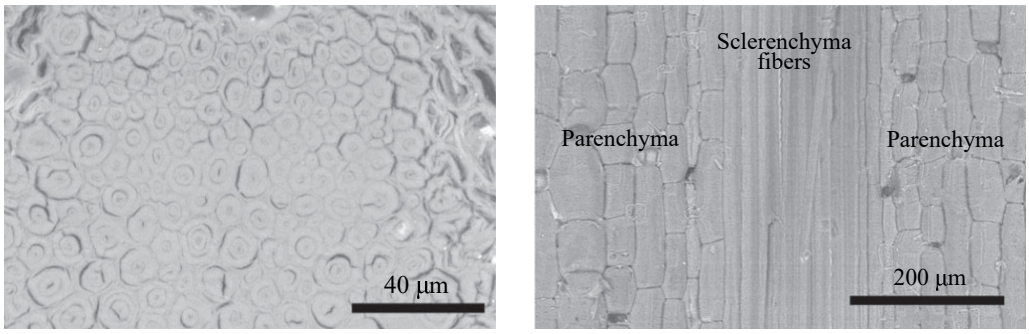

(a) Sclerenchyma fibers (transverse cut).

(b) Sclerenchyma fibers and surrounding parenchyma (longitudinal cut).

Fig. 3.3: *SEM images showing thick cell and long sclerenchyma fibers surrounded by parenchyma matrix tissue. The images are reported by* Gibson *and* Dixon *[49] and reproduced with kind permission from Royal Society Publishing.*

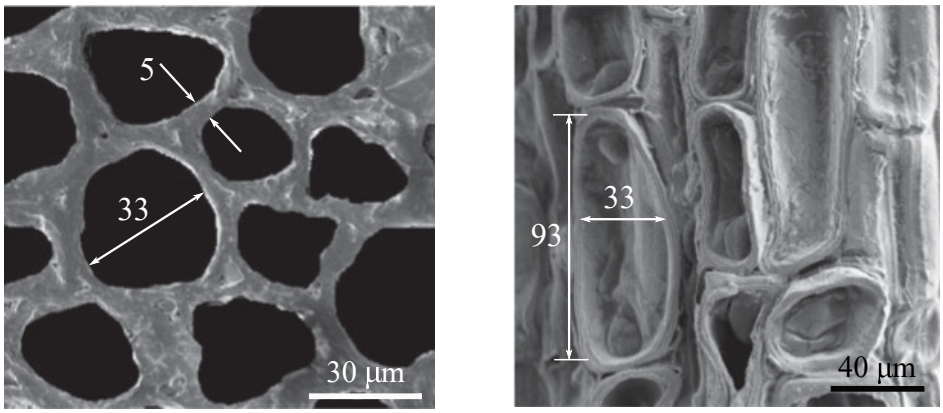

(a) Parenchyma cells (transverse cut).

(b) Parenchyma cells (longitudinal cut).

Fig. 3.4: *SEM images showing the internal structure of parenchyma cells. The images are reported by* Mannan, Knox *and* Basu *[121] and reproduced with kind permission from Royal Society Publishing under the license CC BY 4.0.*

vessels in vascular bundles can be determined by SEM images at a suitable scale. Figure 3.2b, which is provided by Gibson and Dixon [49], shows an example of a SEM image.

The *sclerenchyma cells* in the fibers are long hollow tubes oriented in the stem direction with a characteristic length scale in the order of $10 - 20\mu$m. Sclerenchyma cells have thick cell walls surrounding holes (lumen) with a polygonic or circular cross section. The thickness of the cell wall in the sclerenchyma cells varies radially in the cross-section. These characteristics of the sclerenchyma fibers can be quantified with the help of SEM images such as the ones in Figs. 3.3a and 3.3b given by Gibson and Dixon [49].

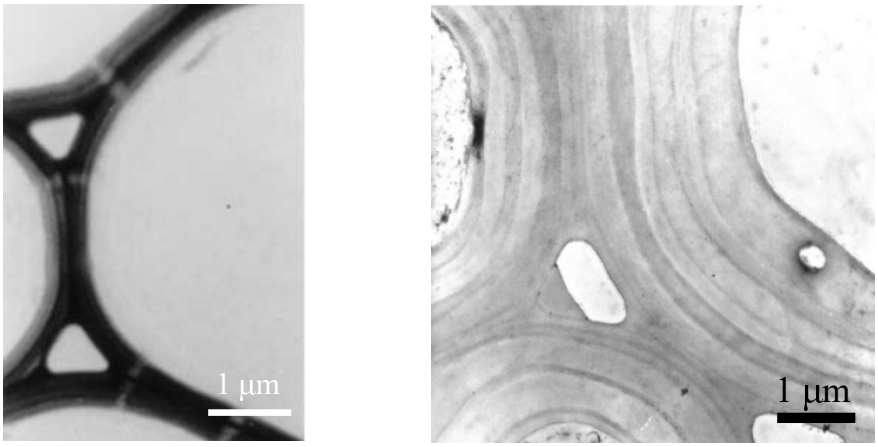

(a) Parenchyma cell wall.

(b) Cell wall in sclerenchyma fibers.

Fig. 3.5: *Cell wall characterization: (a) Cell wall in parenchyma region observed with UV microscopy reported by* Suzuki *and* Itoh *[169]. (b) TEM image of layered cell wall in matured sclerenchyma fibers reported by* Gritsch *and* Murphy *[76]. Reproduced with kind permission from Springer Publication Group and Oxford University Press.*

The *parenchyma cells* form the base of the stem cross section and exhibit polyhedral geometry. They consist of thin cell walls filled with living protoplasm that contain water and molecules. The typical length scale of parenchyma cells is $5 - 10\mu$m [72]. Figures 3.4a and 3.4b plot SEM images of transverse and longitudinal cuts through parenchyma tissue taken by Mannan, Knox and Basu [121]. We note that the morphology and volume fractions of different phases in all mesoscale regions can be determined with the help of these images.

3.1.3 Microscale: cell walls and their components

The *cell wall material* corresponds to an observation scale of 100-300 nm. Both the parenchyma and sclerenchyma cells are made up of cellulose fibers embedded into a non-cellulosic matrix of hemicellulose and lignin. In the cell wall material, cellulose fibrils are helically wound with an average microfibril angle (MFA) to the cell axis that we denote by $\bar{\theta}$. Figure 3.5a plots microimages of cell walls of parenchyma that are produced via ultraviolet (UV) microscopy by Suzuki and Itoh [169]. Here, the color intensity reflects the lignin concentration in the cell wall region. Figure 3.5b depicts transmission electron microscopy (TEM) images showing the multi-layered cell wall structure in a matured sclerenchyma fiber from a paper by Gritsch and Murphy [76]. We note that cell wall structures in the different regions can be characterized with the help of these images.

Table 3.1: *Mass densities and stiffness properties of constituent phases.*

Constituent	Density	Material behavior	Elastic coefficients			References
Cellulose	1.59	Transversely isotropic	$E_A = 130$ $\nu_A = 0.087$	$E_T = 15$ $\nu_T = 0.49$	$G_A = 3$	[125], [140], [123] [173], [83]
Hemicellulose	1.50	Transversely isotropic	$E_A = 14$ $\nu_A = 0.10$	$E_T = 3$ $\nu_T = 0.40$	$G_A = 1$	[40], [20], [146]
Lignin	1.37	Isotropic	$k_l = 5.25$	$\mu_l = 1.97$		[39], [146]
Water	1	Isotropic	$k_w = 2.30$	$\mu_w = 0$		

E_A and E_T denote axial and transverse stiffness moduli, G_A denotes the axial shear modulus, and ν_A and ν_T are Poisson's ratios. k and μ denote bulk and shear moduli for isotropic material.
Values of E, G, k and μ are in GPa, density (g/cm^3) is obtained from [46] and references therein.

The *non-cellulosic host matrix* for cellulose microfibrils is made up primarily from hemicellulose and lignin. The typical length scale of the hemicellulose-lignin matrix is 8-20 nm. Lignin and hemicellulose are also hydrophilic sites within the cell wall material such that the properties of lignin and hemicellulose depend on moisture content [39, 40].

3.1.4 Nano- and atomic scale: elastic and failure properties of base materials

The elastic and failure properties of the base materials stem from microstructure behavior at the nano- and atomic scale, which we do not resolve, but choose empirically. Native cellulose is a highly crystalline material which is assumed to exhibit a transversely isotropic behavior. This assumption has been confirmed experimentally in [125, 140], where the longitudinal elastic properties of cellulose were determined by using x-ray diffraction, and computationally in [123, 173], where the full anisotropic behavior of cellulose was investigated via molecular dynamics simulations. As cellulose macromolecules exhibit a strong transversely isotropic behavior, its strength properties in axial and transverse directions differ hugely. Experimental investigations [183, 184] suggest the axial tensile strength σ_A^{ult} of cellulose fibers in the range of 750 to 1080 MPa. Based on these observations, their ultimate strength is assumed to be 1 GPa. In the absence of data for the transverse strength of cellulose fibers, their ultimate strength σ_T^{ult} in the transverse direction is assumed proportional to the stiffness values in both directions, that is, $\sigma_T^{ult} = \frac{E_T}{E_A}\sigma_A^{ult}$. We summarize all values in Table 3.2.

Hemicellulose molecules tend to be aligned with cellulose chains. Hence, hemicellulose can also be considered as a transversely isotropic material. Cousins tested the stiffness of isolated hemicellulose by indentation tests at various levels of moisture content and

Table 3.2: *Strength properties of constituent phases.*

Constituent	Strength properties	References
Cellulose	$\sigma_A^{ult} = 1.0$ GPa $\sigma_T^{ult} = 0.115$ GPa	[183], [184], [72]
Lignin	$s_{lig} = 20.2$ MPa	[94]

s_{lig} is shear strength of lignin, σ_L^{ult} and σ_T^{ult} are ultimate strengths of cellulose in longitudinal and transverse directions, respectively.

concluded that the stiffness decreases with increasing moisture content up to the point of saturation [40]. Lignin is an amorphous material with moisture dependent stiffness [39]. The living protoplasm of the cell has many different compounds for different biological activities. These compounds are generally in a solute state. Hence, from a mechanical point of view, they all can be treated as water. We also assume that this water is in a drained state and therefore does not exert any pore pressure. The elastic constants of all constituent materials are reported in Table 3.1. Lignin is known to fail in shear [11]. The shear strength of lignin is listed in Table 3.2.

3.2 From multiscale characterization to multistep micromechanics modeling

In this section, we describe the transfer of the hierarchical scales identified from a physics viewpoint in the previous section into a multistep micromechanical representation. Figure 3.6 provides a detailed summary of our multistep micromechanics model. Below, we describe each RVE of the multistep model:

↪ At the finest scale, we consider the *non-cellulosic matrix* of lignin and hemicellulose in parenchyma and sclerenchyma regions, represented by level (a_1) and (a_2) in Fig. 3.6. The constituent phases of each RVE are hemicellulose and lignin. Since the two phases are in a morphologically disordered state, we assume that they form spherical inclusions within an "average" transversely isotropic matrix that consists of both phases.

↪ At the next level (b_1) and (b_2), we consider RVEs of the *cell wall material* in the parenchyma and sclerenchyma region. We assume a composite, in which cylindrical crystalline cellulose fibrils are embedded into the hemicellulose-lignin matrix. The latter emanates from the previous homogenization step at levels (a_1) and (a_2). The fibrils

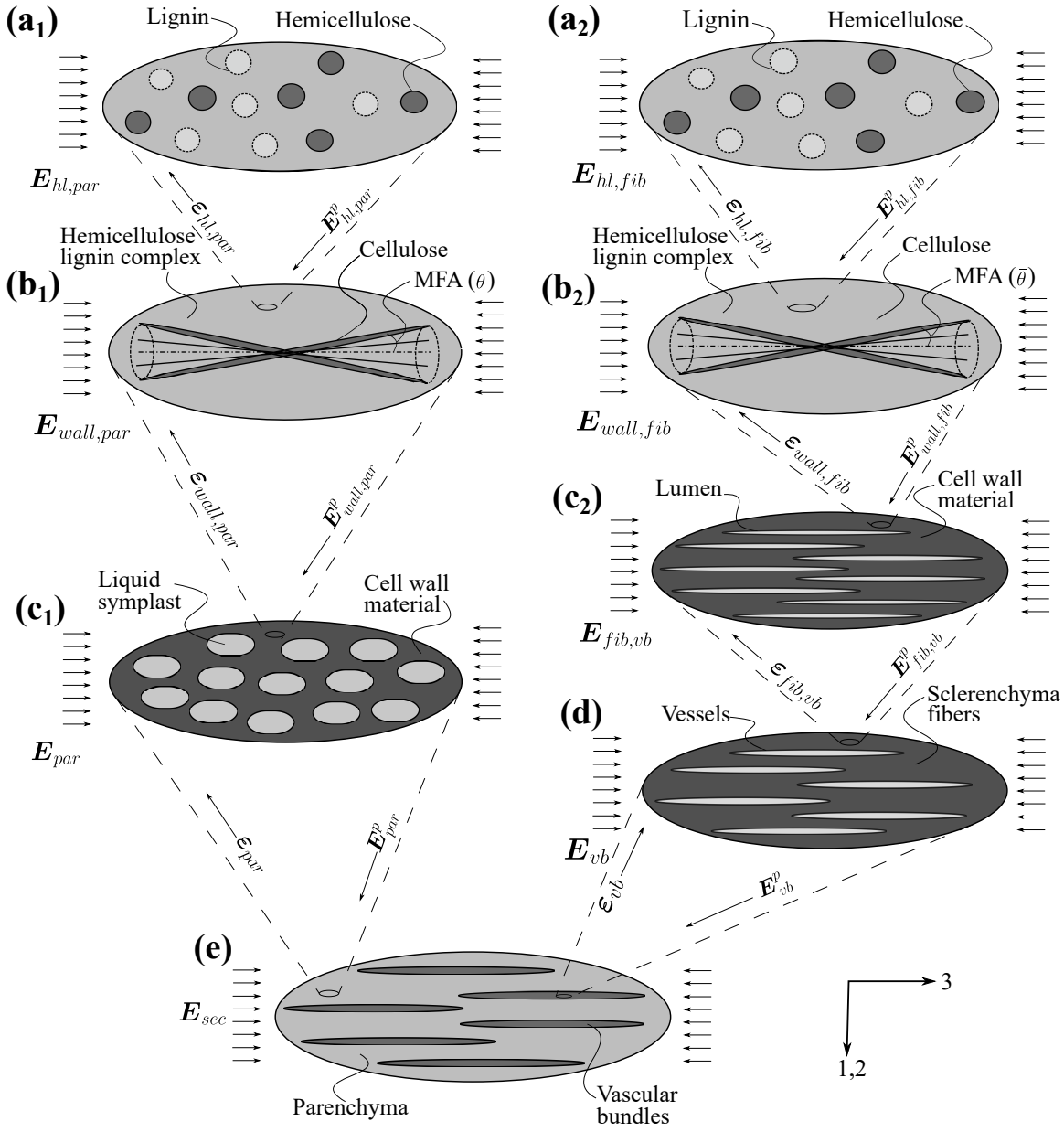

Fig. 3.6: *Multistep micromechanical representation of bamboo culm material, described in terms of appropriate RVEs at each hierarchical level. The two columns in the upper part represent individual models for the parenchyma region and vascular bundles that are combined at the cross-section level.*

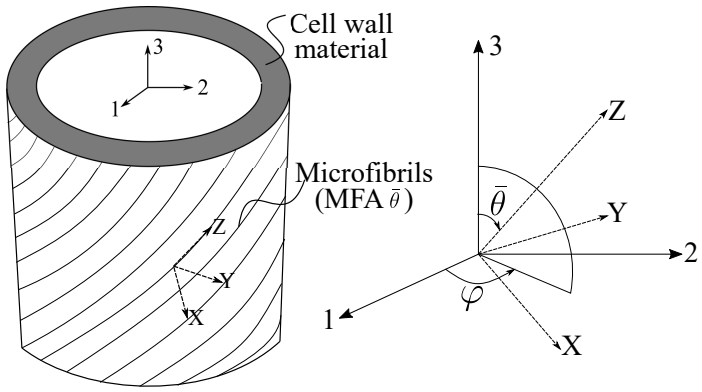

Fig. 3.7: *Helical orientation of cellulose microfibrils in a cell wall matrix material.*

helically wound around the lumen within the cell wall with an average inclination angle to the cell axis denoted as microfibril angle (MFA) $\bar{\theta}$ (see Fig. 3.6).

↪ The RVE at level (c_1) represents the *parenchyma* base tissue of the culm cross section. It contains two phases, the cell wall material and living symplast. The mechanical properties of living symplast can be assumed to be equivalent to water. Due to its polyhedral geometry, it is assumed that the living symplast forms spheroidal inclusions in the matrix of the cell wall material.

↪ The RVE at level (c_2) represents a *sclerenchyma fiber*, that consists of a matrix of cell wall material hosting cylindrical inclusions of lumen. The RVE at level (d) represents a *vascular bundle*, where xylem and phloem tissues are surrounded by sclerenchyma sheath. Therefore, the constituent phases of this RVE are sclerenchyma fibers (matrix) and vessels (cylindrical inclusion assumed to be filled with water).

↪ Finally, parenchyma base material and vascular bundles are brought together at the *cross-section* level (e). Hence, the RVE consists of two phases. The vascular bundles are radially distributed in the parenchyma matrix. As they run through the whole length of the stem, they are modeled as cylindrical inclusions.

3.3 Microstructure-stiffness relationships in the elastic range

In a first step, we describe the homogenization procedure for the elastic stiffness coefficients for the example of bamboo. To this end, we consider the hierarchical structure in terms of

the RVEs illustrated in Fig. 3.6. Homogenization in the elastic range is mainly based on the central relation (2.21) developed in Chapter 2.

3.3.1 Non-cellulosic matrix and cell wall materials

In the RVE that corresponds to the *non-cellulosic matrix* in the parenchyma region (level a_1 in Fig. 3.6), we denote the volume fractions of hemicellulose and lignin as $\phi_l^{hl,par}$ and $\phi_h^{hl,par}$, such that $\phi_l^{hl,par} + \phi_h^{hl,par} = 1$. Here, subscripts l and h stand for the phases lignin and hemicellulose and superscript (hl, par) stands for the RVE of the hemicellulose-lignin matrix in the parenchyma region. The stiffness tensors of hemicellulose and lignin, that is, $\mathbb{c}_h$ and $\mathbb{c}_l$, can be filled with values from Table 3.1. The intimate mixture of hemicellulose and lignin results in a disordered arrangement that motivates the use of the self-consistent scheme with spherical inclusions for both phases. The Hill tensor $\mathbb{P}_{sph}^{hl,par}$ describes this morphological distribution for the RVE. Here, the subscript (sph) and the superscript (hl, par) refer to the shape of the inclusion (spherical) and the hosting 'average' transversely isotropic matrix (hemicellulose-lignin complex). We note that we will follow an identical notation for all Hill tensors throughout the chapter. For the calculation of the components of $\mathbb{P}_{sph}^{hl,par}$, we refer to the appendix A.2 in [62]. The homogenized stiffness tensor $\mathbb{C}_{hl}^{par}$ of the RVE follows from (2.21) with $\mathbb{P}_r^0 = \mathbb{P}_{sph}^{hl,par}$ and $\mathbb{C}^0 = \mathbb{C}^{hom} = \mathbb{C}_{hl}^{par}$ as:

$$\mathbb{C}_{hl}^{par} = \sum_r \phi_r^{hl,par} \mathbb{c}_r : [\mathbb{I} + \mathbb{P}_{sph}^{hl,par} : (\mathbb{c}_r - \mathbb{C}_{hl}^{par})]^{-1} : \Big[\sum_s \phi_s^{hl,par} [\mathbb{I} + \mathbb{P}_{sph}^{hl,par} : (\mathbb{c}_s - \mathbb{C}_{hl}^{par})]^{-1}\Big]^{-1};\ r, s \in [h, l] \tag{3.1}$$

Due to its implicit format with respect to $\mathbb{C}_{hl}^{par}$, (3.1) must be solved iteratively [84, 85].

For the RVE of the *non-cellulosic matrix* in the sclerenchyma region (level a_2 in Fig. 3.6), we denote the volume fraction of hemicellulose and lignin as $\phi_l^{hl,fib}$ and $\phi_h^{hl,fib}$. With the Hill tensor $\mathbb{P}_{sph}^{hl,fib}$, the homogenized stiffness tensor $\mathbb{C}_{hl}^{fib}$ of the RVE follows as:

$$\mathbb{C}_{hl}^{fib} = \sum_r \phi_r^{hl,fib} \mathbb{c}_r : [\mathbb{I} + \mathbb{P}_{sph}^{hl,fib} : (\mathbb{c}_r - \mathbb{C}_{hl}^{fib})]^{-1} : \Big[\sum_s \phi_s^{hl,fib} [\mathbb{I} + \mathbb{P}_{sph}^{hl,fib} : (\mathbb{c}_s - \mathbb{C}_{hl}^{fib})]^{-1}\Big]^{-1};\ r, s \in [h, l] \tag{3.2}$$

As discussed in the previous subsection, the *cell wall material* in the parenchyma region (level b_1 in Fig. 3.6) contains helically wound cellulose fibrils (volume fraction $\phi_c^{wall,par}$) embedded into the non-cellulosic matrix of the hemicellulose-lignin complex (volume fraction

$\phi_{hl}^{wall,par}$). We note that the the cell wall material is a polylamellate structure with alternating smaller and larger microfibril angles as shown in Fig. 3.5. We assume, however, a unilamellar structure with an average microfibril angle $\bar{\theta}$. This assumption corresponds to the fact that the average microfibril orientation is easily accessible via optical and X-ray diffraction methods. In [121], it is shown that the unilamellar approach provides a reasonable bound to the polylamellate approach. Hence, we consider the cell wall material as a unilamellar structure with helically wound cellulose microfibrils.

One of the possible way to represent this morphology is by the Mori-Tanaka scheme where the homogenized hemicellulose-lignin complex acts as the matrix and the cellulose fibers form cylindrical inclusions. To account for the helical orientation of fibrils, we assume that in the RVE of the cell wall material there are an infinite number of cylindrical cellulose fibrils embedded in the matrix of the hemicellulose-lignin complex [93]. The orientation of these inclusions is defined by the two angles $\varphi, \bar{\theta}$ (see Fig. 3.7).

We know the stiffness tensor $\mathbb{c}_c$ of crystalline cellulose from Table 3.1 and the Hill tensor $\mathbb{P}_r^0 = \mathbb{P}_{cyl}^{hl,par}$ for a cylindrical inclusion in a transversely isotropic hemicellulose-lignin matrix that refers to a local coordinate system (see appendix A.1 in [62]). We also know the tensors $\mathbb{c}_c(\varphi, \bar{\theta})$ for one such RVE in the global coordinate system. The tensor $\mathbb{P}_{cyl}^{hl,par}(\varphi, \bar{\theta})$ can be obtained by standard tensor transformations [13, 156]. Following (2.21) with $\mathbb{C}^0 = \mathbb{C}^{hom} = \mathbb{C}_{hl}^{par}$, we arrive at the stiffness tensor $\mathbb{C}_{wall}^{par}$ of the cell wall material in the parenchyma region,

$$\mathbb{C}_{wall}^{par} = \Big\{\phi_{hl}^{wall,par}\mathbb{C}_{hl}^{par} + \phi_c^{wall,par}\langle \mathbb{c}_c(\varphi,\bar{\theta}) : [\mathbb{I} + \mathbb{P}_{cyl}^{hl,par}(\varphi,\bar{\theta}) : (\mathbb{c}_c(\varphi,\bar{\theta}) - \mathbb{C}_{hl}^{par})]^{-1}\rangle\Big\} : \Big\{\phi_{hl}^{wall,par}\mathbb{I} + \phi_c^{wall,par}\langle [\mathbb{I} + \mathbb{P}_{cyl}^{hl,par}(\varphi,\bar{\theta}) : (\mathbb{c}_c(\varphi,\bar{\theta}) - \mathbb{C}_{hl}^{par})]^{-1}\rangle\Big\}^{-1} \tag{3.3}$$

where we define the operator $< . >$ as:

$$< g(\varphi) >= \frac{1}{2\pi}\int_0^{2\pi} g(\varphi) d\varphi. \tag{3.4}$$

We note that the integration over φ in (3.4) is performed numerically with a simple rectangle rule.

We would like to point out again that representing the helical morphology of the cell wall material in a single RVE is a modeling assumption. The same idea was already used in other published work [93, 94], since it fits well into the framework of continuum micromechanics. It is, however, possible that some structural effects at the cell wall level might be neglected by invoking a single RVE that mixes the orientations. We therefore emphasize

that this assumption warrants further analysis and testing in future work. Alternatively, this morphology can be explored in a different theoretical or numerical framework that can be integrated with the current micromechanics model. One such possible approach is explored in [82] in the context of homogenization of osteon tissues in cortical bone where axisymmetric morphological patterns are utilized.

We can deal with the sclerenchyma region in a similar fashion, where the *cell wall material* (level b_2 in Fig. 3.6) consists of the hemicellulose-lignin complex with volume fraction $\phi_{hl}^{wall,fib}$ and of cellulose fibrils with volume fraction $\phi_c^{wall,fib}$. The corresponding homogenized stiffness tensor $\mathbb{C}_{wall}^{fib}$ of the RVE follows as:

$$\mathbb{C}_{wall}^{fib} = \left\{\phi_{hl}^{wall,fib}\mathbb{C}_{hl}^{fib} + \phi_c^{wall,fib}\langle \mathbb{c}_c(\varphi,\bar{\theta}) : [\mathbb{I} + \mathbb{P}_{cyl}^{hl,fib}(\varphi,\bar{\theta}) : (\mathbb{c}_c(\varphi,\bar{\theta}) - \mathbb{C}_{hl}^{fib})]^{-1}\rangle\right\} : \left\{\phi_{hl}^{wall,fib}\mathbb{I} + \phi_c^{wall,fib}\langle [\mathbb{I} + \mathbb{P}_{cyl}^{hl,fib}(\varphi,\bar{\theta}) : (\mathbb{c}_c(\varphi,\bar{\theta}) - \mathbb{C}_{hl}^{fib})]^{-1}\rangle\right\}^{-1}. \tag{3.5}$$

3.3.2 Parenchyma region and sclerenchyma fibers

In the RVE of the *parenchyma region* (level c_1 in Fig. 3.6), we denote the volume fraction of the cell wall material and the liquid symplast as ϕ_{wall}^{par} and ϕ_{ls}^{par}. They satisfy the relation $\phi_{wall}^{par}+\phi_{ls}^{par} = 1$. We assume that liquid symplast has same material properties as water. The stiffness $\mathbb{c}_w$ of water can be obtained from Table 3.1. The cell wall material acts as a matrix, in which the water of the liquid symplast forms spheroidal inclusions, which motivates the use of the Mori-Tanaka scheme. We assume that $\mathbb{C}^0 = \mathbb{C}_{wall}^{par}$ and the Hill tensor $\mathbb{P}_r^0 = \mathbb{P}_{sphrd}^{wall}$, which corresponds to spheroidal inclusions with a known elongation ratio in the transversely isotropic matrix of the cell wall material [113]. Here, the subscript (*sphrd*) refers to the spheroidal shape of the inclusion. With these assumptions, the homogenized stiffness tensor $\mathbb{C}_{par}$ for the RVE of the parenchyma region follows as:

$$\mathbb{C}_{par} = \left\{\phi_{wall}^{par}\mathbb{C}_{wall}^{par} + \phi_{ls}^{par}\mathbb{c}_w : [\mathbb{I}+\mathbb{P}_{sphrd}^{wall} : (\mathbb{c}_w - \mathbb{C}_{wall}^{par})]^{-1}\right\} : \left\{\phi_{wall}^{par}\mathbb{I} + \phi_{ls}^{par}[\mathbb{I} + \mathbb{P}_{sphrd}^{wall} : (\mathbb{c}_w - \mathbb{C}_{wall}^{par})]^{-1}\right\}^{-1}. \tag{3.6}$$

In the RVE of the sclerenchyma fibers (level c_2 in Fig. 3.6), we denote the volume fractions of the cell wall material in the matrix phase as ϕ_{wall}^{fib} and the cylindrical inclusions of the lumen as ϕ_{lum}^{fib}, where $\phi_{wall}^{fib}+\phi_{lum}^{fib} = 1$. The stiffness of the lumen material is the same as the stiffness $\mathbb{c}_w$ of water. The RVE can be suitably modeled by the Mori-Tanaka scheme. Hence,

we assume that $\mathbb{C}^0 = \mathbb{C}^{fib}_{wall}$ and $\mathbb{P}^0_r = \mathbb{P}^{wall}_{cyl}$, which corresponds to cylindrical inclusions in the transversely isotropic matrix of the cell wall material in sclerenchyma fibers [62]. Following (2.21), the stiffness tensor $\mathbb{C}_{fib}$ for the RVE of the sclerenchyma region can be obtained as:

$$\mathbb{C}_{fib} = \left\{\phi^{fib}_{wall}\mathbb{C}^{fib}_{wall} + \phi^{fib}_{lum}\mathbb{c}_w : [\mathbb{I}+\mathbb{P}^{wall}_{cyl} : (\mathbb{c}_w - \mathbb{C}^{fib}_{wall})]^{-1}\right\} : \left\{\phi^{fib}_{wall}\mathbb{I} + \phi^{fib}_{lum}[\mathbb{I} + \mathbb{P}^{wall}_{cyl} : (\mathbb{c}_w - \mathbb{C}^{fib}_{wall})]^{-1}\right\}^{-1}. \tag{3.7}$$

3.3.3 Vascular bundles and macroscopic cross section

In the RVE of a *vascular bundle* (level d in Fig. 3.6), we denote the volume fractions of the sclerenchyma fibers and the vessels as ϕ_{fib} and ϕ_v, where $\phi_{fib} + \phi_v = 1$. The vessels form cylindrical inclusions in the matrix of sclerenchyma fibers, which motivates the use of the Mori-Tanaka scheme. We are given the Hill tensor $\mathbb{P}^0_r = \mathbb{P}^{fib}_{cyl}$, which corresponds to cylindrical inclusions in the transversely isotropic matrix of the sclerenchyma fibers [62]. Hence, with $\mathbb{C}^0 = \mathbb{C}_{fib}$, the elastic stiffness tensor $\mathbb{C}_{vb}$ of a vascular bundle RVE can be determined as:

$$\mathbb{C}_{vb} = \left\{\phi_{fib}\mathbb{C}_{fib} + \phi_v\mathbb{c}_w : [\mathbb{I} + \mathbb{P}^{fib}_{cyl} :(\mathbb{c}_w - \mathbb{C}_{fib})]^{-1}\right\} : \left\{\phi_{fib}\mathbb{I} + \phi_v[\mathbb{I} + \mathbb{P}^{fib}_{cyl} : (\mathbb{c}_w - \mathbb{C}_{fib})]^{-1}\right\}^{-1}. \tag{3.8}$$

Finally, we consider the RVE of the macroscopic bamboo section (level e in Fig. 3.6), where the volume fractions of the parenchyma region and the vascular bundles are ϕ_{par} and ϕ_{vb}, such that $\phi_{par}+\phi_{vb} = 1$. The vascular bundles are embedded into the matrix of parenchyma base tissues. The RVE can be suitably modeled by the Mori-Tanaka scheme. Hence, we assume that $\mathbb{C}^0 = \mathbb{C}_{par}$ and the Hill tensor $\mathbb{P}^0_r = \mathbb{P}^{par}_{cyl}$, which corresponds to cylindrical inclusions in the transversely isotropic matrix of the parenchyma [62]. Following (2.21), we arrive at the homogenized stiffness tensor $\mathbb{C}_{sec}$ of the cross section:

$$\mathbb{C}_{sec} = \left\{\phi_{par}\mathbb{C}_{par} + \phi_{vb}\mathbb{C}_{vb} : [\mathbb{I}+\mathbb{P}^{par}_{cyl} : (\mathbb{C}_{vb} - \mathbb{C}_{par})]^{-1}\right\} : \left\{\phi_{par}\mathbb{I} + \phi_{vb}[\mathbb{I} + \mathbb{P}^{par}_{cyl} : (\mathbb{C}_{vb} - \mathbb{C}_{par})]^{-1}\right\}^{-1}. \tag{3.9}$$

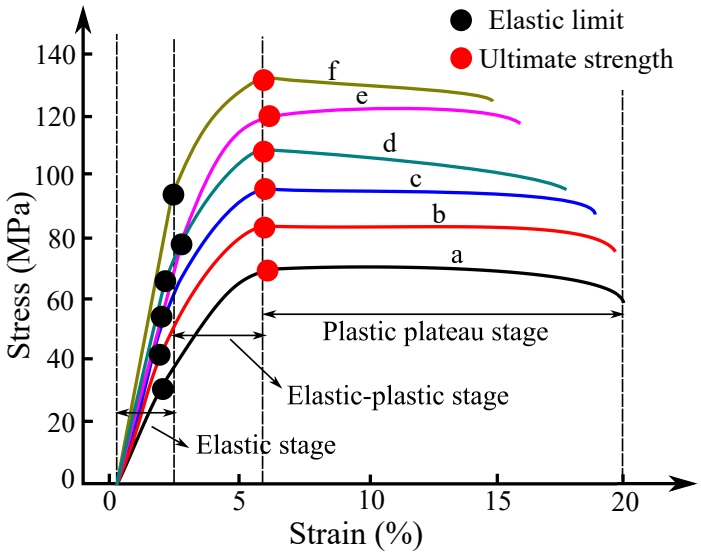

Fig. 3.8: *Experimental stress-strain curves for bamboo material for different volume fractions of vascular bundles, reported by* Zhang *and collaborators [205]. Curves* ***a-f*** *correspond to volume fractions of 0.15, 0.17, 0.22, 0.24, 0.37 and 0.46, respectively.*

3.4 Microstructure-strength relationships in the inelastic/failure range

In the next step, we proceed to modeling inelastic behavior of the culm material in terms if its local ultimate strength. To this end, we first review and extend basic assumptions on multiscale plastification and failure in hierarchical culm materials.

3.4.1 Basic proposition: sequential failure of lignin and cellulose

Of particular interest is the propagation of plastic strains that result from yielding at a specific microscale across hierarchical RVEs up to the macroscopic cross section level. Recently, Zhang and co-authors [205] performed compression experiments on bamboo specimens with different vascular bundle densities in the cross section. Figure 3.8 illustrates the inelastic response of different specimens with a stress-strain diagram. We observe that the bamboo material exhibits different stages in the stress-strain behavior before failure: the initial linear elastic deformation stage is followed by an elastoplastic stage, in which stress varies with strain nonlinearly. Finally, a plastic plateau is reached, where the stress shows almost no variation with strain. To model this behavior, we need to make assumptions on the plastification and failure sequence of the base materials. Several experimental investigations of the failure in bamboo at the microstructure level [79, 150] concur in suggesting

that failure is initiated by yielding of lignin, which then leads to a redistribution of stresses to the cellulose through a bridging effect.

Based on these observations, we conceptualize that the microstructural origin of failure of the bamboo cross section is a sequential failure of the constituent materials lignin and cellulose in that order. In the elastic range of the stress-strain curve of bamboo, both lignin and cellulose respond purely elastically. The elastic limit point in the curve corresponds to the plastification of lignin. After the onset of plastic yielding of lignin, stresses due to further loading are transferred exclusively to the cellulose microfibrils. On the macroscopic level, this mechanism manifests itself in the elastoplastic part of the stress-strain behavior of bamboo. Once a certain macroscopic stress level is reached, the cellulose microfibrils suddenly fail due to brittle fracture, which corresponds to the ultimate strength of the bamboo section. Similar observations on the microstructural origin of strength have been made for other hierarchical multiscale materials with a similar matrix-fibril composition, for instance bone [30, 62, 151], which tentatively supports our assumption of sequential failure of the basic constituents lignin and cellulose. We therefore believe that this conceptual model is appropriate for a large range of culm materials beyond bamboo.

3.4.2 Von-Mises-type failure criteria and average stress tensors

With the basic failure concepts established, we proceed to the modeling of the two individual materials lignin and cellulose. Lignin is an amorphous material and it is known to fail in shear [11]. The shear strength of lignin is listed in Table 3.2. Its stress-strain response is assumed to be first elastic and then perfectly plastic, following the von Mises failure criterion expressed as:

$$\mathfrak{f}_{lig}(\boldsymbol{\sigma}_l) = \frac{1}{6}[(\sigma_{11}-\sigma_{22})^2+(\sigma_{22}-\sigma_{33})^2+(\sigma_{33}-\sigma_{11})^2+6(\sigma_{23}^2+\sigma_{31}^2+\sigma_{12}^2)]-s_{lig}^2 \leq 0, \quad (3.10)$$

where $\boldsymbol{\sigma}_l$ is the stress in the lignin phase that consists of the stress components σ_{ij} in index notation, and s_{lig} is the yield stress in pure shear.

As discussed in Section 3.3.1, crystalline cellulose exhibits strong anisotropy during brittle failure. The failure of cellulose can be described by the Hill failure criterion [89] for generalized anisotropy, which can be expressed as:

$$\begin{aligned}\mathfrak{f}_c(\boldsymbol{\sigma}_{\varphi\bar{\theta}}) = \max_{\varphi}\{&F(\sigma_{yy}-\sigma_{zz})^2 + G(\sigma_{zz}-\sigma_{xx})^2 + \\ &H(\sigma_{xx}-\sigma_{yy})^2 + 2L\sigma_{yz}^2 + 2M\sigma_{zx}^2 + 2N\sigma_{xy}^2\} - 1 \leq 0\end{aligned} \quad (3.11a)$$

$$F = \frac{1}{2}[\frac{1}{(\sigma_y^0)^2} + \frac{1}{(\sigma_z^0)^2} - \frac{1}{(\sigma_x^0)^2}];\ G, H \text{ are permutations with x,y,z} \tag{3.11b}$$

$$L = 1/S_{yz}^2;\ M, N \text{ are permutations with x,y,z} \tag{3.11c}$$

Here, the material parameters $\sigma_x^0, \sigma_y^0, \sigma_z^0$ and S_{yz}, S_{zx}, S_{xy} denote ultimate strength values and ultimate shear strength values, respectively, in the given directions. The stress tensor $\boldsymbol{\sigma}_{\varphi\bar{\theta}}$ for a cellulose fiber with orientation $\varphi \in [0, 2\pi)$ is given in the local coordinate system of the cellulose fibers (see Fig. 3.7). For the computation of the failure criterion for cellulose, we need to check the criterion value for the stress level $\boldsymbol{\sigma}_{\varphi\bar{\theta}}$ in each fibril defined by the Euler angle $\varphi \in [0, 2\pi)$ and take the maximum value as shown in equation (3.11). For

$$F = G = H = \frac{1}{2(\sigma^{ult})^2} \quad \text{and} \quad L = M = N = \frac{3}{2}F, \tag{3.12}$$

equation (3.11) simplifies to the isotropic von Mises criterion, where σ^{ult} is the ultimate strength in the isotropic case. The cellulose fibers, however, exhibit a transversely isotropic behavior with respect to the perpendicular axial direction and the transverse isotropic xy plane. Hence, in the limit of transverse isotropy, the parameters in (3.11) are:

$$F = G = \frac{1}{2(\sigma_A^{ult})^2}, \quad H = \frac{1}{2}\Big[\frac{2}{(\sigma_T^{ult})^2} - \frac{1}{(\sigma_A^{ult})^2}\Big] \tag{3.13a}$$

$$L = M = \frac{3}{2}F, \ \ N = \frac{3}{2}H \tag{3.13b}$$

with ultimate strength values σ_A^{ult} and σ_T^{ult} in axial and transverse directions, respectively.

In this chapter, our focus is on macroscopic uniaxial and shear loading. For these basic load cases and the given morphology, we adopt the strategy based on average tensors as an engineering simplification. We illustrate the effect of this assumption by considering a two-phase RVE that consists of perfectly plastic cylindrical inclusions embedded in an elastic matrix. First, we assume the RVE undergoes a macroscopic strain in the axial direction of the inclusions. In this case, the strain tensors per phase is constant and the average tensor based model accurately captures the plastic behavior in the inclusions. We then assume the

RVE undergoes a macroscopic strain perpendicular to the axial direction of the inclusions. In this case, the strain distribution inside the inclusions is not uniform. Therefore, average tensors in a von-Mises-type yield criterion cannot represent the plastic behavior of the inclusion phase with full accuracy. Our model assumes that perfectly elastoplastic lignin forms spherical inclusions inside an average fictitious matrix of hemicellulose and lignin, see the levels a_1 and a_2 in Fig. 3.6. Due to the spherical geometry of lignin, no directional dependence holds and the accuracy of the approximation is curtailed in between the two cases discussed above. For a critical assessment of different methods to tackle this problem, we refer the interested reader to the comprehensive lecture notes by SUQUET [166].

3.4.3 Upscaling/downscaling of elastoplastic strains across hierarchical levels

Using the assumptions discussed in the previous subsection, we can now establish concentration relations for upscaling and downscaling total and plastic strains across all hierarchical RVEs. Our discussion in Section 2.3.2 forms the basis of the developed micromechanical relations in this section. We note that we will use the superscript p to refer to quantities related to plasticity. We also use the same RVEs defined in Fig. 3.6.

We start with homogenization of the *non-cellulosic matrix* in the parenchyma region (level a_1 in Fig. 3.6). When the macroscopic applied strain $\boldsymbol{E}_{hl,par}$ reaches a specific limit, lignin yields and accumulates the plastic strain $\boldsymbol{\varepsilon}^p_{l,par}$. We assume that hemicellulose does not accumulate any plastic strain, such that $\boldsymbol{\varepsilon}^p_{h,par} = 0$ at all times. As mentioned in Section 3.3.1, we assume that lignin is an isotropic material which forms spherical inclusions in the hemicellulose-lignin complex. The assumptions of isotropy and spherical geometry eliminate possible asymmetries in the lignin phase. Hence, in this special case, the plastic flow can be represented by assuming a single volume for the lignin phase. Having derived the stiffness tensor $\mathbb{C}^{par}_{hl}$ of this RVE from (3.1), we can utilize the strain concentration relation (2.39) of the self-consistent scheme for hemicellulose and lignin to compute the strain in the lignin phase in response to the macroscopic strain $\boldsymbol{E}_{hl,par}$. The resulting expression is:

$$\begin{aligned}\boldsymbol{\varepsilon}_{l,par} =&[\mathbb{I} + \mathbb{P}^{hl,par}_{sph} : (\mathbb{c}_l - \mathbb{C}^{par}_{hl})]^{-1} : \Big\{ \Big\{ \sum_i \phi^{hl,par}_i [\mathbb{I} + \mathbb{P}^{hl,par}_{sph} : (\mathbb{c}_i - \mathbb{C}^{par}_{hl})]^{-1} \Big\}^{-1} : \\ &\Big\{ \boldsymbol{E}_{hl,par} - \phi^{hl,par}_l [\mathbb{I} + \mathbb{P}^{hl,par}_{sph} : (\mathbb{c}_l - \mathbb{C}^{par}_{hl})]^{-1} : \mathbb{P}^{hl,par}_{sph} : \mathbb{c}_l : \boldsymbol{\varepsilon}^p_{l,par} \Big\} + \\ &\mathbb{P}^{hl,par}_{sph} : \mathbb{c}_l : \boldsymbol{\varepsilon}^p_{l,par} \Big\}; \quad i \in [h, l]\end{aligned} \tag{3.14}$$

In the *non-cellulosic matrix* in the sclerenchyma region (level a_2 in Fig. 3.6), lignin reaches the plastic strain $\boldsymbol{\varepsilon}^p_{l,fib}$ against a specific level of the macroscopic applied strain $\boldsymbol{E}_{hl,fib}$. Similar to equation (3.14), we can write a strain concentration relation for this RVE:

$$\begin{aligned}\boldsymbol{\varepsilon}_{l,fib} = [\mathbb{I} + \mathbb{P}^{hl,fib}_{sph} : (\mathbb{c}_l - \mathbb{C}^{fib}_{hl})]^{-1} : \Big\{ \Big\{ \sum_i \phi^{hl,fib}_i [\mathbb{I} + \mathbb{P}^{hl,fib}_{sph} : (\mathbb{c}_i - \mathbb{C}^{fib}_{hl})]^{-1} \Big\}^{-1} : \\ \Big\{ \boldsymbol{E}_{hl,fib} - \phi^{hl,fib}_l [\mathbb{I} + \mathbb{P}^{hl,fib}_{sph} : (\mathbb{c}_l - \mathbb{C}^{hl,fib}_{hl})]^{-1} : \mathbb{P}^{hl,fib}_{sph} : \mathbb{c}_l : \boldsymbol{\varepsilon}^p_{l,fib} \Big\} + \\ \mathbb{P}^{hl,fib}_{sph} : \mathbb{c}_l : \boldsymbol{\varepsilon}^p_{l,fib} \Big\}; \quad i \in [h, l]\end{aligned} \tag{3.15}$$

Plastic strains in the lignin phase at the two levels a_1 and a_2 lead to plastic strains at the RVE scale. Hence, the accumulated plastic strains $\boldsymbol{E}^p_{hl,par}$ and $\boldsymbol{E}^p_{hl,fib}$ in the RVE of the parenchyma and sclerenchyma fiber regions can be evaluated from (2.34).

In the *cell wall material* in the parenchyma region (level b_1 in Fig. 3.6), we assume a brittle behavior for the crystalline cellulose fibrils. The assumption of brittleness implies that no plasticity occurs in the crystalline cellulose phase, such that $\boldsymbol{\varepsilon}^p_{c,par} = 0$ holds at all times. The plastic strain $\boldsymbol{\varepsilon}^p_{hl,par}$ in the hemicellulose-lignin matrix has been calculated in the previous step, since $\boldsymbol{\varepsilon}^p_{hl,par} = \boldsymbol{E}^p_{hl,par}$. The homogenized stiffness tensor of this RVE has been derived in (3.3). Now, we can utilize the strain concentration relation for the Mori-Tanaka scheme in (2.38) to compute the strain in the constituent phases in response to the macroscopic strain $\boldsymbol{E}_{wall,par}$. With $\mathbb{c}_M = \mathbb{C}^{par}_{hl}$ and $\boldsymbol{\varepsilon}^p_M = \boldsymbol{\varepsilon}^p_{hl,par}$, the strain concentration relation for the hemicellulose-lignin complex is:

$$\begin{aligned}\boldsymbol{\varepsilon}_{hl,par} = \Big\{ \phi^{wall,par}_{hl} \mathbb{I} + \phi^{wall,par}_c \langle [\mathbb{I} + \mathbb{P}^{hl,par}_{cyl}(\varphi, \bar{\theta}) : (\mathbb{c}_c(\varphi, \bar{\theta}) - \mathbb{C}^{par}_{hl})]^{-1} \rangle \Big\}^{-1} : \\ \Big\{ \boldsymbol{E}_{wall,par} - \phi^{wall,par}_c \langle [\mathbb{I} + \mathbb{P}^{hl,par}_{cyl}(\varphi, \bar{\theta}) : (\mathbb{c}_c(\varphi, \bar{\theta}) - \mathbb{C}^{par}_{hl})]^{-1} : \\ [\mathbb{P}^{hl,par}_{cyl}(\varphi, \bar{\theta}) : (-\mathbb{C}^{par}_{hl} : \boldsymbol{\varepsilon}^p_{hl,par})] \rangle \Big\}.\end{aligned} \tag{3.16}$$

We note that the microscopic strain $\boldsymbol{\varepsilon}_{hl,par}$ for this RVE is identical to $\boldsymbol{E}_{hl,par}$ in (3.14), which represents the macroscopic strain for the RVE of the hemicellulose-lignin matrix. The strain concentration relation for cellulose fibers with a specific orientation $(\varphi, \bar{\theta})$ in this

RVE can be expressed as:

$$\begin{aligned}\boldsymbol{\varepsilon}^{par}_{c\varphi\bar{\theta}} = &[\mathbb{I} + \mathbb{P}^{hl,par}_{cyl}(\varphi,\bar{\theta}) : (\mathbb{c}_c(\varphi,\bar{\theta}) - \mathbb{C}^{par}_{hl})]^{-1} : \\ &\Big\{\Big\{\phi^{wall,par}_{hl}\mathbb{I} + \phi^{wall,par}_{c}\langle[\mathbb{I} + \mathbb{P}^{hl,par}_{cyl}(\varphi,\bar{\theta}) : (\mathbb{c}_c(\varphi,\bar{\theta}) - \mathbb{C}^{par}_{hl})]^{-1}\rangle\Big\}^{-1} : \\ &\Big\{\boldsymbol{E}_{wall,par} - \phi^{wall,par}_{c}\langle[\mathbb{I} + \mathbb{P}^{hl,par}_{cyl}(\varphi,\bar{\theta}) : (\mathbb{c}_c(\varphi,\bar{\theta}) - \mathbb{C}^{par}_{hl})]^{-1} : \\ &[\mathbb{P}^{hl,par}_{cyl}(\varphi,\bar{\theta}) : (-\mathbb{C}^{par}_{hl} : \boldsymbol{\varepsilon}^{p}_{hl,par})]\rangle + \mathbb{P}^{hl,par}_{cyl}(\varphi,\bar{\theta}) : (-\mathbb{C}^{par}_{hl} : \boldsymbol{\varepsilon}^{p}_{hl,par})\Big\}\Big\}.\end{aligned} \tag{3.17}$$

For the *cell wall material* in the sclerenchyma region (level b_2 in Fig. 3.6), we can write a similar expressions for the micro-strain $\boldsymbol{\varepsilon}_{hl,fib}$ of the hemicellulose-lignin complex and the micro-strain $\boldsymbol{\varepsilon}^{par}_{c\varphi\bar{\theta}}$ of the cellulose fiber with orientation $(\varphi,\bar{\theta})$ as against to the macroscopic strain $\boldsymbol{E}_{wall,fib}$:

$$\begin{aligned}\boldsymbol{\varepsilon}_{hl,fib} = &\Big\{\phi^{wall,fib}_{hl}\,\mathbb{I} + \phi^{wall,fib}_{c}\langle[\mathbb{I} + \mathbb{P}^{hl,fib}_{cyl}(\varphi,\bar{\theta}) : (\mathbb{c}_c(\varphi,\bar{\theta}) - \mathbb{C}^{fib}_{hl})]^{-1}\rangle\Big\}^{-1} : \\ &\Big\{\boldsymbol{E}_{wall,fib} - \phi^{wall,fib}_{c}\langle[\mathbb{I} + \mathbb{P}^{hl,fib}_{cyl}(\varphi,\bar{\theta}) : (\mathbb{c}_c(\varphi,\bar{\theta}) - \mathbb{C}^{fib}_{hl})]^{-1} : \\ &[\mathbb{P}^{hl,fib}_{cyl}(\varphi,\bar{\theta}) : (-\mathbb{C}^{fib}_{hl} : \boldsymbol{\varepsilon}^{p}_{hl,fib})]\rangle\Big\},\end{aligned} \tag{3.18}$$

$$\begin{aligned}\boldsymbol{\varepsilon}^{fib}_{c\varphi\bar{\theta}} = &[\mathbb{I} + \mathbb{P}^{hl,fib}_{cyl}(\varphi,\bar{\theta}) : (\mathbb{c}_c(\varphi,\bar{\theta}) - \mathbb{C}^{fib}_{hl})]^{-1} : \\ &\Big\{\Big\{\phi^{wall,fib}_{hl}\mathbb{I} + \phi^{wall,fib}_{c}\langle[\mathbb{I} + \mathbb{P}^{hl,fib}_{cyl}(\varphi,\bar{\theta}) : (\mathbb{c}_c(\varphi,\bar{\theta}) - \mathbb{C}^{fib}_{hl})]^{-1}\rangle\Big\}^{-1} : \\ &\Big\{\boldsymbol{E}_{wall,fib} - \phi^{wall,fib}_{c}\langle[\mathbb{I} + \mathbb{P}^{hl,fib}_{cyl}(\varphi,\bar{\theta}) : (\mathbb{c}_c(\varphi,\bar{\theta}) - \mathbb{C}^{fib}_{hl})]^{-1} : \\ &[\mathbb{P}^{hl,fib}_{cyl}(\varphi,\bar{\theta}) : (-\mathbb{C}^{par}_{hl} : \boldsymbol{\varepsilon}^{p}_{hl,fib})]\rangle + \mathbb{P}^{hl,fib}_{cyl}(\varphi,\bar{\theta}) : (-\mathbb{C}^{fib}_{hl} : \boldsymbol{\varepsilon}^{p}_{hl,fib})\Big\}\Big\},\end{aligned} \tag{3.19}$$

where we assume $\mathbb{C}^0 = \mathbb{c}_M = \mathbb{C}^{fib}_{hl}$ and $\boldsymbol{\varepsilon}^{p}_{hl,fib} = \boldsymbol{\varepsilon}^{p}_{M} = \boldsymbol{E}^{p}_{hl,fib}$. In the parenchyma and sclerenchyma fiber regions, plastic strains in the hemicellulose-lignin complex in the RVE of the cell wall lead to a plastic strain at the RVE level. Hence, accumulated plastic strains $\boldsymbol{E}^{p}_{wall,par}$ and $\boldsymbol{E}^{p}_{wall,fib}$ in these RVEs can be evaluated from (2.34).

In the parenchyma region (level c_1 in Fig. 3.6), no plasticity occurs in the living symplast (water) phase, such that $\boldsymbol{\varepsilon}^{p}_{ls,par} = 0$ at all times. The plastic strain in the cell wall matrix is $\boldsymbol{\varepsilon}^{p}_{wall,par} = \boldsymbol{E}^{p}_{wall,par}$. With $\mathbb{c}_M = \mathbb{C}^{par}_{wall}$ and $\boldsymbol{\varepsilon}^{p}_{M} = \boldsymbol{\varepsilon}^{p}_{wall,par}$, the strain concentration relation for the cell wall material in the RVE of the parenchyma in response to the macroscopic strain

$\boldsymbol{E}_{par}$ can be derived from (2.38) as:

$$\boldsymbol{\varepsilon}_{wall,par} = \Big\{\phi^{par}_{wall}\mathbb{I} + \phi^{par}_{ls}[\mathbb{I} + \mathbb{P}^{wall}_{sphrd} : (\mathbb{c}_w - \mathbb{C}^{par}_{wall})]^{-1}\Big\}^{-1} : \\ \Big\{\boldsymbol{E}_{par} - \phi^{par}_{ls}[\mathbb{I} + \mathbb{P}^{wall}_{sphrd} : (\mathbb{c}_w - \mathbb{C}^{par}_{wall})]^{-1} : [\mathbb{P}^{wall}_{sphrd} : (-\mathbb{C}^{par}_{wall} : \boldsymbol{\varepsilon}^{p}_{wall,par})]\Big\}. \tag{3.20}$$

According to (2.34), plastic strains in the cell wall material imply the accumulation of plastic strains $\boldsymbol{E}^{p}_{par}$ at the RVE level of the parenchyma region.

In sclerenchyma fibers (level c_2 in Fig. 3.6), cylindrical inclusions of lumen are considered as water, where no plasticity can occur ($\boldsymbol{\varepsilon}^{p}_{lum,fib} = 0$). With the plastic strain $\boldsymbol{\varepsilon}^{p}_{M} = \boldsymbol{\varepsilon}^{p}_{wall,fib} = \boldsymbol{E}^{p}_{wall,fib}$ in the cell wall material, $\mathbb{c}_M = \mathbb{C}^{fib}_{wall}$ and given the macroscopic strain $\boldsymbol{E}_{fib,vb}$, the strain concentration relation for the cell wall material follows from (2.38) as:

$$\boldsymbol{\varepsilon}_{wall,fib} = \Big\{\phi^{fib}_{wall}\mathbb{I} + \phi^{fib}_{lum}[\mathbb{I} + \mathbb{P}^{wall}_{cyl} : (\mathbb{c}_w - \mathbb{C}^{fib}_{wall})]^{-1}\Big\}^{-1} : \\ \Big\{\boldsymbol{E}_{fib,vb} - \phi^{fib}_{lum}[\mathbb{I} + \mathbb{P}^{wall}_{cyl} : (\mathbb{c}_w - \mathbb{C}^{fib}_{wall})]^{-1} : [\mathbb{P}^{wall}_{cyl} : (-\mathbb{C}^{fib}_{wall} : \boldsymbol{\varepsilon}^{p}_{wall,fib})]\Big\}. \tag{3.21}$$

Accumulated plastic strains in the cell wall material result in plastic strains $\boldsymbol{E}^{p}_{fib,vb}$ from (2.34) at the RVE level of the sclerenchyma region.

In vascular bundles (level d in Fig. 3.6), no plastic strains occur in the vessels, that is, $\boldsymbol{\varepsilon}^{p}_{v,vb} = 0$. With plastic strains $\boldsymbol{\varepsilon}^{p}_{M} = \boldsymbol{\varepsilon}^{p}_{fib,vb} = \boldsymbol{E}^{p}_{fib,vb}$ in the sclerenchyma fiber matrix and $\mathbb{c}_M = \mathbb{C}_{fib}$, the strain concentration relation for sclerenchyma fibers in response to the macroscopic strain $\boldsymbol{E}_{vb}$ follows from (2.38) as:

$$\boldsymbol{\varepsilon}_{fib,vb} = \Big\{\phi_{fib}\mathbb{I} + \phi_v[\mathbb{I} + \mathbb{P}^{fib}_{cyl} : (\mathbb{c}_w - \mathbb{C}_{fib})]^{-1}\Big\}^{-1} : \Big\{\boldsymbol{E}_{vb} - \phi_v[\mathbb{I} + \mathbb{P}^{fib}_{cyl} : (\mathbb{c}_w - \\ \mathbb{C}_{fib})]^{-1} : [\mathbb{P}^{fib}_{cyl} : (-\mathbb{C}_{fib} : \boldsymbol{\varepsilon}^{p}_{fib,vb})]\Big\}. \tag{3.22}$$

In this RVE, accumulated plastic strains $\boldsymbol{E}^{p}_{vb}$ can be computed from (2.34).

Finally, at the macroscopic section level (level e in Fig. 3.6), plastic strains in the parenchyma and vascular bundles are calculated from the previous homogenization steps, that is, $\boldsymbol{\varepsilon}^{p}_{par} = \boldsymbol{E}^{p}_{par}$ and $\boldsymbol{\varepsilon}^{p}_{vb} = \boldsymbol{E}^{p}_{vb}$. We can employ the concentration relation (2.38) for this RVE to compute the "micro-strains" $\boldsymbol{\varepsilon}_{vb}$ and $\boldsymbol{\varepsilon}_{par}$ in the vascular bundles and parenchyma in response to the applied macroscopic strain $\boldsymbol{E}_{sec}$. With $\boldsymbol{\varepsilon}^{p}_{M} = \boldsymbol{\varepsilon}^{p}_{par} = \boldsymbol{E}^{p}_{par}$ and $\mathbb{c}_M = \mathbb{C}_{par}$,

we find:

$$\boldsymbol{\varepsilon}_{vb} = [\mathbb{I} + \mathbb{P}^{par}_{cyl} : (\mathbb{C}_{vb} - \mathbb{C}_{par})]^{-1} : \Big\{ \Big\{ \phi_{par}\mathbb{I} + \phi_{vb}[\mathbb{I} + \mathbb{P}^{par}_{cyl} : (\mathbb{C}_{vb} - \mathbb{C}_{par})]^{-1} \Big\}^{-1} : \Big\{ \boldsymbol{E}_{sec} - \phi_{vb}[\mathbb{I} + \mathbb{P}^{par}_{cyl} : (\mathbb{C}_{vb} - \mathbb{C}_{par})]^{-1} : [\mathbb{P}^{par}_{cyl} : (\mathbb{C}_{vb} : \boldsymbol{\varepsilon}^{p}_{vb} - \mathbb{C}_{par} : \boldsymbol{\varepsilon}^{p}_{par})] \Big\} + \mathbb{P}^{par}_{cyl} : (\mathbb{C}_{vb} : \boldsymbol{\varepsilon}^{p}_{vb} - \mathbb{C}_{par} : \boldsymbol{\varepsilon}^{p}_{par}) \Big\}, \tag{3.23}$$

$$\boldsymbol{\varepsilon}_{par} = \Big\{ \phi_{par}\mathbb{I} + \phi_{vb}[\mathbb{I} + \mathbb{P}^{par}_{cyl} : (\mathbb{C}_{vb} - \mathbb{C}_{par})]^{-1} \Big\}^{-1} : \Big\{ \boldsymbol{E}_{sec} - \phi_{vb}[\mathbb{I} + \mathbb{P}^{par}_{cyl} : (\mathbb{C}_{vb} - \mathbb{C}_{par})]^{-1} : [\mathbb{P}^{par}_{cyl} : (\mathbb{C}_{vb} : \boldsymbol{\varepsilon}^{p}_{vb} - \mathbb{C}_{par} : \boldsymbol{\varepsilon}^{p}_{par})] \Big\}. \tag{3.24}$$

The accumulated plastic strains $\boldsymbol{\varepsilon}^{p}_{par}$ and $\boldsymbol{\varepsilon}^{p}_{vb}$ in the parenchyma and vascular bundles imply plastic strains $\boldsymbol{E}^{p}_{sec}$ at the macroscopic level. This macroscopic plastic strain can be calculated from (2.34).

While microstructure-stiffness relationships for elastic stiffness moduli can be computed directly from the relations given in Section 3.3, the ultimate strength can only be computed iteratively with respect to a given stress (or strain) increment. A bird's eye view of the corresponding computer implementation is given in Algorithm 1.

3.5 Validation and discussion of model results for bamboo

In a recent paper, Dixon and Gibson report experimental results on the mechanical properties of Moso bamboo [49]. Measured quantities include axial stiffness and axial transverse ultimate strength. The test samples were taken from internode regions at different heights (i.e., age) and at different radial positions (i.e., cross section anatomy). Figure 3.9 illustrates geometry and position of test specimens along the radial direction in one internode culm region. For each of the tested samples, the study also reports their microstructure variations, classified with the help of SEM images, which constitutes an essential prerequisite for setting up our model. In this section, we first describe the evidence-based identification of model parameters for bamboo. We then illustrate the predictive power of our model, comparing predictions of stiffness moduli and ultimate strength to corresponding measurements reported in [49]. We demonstrate how micromechanics modeling

Result: The ultimate strength $\Sigma_{ij}^{ult} = \Sigma_{ij,n+1}$ of the macroscale cross section.

Define stress increment $\Delta\Sigma_{ij}$;
Set $\Sigma_{ij} = 0 \Rightarrow \boldsymbol{E}_{sec,0} = 0, \boldsymbol{E}_{sec,0}^{p} = 0$;
Set index number n=0;
while $\mathfrak{f}_{c,par} \leq 0$ *and* $\mathfrak{f}_{c,fib} \leq 0$ **do**
    $\boldsymbol{\Sigma}_{sec,n+1} = (\Sigma_{ij,n} + \Delta\Sigma_{ij})\, \boldsymbol{e}_i \otimes \boldsymbol{e}_j$;
    Update $\boldsymbol{E}_{sec,n+1}^{p} = \boldsymbol{E}_{sec,n}^{p}$;
    while $\mathfrak{f}_{lig}(\boldsymbol{\sigma}_{l,par(n+1)}^{trial}) \geq 0$ *or* $\mathfrak{f}_{lig}(\boldsymbol{\sigma}_{l,fib(n+1)}^{trial}) \geq 0$ **do**
        $\boldsymbol{E}_{sec,n+1}^{trial} = \mathbb{C}_{sec}^{-1} : \boldsymbol{\Sigma}_{sec,n+1} + \boldsymbol{E}_{sec,n+1}^{p}$;
        Propagate ("downscale") trial strains $\boldsymbol{E}_{sec,n+1}^{trial}$ to lower-scale RVEs;
        Calculate trial stresses in lignin, $\boldsymbol{\sigma}_{l,par(n+1)}^{trial}, \boldsymbol{\sigma}_{l,fib(n+1)}^{trial}$, in parenchyma and sclerenchyma regions;
        if $\mathfrak{f}_{lig}(\boldsymbol{\sigma}_{l,par(n+1)}^{trial}) < 0$ *and* $\mathfrak{f}_{lig}(\boldsymbol{\sigma}_{l,fib(n+1)}^{trial}) < 0$ **then**
            $\boldsymbol{E}_{sec,n+1} = \boldsymbol{E}_{sec,n+1}^{trial}$;
        else
            Calculate plastic strain increment for lignin, $d\boldsymbol{\varepsilon}_{l,n+1}^{p(1)}$, using return mapping algorithm;
            Upscale plastic strain $\boldsymbol{\varepsilon}_{l,n+1}^{p(1)}$ to obtain approximation for "macroscopic" plastic strains $\boldsymbol{E}_{sec,n+1}^{p(1)}$;
            $\boldsymbol{E}_{sec,n+1}^{p} = \boldsymbol{E}_{sec,n+1}^{p(1)}$;
        end
    end
    Calculate stress level $\boldsymbol{\sigma}_{\varphi\bar{\theta}}$ in each fibril defined by Euler angle $\varphi \in [0, 2\pi)$ in each region from $\boldsymbol{E}_{sec,n+1}^{p}$ and $\boldsymbol{E}_{sec,n+1}$;
    Calculate failure criteria for cellulose, $\mathfrak{f}_{c,par}$ and $\mathfrak{f}_{c,fib}$, in both regions based on stress level in each fibril and taking the maximum value;
end

Algorithm 1: Iterative computation of strength for a given stress increment $\Delta\Sigma_{ij}$.

provides rational insight into the plant physics of bamboo and its associated mechanical properties. Finally, we show for sclerenchyma fiber strength in ten different plants that our modeling approach is indeed general and accurate for any plant culm material.

3.5.1 Evidence-based identification of model parameters

"Universal" properties of the three elementary base materials cellulose, hemicellulose and lignin constitute one essential input of our micromechanics model. For bamboo, they are listed in Table 3.1 and 3.2 and have been discussed in Section 3.1.4. The volume fractions of the different phases constitute the second essential input. The RVEs illustrated in Fig. 3.6 and the corresponding micromechanics models account for the morphological relationships

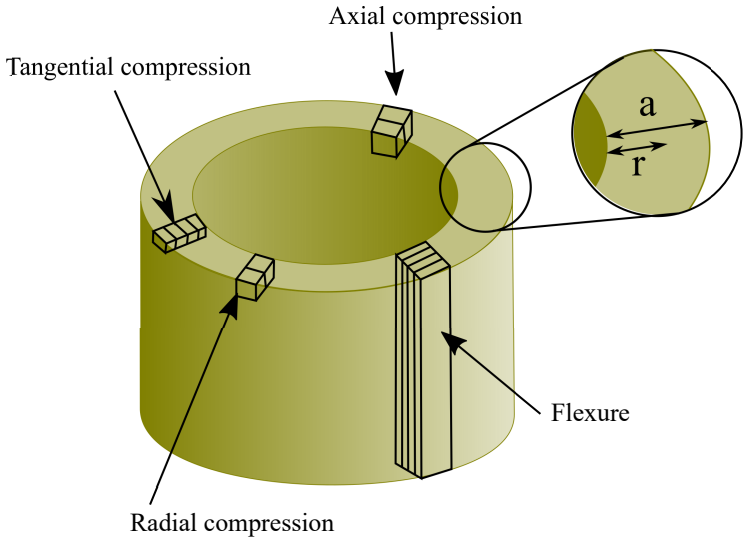

Fig. 3.9: *Geometry and position of specimens in an internode section of bamboo culm (adapted from [49]). The inner, middle and outer regions are defined by* $0 < r/a \leq 0.35$, $0.35 < r/a \leq 0.65$ *and* $0.65 < r/a \leq 1$, *respectively.*

between the microstructure components at each observational scale of the bamboo culm material.

Volume fractions and fiber angles in the cell walls

The chemical composition of the cell wall material in bamboo can be expressed in terms of the relative weight fractions of cellulose, hemicellulose and lignin, which we denote as w_c, w_{hc} and w_l, respectively. According to [101], the average relative weight fractions of the constituents are $w_c = 0.55$, $w_{hc} = 0.20$ and $w_l = 0.25$. The mass densities of these constituents are listed in Table 3.1. The share of crystalline cellulose in relation to the volume of the whole cellulose is given by the crystallinity index (CI), which has been experimentally predicted for bamboo as $CI = 0.85$ [2, 121]. As amorphous cellulose and hemicellulose have the same density and similar mechanical behavior, we treat both in the same way. According to [46], the weight fraction of the crystalline part of cellulose is $w_{cc} = \zeta_w w_c$ and

$$\zeta_w = \frac{CI}{CI + (1 - CI)\rho_{hc}/\rho_{cc}}, \tag{3.25}$$

where ρ_{hc} and ρ_{cc} denote the densities of hemicellulose and crystalline cellulose (see Table 3.1). The equivalent weight fraction of hemicellulose (that is, the weight fraction of amorphous cellulose and hemicellulose) is $w_h = w_{hc} + (1 - \zeta_w)w_c$. The density of the

cell wall material based on the law of mixture can be expressed as:

$$\rho_{wall} = \Big(\frac{w_{cc}}{\rho_{cc}} + \frac{w_h}{\rho_{hc}} + \frac{w_l}{\rho_l}\Big)^{-1}. \tag{3.26}$$

We can compute the volume fractions of the constituents in the cell wall material as:

$$\phi_i^{wall} = w_i \frac{\rho_{wall}}{\rho_i}, \quad i \in [cc, h, l] \tag{3.27}$$

In both the parenchyma and sclerenchyma tissues, the RVE of the cell wall material consists of a hemicellulose-lignin matrix phase that hosts cylindrical crystalline cellulose fibers. The latter are helically oriented with mean fibril angle to the cell axis (see Fig. 3.7). For the RVE of the cell wall in the parenchyma region (level b_1 in Fig. 3.6), the volume fraction of the hemicellulose-lignin matrix phase and the volume fraction of the cellulose inclusions can be computed as $\phi_{hl}^{wall,par} = \phi_h^{wall} + \phi_l^{wall}$ and $\phi_c^{wall,par} = \phi_{cc}^{wall}$, respectively. We can do the same for the volume fractions of the phases in the cell wall RVE of the sclerenchyma fibers (level b_2 in Fig. 3.6). For bamboo, Mannan and co-authors [122] conducted an extensive experimental study on the mean fibril angle in the sclerenchyma and parenchyma regions. They found that the MFA ranges between 4° to 29° for the sclerenchyma region and between 25° to 55° for the parenchyma region. In our study, we adopt average values of 15° and 35° for each of the two regions, respectively. With relations (3.27), the volume fractions for the RVEs at levels a_1 and a_2 (see Fig. 3.6) are simply $\phi_l^{hl,par} = \phi_l^{hl,fib} = \phi_l^{wall}/(\phi_l^{wall} + \phi_h^{wall})$ and $\phi_h^{hl,par} = \phi_h^{hl,fib} = \phi_h^{wall}/(\phi_l^{wall} + \phi_h^{wall})$.

Volume fractions in functional regions and the cross section

The RVE of parenchyma (level c_1 in Fig. 3.6) is made up of solid cell wall material and living symplast. Dixon and Gibson observed that the volume fraction of the cell wall material did not vary significantly throughout the test specimens [49]. In our study, we adopt an average value of $\phi_{wall}^{par} = 0.22$. Living symplast that forms spheroidal inclusions in the transversely isotropic cell wall material has a volume fraction of $\phi_{ls}^{par} = 1 - \phi_{wall}^{par}$. The average elongation ratio of spheroidal symplast inclusions can be directly determined from the longitudinal cut through parenchyma cells that is provided by SEM imaging (see Fig. 3.4b). The ratio is found to be 1.9.

The sclerenchyma fibers (RVE at level c_2 in Fig. 3.6) consists of cell wall material and lumen with volume fractions ϕ_{wall}^{fib} and ϕ_{lum}^{fib}, respectively. Mannan and co-authors [121] extracted several fibers from different locations in the bamboo cross section and measured the inner and outer fiber diameters d_i and d_o. They provide probability distribution functions for d_i

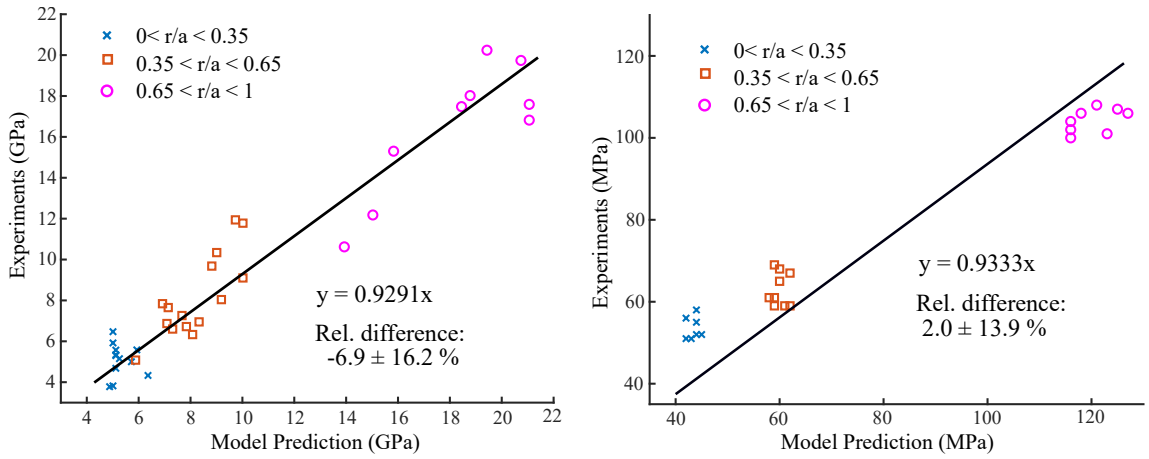

(a) Axial stiffness modulus. **(b)** Axial ultimate strength.

Fig. 3.10: *Comparison of results from the micromechanics model and the experimental tests at different locations of the bamboo cross section. The experimental results are reported by* Dixon *and* Gibson *[49].*

and d_o in the inner, middle and outer regions along the radial direction in the cross section. Using the mean value of d_i and d_o in each region, we can determine the volume fraction of the sclerenchyma fibers in the cell wall material as $\phi_{wall}^{fib} = 0.36$ in the inner region ($0 < r/a \leq 0.35$), $\phi_{wall}^{fib} = 0.48$ in the middle region ($0.35 < r/a \leq 0.65$) and $\phi_{wall}^{fib} = 0.75$ in the outer region ($0.65 < r/a \leq 1$). We refer to Fig. 3.9 for an illustration of these regions.

In the vascular bundles (RVE at level d in Fig. 3.6), vessels form cylindrical inclusions in the matrix of sclerenchyma fibers. The volume fraction of sclerenchyma fibers S_f in the vascular bundles for each test specimen as measured in [49] are reported in Table A.1. The volume fractions of sclerenchyma fibers and vessels in the vascular bundle RVE can be written as $\phi_{fib}^{vb} = S_f$ and $\phi_v^{vb} = 1 - S_f$, respectively. At the cross section scale (RVE at level e in Fig. 3.6), the volume fractions V_{vb} of vascular bundles can be determined from SEM images given in [49]. The V_{vb} values for all specimens obtained from different radial positions in each internode are listed in Table A.1. The volume fractions of vascular bundles and parenchyma in the cross section RVE can now be calculated as $\phi_{vb} = V_{vb}$ and $\phi_{par} = 1 - V_{vb}$, respectively.

3.5.2 Comparison of micromechanics modeling and experimental results

With the model parameters known, we can compute macroscopic elastic stiffness moduli and ultimate strength properties for bamboo in different cross section locations. The results of stiffness and strength properties are listed in Appendix **A** (Tables A.1 and A.2) along with measured volume fractions and model parameters. To obtain a first idea of the predictive

capability of our model, we compute the mean percentage difference and standard deviation of the relative difference in percent between experimental results and model predictions,

$$\bar{e} = \frac{1}{n}\sum e_i = \frac{1}{n}\sum \frac{q_i^{exp} - q_i^{pred}}{q_i^{exp}} \times 100 \tag{3.28}$$

$$e_{sd} = \Big[\frac{1}{n-1}\sum (e_i - \bar{e})^2\Big]^{1/2} \tag{3.29}$$

where q is either axial stiffness (Table A.1) or axial strength (Table A.2). We find that the relative difference $\bar{e} \pm e_{sd}$ is in the range $-6.9 \pm 16.2\%$ for the axial stiffness modulus and in the range $2.0 \pm 13.9\%$ for the ultimate axial strength.

Figures 3.10a and 3.10b plot the micromechanics model prediction versus each available experimental test result at different locations of the bamboo cross section for the axial stiffness modulus and the ultimate axial strength, respectively. These results and figures show an excellent agreement between the micromechanics model and the results of the experimental tests. We also calculate elastic limit points $\mathbf{\Sigma}^{\mathbf{el,c}}_{\mathbf{est}}$ that we report in Table A.2. As experimental results on elastic limits are not reported in [49], the model results cannot be validated quantitatively. The complete elastoplastic stress-strain evolution curves given in Fig. 3.8 can also not be used for a quantitative validation of the model, as Zhang and collaborators [205] did not report the microimaging information at the lower scales, required as an input for our micromechanics model. From a qualitative viewpoint, however, the elastic limit points of our model are in good agreement with the elastic limit points given in Fig. 3.8.

3.5.3 The structural behavior of bamboo from a multiscale viewpoint

Figures 3.11a and 3.11b illustrate the functionally graded response of bamboo at the cross section level, illustrated by the stiffness moduli E_A and E_T and the compressive strengths Σ_A and Σ_T in axial and transverse directions for different radial positions. The data points for each parameter, obtained from the micromechanics model, are fitted with a two-term exponential curve of the form $f(x) = A\exp(B\,x) + C\exp(D\,x)$, with fitting parameters A to D and radial position $x = r/a$ (see Fig. 3.9).

Radial gradation of stiffness and strength

On the one hand, we can observe in Figs. 3.11a and 3.11b that axial stiffness and strength show a strong gradient towards the outer part of the bamboo culm, which correlates with the increasing density of vascular bundles. On the other hand, the transverse stiffness

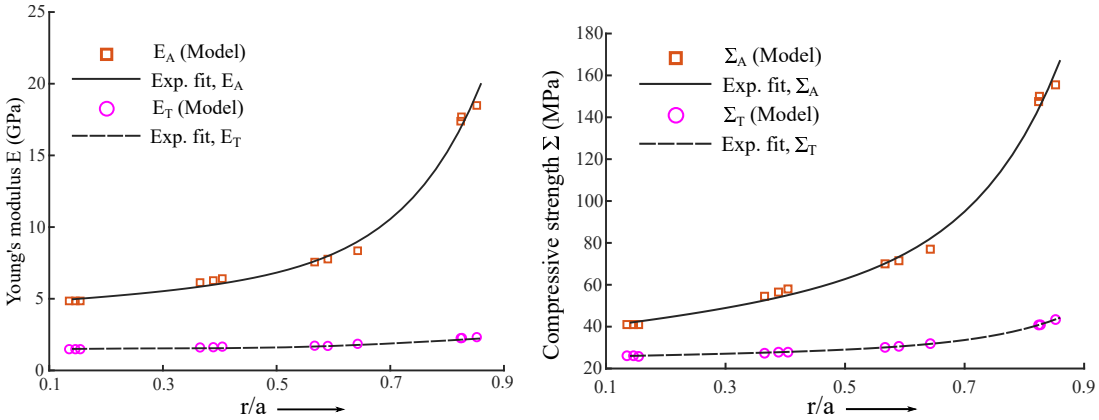

(a) Stiffness moduli. **(b)** Ultimate compressive strength.

Fig. 3.11: *Variation and exponential fit of results in axial (subscript A) and transverse (subscript T) directions from the micromechanics model at different radial positions of the bamboo cross section.*

and strength properties exhibit a comparatively mild gradient as compared to the axial properties. From a practical standpoint, these observations indicate a natural structure optimization to optimally resist bending caused by lateral loads on the bamboo culm.

With the help of various empirical and experimental investigations, one can represent different strength and stiffness components as a function of density [179]. In the case of axial stiffness and strength, this correlation has been found to be linear [49, 102]. For other components such as shear and transverse strength, however, the correlation with density is not apparent [130]. Figures 3.12a and 3.12b plot the axial and transverse strength results that correspond to the 36 experimental sets from Table A.1. In the case of axial strength, we can observe a clear correlation with density. Given the strong spread in data, however, we assume that density alone cannot represent the mechanical properties and a simple model based on an empirical linear relation with density cannot predict their variation accurately. For axial compressive strength, transverse normal strength and transverse shear strength, we do not observe a pronounced variation with density.

The reason for the strong anisotropy in stiffness and strength is the need for optimizing the material response with respect to lateral loading. As a consequence, the structure is strong in axial bending, but significantly weaker in shear. For instance, we can see from Fig. 3.12b that the transverse shear strength attains only 8-10% of the total compressive strength. When bamboo components are used as load-bearing components in man-made structures, structural failure is often initiated due to splitting of the material near joints, with subsequent local buckling of the culm [101, 129, 179]. These failure patterns are influenced significantly by the comparatively low transverse compressive and shear strengths. Hence, the lack of shear and transverse strength seems to be a limiting factor for the use of

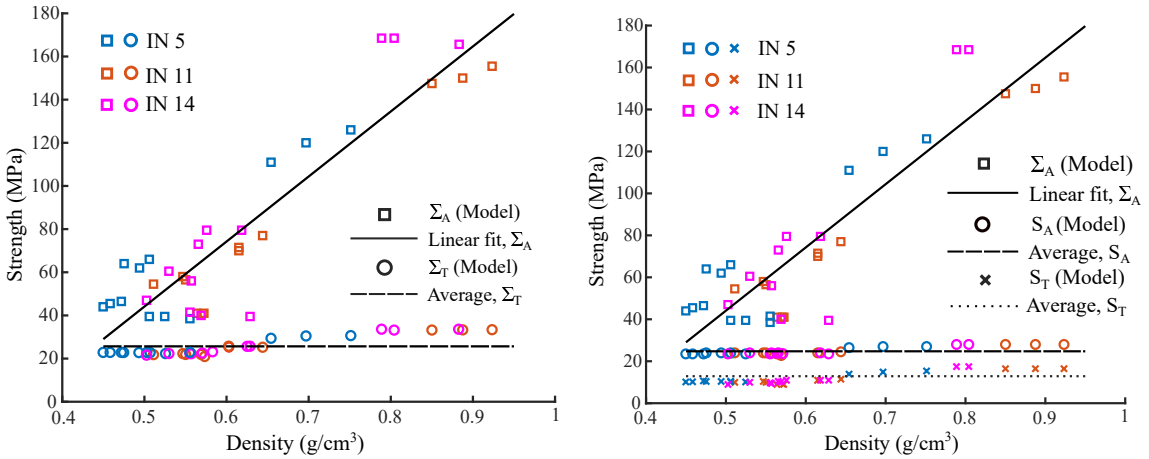

(a) Compressive strengths Σ_A and Σ_T.

(b) Compressive strength Σ_A, shear strength S_A and shear strength S_T.

Fig. 3.12: *Variation with density of different strength results in axial (subscript A) and transverse (subscript T) directions obtained with the micromechanics model. IN is the internode number (see Table A.1).*

bamboo as an effective building material.

Insights through micromechanics model results

Our micromechanics modeling approach provides a tool to rationally interpret and explain the strongly anisotropic and functionally graded behavior of bamboo. In our model, the axial strength Σ_A is governed by sclerenchyma fibers that attract most of the stress due to their high stiffness. Their failure is triggered by a sequential failure of lignin and cellulose microfibrils. After failure of lignin, cellulose microfibrils are able to bear stress with the help of a bridging mechanism that leverages the high strength of crystalline cellulose in axial direction. Hence, the increasing density of vascular bundles leads to very high axial strength, with a peak towards the outer part of the culm. The transverse normal strength Σ_T and the transverse shear strength S_T mainly depend on cellulose microfibrils that fail immediately after failure of lignin in the sclerenchyma regions, as crystalline cellulose is relatively weak in the transverse direction. Since there are no bridging mechanisms, the strength mainly depends on the lignin content in the sclerenchyma fibers. Hence, a slight increase in Σ_T and S_T with density can be attributed to the relatively high lignin content in the outer region of the bamboo culm.

The main mechanical function of the parenchyma matrix in the bamboo cross section is to provide resistance to axial shear stresses. Hence, in the case of loading scenarios that involve axial shear (Σ_{31}, Σ_{32}), the parenchyma matrix plays a major role in the load-bearing

Table 3.3: *Experimental data and prediction of axial strength for different natural fibers.*

Fiber type	**Density** (ρ_{fib})	**Cellulose**	**Hemicellulose**	**Lignin**	**MFA**	$\boldsymbol{\Sigma^{ult}_{exp}}$	$\boldsymbol{\Sigma^{ult}_{est}}$
Hemp	1.48	70.2 - 74.4	17.9-22.4	3.7-5.7	6	690 - 873	698
Jute	1.3-1.45	61 - 73.2	13.6 - 20.4	12.0 - 16.0	8	393-773	595
Kenaf	0.749	31 - 71	21.5 - 25	15 - 22.7	10	223-624	323
Ramie	1.45	68.6 - 76.2	13.1 - 16.7	0.6 - 1	10	400-938	728
Sisal	1.45	56.5 - 78	5.6 - 16.5	8.0 - 14.0	20	80-640	577
Cotton	1.5-1.6	82.7 - 92	5.7 - 6	1	25	287-800	637
Alfa	0.89	45.4	38.5	14.9	10	350	268
Banana	1.35	63 - 67.6	19	5	11	529-914	601
Softwood	0.3-0.59	42 - 44	22 - 27	28 - 31	30	45.5-111.7	88
Hardwood	0.3-0.88	37.6	32.9	31-33	14	51-120.7	118

Please refer [14, 64, 107] and the references therein for further details on the experimental data.

behavior. The immediate failure of cellulose microfibrils after the failure of lignin in the parenchyma region governs the axial shear strength S_T of the bamboo material. As the cell wall volume fraction in the parenchyma region is constant through the cross section, the axial shear strength S_T remains almost constant throughout the section, which is confirmed by the model results plotted in Fig. 3.12b. Hence, we can conclude that the strength of bamboo material in different direction is the result of the hierarchical organization of microheterogeneous structures at different scales. On the one hand, our results indicate that it cannot be represented adequately with a few physical parameters. On the other hand, our micromechanics model is able to accurately predict strength properties and enables insights into the corresponding failure mechanisms at different microstructure levels.

3.5.4 Prediction of ultimate strength for other culm materials

Finally, we would like to briefly illustrate that our model can be easily transferred to other culm materials. To this end, we focus on the axial strength property of sclerenchyma fibers that can be extracted from different plant materials. Following [64] and the references therein, we collect experimental data on density, weight fraction of constituents, mean fibril angle and ultimate strength in sclerenchyma fibers of ten different plant materials. The values listed in Table 3.3 illustrate that the properties of these fibers vary significantly.

Since we focus on sclerenchyma fibers only, our micromechanics model considers only a subset of the hierarchical levels given in Fig. 3.6, namely the RVEs at levels a_2, b_2 and c_2. Following our discussion in Section 3.5.1, our model requires input parameters in terms of the volume fractions $\phi_h^{hl,fib}$, $\phi_l^{hl,fib}$ and $\phi_c^{wall,fib}$ along with the microfibril angle. Given the relative weight fraction of the constituents of the cell wall material, we can estimate these volume fractions, following the arguments of Section 3.5.1. Similarly, we require the volume fraction ϕ_{wall}^{fib} of the cell wall material in sclerenchyma fibers. Suitable microimages to help

quantify ϕ_{wall}^{fib} are not available here. Therefore, we use the density of the extracted fibers (ρ_{fib} in Table 3.3) to estimate $\phi_{wall}^{fib} = \rho_{wall}/\rho_{fib}$, where we refer to (3.26) for calculating the density ρ_{wall}. To estimate the relative weight fraction of the constituents of the cell wall material, we assume average values of cellulose, hemicellulose and lignin fractions as reported in Table 3.3. We then employ (3.2) and (3.5) to derive the homogenized stiffness moduli of the RVEs at levels a_2, b_2 and c_2. We can then use the strain concentration relations (3.15), (3.18), (3.19) and (3.20) to upscale/downscale elastoplastic strains. Following Algorithm 1, we can predict the axial ultimate strength Σ_{est}^{ult} for all fibers.

The results of our analysis are summarized in Table 3.3. We observe that for all fibers, the model predictions fall within the range of experimentally obtained axial strength values. We emphasize again that all fibers follow a "universal" hierarchical structure, but differ in terms of multiscale composition. This difference in composition results in the wide range of ultimate strength. The results shown in Table 3.3 indicate that our model is able to accurately predict mechanical properties for a range of culm materials.

Chapter 4

Experimental characterization and micromechanical modeling of cereal stem materials

In the previous chapter, we established an approach for evidence based multiscale modeling of hierarchical culm material within continuum micromechanics framework. In the next step, we transfer this approach for the material modeling of cereal stems with a focus on oats, which is of particular focus of this thesis from application viewpoint. In contrast to the previous chapter that focused on functionally graded culm materials, we focus here on the configuration of an inner layer of foam-like parenchyma cells surrounded by a dense outer shell, which is typical for cereal stems. This morphology brings along specific challenges for deriving microstructure-property relationships, which we describe and suggest solutions for.

This chapter presents a model for the stiffness and strength of cereal stem materials utilizing the cascade continuum micromechanics approach for a broad range of inclusion morphologies, summarized in Section 2.2.3. We first discuss the experimental multiscale characterization based on microimaging (micro-CT, light microscopy, transmission electron microscopy) and chemical analysis for oat stems, working with our collaborators **D. Jo Heuschele**, **Kevin P. Smith** from Agronomy and Plant Genetics, **George Annor** from the Department of Food Science and Nutrition, and **Alex Fok** from Minnesota Dental Research Center for Biomaterials and Biomechanics at the University of Minnesota. We then derive in detail a general micromechanics based model of macroscale stiffness and strength following our discussion in Chapter 2. We specify our model for oats and validate

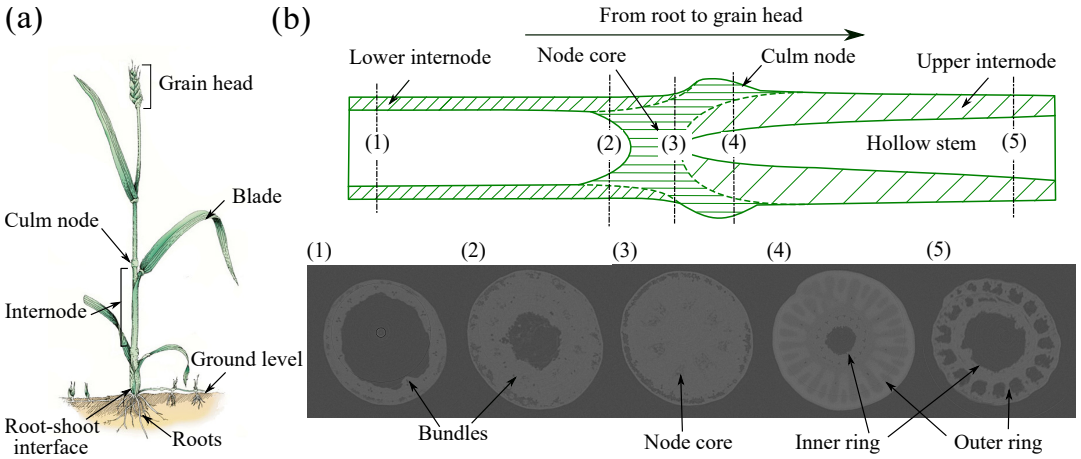

Fig. 4.1: *Typical anatomy of a cereal plant and nodal region characterization with the help of micro-CT images.*

it against a series of bending experiments that we conducted with oat stem samples. In the context of biomechanical tailoring, we demonstrate that our model can predict the effects of genetic modifications of microscale composition and morphology on macroscale mechanical properties of thale cress reported in the literature.

This chapter is organized as follows: Section 4.1 characterizes the multiscale nature of cereal stem material for the example of oat, using chemical analysis and microimaging technologies. Section 4.2 describes our micromechanics modeling approach for the stiffness and elastic limit strength of cereal stem material and discusses essential modeling assumptions directly derived from plant physics. In Section 4.3, we validate model predictions that we obtained for parameters retrieved from the microimages reported in Section 4.1 with four-point bending flexural tests that we performed on oat stems. In Section 4.4, we demonstrate the ability of our model to quantify the effect of gene mutations and the associated compositional and morphological changes at multiple length scales on the macroscale mechanical properties.

4.1 Experimental characterization of oat stem material

Cereal stems usually consist of hollow and cylindrical internode regions separated by nodes, where leaves are attached. The length of the internodes increases from the ground to the top (root to grain head). Figure 4.1a illustrates a typical macroscale anatomy. An in-depth geometric and material characterization enables a better physics-based understanding of the mechanical behavior. In this section, working with our collaborators, we profile the compositional and morphological properties across scales for the example of the node and

internode regions of oats. Advanced microimaging technologies such as computed tomography (CT), light microscopy, and transmission electron microscopy (TEM), along with chemical composition analysis enable the qualitative and quantitative description of various hierarchical levels in the plant stem organization. The oat stem specimens used for the analysis were grown at the University of Minnesota in greenhouses and fields in St. Paul, MN. Four commercial varieties of oats – Gopher, Reins, ND021052, and IL07-8721 – were selected for the analysis. All specimens were checked for disease, pest damage, and other mechanical damage. Only specimens with no visible damage were included for the imaging and chemical analysis.

4.1.1 Node morphology through micro-CT images

We explored the node architecture in oat stems with the help of micro-CT images (see Fig. 4.1b). Test specimens for the micro-CT study were obtained from the greenhouse two weeks after the flowering stage. The nodal region next to the root-shoot interface was removed and air-dried for 24 hours. The specimens were imaged using a micro-CT machine (XT H 225, Nikon Metrology Inc., Brighton, MI, USA). The scanning parameters were as follows: 80kV, 85 μA, 708 ms of exposure, 720 projections, and four frames per projection with a resolution of 7.44 μm. The lower exposure time (ms) and currant (μA) create sharper images as long as the kV signal to noise is kept at the 10,000 level. The total scanning time was approximately 35 minutes for each specimen. The imaging data was exported to a series of DICOM files using VGStudio MAX 2.1 (Volume Graphics GmbH, Heidelberg, Germany). The DICOM files were further analyzed using semi-automatic image processing tools developed in MATLAB.

Figure 4.1b schematically describes the morphology of the node in the longitudinal direction, moving towards the grain head. This figure also shows the selected micro-CT images indicating their position in the node region. It is apparent from the micro-CT images that the morphology changes from left to right (moving upwards to the grain head) in the node region. Image 3 depicts the dense node core material, which is the hardest anatomical part of the oat stem. In images 4 and 5, the distinction between the outer and inner elliptical rings is apparent. In images 2 and 3, however, the elliptical rings are absent. This investigation reveals that the internode starts after the node core zone and the elliptical rings become smaller until they disappear, marking the start of the hollow upper internode. In conclusion, the structure of the node is asymmetrical along the length direction, which makes the node an important anatomical site in the context of the mechanical behavior of the plant. Similar morphological observations are reported for a wheat nodal region [70]. In this chapter, however, we focus on the internode region.

(a) Elliptical rings in upper internode.

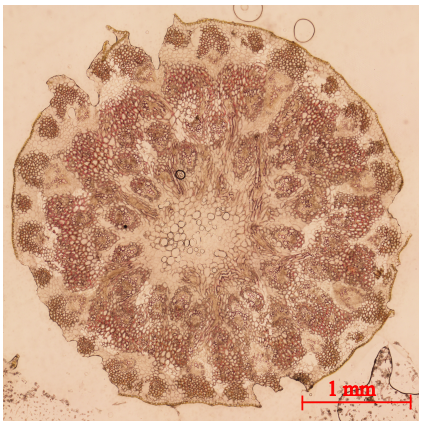

(b) Dense node material.

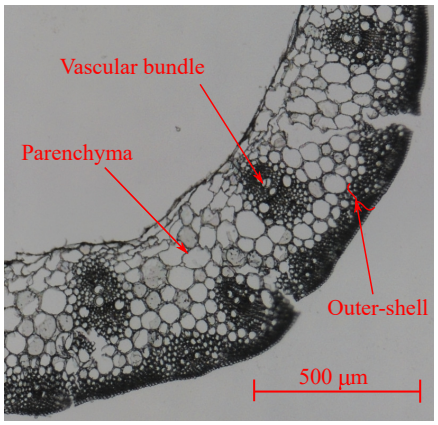

(c) Internode cross-section.

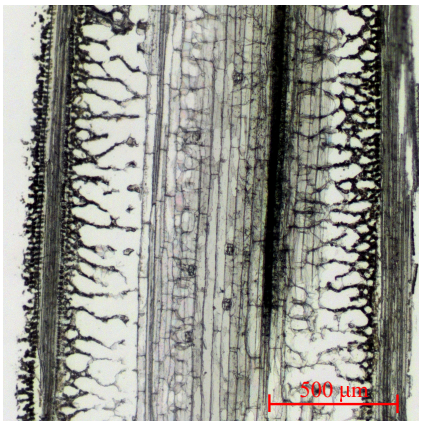

(d) Internode transverse section.

Fig. 4.2: *Cross-section profile of an oat stem through light microscopy images.*

4.1.2 Cross-section through light microscopy images

We examined the cross-section of the oat stem by light microscopy images at different heights in the stem (see Fig. 4.2). Fresh stem segments were collected from field-grown plants two weeks after flowering. The plant tissues were preserved using a Carnoy's solution made up of 60% ethanol, 30% chloroform, 10% glacial acetic acid, and 1 gm of ferric chloride. All chemicals were research grade (Sigma-Aldrich, St. Louis, MO, USA). Thereafter, the tissues were embedded into a 2 cm parafilm block for sectioning. The samples were sectioned into 20 μm thick slices and placed onto slides. The slides were stained with 3% phloroglucinol and visualized on a Nikon Eclipse 90i light microscope (Nikon Metrology, Inc., Brighton, MI, USA) at 4x magnification within 30 minutes of staining. Multiple images of a cross-section were stitched together using the NIS software (Nikon Metrology, Inc., Brighton, MI,

USA).

Figure 4.2 illustrates anatomical details of the oat stem cross-section in different regions via selected light microscopy images. Figures 4.2a and 4.2b outline the elliptical rings in the upper internode region and the dense node core material, respectively. Figures 4.2c and 4.2d show the cross-section and the transverse-section of the oat stem internode region. The morphological longitudinal profile of the internode region is consistent, excluding the beginning and the termination stages of the internode. These images confirm the observations described in Section 4.1.1.

In Figs. 4.2c and 4.2d, dense epidermal layers with elongated collenchyma cell layers can be identified in the outer part of the internode cross-section. In this paper, we call these layers collectively the outer shell. The primary function of the outer shell is considered to stiffen the stem structure. In the inner part, vascular bundles are embedded in a matrix made up of parenchyma tissues. The vascular bundle tissues run through the length of the stem and have the main axis parallel to the longitudinal direction of the stem. The vascular bundles integrated with the parenchyma tissues are anticipated to act as a compliant core supporting the outer shell against loads beard during the lifetime of a plant.

4.1.3 Functional regions through transmission electron microscopy images

We examined functional regions including vascular bundles, parenchyma, and outer shell with the help of transmission electron microscopy (TEM) images (Fig. 4.3). We followed Sato's protocols for the imaging [157]. Stem cross-sections were cut approximately 2 mm thick, placed in 2.5% glutaraldehyde in 0.1M sodium cacodylate buffer under vacuum for at least 1 hour, then stored overnight at 4 °C. Sections were then cut into quarters, rinsed in the buffer (3x for 10 min each), and post-fixed in 1% osmium tetroxide in 0.1M sodium cacodylate buffer overnight at 4 °C. Following three rinses in ultra-pure water for 10 min each, stem pieces were dehydrated in an ethanol series (25%, 50%, 75%, 95%, 2x each for 20 min; 100% dry ethanol 3x each for 20 min) followed by propylene oxide (2x, 20 min), and embedded in Embed 812 resin. Ultrathin sections (70-100 nm) were cut with a diamond knife on a Leica Ultracut UCT ultramicrotome, collected on formvar/carbon-coated 200-mesh grids, stained with uranyl acetate (20 min) and Sato's triple lead stain (3 min), and observed under a FEI Philips CM 12 transmission electron microscope operating at 60 kV. Images were recorded with a Maxim DL digital capture system.

Figure 4.3a demonstrates the morphology of fibers and vessels (Xylems and phloems) in a vascular bundle. The sclerenchyma fibers are long hollow tubes with thick cell walls

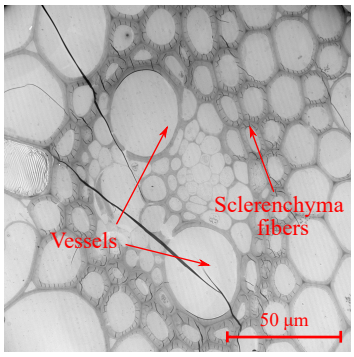

(a) Microstructure vascular bundle.

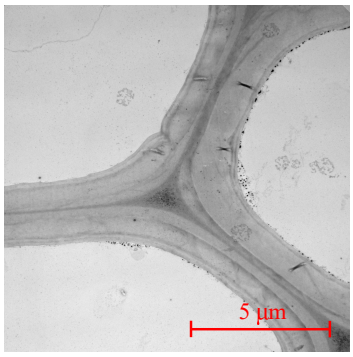

(b) Parenchyma cell wall.

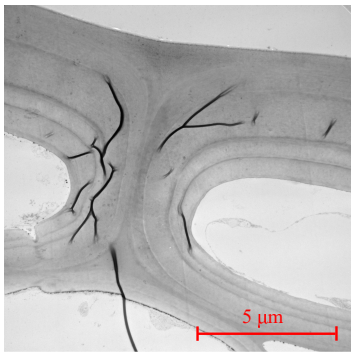

(c) Epidermis cell wall.

Fig. 4.3: *Functional region characterization through transmission electron microscopy (TEM).*

oriented in the stem direction. The bundles are embedded in the parenchyma matrix. The parenchyma cells consist of thin cell walls and exhibit polyhedral geometry (see Fig. 4.3b). The cells are filled with living protoplasm and a major storage place for nutrients in the plant. The outer-shell region exhibits a similar morphology as sclerenchyma fibers. They have elongated thick cell walls surrounding holes (lumen) with a polygonic or circular cross-section (see Fig. 4.3c). The biological function of the epidermis is to control gas exchange and water balance.

The cell wall material in the functional regions is made up of cellulose, hemicellulose, and lignin. In the cell wall material, cellulose fibrils are helically wound with an average microfibril angle (MFA) to the cell axis that we denote by $\bar{\theta}$. Figures 4.3b and 4.3c depict TEM images showing the multi-layered cell wall structure in the parenchyma and epidermis cells in the oat stem, respectively.

Table 4.1: *Chemical composition of the oat stem in percentage of total dry mass.*

Variety	**Lignin** w_c	**Hemicellulose** w_{hc}	**Cellulose** w_c
Gopher	50.69	18.80	30.51
Reins	65.30	15.28	19.42
ND021052	61.20	17.83	20.97
IL07-8721	62.47	18.24	19.29

4.1.4 Chemical composition of the oat stem

Table 4.1 summarizes the chemical composition as the percentage of total dry mass in the oat stem. Field-grown plants were collected two weeks after flowering, and oven-dried for two days to preserve samples. Tissue samples were grounded and further divided into three types of chemical analysis. All chemicals used were research grade (Sigma-Aldrich, St. Louis, MO, USA). Hemicellulose concentration was determined by HPLC-MS [9, 10]. Lignin was digested using a modified Klauson method to determine acid-soluble lignin [4], while cellulose was determined by the one-step/two-step method [199, 200]. The percent of the total dry mass was calculated for each material and reported into Table 4.1.

4.2 Multiscale modeling of stiffness and strength of cereal stem material

In this section, we describe in detail our micromechanics based modeling approach for cereal stem materials. We describe the multistep micromechanical representation of the hierarchical organization of cereal stem materials and establish microstructure-stiffness and microstructure-strength relationships. Our modeling decisions and required parameters are based on the multiscale characterization data discussed in the previous section.

4.2.1 From hierarchical representation to multistep micromechanics modeling

Figure 4.4 provides a summary of our multistep micromechanics model. Following Section 2, we transfer the multiscale characterization (given here for the example of an oat stem) in a multistep micromechanical representation. The cross-section of a cereal stem consists of an outer shell and the inner foam-like soft pith. To this end, we build multistep micromechanics models for both regions independently and combine them together in the cereal stem cross-section (see Fig. 4.4C). Here, we describe each RVE of the multistep model for outer-shell and soft-pith regions.

↪ At the finest scale in the soft-pith, we consider RVEs of the *cell wall material* in the parenchyma and sclerenchyma region, represented by level (a_1) and (a_2) in Fig. 4.4. Each RVE is regarded as a three-phase material, consisting of crystalline cellulose, hemicellulose, and lignin. The cylindrical cellulose fibrils helically wind around the lumen within the cell wall with an average inclination angle to the cell axis denoted as microfibril angle

(MFA) $\bar{\theta}$. Since all three phases have contact with each other, we assume that they form an "average" transversely isotropic matrix. The "average" matrix hosts spherical inclusions of hemicellulose and lignin, and helically wound cylindrical inclusions of the cellulose fibrils.

↪ The RVE at level (b_1) represents the *parenchyma* base tissues in the soft-pith region. It contains two phases: the cell wall material and the living symplast. The mechanical properties of living symplast are assumed equivalent to water. Due to its polyhedral geometry, we assume that the living symplast forms spheroidal inclusions in the matrix of the cell wall material.

↪ The RVE at level (b_2) represents a *sclerenchyma fiber*, that consists of a matrix of cell wall material hosting cylindrical inclusions of lumens. The RVE at level (c) represents a *vascular bundle* in soft pith, where xylem and phloem tissues are surrounded by sclerenchyma sheath. The constituent phases of this RVE are sclerenchyma fibers (matrix) and vessels (cylindrical inclusion assumed to be filled with water).

↪ At the RVE level (d), the parenchyma base material and the vascular bundles are brought together to form *soft pith*. The vascular bundles are distributed in the parenchyma matrix. They run through the whole length of the stem and are modeled as cylindrical inclusions.

↪ The multistep model for the outer shell consists of two RVEs (see Fig. 4.4B). The RVE at level (e) represents a *cell wall material* for the outer-shell region. It is equivalent to the level (a_2) in the soft-pith region. Level (e) forms matrix and hosts cylindrical inclusions of lumens for the RVE of a *outer-shell* material at level (f).

4.2.2 Microstructure-stiffness relationship in the elastic range

We describe the homogenization procedure for the elastic stiffness coefficients for the example of oat. To this end, we consider the hierarchical structure in terms of the RVEs illustrated in Fig. 4.4. Again, homogenization in the elastic range is mainly based on the central relation (2.21) developed in Chapter 2.

Cell wall materials

In the RVE that corresponds to the *cell wall material* in the parenchyma region (level a_1 in Fig. 4.4), we denote the volume fractions of hemicellulose, lignin, and crystalline cellulose as $\phi_h^{wall,par}$, $\phi_l^{wall,par}$, and $\phi_c^{wall,par}$, which satisfy $\phi_l^{wall,par} + \phi_h^{wall,par} + \phi_c^{wall,par} = 1$. The

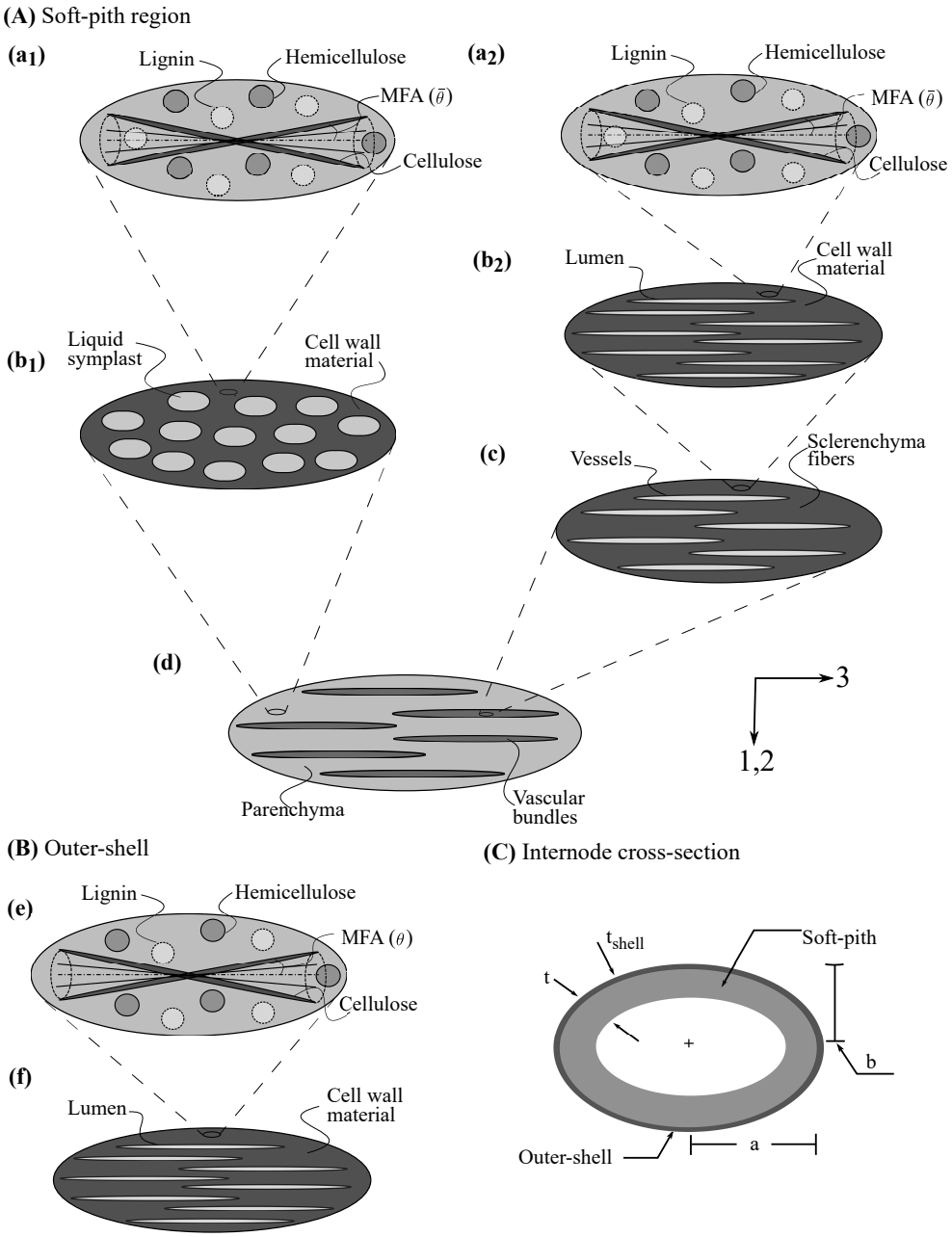

Fig. 4.4: *Multistep micromechanical representation of cereal stem material. The two columns in (A) represent individual models for the parenchyma and vascular bundles in the soft-pith region. (B) depicts the multistep model for the outer-shell region and (C) a schematic representation of the stem cross-section.*

stiffness tensors of hemicellulose, lignin, and cellulose, $\mathbb{c}_h$, $\mathbb{c}_l$, and $\mathbb{c}_c$, can be filled with values from Table 3.1 from Chapter 3. All three phases are in contact with each other and form an intimate mixture. Therefore, we assume the self-consistent scheme with an "average" host matrix for this RVE. As discussed in the previous section, helically wound cylindrical inclusions of cellulose fibrils, and spherical inclusions of hemicellulose and lignin are embedded in this "average" matrix. The helical orientation of the fibrils are accounted following the strategy outlined in the previous chapter (see Section 3.3.1). Following (2.21) with $\mathbb{C}^0 = \mathbb{C}^{hom} = \mathbb{C}^{par}_{wall}$ and $r, s \in [h, l]$, we arrive at the stiffness tensor $\mathbb{C}^{par}_{wall}$ of the cell wall material in the parenchyma region as:

$$\begin{aligned}\mathbb{C}^{par}_{wall} = \Big\{ \sum_r \phi_r^{wall,par} \mathbb{c}_r : [\mathbb{I} + \mathbb{P}^{wall,par}_{sph} : (\mathbb{c}_r - \mathbb{C}^{par}_{wall})]^{-1} + \ \phi_c^{wall,par} \langle \mathbb{c}_c(\varphi,\bar{\theta}) : [\mathbb{I} + \\ \mathbb{P}^{wall,par}_{cyl}(\varphi,\bar{\theta}) : (\mathbb{c}_c(\varphi,\bar{\theta}) - \mathbb{C}^{par}_{wall})]^{-1} \rangle \Big\} : \Big\{ \sum_s \phi_s^{wall,par} [\mathbb{I} \ + \mathbb{P}^{wall,par}_{sph} : (\mathbb{c}_s - \\ \mathbb{C}^{par}_{wall})]^{-1} + \phi_c^{wall,par} \langle [\mathbb{I} + \mathbb{P}^{wall,par}_{cyl}(\varphi,\bar{\theta}) : (\mathbb{c}_c(\varphi,\bar{\theta}) - \mathbb{C}^{par}_{wall})]^{-1} \rangle \Big\}^{-1}.\end{aligned} \tag{4.1}$$

All other notations in (4.1) are introduced in Section 3.3.1. Due to its implicit format with respect to $\mathbb{C}^{par}_{wall}$, relation (4.1) is computed iteratively [84, 85].

We deal with the RVE of the *cell wall material* in the sclerenchyma region (level a_2 in Fig. 4.4) in a similar fashion, where the volume fraction of hemicellulose, lignin, and cellulose are $\phi_l^{wall,fib}$, $\phi_h^{wall,fib}$, and $\phi_c^{wall,fib}$. With $r, s \in [h, l]$, the corresponding homogenized stiffness tensor $\mathbb{C}^{fib}_{wall}$ of the RVE follows as:

$$\begin{aligned}\mathbb{C}^{fib}_{wall} = \Big\{ \sum_r \phi_r^{wall,fib} \mathbb{c}_r : [\mathbb{I} + \mathbb{P}^{wall,fib}_{sph} : (\mathbb{c}_r - \mathbb{C}^{fib}_{wall})]^{-1} + \phi_c^{wall,fib} \langle \mathbb{c}_c(\varphi,\bar{\theta}) : [\mathbb{I} + \\ \mathbb{P}^{wall,fib}_{cyl}(\varphi,\bar{\theta}) : (\mathbb{c}_c(\varphi,\bar{\theta}) - \mathbb{C}^{fib}_{wall})]^{-1} \rangle \Big\} : \Big\{ \sum_s \phi_s^{wall,fib} [\mathbb{I} + \mathbb{P}^{wall,fib}_{sph} : (\mathbb{c}_s - \\ \mathbb{C}^{fib}_{wall})]^{-1} + \phi_c^{wall,fib} \langle [\mathbb{I} + \mathbb{P}^{wall,fib}_{cyl}(\varphi,\bar{\theta}) : (\mathbb{c}_c(\varphi,\bar{\theta}) - \mathbb{C}^{fib}_{wall})]^{-1} \rangle \Big\}^{-1}.\end{aligned} \tag{4.2}$$

Parenchyma region

The RVE of the parenchyma (level b_1 in Fig. 4.4) contains the inclusions of the living symplast in the matrix of the cell wall material. The inclusion volume fraction in the parenchyma is in the range of $0.8 - 0.9$ for cereals as summarized in Table B.1 for the example of oat. Neither the Mori-Tanaka scheme nor the self-consistent scheme are suitable

at higher inclusion volume fractions. In Section 2.2.3, we summarize the cascade continuum micromechanics (CCM) model to estimate elastic properties for a broad range of inclusion volume fractions [176, 177]. Following [176], the morphology of the parenchyma region is identical to foam, and cascade level $n = 2$ leads to good agreement with experimental results. We use the CCM model with $n = 2$ to estimate the homogenized stiffness of the parenchyma region following (2.22).

We denote the volume fraction of the living symplast inclusions and the cell wall material matrix as ϕ_{ls}^{par} and ϕ_{wall}^{par}, which satisfy $\phi_{ls}^{par} + \phi_{wall}^{par} = 1$. The elastic properties of the living symplast can be assumed to be equivalent to water, that is, $\mathbb{c}_w$. At cascade level $n = 1$, the cell wall material acts as a matrix, that is, $\mathbb{c}_m = \mathbb{C}_{wall}^{par}$ in (2.23a), in which the symplast forms spheroidal inclusions. With the Hill tensor $\mathbb{P}_r^0 = \mathbb{P}_{sphrd}^{wall}$, which corresponds to spheroidal inclusions with a known elongation ratio in the transversely isotropic matrix of the cell wall material [113], the homogenized stiffness tensor $\mathbb{C}_{par}^{(1)}$ at cascade level $n = 1$ can be expressed as:

$$\mathbb{C}_{par}^{(1)} = \left\{\phi_{wall}^{par}\mathbb{C}_{wall}^{par} + \phi_{ls}^{par}\mathbb{c}_w : [\mathbb{I} + \mathbb{P}_{sphrd}^{wall} : (\mathbb{c}_w - \mathbb{C}_{wall}^{par})]^{-1}\right\} : \left\{\phi_{wall}^{par}\mathbb{I} + \phi_{ls}^{par}[\mathbb{I} + \mathbb{P}_{sphrd}^{wall} : (\mathbb{c}_w - \mathbb{C}_{wall}^{par})]^{-1}\right\}^{-1} . \tag{4.3}$$

The homogenized stiffness tensor $\mathbb{C}_{par}^{(1)}$ acts as a matrix for cascade level $n = 2$. Following (2.23b) with analogous notations, we obtain the stiffness tensor of the parenchyma $\mathbb{C}_{par}$ as:

$$\mathbb{C}_{par} = \left\{\phi_{wall}^{par}\mathbb{C}_{par}^{(1)} + \phi_{ls}^{par}\mathbb{c}_w : [\mathbb{I} + \mathbb{P}_{sphrd}^{par,(1)} : (\mathbb{c}_w - \mathbb{C}_{par}^{(1)})]^{-1}\right\} : \left\{\phi_{wall}^{par}\mathbb{I} + \phi_{ls}^{par}[\mathbb{I} + \mathbb{P}_{sphrd}^{par,(1)} : (\mathbb{c}_w - \mathbb{C}_{par}^{(1)})]^{-1}\right\}^{-1} . \tag{4.4}$$

Sclerenchyma fibers and vascular bundles

The RVE of the sclerenchyma fibers (level b_2 in Fig. 4.4) and the vascular bundle (level c in Fig. 4.4) are identical to the RVEs demonstrated in level c_2 and d in Fig. 3.6 of Chapter 3. With the identical notations to (3.7), the stiffness tensor $\mathbb{C}_{fib}$ for the RVE of

the sclerenchyma region can be obtained as:

$$\mathbb{C}_{fib} = \left\{\phi^{fib}_{wall}\mathbb{C}^{fib}_{wall} + \phi^{fib}_{lum}\mathbb{c}_w : [\mathbb{I} + \mathbb{P}^{wall}_{cyl} : (\mathbb{c}_w - \mathbb{C}^{fib}_{wall})]^{-1}\right\} : \left\{\phi^{fib}_{wall}\mathbb{I} + \phi^{fib}_{lum}[\mathbb{I} + \mathbb{P}^{wall}_{cyl} : (\mathbb{c}_w - \mathbb{C}^{fib}_{wall})]^{-1}\right\}^{-1} . \tag{4.5}$$

Similarly, following (3.8) the elastic stiffness tensor $\mathbb{C}_{vb}$ of a vascular bundle RVE can be written as:

$$\mathbb{C}_{vb} = \left\{\phi_{fib}\mathbb{C}_{fib} + \phi_v\mathbb{c}_w : [\mathbb{I} + \mathbb{P}^{fib}_{cyl} : (\mathbb{c}_w - \mathbb{C}_{fib})]^{-1}\right\} : \left\{\phi_{fib}\mathbb{I} + \phi_v[\mathbb{I} + \mathbb{P}^{fib}_{cyl} : (\mathbb{c}_w - \mathbb{C}_{fib})]^{-1}\right\}^{-1} . \tag{4.6}$$

Soft-pith and outer-shell materials

The macroscopic section of the cereal stem material is made up of a soft-pith core surrounded by outer-shell material (see Fig. 4.4C). In the RVE of the soft-pith region (level d in Fig. 4.4), the vascular bundles are embedded into the matrix of parenchyma base tissues. The volume fraction of the parenchyma region and the vascular bundles are ϕ_{par} and ϕ_{vb}, such that $\phi_{par} + \phi_{vb} = 1$. The RVE can be suitably modeled by the Mori-Tanaka scheme. Hence, we assume that $\mathbb{C}^0 = \mathbb{C}_{par}$ and the Hill tensor $\mathbb{P}^0_r = \mathbb{P}^{par}_{cyl}$, which corresponds to cylindrical inclusions in the transversely isotropic matrix of the parenchyma [62]. Following (2.21), we arrive at the homogenized stiffness tensor $\mathbb{C}_{pith}$ of the soft-pith as:

$$\mathbb{C}_{pith} = \left\{\phi_{par}\mathbb{C}_{par} + \phi_{vb}\mathbb{C}_{vb} : [\mathbb{I} + \mathbb{P}^{par}_{cyl} : (\mathbb{C}_{vb} - \mathbb{C}_{par})]^{-1}\right\} : \left\{\phi_{par}\mathbb{I} + \phi_{vb}[\mathbb{I} + \mathbb{P}^{par}_{cyl} : (\mathbb{C}_{vb} - \mathbb{C}_{par})]^{-1}\right\}^{-1} . \tag{4.7}$$

Figure 4.4C shows a multistep model for the outer-shell material. The RVE of the cell wall material in this model (level e in Fig. 4.4) is identical to the RVE level (a_2). In the RVE of the *outer-shell* at level (f), we denote the volume fractions of the cell wall material and lumen as ϕ^{shell}_{wall} and ϕ^{shell}_{lum}, where $\phi^{shell}_{wall} + \phi^{shell}_{lum} = 1$. The RVE can be modeled by the Mori-Tanaka scheme. The stiffness of the lumen material is the same as the stiffness $\mathbb{c}_w$ of water. With $\mathbb{C}^0 = \mathbb{C}^{fib}_{wall}$ from (4.2) and $\mathbb{P}^0_r = \mathbb{P}^{wall}_{cyl}$ and following (2.21), the stiffness

tensor for the RVE of the outer shell is

$$\mathbb{C}_{shell} = \Big\{ \phi_{wall}^{shell} \mathbb{C}_{wall}^{fib} + \phi_{lum}^{shell} \mathbb{c}_w : [\mathbb{I} + \mathbb{P}_{cyl}^{wall} : (\mathbb{c}_w - \mathbb{C}_{wall}^{fib})]^{-1} \Big\} : \Big\{ \phi_{wall}^{shell} \mathbb{I} + \phi_{lum}^{shell} [\mathbb{I} + \mathbb{P}_{cyl}^{wall} : (\mathbb{c}_w - \mathbb{C}_{wall}^{fib})]^{-1} \Big\}^{-1} . \tag{4.8}$$

4.2.3 Upscaling elastic limit strength in cereal stem material

In the next step, we estimate the elastic limit strength of the soft-pith and outer-shell materials in the cereal stem cross-section, following the discussion in Section 2.3.1. The elastic limit point in wood and grass stems correspond to the yielding of lignin at microscales [65, 94]. Therefore, we assume that the soft-pith material and the outer-shell material reach the limit state when the elastic limit is reached in the lignin phase at the microscales. Lignin is an amorphous material, and it is known to fail in shear [11]. Its stress-strain response is assumed to be first elastic and then perfectly plastic, following the von Mises failure criterion expressed as:

$$\mathfrak{f}_{lig}(\boldsymbol{\sigma}_l) = \sigma_{eq(l)} - \sigma_{lig}^{y} \leq 0, \tag{4.9}$$

$\sigma_{eq(l)}$ is the von Mises equivalent stress of the quadratic stress average in the lignin phase. σ_{lig}^{y} is the yield strength of lignin and can be written in terms of its shear strength s_{lig} as $\sigma_{lig}^{y} = \sqrt{3} s_{lig}$.

Elastic limit of the soft-pith material

Algorithm 2 outlines how to compute the elastic limit strength of the soft-pith material. The parenchyma base material and the vascular bundles come together to form the soft-pith material (level d in Fig. 4.4). Both parenchyma and vascular bundle branches have lignin at the lowermost cell wall material levels. Therefore, the yielding of lignin within any one of parenchyma or vascular bundle tissues determines the elastic limit state of the soft-pith material.

Utilizing (2.27) with (4.9), we write the failure criterion $\mathfrak{f}_{lig,par}$ for the lignin phase embedded in the parenchyma tissues as:

$$\mathfrak{f}_{lig,par} = \sqrt{\boldsymbol{E}_{pith} : \frac{\partial\, \mathbb{C}_{pith}}{\partial \mu_{lig,par}} : \boldsymbol{E}_{pith}} \; - \; \sqrt{\frac{\overline{\phi}_{lig,par}}{3}} \, \frac{\sigma_{lig}^{y}}{\mu_{lig}}, \tag{4.10}$$

Result: The elastic limit strength $\Sigma_{pith}^{el} = \Sigma_{ij}^{n+1}$ of the soft pith material.

Define stress increment $\Delta\Sigma_{ij}$;
Set $\Sigma_{ij} = 0 \Rightarrow \boldsymbol{E}_{pith,0} = 0$;
Set index number n=0;
while $\mathfrak{f}_{lig,par} \leq 0$ *or* $\mathfrak{f}_{lig,fib} \leq 0$ **do**
    $\boldsymbol{\Sigma}_{ij}^{n+1} = (\Sigma_{ij}^{n} + \Delta\Sigma_{ij})\, \boldsymbol{e}_i \otimes \boldsymbol{e}_j$;
    $\boldsymbol{E}_{pith}^{n+1} = [\mathbb{C}_{pith}]^{-1} : \boldsymbol{\Sigma}_{ij}^{n+1}$;
    Calculate the failure criteria for the lignin, $\mathfrak{f}_{lig,par}$ and $\mathfrak{f}_{lig,fib}$, in both regions;
end

Algorithm 2: Computation of the elastic limit strength of the soft-pith material.

where $\overline{\phi}_{lig,par}$ is the equivalent volume fraction of the lignin in the parenchyma, computed as $\overline{\phi}_{lig,par} = \phi_{par} \cdot \phi_{wall}^{par} \cdot \phi_{l}^{wall,par}$. The derivative term $\partial\mathbb{C}_{pith}/\partial\mu_{lig,par}$ denotes the change in the elasticity tensor of soft-pith material with respect to the change in the shear modulus of the lignin phase in the cell wall material of the parenchyma region. This derivative can be evaluated via a finite difference approximation (see Appendix 3 in [148]). Uniform macrostrain $\boldsymbol{E}_{pith}$ imposed on the RVE of the soft-pith material is related to the macrostress $\boldsymbol{\Sigma}_{pith}$ as

$$\boldsymbol{E}_{pith} = [\mathbb{C}_{pith}]^{-1} : \boldsymbol{\Sigma}_{pith} \; . \tag{4.11}$$

We emphasize that we do not “successively" propagate from one RVE to the other. The term $\partial\mathbb{C}_{pith}/\partial\mu_{lig,par}$ implicitly accounts for all hierarchical scales, and directly provides access down to the lignin phase. In [147], a similar approach is used for upscaling the strength of cement paste and mortar.

Similarly, we write the failure criterion $\mathfrak{f}_{lig,fib}$ for the lignin phase embedded in the the fibers embedded in the bundles as:

$$\mathfrak{f}_{lig,fib} = \sqrt{\boldsymbol{E}_{pith} : \frac{\partial\, \mathbb{C}_{pith}}{\partial\mu_{lig,fib}} : \boldsymbol{E}_{pith}} \; - \; \sqrt{\frac{\overline{\phi}_{lig,fib}}{3}}\, \frac{\sigma_{lig}^{y}}{\mu_{lig}}, \tag{4.12}$$

where $\overline{\phi}_{lig,fib}$ is the equivalent volume fraction of the lignin in the bundle regions, computed as $\overline{\phi}_{lig,fib} = \phi_{vb} \cdot \phi_{fib} \cdot \phi_{wall}^{fib} \cdot \phi_{l}^{wall,fib}$. The stress level $\boldsymbol{\Sigma}_{pith}$ that violates (4.11) or (4.12) is the elastic limit strength Σ_{pith}^{el} of the soft-pith region (see also Algorithm 2).

The elastic limit of the outer-shell region

Following the above discussion, determining the elastic limit strength of the outer shell (see Fig. 4.4) is straightforward. Following (4.9) and (2.27), the failure criterion $\mathfrak{f}_{lig,shell}$ for the lignin phase embedded in the outer-shell region reads as:

$$\mathfrak{f}_{lig,shell} = \sqrt{\boldsymbol{E}_{shell} : \frac{\partial\, \mathbb{C}_{shell}}{\partial \mu_{lig,shell}} : \boldsymbol{E}_{shell}} \; - \; \sqrt{\frac{\overline{\phi}_{lig,shell}}{3}}\, \frac{\sigma^{y}_{lig}}{\mu_{lig}}, \tag{4.13}$$

where $\overline{\phi}_{lig,shell}$ is the equivalent volume fraction of lignin in the outer-shell region, computed as $\overline{\phi}_{lig,shell} = \phi^{shell}_{wall} \cdot \phi^{wall,fib}_{l}$. The macroscopic strain $\boldsymbol{E}_{shell}$ can be expressed in terms of macrostress $\boldsymbol{\Sigma}_{shell}$ with the help of the homogenized elasticity tensor $\mathbb{C}_{shell}$ as:

$$\boldsymbol{E}_{shell} = [\mathbb{C}_{shell}]^{-1} : \boldsymbol{\Sigma}_{shell} \; . \tag{4.14}$$

Equation (4.13) together with (4.14) affect the macroscopic failure criterion for the outer-shell region. The stress level $\boldsymbol{\Sigma}_{shell}$ that results in the failure of lignin according to (4.13) is the elastic limit strength $\boldsymbol{\Sigma}^{el}_{shell}$ of the outer-shell region.

4.3 Results and discussion

In this section, we first validate our micromechanics based model against four-point bending tests that we performed on oat stems. To this end, we integrate our multiscale material model with macroscale finite element analysis. We then illustrate the potential of our model for simulating and understanding the biomechanical tailoring of cereal stems. To this end, we quantify the effect of genetic modifications on the mechanical properties of thale cress as predicted by our micromechanics model and compare the predictions with experimental evidence reported in the literature.

4.3.1 Model validation against four-point bending experiments with oat stems

To validate our micromechanics model against cereal stem experiments, we conducted a series of standard four-point bending tests with oat stems. The stem specimens used in the tests were grown in the fields at the University of Minnesota in St. Paul, MN. Four

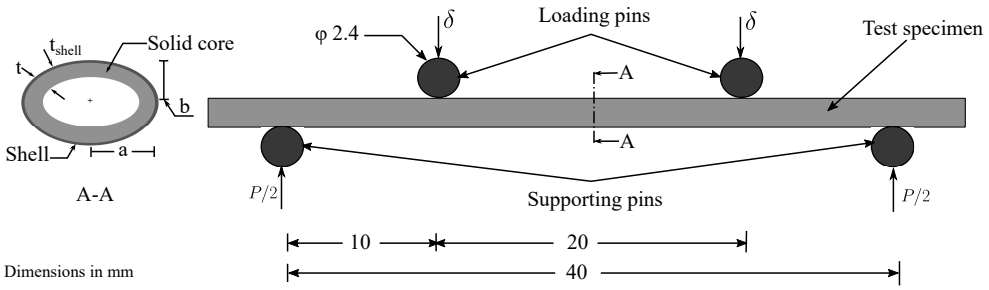

(a) Schematic representation of four point bending test setup for oat stems.

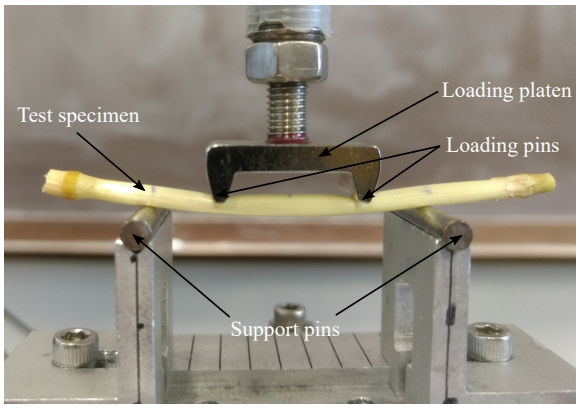

(b) Four point bending test setup.

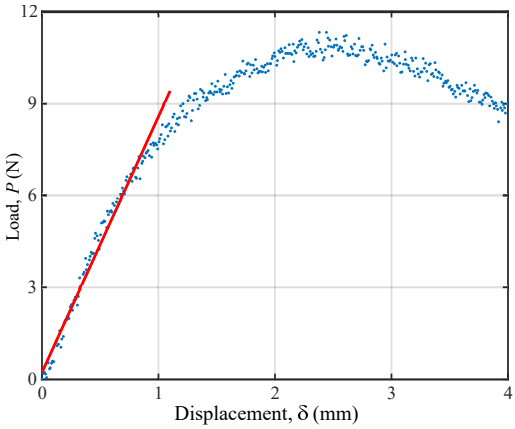

(c) Typical load-displacement curve for a bending test with best fitted line (red) for the elastic part.

Fig. 4.5: *Material characterization of oat stems.*

commercial varieties of oats — Gopher, Reins, ND021052, and IL07-8721 — were planted in the summer of 2017 with four different sowing dates for each variety. Plants were randomly selected for the tests including all of the varieties. The plants were carefully plucked with visually intact roots and kept for 24 hours with the roots submerged in water. Test specimens were prepared from different internode locations for each plant. The leaf sheath was carefully removed, and adjacent nodes were kept to maintain the integrity of the specimens. Only specimens with no visible damage were included in the four-point bending tests.

Figure 4.5a shows the schematic diagram of the four-point bending test apparatus. The total span length and loading span length were fixed at 40 mm and 20 mm. The oat stem specimen can be approximated as a hollow cylinder with an elliptical cross-section. The major axis was kept perpendicular to the transverse loading axis in the tests. The major axis a, the minor axis b, and the thickness t were measured at different locations with Vernier calipers, and the average values are reported in Table B.2. The tests were conducted via a

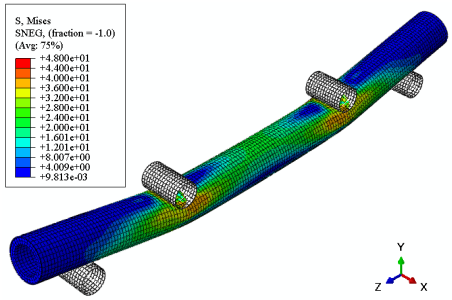

(a) Finite element model of the four-point bending test.

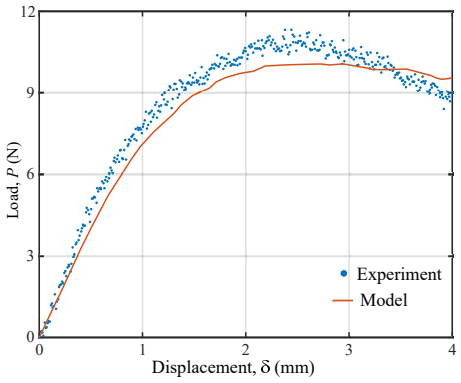

(b) Load-displacement curve obtained from the simulation and a bending test.

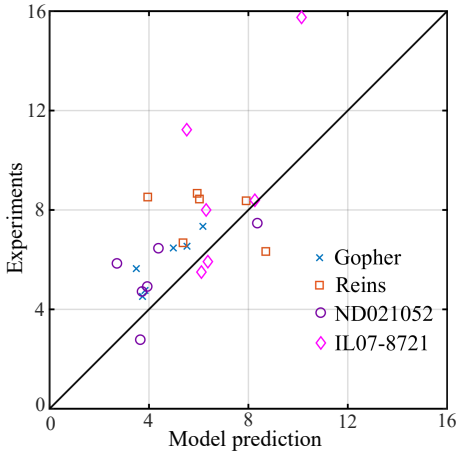

(c) Linear-elastic slope $\Delta P/\Delta\delta$.

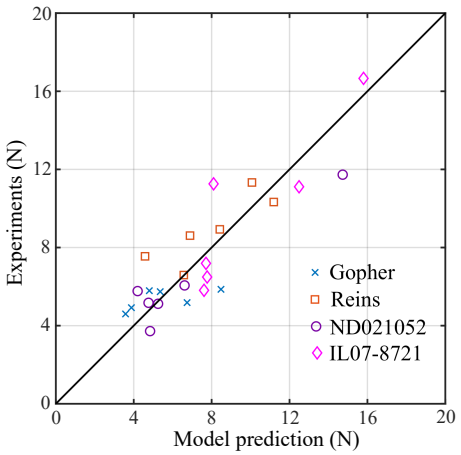

(d) Failure load P^{max}.

Fig. 4.6: *Comparison of results from the micromechanics model and the experimental tests.*

universal testing frame (MTS Instron 858 Mini Bionix II) with a 500 N load cell. The loading platen was displaced at a slow rate of 0.01 mm/s during the tests (see Fig. 4.5b). Load P and displacement data were recorded every second until a clear failure of the specimen. Failure is when the specimen loses structural integrity after a complete ovalization of the cross-section under the loading pins. Thereafter, the load begins to decrease with an increasing deflection in the recorded load-displacement curve (Fig. 4.5c). The failure load along with the slope of the load-displacement curve in the linear elastic region (red line in Fig. 4.5c) is reported in Table B.2.

We then build a finite element model for each specimen in the commercial software ABAQUS, discretizing the inner solid core region with twenty-node brick elements

(C3D20R) and the outer shell region with eight-node shell elements (S8R), respectively. Since the basis functions of the shell conform with those of the solids at the coupling surface, surface locking between shell and solid elements is prevented [158]. Once the model parameters are known for each oat variety (see Appendix **B**), we calculate and assign the macroscopic elastic stiffness moduli and strength properties for both the solid core and shell region. We model the loading and supporting pins using three-dimensional rigid elements (R3D4). We define surface-to-surface interactions between the specimen model and the rigid pins with a tangential friction coefficient of 0.2. We fix the support pins and apply the vertical displacement at the loading pins, keeping other displacement components zero. We perform nonlinear finite element analysis using the displacement control static-general algorithm in ABAQUS. We also considered the nonlinear geometric effects in the simulations. A typical load-displacement curve for one of the specimens obtained from the simulation and from the experimental observations is shown in Fig. 4.6b. A linear part, a peak and a softening branch are apparent in this figure. The softening branch is a result of the interaction of geometric nonlinearities and material yielding. However, in this work, we mainly focus on the linear elastic slope and peak failure load predictions. In the softening region, large macroscopic deformation gradients may invoke second-order effects on the microscales. In the scope of the present work, we do not account for these effects in the material model.

Figures 4.6c and 4.6d plot 24 four-point bending simulation predictions versus the experimental values for the linear elastic slope and the failure load, respectively. These plots show good agreement between the simulations and the experiments. The correlation coefficient R between the experimental and simulation results for the linear-elastic slope and failure load is 0.65 and 0.88, respectively. We also compute the mean percentage difference and standard deviation of the relative difference in percent between the experimental results and model predictions following (3.28) and (3.29). We find that the relative difference $\bar{e} \pm e_{sd}$ is in the range of $16.9 \pm 23.9\%$ for the linear elastic slope and in the range $-0.4 \pm 22.0\%$ for the failure load. The variance in the experimental observations and model predictions is mainly because of possible measurement and experimental errors. Overall, the results confirm that our material model is able to accurately predict the stiffness and strength properties of oat stem sections.

4.3.2 Model comparison with isotropic flexural constants

To emphasize the importance of a properly calibrated multiscale material model, we compare the model predictions obtained with our micromechanics based model against predictions based on standard isotropic material constants. Using standard beam flexural

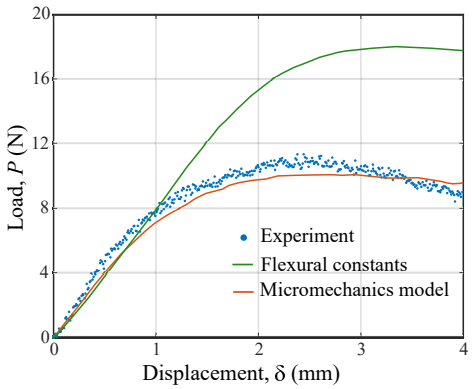

(a) Load-displacement curves.

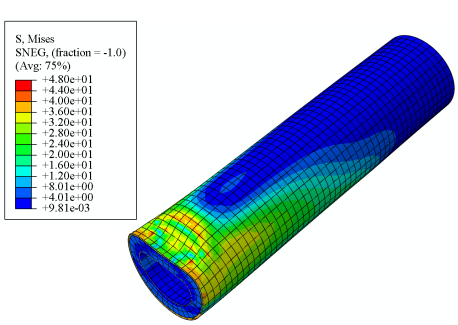

(b) Stress and deformation obtained with micromechanics based material model.

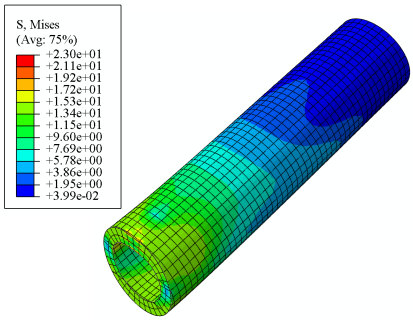

(c) Stress and deformation obtained with experimentally determined flexural constants.

Fig. 4.7: *Comparison of simulation results based on our micromechanics material model and based on experimentally calibrated flexural constants.*

theory and the available experimental results, one can compute Young's modulus to be $L^3(\Delta P/\Delta\delta)/(96\,I)$, where $\Delta P/\Delta\delta$ is the linear-elastic slope of the load-displacement curve, L is the span length, and I is the second moment of area of the section. The elastic limit strength of the material follows from $P^{max}Lb/4I$, where P^{max} is the maximum force value in the load-displacement curve. We can now use these material parameters in the finite element simulations, where we obtain the load-displacement curve shown in Fig. 4.7a. We observe, however, that the simulated material response based on flexural theory based isotropic constants grossly overestimates the maximum strength.

The reason for the large deviation can be traced back to the assumption of isotropy, where the two elastic material parameters are associated with the axial response of the structure. Taking the same constants in all directions, the structural response in the transverse direction, which is essential to resist ovalization and thus local buckling, is stiffer than it is in reality. The consequence is illustrated via the deformation and stress

plots in Figs. 4.7b and 4.7c that show a quarter of a simulated structure from one of the supports to the nearest leading pin location. While the result based on our micromechanics based material model clearly indicates ovalization, the result based on the experimentally calibrated material model still maintains an intact circular cross-section. Therefore, taking into account the anisotropy and associated material parameters is essential to accurately predict the mechanical response of plant stems. Anisotropy in plant materials is the outcome of different microstructures across several scales. Our micromechanics based model naturally accounts for the anisotropic material properties from the underlying plant physiology, accurately predicting their effects on the macroscale mechanical behavior.

4.4 Predicting and explaining the mechanical behavior of mutants

The stem material properties depend on the specific combination of morphological and compositional parameters that vary across different length scales from the cell wall to the cross-section level. Brule and co-authors [29] reviewed the effect of genetic modification of these parameters on the stiffness and strength for the genetic reference plant *Arabidopsis thaliana* (Arabidopsis), commonly known as thale cress. In their study, a consistent explanation of their findings was not possible as the genetic modifications affected the plant structure and the physiological response at multiple levels. The authors concluded: "*What is needed is a comprehensive, systematic and consistent multiscale mechanical analysis of structural parameters across length scales to feed into an integrated model of the development of plant stiffness.*"

In Table 4.2, we compile experimentally determined changes in the mechanical properties of the primary cell wall, secondary cell wall, and functional region mutants of *Arabidopsis* from [29]. In the following, we demonstrate that our multiscale modeling approach is capable of rationally interpreting and quantifying the effect of compositional and morphological parameters across multiple length scales on the mechanical response of *Arabidopsis*.

Remark: We note that for the *Arabidopsis* mutant tensile test samples, not all of the required parameters are available. To enable model predictions, we chose our base specimen as the oat variety Gopher with measured parameters reported in Appendix **B**. We characterize morphological and compositional changes in the respective mutants and assume that oat will experience similar changes in the composition and morphology against similar genetic alterations. We calculate and apply these changes in our model to predict the axial stiffness and the strength of the "mutant" oat. In Table 4.2, we report percentage changes

in the stiffness and strength compared to our base specimen and use these results in the following discussion.

Table 4.2: *Comparison of model predictions with experiments for mutants.*

Gene	Phenotype	Experiment (% of WT)		Model (% of Base)		Reference
		Stiffness	Strength	Stiffness	Strength	
Primary cell wall (expressed in parenchyma cell wall) mutants:						
atkin/frac2/bot	Reduced cellulose	40-60%	40-60%	66%	71%	[155]
mur2/xxt1xxt2	Reduced hemicellulose	80-100%	80%	85%	85%	[32, 34, 155]
qua2	Reduced pectin	80-100%	100%	NA	NA	[1, 32]
Second cell wall (expressed in fiber cell wall) mutants:						
cesa7/irx3/frac5	Reduced cellulose	20-40%	60-80%	56%	58%	[181]
irx4/ccr1	Reduced lignin	40%	40%	56%	65%	[104]
Functional region (vascular bundles, sclerenchyma fibers, outer-shell tissues) mutants:						
parvus/gatl1/irx7/frac8	Reduced xylan	NA	20%	40%	40%	[115, 145, 207]
abv1/ifl1/rev	Modified bundle arrangements	NA	60%	68%	70%	[209]
ifl1/rev	Missing outer-shell	NA	20%	48%	48%	[208]

4.4.1 Primary cell wall mutants

Experimental tests in Table 4.2 indicate a reduction in the stiffness and strength as a result of mutations that reduce constituent materials in the primary cell wall. For experimental determination, one can use tensile tests on hypocotyl tissues [155]. The tissues were obtained from the basal region of *Arabidopsis* in the early growth stage with the assumption that no secondary cell wall growth has happened. Cell wall material in the parenchyma region is largely made up of primary cell walls. Therefore, the parenchyma region from our micromechanics model that consists of the RVEs (a_1) and (b_1) shown in Fig. 4.4 can represent the test specimen. We use (4.1) and (4.4) to derive stiffness tensor $\mathbb{C}_{par}$ and the axial stiffness modulus as $1/\mathbb{C}^{-1}_{par,33}$, where $\mathbb{C}_{par,33}$ is the longitudinal component of the stiffness tensor $\mathbb{C}_{par}$. We estimate the axial strength following the procedure disucssed in Section 4.2.3 and Algorithm 2.

A reduction in cellulose content results in a drastic decrease in stiffness and strength. In [155], a 40% decrease in the cellulose content was reported due to the presence of a cellulose synthesis inhibitor gene. This alteration resulted in a 40% axial stiffness and strength decrease with respect to the respective wild-type (WT) specimen. We can now use our model to predict the new cell wall fraction parameters in (4.1), i.e., $\phi_i^{wall,par}$ with $i \in [c, h, l]$, and ϕ_{wall}^{par} in (4.4). The axial stiffness and strength are computed with the parameters that correspond to mutants with 40% reduced cellulose. The stiffness and strength values are reduced to 66% and 71% compared to the base oat material. In Table 4.2, we observe that

the model predictions are in line with the experimental results. Our observations reconfirm the role of cellulose as a load-bearing polymer in the cell wall.

Mutants *mur2* and *xx1xx2* show a significant reduction of the hemicellulose component xyloglucan in the primary cell wall [32, 155]. The corresponding loss of stiffness and strength, however, is not as severe as in the case of reduced cellulose (see Table 4.2). To enable a comparison with cellulose reduction, we assume an identical 40% reduction in hemicellulose content in the cell wall material. Using our model, we find that the axial stiffness and strength is reduced to 85% of the base oat material, consistent with the experimental observations. This result is plausible as the axial stiffness modulus of hemicellulose is approximately 15 times smaller than that of cellulose. Therefore, cellulose contributes to a much larger extent to the macroscale mechanical properties than hemicellulose. We anticipate that our micromechanics model could help settle the current controversial discussion in the literature about the role of hemicellulose as a load-carrying polymer in the cell wall material [38, 141].

Pectin, a major component of middle lamella, is a complex set of polysaccharides. Pectin rich middle lamella forms a continuous layer between the adjacent cells in the primary cell wall (see Fig. 4.4b). This layer presumably acts as a binding agent between the cells [28]. Table 4.2 indicates a minimal effect on the stiffness and strength in the reduced pectin mutants. Our model does not explicitly account for the role of middle lamella in the homogenized properties. A fundamental assumption of the continuum micromechanics frameworks, however, is perfect bond between the different phases in a RVE. The experimental results in Table 4.2 suggest that if "sufficient" pectin is present in the middle lamella to ensure perfect bond, it will not have a major effect on the overall stiffness and strength properties. For a detailed quantitative investigation on the role of pectin, however, more detailed computational models supported by physiological investigations at relevant length scales are needed.

4.4.2 Secondary cell wall mutants

Secondary cell wall mutants result in a loss of stiffness and strength as shown in Table 4.2. For mechanical testing, one can use three-point bending tests [104, 181]. The reported strength corresponds to $P^{max}Lr/4I$, where P^{max} is the maximum force the sample withstands before failure, L is the span length, r is the radius of the stem, and I is the second moment of area. The axial stiffness modulus is simply $L^3(\Delta P/\Delta\delta)/(48I)$, where $\Delta P/\Delta\delta$ is the linear-elastic slope of the load-displacement curve. For consistent comparison, we simulate the three-point bending test, where we follow the procedure outlined in Section 4.3.2, using the whole-stem specimen. The complete model described in

Section 4.2 is used to predict the material parameters for the mutants after accommodating the compositional and morphological changes. Based on our simulations results, we report percentage changes in stiffness and strength compared to the oat base specimen.

Cellulose is a major load-bearing polymer in the secondary cell walls. A reduction in the cellulose content is expected to decrease stiffness and strength, as shown in Table 4.2. In [181], the percentage of cellulose content in the cell wall is reported as low as 18% of the WT variety after genetic alteration. The reduction is also reflected in the thinning of the secondary cell walls in the fibers (Figs. 3 and 6 in [181]). Using our model, we recalculate the volume fractions in the RVEs that involve secondary cell walls, considering the mutant cellulose content (18% of the WT variety). The resulting stiffness and strength parameters are fed in the three-point bending simulations and the percentage change is reported in Table 4.2. We observe that the model predictions are in good agreement with the experimental observations, confirming the importance of cellulose for the overall stiffness and strength of plants.

Lignin reduction is a crucial process in various bioengineering applications such as biomass conversion to paper, fuel, and cattle feedstock. The genetic reduction in lignin content, however, results in a drastic loss of stiffness and strength as summarized in Table 4.2. In [104], a 50% reduction in lignin content in the secondary cell wall is reported as a consequence of mutant gene *irx4*. In addition, other morphological changes were observed such as the reduction of sclerenchyma fiber fractions in bundles and physiological changes in the outer-shell region (Figs. 2 and 5 in [104]). To predict and quantify the effect of these changes, we use the three-point bending simulation, where we assume a 50% reduction in fiber volume fraction ϕ_{fib} in the bundles and shell thickness t_{shell}. Based on these changes, we predict a 56% and 65% reduction in stiffness and strength, respectively, compared to the base oat material. These results confirm the importance of considering morphological changes at multiple levels in mutants. In [96, 105, 106], similar observations in reduced lignin mutants for wood are reported.

4.4.3 Functional region mutants

Using our model, we finally assess the stiffness and strength impact of mutants that result in morphological changes in the functional regions such as vascular bundles, sclerenchyma fibers, and outer-shell tissues. Table 4.2 indicates a severe reduction in the axial strength as a consequence of these mutants. We note that the axial strength was measured through tensile tests with matured whole-stem specimens. In each case, we accommodate the observed changes in the morphology for the specific mutants in the model and predict the stiffness and strength for both pith and outer-shell region. For comparison, we compute the volumetric

average of the predicted axial stiffness and strength components of the pith and outer-shell properties.

Xylans are found in sclerenchyma fibers in bundles and outer-shell tissues. The disruption of genes involved in xylan synthesis leads to a reduction of up to 50% of the WT xylan level and results in a severe decrease in tensile strength (see Table 4.2). Xylan mutants such as *PARVUS* resulted in compositional and morphological changes in the hierarchical structure of the reference plant [115]. A reduction of 50% and 64% cell wall thickness was reported in the sclerenchyma fibers in the bundles and outer-shell regions, respectively. Overall, a 25% reduction in the cellulose content in the cell walls was reported. We incorporate these changes in our model and modify ϕ_{wall}^{fib}, ϕ_{wall}^{shell}, and the constituent cell wall fractions, i.e., $\phi_c^{wall,fib}$ with $i \in [c, h, l]$ (see Appendix **B** for details), leading to a 60% reduction in the axial stiffness and strength. These results confirm the drastic changes in the mechanical properties as a result of xylan mutants.

The spatial arrangement and proportion of tissue types in the cross-section of cereal stems affect their mechanical properties. The mutant *abv1* [209] alters the organization of vascular bundles from a "collateral pattern" to a "amphivasal pattern." In the collateral pattern, bundles are arranged in a ring-like configuration near the periphery of the cross-section. In the amphivasal pattern, bundles are irregularly distributed in the pith. As a result of this mutation, a gross thinning of the outer-shell fiber cell wall was also observed (see Fig. 6 in [209]). Assuming a 60% reduction in the cell wall fraction in outer-shell tissues, our model predicts a 30% reduction in the axial stiffness and strength of the stem cross-section. Similarly, a diminished outer shell is reported in [208] after *ifl1/rev* mutation, resulting in the severe loss of axial strength as reported in Table 4.2. Our model predicts the axial stiffness and strength as 48% of the base oat material for this alteration in the cross-section morphology. This result is consistent with experimental observations.

Summary and conclusions

In this part, we presented a modeling approach that rationally predicts the stiffness and strength of hierarchical plant materials based on their hierarchical microstructure. We focus on two broad classes of plant materials: (1) functionally graded culm type materials and (2) cereal stems configuration with an inner layer of foam-like parenchyma cells surrounded by a dense outer shell. Built within the framework of continuum micromechanics, our model consists of a sequence of homogenization steps whose RVEs can be fully described by simple quantitative and qualitative properties of the constituent phases such as volume fractions, shape, orientation and distribution. The RVE morphology at the different scales is characterized by chemical analysis and imaging data from transmission electron microscopy, scanning electron microscopy, light microscopy, and micro-CT scans. The models are extensively validated for macroscale elastic and inelastic properties against the independently reported and performed experiments.

A significant advantage of our multiscale model over simpler phenomenological approaches is the physiologically correct relation of the mechanical properties with compositional and morphological parameters across multiple length scales. This connection enables a physics-based understanding of the multiscale origin of stiffness and strength, as shown in bamboo. We also demonstrated this opportunity by explaining the effect of genetic modifications on the stiffness and strength reported for thale cress from our model that predicted the observed behavior correctly in all cases. From a plant breeding perspective, this connection opens the door for tailoring plant materials in situations where their mechanical properties are of key importance. This model is later used in Part III to simulate the lodging behavior of oats, with the goal of identifying significant traits in their genome to enable the breeding of lodging-resistant oats.

PART II

Concurrent material and structure optimization of multiphase hierarchical systems

Introduction

Biological multiphase hierarchical systems such as plants and bone are not statically determined systems by their genetic blueprints. Instead, they actively respond to the biophysical stimuli of their environment and develop self-adapting mechanisms for improved performance [66, 72, 193]. In other words, biological systems adapt their "*form*" (or shape/structure) against the dynamic external environment and improve the "*microstructure architecture*," fulfilling the local needs imposed by physiological, phylogenetic, and reproductive constraints. This dual optimization of the structure and material microstructure is intimately related to biological systems' hierarchical organization [54, 175]. Readers are advised to refer to the excellent review by Fratzl and Weinkamer [59] and references within for more details on this functional adaption.

Topology optimization methods constitute a broad class of general design approaches [16, 17, 19, 163, 187], which have been extended to optimize multiscale systems [33, 36, 67, 149, 170, 171, 186]. In our context, the dual optimization of the structure and material microstructure for multiphase hierarchical systems naturally fits to recently developed concurrent multiscale analysis and topology optimization methods [37, 133, 152, 194, 195]. The idea is to divide the multiscale problem into two nested sub-problems, one at the macroscale (structure) and the other at the microscale (material). At each macroscale material point, the microstructure is optimized under macroscale influence. In turn, the microscale sub-problems at material points provide the constitutive material behavior for the macroscale structure optimization problem. Due to their large computational cost, existing methods are limited to small two-scale problems with linear elastic material behavior.

The computational burden posed by multiphase hierarchical systems for multiscale analysis through computational homogenization grows exponentially with each scale characterization [24, 114, 119, 203]. Combining topology optimization results in even higher computational cost, since it requires solving many multiscale problems for different realizations of structure topology during a typical optimization algorithm. This drawback explains the incapability of existing methods for handling multiphase hierarchical systems. Even with multiphase hierarchical systems with linear elastic constituents, no research exists in the literature

that considers more than two scales for concurrent material and structure optimization. Research has remained relatively unexplored in the case of inelastic constituents and limited to macroscale structure optimization with a given fixed microstructure definition [45, 63]. No work is reported in the literature that attempts the concurrent optimization of material and structure with inelastic multiphase hierarchical material definition. Continuum micromechanics-based homogenization approaches developed in the previous part provide an opportunity to tackle these computational challenges.

In this part of the thesis, we combine results from the continuum micromechanics and topology optimization frontiers to derive efficient concurrent material and structure optimization approaches that can tackle the computing challenge of optimizing multiphase hierarchical systems, including elastoplastic constituents at material scales. Our approaches are based on the division of the optimization problem into two sub-problems, utilizing the pointwise definition of material design variables. The structure optimization problem optimizes the macroscale distribution of material, whereas material optimization problems act as a reformulated constitutive material law that provides the optimum homogenized properties with respect to microscale design variables expressed within a continuum mechanics framework. For this decomposition, we exploit the saddle point structure of the end-compliance problem in the case of linear elastic constituents at material scales. However, this extension is non-trivial in the case of problems with elastoplastic behavior at the material level. For the first time, we establish the rigorous theoretical foundations of elastoplastic concurrent material and structure optimization, including suitable subproblem formulations for elastoplastic material optimization based on the thermomechanical formulation of elastoplasticity.

This part is structured as follows: Chapter 5 derives a concurrent material and structure optimization formulation for end-compliance problems with an overall linear elastic response at both the material and structure levels. We establish that, with our formulation, the computational cost does not explode exponentially with the number of hierarchical scales. In Chapter 6, we integrate the continuum micromechanics based estimates of macroscale properties in the structure (topology) optimization problems for elastoplastic multiphase hierarchical systems. We also state the basics of solving the elastoplastic initial boundary value problem, including the finite element discretization, the closest point projection return mapping algorithm, and the Newton-Raphson linearization for macroscale equilibrium equations. Chapter 7 establishes a novel thermodynamically consistent theoretical formulation for elastoplastic concurrent material and structure optimization. In particular, we reformulate the material optimization problem based on the maximum plastic dissipation principle such that it assumes the format of an elastoplastic constitutive law. In each chapter, we design benchmarks with several hierarchical scales at the material level,

suitable to test the validity, accuracy, and efficiency of our formulations and the underlying algorithms.

Chapter 5

Concurrent material and structure optimization of multiphase hierarchical systems with elastic constituent materials

In this chapter, we present a concurrent material and structure optimization framework based on continuum micromechanics estimates for end-compliance optimization problems with an overall linear elastic response at both the material and structure levels. We show that the analytical nature of these estimates enables material optimization via a series of inexpensive "discretization-free" constraint optimization problems whose computational cost is independent of the number of hierarchical scales involved. To illustrate the strength of this unique property, we define new benchmark tests with several material scales that, for the first time, become computationally feasible via our framework.

This chapter is structured as follows. Section 5.1 discusses the concurrent material and structure optimization formulation, including a definition of the admissible design space for both sub-problems. In Section 5.2, we discuss the finite element discretization of the structure optimization problem and the implementation of both structure and material optimization problems within a general optimization algorithm. Section 5.3 defines new test problems that illustrate the efficiency of our method.

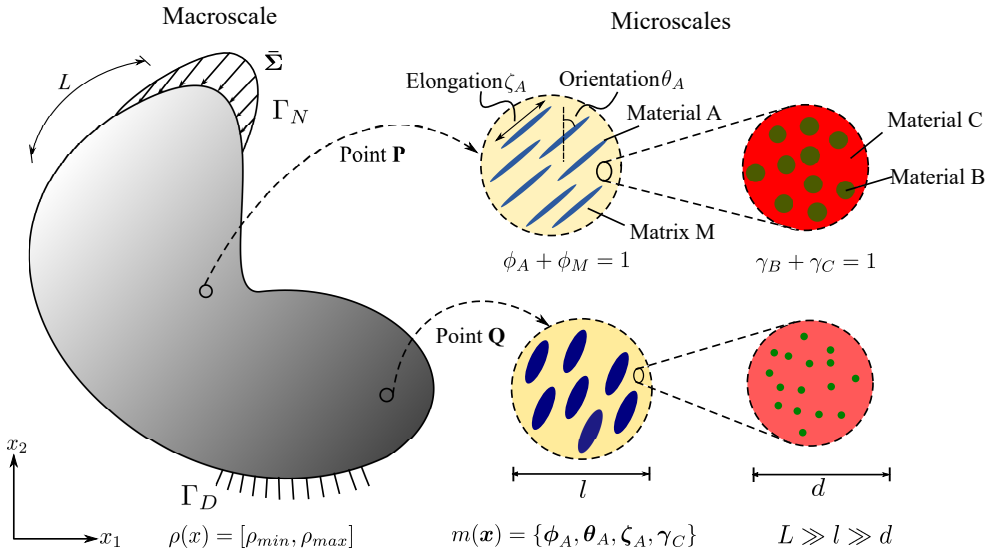

Fig. 5.1: *Sketch of a representative problem for concurrent material and structure optimization in a continuum micromechanics framework.*

5.1 Concurrent material and structure optimization in a micromechanics framework

In this section, we formulate a minimum compliance (or maximum stiffness) problem for concurrent material and structure optimization, departing from [152, 174, 194].

5.1.1 A minimum compliance formulation based on micromechanical design variables

As illustrated in Fig. 5.1, we assume a fixed reference domain Ω subjected to traction $\bar{\boldsymbol{\Sigma}}$ at the Neumann boundary Γ_N and prescribed displacements at the Dirichlet boundary Γ_D with a body force field $\boldsymbol{b}$. At each material point $\boldsymbol{x}$, microstructural heterogeneities are described by a set $\boldsymbol{m}(\boldsymbol{x})$. The set $\boldsymbol{m}(\boldsymbol{x})$ contains the geometric and mechanical characterization of phases that span multiple well-separated microscales, consisting of volume fraction, material properties, shape, and orientation of the different phases in the hierarchical system. Assuming linear elastic behavior of all constituents, the homogenized macroscale stiffness $\mathbb{C}(\rho(\boldsymbol{x}), \boldsymbol{m}(\boldsymbol{x}))$ at each material point $\boldsymbol{x}$ depends on the density $\rho(\boldsymbol{x})$ and the set $\boldsymbol{m}(\boldsymbol{x})$. Our design vector is therefore $[\rho(\boldsymbol{x}), \boldsymbol{m}(\boldsymbol{x})]^T$.

We write a minimum compliance problem in the displacement-based formulation as:

$$\max_{\substack{\rho(\boldsymbol{x})\in\mathcal{A}_{ad}\\ \boldsymbol{m}(\boldsymbol{x})\in E_{ad}}} \min_{\bar{\boldsymbol{u}}\in U} \Big\{ \frac{1}{2}\int_\Omega \boldsymbol{E}(\bar{\boldsymbol{u}}) : \mathbb{C}(\rho(\boldsymbol{x}),\boldsymbol{m}(\boldsymbol{x})) : \boldsymbol{E}(\bar{\boldsymbol{u}})\, d\Omega \; - \int_\Omega \boldsymbol{b}\cdot\bar{\boldsymbol{u}}\, d\Omega \; - \int_{\Gamma_N} \bar{\boldsymbol{\Sigma}}\cdot\bar{\boldsymbol{u}}\, ds \Big\}, \tag{5.1}$$

where U denotes the space of kinematically admissible displacement fields $\bar{\boldsymbol{u}}$, and $\boldsymbol{E}(\bar{\boldsymbol{u}})$ denotes the linearized strains. $\mathcal{A}_{ad}$ and E_{ad} define the set of admissible design variables at the macroscale and microscales, respectively, with possible design constraints. The admissible set $\mathcal{A}_{ad}$ that seeks a limit on the total material mass M_{req} available for design can be written as:

$$\mathcal{A}_{ad} = \Big\{ \rho(\boldsymbol{x}) \mid \rho(\boldsymbol{x}) = [\rho_{min}, \rho_{max}],\ \int_\Omega \rho(\boldsymbol{x}) d\Omega \le M_{req},\ \boldsymbol{x}\in\Omega \Big\}\,, \tag{5.2}$$

where ρ_{min} and ρ_{max} are the bounds on the macroscale material density ρ.

The definition of the admissible set E_{ad} is again illustrated via the multiscale configuration shown in Fig. 5.1. We observe a well-separated three-scale hierarchical system with three base constituent materials denoted as Material A, B, and C with densities ρ_A, ρ_B, and ρ_C, respectively. At a material point P, the volume fraction of Material B and C at the lowermost scale are γ_B and γ_C such that $\gamma_B+\gamma_C = 1$. Material B forms spherical inclusions in the matrix of Material C at this scale. The homogenized material from this scale forms the matrix M that hosts Material A inclusions with the orientation θ_A and the elongation ratio ζ_A at the mesoscale. The density of the matrix M is simply $\rho_M = (\gamma_B\rho_B + \gamma_C\rho_C)$. The volume fraction of Material A and matrix M are ϕ_A and ϕ_M with $\phi_A + \phi_M = 1$. The microstructure characterization field set $\boldsymbol{m}(\boldsymbol{x})$ is $\{\phi_A(\boldsymbol{x}), \theta_A(\boldsymbol{x}), \zeta_A(\boldsymbol{x}), \gamma_C(\boldsymbol{x})\}$.

We can thus write the admissible set E_{ad} as:

$$\begin{aligned} E_{ad} = \Big\{ \boldsymbol{m}(\boldsymbol{x}) \mid\ & \rho(\boldsymbol{x}) = \rho_A\phi_A(\boldsymbol{x}) + \rho_M(\boldsymbol{x})(1-\phi_A(\boldsymbol{x})),\\ & 0 < \phi_A^{min} < \phi_A(\boldsymbol{x}) < \phi_A^{max} \le 1,\\ & \rho_M(\boldsymbol{x}) = \rho_B(1-\gamma_C(\boldsymbol{x})) + \rho_C\,\gamma_C(\boldsymbol{x}),\\ & 0 < \gamma_C^{min} < \gamma_C(\boldsymbol{x}) < \gamma_C^{max} \le 1,\\ & \theta_A(\boldsymbol{x}) \in [-\pi/2, \pi/2],\\ & \zeta_A(\boldsymbol{x}) \in [1, \zeta^{max}],\ \boldsymbol{x}\in\Omega \Big\}. \end{aligned} \tag{5.3}$$

Here, the volume fraction of Material A is bounded by ϕ_A^{min} and ϕ_A^{max}, and the volume

fraction of Material C is bounded by γ_C^{min} and γ_C^{max} at their respected scales. Also, the elongation ratio of the Material A inclusions is bounded by ζ^{max}. These bounds may reflect additive manufacturing constraints on multimaterial composite systems or biological constraints in natural materials. We emphasize again that the multiscale configuration of Fig. 5.1 is used for the purpose of illustration, but is easily generalized to cover any other multiphase hierarchical system.

5.1.2 Decomposition into structure and material optimization problems

We note that for a given macroscale density field $\rho(\boldsymbol{x})$, the admissible set E_{ad} is defined pointwise in the domain Ω. It allows us to decompose the design formulation (5.1) as follows:

$$\max_{\rho(\boldsymbol{x})\in\mathcal{A}_{ad}} \max_{\boldsymbol{m}(\boldsymbol{x})\in E_{ad}(\rho)} \min_{\bar{\boldsymbol{u}}\in U} \Big\{ \int_\Omega \frac{1}{2}\boldsymbol{E}(\bar{\boldsymbol{u}}) : \mathbb{C}(\rho(\boldsymbol{x}),\boldsymbol{m}(\boldsymbol{x})) : \boldsymbol{E}(\bar{\boldsymbol{u}})\, d\Omega - \int_\Omega \boldsymbol{b}\cdot\bar{\boldsymbol{u}}\, d\Omega - \int_{\Gamma_N} \bar{\boldsymbol{\Sigma}}\cdot\bar{\boldsymbol{u}}\, ds \Big\}. \tag{5.4}$$

The variational structure of (5.4) corresponds to a saddle point problem with respect to the admissible set E_{ad} and the space of kinematically admissible displacements U. Lipton worked out in detail and proved the essential conditions that are required for this property to hold [117]. This saddle point nature allows us to interchange the second and third operators (max and min). This interchangeability along with the pointwise definition of E_{ad} is crucial for decomposing the problem into material and structure optimization subproblems [103].

In the following, we exploit this property to define "structure" and "material" subproblems. We rewrite formulation (5.4) as:

$$\max_{\rho(\boldsymbol{x})\in\mathcal{A}_{ad}} \min_{\bar{\boldsymbol{u}}\in U} \Big\{ \int_\Omega \max_{\boldsymbol{m}(\boldsymbol{x})\in E_{ad}(\rho)} \Big\{\frac{1}{2}\boldsymbol{E}(\bar{\boldsymbol{u}}) : \mathbb{C}(\boldsymbol{m}(\boldsymbol{x})) : \boldsymbol{E}(\bar{\boldsymbol{u}})\Big\}\, d\Omega - \int_\Omega \boldsymbol{b}\cdot\bar{\boldsymbol{u}}\, d\Omega - \int_{\Gamma_N} \bar{\boldsymbol{\Sigma}}\cdot\bar{\boldsymbol{u}}\, ds \Big\}. \tag{5.5}$$

As $\rho(\boldsymbol{x})$ dictate the construction of admissible space E_{ad}, we take it out from $\mathbb{C}$ in (5.4) and consider it into E_{ad}. We reformulate (5.5) by defining the pointwise maximum strain energy density Φ and splitting it into two sub-problems. The outer structure optimization problem is:

$$\max_{\rho(\boldsymbol{x})\in\mathcal{A}_{ad}} \min_{\bar{\boldsymbol{u}}\in U} \Big\{ \int_\Omega \Phi(\rho(\boldsymbol{x}),\bar{\boldsymbol{u}})\, d\Omega - \int_\Omega \boldsymbol{b}\cdot\bar{\boldsymbol{u}}\, d\Omega - \int_{\Gamma_N} \bar{\boldsymbol{\Sigma}}\cdot\bar{\boldsymbol{u}}\, ds \Big\}. \tag{5.6}$$

The pointwise maximum strain energy density sub-problem or material optimization problem is:

$$\Phi(\rho(\boldsymbol{x}), \bar{\boldsymbol{u}}) = \max_{\boldsymbol{m}(\boldsymbol{x}) \in E_{ad}(\rho)} \frac{1}{2} \boldsymbol{E}(\bar{\boldsymbol{u}}) : \mathbb{C}(\boldsymbol{m}(\boldsymbol{x})) : \boldsymbol{E}(\bar{\boldsymbol{u}}) \;\; \forall \boldsymbol{x} \in \Omega. \tag{5.7}$$

A combination of (5.6) and (5.7) constitutes the concurrent material and structure optimization model. For a given material density distribution $\rho(\boldsymbol{x})$, the maximization problem (5.7) determines the stiffest material microstructure configuration for the evaluated macroscale strain at each material point $\boldsymbol{x}$. The minimization problem in (5.6) looks for the kinematically admissible equilibrated displacement field for a given density distribution $\rho(\boldsymbol{x})$. The locally optimum strain energies Φ in (5.6) are driven by the pointwise maximization problems in (5.7) that again depend on the displacement field solution $\bar{\boldsymbol{u}}$. This interdependency makes the equilibrium problem a constitutively nonlinear elasticity problem. Finally, the outer maximization problem (5.6) seeks the optimal material distribution $\rho(\boldsymbol{x})$ in the domain Ω.

Remark: A typical topology optimization problem intends to find the optimal distribution of one material as opposed to voids denoted by a "0-1" integer parametrization (often called black and white design). This problem is ill-posed as non-convergent finer geometric details are obtained with mesh refinement [5]. The existence of such solutions relies on relaxation, that is, replacing integer variables with density-like continuous variables. The relaxation is achieved by "homogenization / interpolation" between solid material and void. One such example is the famous solid isotropic material with penalization (SIMP) model. Bendsøe and Sigmund showed in [18] that these artificial interpolation models fall within a framework of micromechanics-based models in many physically realizable circumstances. Thus, the relaxation is naturally built in our continuum micromechanics-based homogenization approach. This allows us to use gradient-based optimization approaches as outlined in this chapter.

5.2 Finite element discretization and implementation

In this section, we focus on the finite element discretization of the concurrent material and structure optimization formulation and corresponding algorithmic aspects. This includes the treatment of the nonlinearity that results from the interaction between material-scale and structure-scale optimization, and a review of macroscale density optimization, including essential sensitivity analysis. For illustration purposes, we continue to write out our formulation for the special case of the multiscale configuration shown in Fig. 5.1, but emphasize

again that it is easily generalized to cover any other multiphase hierarchical system. In the following, we use vector-matrix notation to represent the introduced quantities, consistent with standard finite element literature [99]. However, we keep the same symbols for the respective vector-matrix notation.

5.2.1 Structure optimization problem

We discretize the concurrent material and structure design formulation presented in Section 5.1 with standard finite elements [99]. To this end, we split the domain Ω into N_e finite elements, where each element has N_{gp} Gauss quadrature points. For our example material in Fig. 5.1, the topology design variables $[\rho(\boldsymbol{x}), \boldsymbol{m}(\boldsymbol{x})]^T$ can now be defined elementwise as:

$$\begin{aligned} \boldsymbol{\rho} &= [\rho_1, \rho_2, \rho_3, ..., \rho_{N_e}], \\ \boldsymbol{m} &= [(m_1^1, .., m_1^{N_{gp}}), (m_2^1, .., m_2^{N_{gp}}), ..., (m_{N_e}^1, .., m_{N_e}^{N_{gp}})], \\ m_j^x &= [\phi_A^{x,j}, \theta_A^{x,j}, \zeta_A^{x,j}, \gamma_C^{x,j}], \quad x = 1, ..., N_{gp},\ j = 1, ..., N_e. \end{aligned} \tag{5.8}$$

The macroscale density ρ_j is assumed to be constant in each element, with j being the element index. The microscale design variable set $\boldsymbol{m}$ is defined at each (macroscale) Gauss point, with x being the Gauss point index. The microscale design variable m_j^x consists of volume fraction $\phi_A^{x,j}$, orientation $\theta_A^{x,j}$, elongation $\zeta_A^{x,j}$, all for Material A, and volume fraction $\gamma_C^{x,j}$ of Material C.

We can relate the macroscale stress $\boldsymbol{\Sigma}$ with the macroscale strain $\boldsymbol{E}$ at a Gauss point $\boldsymbol{x}$ inside element j in terms of the design variables ρ_j and m_j^x as:

$$\boldsymbol{\Sigma}(\boldsymbol{x}, \rho_j) = \mathbb{C}(\rho_j, m_j^x)\boldsymbol{E}(\boldsymbol{x}), \tag{5.9}$$

where $\mathbb{C}(\rho_j, m_j^x)$ is the homogenized stiffness at this point. Interested readers can find the analytical expression for $\mathbb{C}$, derived from continuum micromechanics, in Appendix **C**. The macroscale strain $\boldsymbol{E}(\boldsymbol{x})$ at a point $\boldsymbol{x}$ inside element j is approximated by the element displacement vector $\bar{\boldsymbol{u}}_j$ of the element j and the strain-displacement matrix $\boldsymbol{B}(\boldsymbol{x})$ that contains shape function information:

$$\boldsymbol{E}(\boldsymbol{x}) \approx \boldsymbol{B}(\boldsymbol{x})\, \bar{\boldsymbol{u}}_j\ . \tag{5.10}$$

Using the definitions (5.8) to (5.10), we obtain the following discretized formulation of the

structure optimization problem (5.6):

$$\begin{aligned} \min_{\boldsymbol{\rho}} :\ & f_c(\boldsymbol{\rho}) = \boldsymbol{f}_{ext}^T \bar{\boldsymbol{u}} \\ \text{s.t.} :\ & \bar{\boldsymbol{r}}(\bar{\boldsymbol{u}}, \boldsymbol{\rho}, \bar{\boldsymbol{m}}) = 0 \\ & M(\boldsymbol{\rho}) = \sum_{j=1}^{N_e} \rho_j |\Omega_j| = M_{req} = M_{frac} \times \rho_C \times |\Omega| \\ & \rho_j \in [\rho_{min}, \rho_{max}],\ \forall j = 1, 2, ..., N_e. \end{aligned} \tag{5.11}$$

The quantities in (5.11) require further explanation: $\boldsymbol{f}_{ext}$ is the external force vector, $\bar{\boldsymbol{u}}$ is the global displacement vector that represents the converged macroscale displacement solution, and $M(\boldsymbol{\rho})$ is the total mass of the occupying domain, where ρ_j and $|\Omega_j|$ are the density and the volume of element j, respectively. The total available mass M_{req} can be expressed in terms of fraction M_{frac} with respect to the mass when the densest material occupies the complete domain. The force residual at the macroscale scale is defined as:

$$\bar{\boldsymbol{r}}(\bar{\boldsymbol{u}}, \boldsymbol{\rho}, \bar{\boldsymbol{m}}) = \boldsymbol{f}_{ext} - \sum_{j=1}^{N_e} \left[\sum_{x=1}^{N_{gp}} \boldsymbol{B}^T\, \mathbb{C}(\bar{m}_j^x)\, \boldsymbol{B}\, w_x \right] \bar{\boldsymbol{u}}_j, \tag{5.12}$$

where w_x contains the Gauss point weight and the determinant of the Jacobian matrix and $\bar{\boldsymbol{u}}_j$ is again the element displacement vector of element j. We observe that the microstructure design variables $\boldsymbol{m}$ are implicitly accounted for by $\bar{\boldsymbol{r}}$. At each Gauss point $\boldsymbol{x}$, the homogenized stiffness $\mathbb{C}$ is evaluated based on a microstructure configuration $\bar{\boldsymbol{m}}$ that maximizes the local strain energy.

Identifying the term in the bracket inside (5.12) as the element stiffness matrix for element j, we can rewrite (5.12):

$$\bar{\boldsymbol{r}}(\bar{\boldsymbol{u}}, \boldsymbol{\rho}, \bar{\boldsymbol{m}}) = \boldsymbol{f}_{ext} - \boldsymbol{K}(\bar{\boldsymbol{m}}(\boldsymbol{\rho}, \bar{\boldsymbol{u}}))\bar{\boldsymbol{u}}, \tag{5.13}$$

where $\boldsymbol{K}$ denotes the global stiffness matrix of the system. For a given macroscale density distribution $\boldsymbol{\rho}$, the microstructure $\boldsymbol{m}$ defined at each Gauss point is optimized with respect to the macroscale strains evaluated at each Gauss point according to (5.7). The optimized microstructure configuration $\bar{\boldsymbol{m}}$ updates the macroscale constitutive behavior that is incorporated in $\boldsymbol{K}$.

5.2.2 Material optimization problem

For a given material distribution $\boldsymbol{\rho}$ and displacement solution $\bar{\boldsymbol{u}}$, the formulation of a material optimization problem (5.7) at a Gauss point $\boldsymbol{x}$ inside element j is:

$$
\begin{aligned}
\bar{m}_j^x = \underset{m_j^x(\rho_j)}{\arg\max}\ & \frac{1}{2}\boldsymbol{E}(\boldsymbol{x}) : \mathbb{C}(m_j^x) : \boldsymbol{E}(\boldsymbol{x}) \\
\text{s.t. :}\ & \nabla_y \cdot \boldsymbol{\sigma}(\boldsymbol{x},\boldsymbol{y}) = 0 \\
& \langle \boldsymbol{\varepsilon}(\boldsymbol{x},\boldsymbol{y}) \rangle_{\Omega_y} = \boldsymbol{E}(\boldsymbol{x}) \\
& \rho_j = \rho_A \phi_A^{x,j} + \rho_M (1 - \phi_A^{x,j}) \\
& \rho_M = \rho_B (1 - \gamma_C^{x,j}) + \rho_C \gamma_C^{x,j} \\
& \phi_A^{x,j} \in [\phi_A^{min}, \phi_A^{max}];\ \ \theta_A^{x,j} \in [-\pi/2, \pi/2];\ \ \zeta_A^{x,j} \in [1, \zeta^{max}] \\
& \gamma_C^{x,j} \in [\gamma_C^{min}, \gamma_C^{max}]\ .
\end{aligned}
\tag{5.14}
$$

where $\boldsymbol{\sigma}$ and $\boldsymbol{\varepsilon}$ are the stress and strain fields inside the microscale RVE region Ω_y situated at the Gauss point $\boldsymbol{x}$. It is important to note that we keep (5.14) in tensor notation, considering its direct relation with Chapter 2. The optimized configuration $\bar{m}_j^x$ that maximizes the strain energy density is sought in the microscale design variable space $m_j^x = [\phi_A^{x,j}, \theta_A^{x,j}, \zeta_A^{x,j}, \gamma_C^{x,j}]$. All the microstructure constraints directly follow from the admissible set E_{ad} defined in (5.3).

The first two conditions in (5.14) represent equilibrium and strain compatibility in the microscale RVE as discussed in Section 2.1.2, and correspond to the strong form of the variational statements (2.10) and (2.11) derived in Chapter 2. If the microstructure is deterministic, these equations can be discretized and solved using the finite element method. The volumetric average of the stress $\boldsymbol{\sigma}$ over the microscale RVE volume uses the macroscale stress, and hence the homogenized stiffness $\mathbb{C}$. In Section 2.2, we derived the estimates for $\mathbb{C}$ based on continuum micromechanics, when only partial statistical information about the microstructure is available (see also Appendix **C**). The analytical expression (C.3) renders (5.14) a straightforward "discretization free" constraint optimization problem that can be solved by standard gradient-based methods [27]. Interested readers are referred to Appendix **C** for a brief discussion on solving the microscale optimization problem. The solution of (5.14) at each Gauss point yields the optimized microstructure configuration set $\bar{\boldsymbol{m}}$.

5.2.3 Interaction of material and structure scales

Due to the interaction of the material and structure scales, the equilibrium equation (5.13) is nonlinear. Our approach to resolve this nonlinearity is based on [194]. For a given macroscale density distribution, we intend to find the equilibrium solution that minimizes the compliance of the system. We may find many possible solutions of the microstructure variable set $\boldsymbol{m}$ that can potentially satisfy the macroscale equilibrium. We illustrate this point in Fig. 5.2. For a given external force vector $\boldsymbol{f}_{ext}$, many equilibrium solutions exist at the structure scale, depending on different macroscale variable sets. However, we are only interested in the admissible equilibrium solution that minimizes the compliance (or maximizes the stiffness) of the system, lying on a representative load-displacement curve. We can write this preposition mathematically as follows:

$$\min_{\bar{\boldsymbol{u}} \in \bar{\boldsymbol{u}}_{sol}} \ \boldsymbol{f}_{ext}^{T} \bar{\boldsymbol{u}}, \quad \text{s.t.} : \ \boldsymbol{K}_{sol}(\bar{\boldsymbol{m}}(\boldsymbol{\rho}, \bar{\boldsymbol{u}}_{sol}))\bar{\boldsymbol{u}}_{sol} = \boldsymbol{f}_{ext} \ , \tag{5.15}$$

where $\bar{\boldsymbol{u}}_{sol}$ is the set of admissible equilibrium displacement solutions and $\boldsymbol{K}_{sol}$ is the stiffness matrix of the system.

It is apparent from Fig. 5.2 that the solution $\bar{\boldsymbol{u}}$ that satisfies (5.15) is the first converged displacement solution highlighted by the solid-red line. We can iteratively find this solution, using a quasi-Newton method based on the initial stiffness $\boldsymbol{K}_0$. We illustrate this procedure in Fig. 5.2 by the displacement solutions shown in dashed-red lines. Given the known solution $\bar{\boldsymbol{u}}^k$ at the k^{th} iteration, we find the increment in the solution $\Delta\bar{\boldsymbol{u}}^k$ as:

$$\boldsymbol{K}_0 \Delta\bar{\boldsymbol{u}}^k = \boldsymbol{f}_{ext} - \boldsymbol{f}_{int}^k \ . \tag{5.16}$$

The internal force vector $\boldsymbol{f}_{int}^k$ is evaluated with the known displacement solution $\bar{\boldsymbol{u}}^k$ as:

$$\boldsymbol{f}_{int}^k = \sum_{j=1}^{N_e} \left[\sum_{x=1}^{N_{gp}} \boldsymbol{B}^T \mathbb{C}(\bar{m}_j^{x,k}) \, \boldsymbol{B} \, w_x \right] \bar{\boldsymbol{u}}^k, \tag{5.17}$$

$\bar{m}_j^{x,k}$ is obtained by solving the microstructure optimization problem (5.14), where kinematic boundary conditions are derived from the displacement solution $\bar{\boldsymbol{u}}^k$ and given density $\boldsymbol{\rho}$ defines the admissible set E_{ad}. The iterative solution stops when the displacement convergence criteria is met. The optimum solution of the microscale design variables and the corresponding stiffness at the converged displacement solution $\bar{\boldsymbol{u}}$ are $\bar{\boldsymbol{m}}$ and $\boldsymbol{K}_{opt}(\bar{\boldsymbol{m}}(\boldsymbol{\rho}, \bar{\boldsymbol{u}}))$,

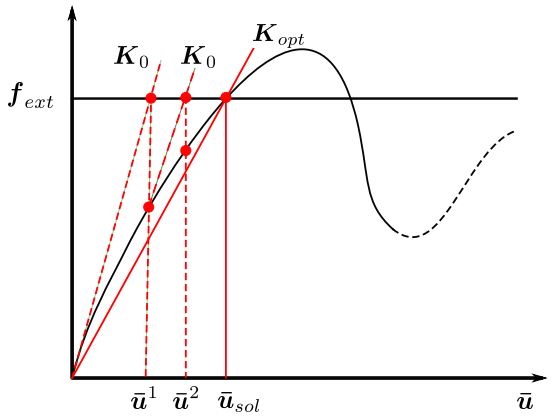

Fig. 5.2: *Quasi-Newton method with initial stiffness that resolves the nonlinearity based on the interaction of material and structure scales.*

respectively. The objective function is:

$$f_c(\boldsymbol{\rho}) = \boldsymbol{f}_{ext}^T \bar{\boldsymbol{u}} = \bar{\boldsymbol{u}}^T \boldsymbol{K}_{opt}(\bar{\boldsymbol{m}}(\boldsymbol{\rho}, \bar{\boldsymbol{u}}))\bar{\boldsymbol{u}}. \tag{5.18}$$

5.2.4 Sensitivity analysis and macroscale design update

The macroscale design problem (5.11) can be solved by well-established optimization algorithms [19, 196]. First, we need to derive the sensitivity of the objective function with respect to the design variables. Using the adjoint method, we write the sensitivity of the objective function f_c with respect to the macroscale design variable $\boldsymbol{\rho}$ as [19]:

$$\frac{\partial f_c}{\partial \boldsymbol{\rho}} = -\bar{\boldsymbol{u}}^T \frac{\partial \boldsymbol{K}_{opt}(\bar{\boldsymbol{m}}(\boldsymbol{\rho}, \bar{\boldsymbol{u}}))}{\partial \boldsymbol{\rho}} \bar{\boldsymbol{u}}. \tag{5.19}$$

Using (5.12), we rewrite the sensitivity for each element j with respect to its density ρ_j as:

$$\frac{\partial f_c}{\partial \rho_j} = -\bar{\boldsymbol{u}}_j^T \left[\sum_{x=1}^{N_{gp}} \boldsymbol{B}^T \frac{\partial\, \mathbb{C}(\bar{m}_j^x)}{\partial \rho_j} \boldsymbol{B}\, w_x \right] \bar{\boldsymbol{u}}_j \,. \tag{5.20}$$

The homogenized stiffness $\mathbb{C}(\bar{m}_j^x)$ at each Gauss point inside an element j is a function of microscale variables $\phi_A^{x,j}, \theta_A^{x,j}, \zeta_A^{x,j}$, and $\gamma_C^{x,j}$ (see Appendix **C**). Furthermore, $\phi_A^{x,j}$ and $\gamma_C^{x,j}$ relate to ρ_j via (5.14). Using the chain rule, we find the first derivative of $\mathbb{C}$ with respect

to ρ_j as:

$$\frac{\partial\ \mathbb{C}(\rho_j, \bar{m}_j^x)}{\partial \rho_j} = \frac{\partial\ \mathbb{C}}{\partial \phi_A^{x,j}} \frac{\partial \phi_A^{x,j}}{\partial \rho_j} + \frac{\partial\ \mathbb{C}}{\partial \gamma_C^{x,j}} \frac{\partial \gamma_C^{x,j}}{\partial \rho_j}, \tag{5.21}$$

where the partial derivatives of $\mathbb{C}$ with respect to $\phi_A^{x,j}$ and $\gamma_C^{x,j}$ are evaluated at the optimum solution $\bar{\boldsymbol{m}}$ of the microscale design variables. We evaluate these derivatives using finite difference approximations. Using (5.14) and standard algebraic manipulation, we arrive at the following expressions:

$$\frac{\partial\ \mathbb{C}}{\partial \rho_j} = \frac{\partial\ \mathbb{C}}{\partial \phi_A^{x,j}} \frac{1}{\rho_A - \rho_B(1 - \bar{\gamma}_C^{x,j}) - \rho_C \bar{\gamma}_C^{x,j}} + \frac{\partial\ \mathbb{C}}{\partial \gamma_C^{x,j}} \frac{1}{(\rho_C - \rho_B)(1 - \bar{\phi}_A^{x,j})}\ . \tag{5.22}$$

Sensitivity numbers rank the element sensitivities that are used to update the macroscale design variable. The sensitivity numbers for the compliance minimization problem are:

$$\alpha_j = -\frac{\partial f_c}{\partial \rho_j}. \tag{5.23}$$

To avoid mesh dependency and checkerboard patterns, the sensitivity numbers are first smoothed with a filtering scheme defined as:

$$\alpha_j = \frac{\sum_{j'=1}^{N_j} g_{jj'}\ \alpha_j}{\sum_{j'=1}^{N_j} g_{jj'}}, \tag{5.24}$$

where N_j is the set of neighboring elements for which center-to-center distance $\Delta(j, j^{'})$ to element $j^{'}$ is smaller than the filter radius r_{min}. The weight factor $g_{jj'}$ is defined as:

$$g_{jj'} = \max\ \{0, r_{min} - \Delta(j, j^{'})\}. \tag{5.25}$$

To improve convergence, the sensitivity numbers are further averaged with the sensitivity numbers of the previous design iteration as:

$$\alpha_j^{i+1} \rightarrow (\alpha_j^{i+1} + \alpha_j^i)/2. \tag{5.26}$$

The ratio of sensitivity numbers and the mass constraints is written as:

$$B_j^i = \Big(\frac{\alpha_j^i}{\Lambda^i |\Omega_j|}\Big)^{\eta}, \tag{5.27}$$

where Λ^i is the Lagrange multiplier corresponding to the total material mass constraint in design update i, and η is a damping parameter. The macroscale density is updated using the well-known optimality criteria method [162]:

$$\rho_j^{i+1} = \begin{cases} \max(\rho_{min}, \rho_j^i - \mu) & \text{if } \rho_j^i B_j^i \leq \max(\rho_{min}, \rho_j^i - \mu) \\ \min(\rho_j^i + \mu, \rho_{max}) & \text{if } \min(\rho_j^i + \mu, \rho_{max}) \geq \rho_j^i B_j^i \\ \rho_j^i B_j^i & \text{otherwise} \end{cases} \tag{5.28}$$

To prevent a singular global stiffness matrix, the lower limit ρ_{min} on ρ_j is limited by a small value of 0.001. The maximum possible element density, ρ_{max}, depends on the density of the constituents at the microscales and the prescribed bounds in (5.3). μ is a small move parameter that improves the stability, for instance by preventing multiple holes appearing and disappearing during optimization. The Lagrange multiplier Λ^i is updated using the bisection method to satisfy the mass constraint. The design iterations stop when the density convergence criteria is met.

5.2.5 Algorithmic framework

We cast our developments in the algorithmic framework summarized in Algorithm 3 that mainly consists of three blocks. The outer block represents the macroscale structure optimization iterations using the optimal-criteria method. It stops when the macroscale density $\boldsymbol{\rho}$ reaches convergence. The innermost block optimizes the microstructure with respect to the microscale design variables $\boldsymbol{m}$ for all Gauss points with the prescribed macroscale strain $\boldsymbol{E}(\boldsymbol{x})$. The middle block combines the structure and material scales and solves the boundary value problem for displacements for a given distribution of macroscale density, following our discussion in Section 5.2.3.

We note that in our context the optimal design can take any value of macroscale density within the allowable range or so-called "gray" intermediate densities. However, the design framework can be modified for the discrete topology optimization setting with 0-1 type designs. We also note that Bi-directional Evolutionary Structural Optimization (BESO) and level-set methods [6, 98, 161, 198] could replace the optimality criteria method in the current framework for 0-1 type design problems.

5.2.6 Computational cost

Integrating homogenization estimates based on continuum micromechanics in concurrent material and structure optimization leads to an algorithmic framework whose computa-

Result: Design solution vector $[\boldsymbol{\rho}, \bar{\boldsymbol{m}}]^T$

Initialize $\boldsymbol{\rho}^0$, and $\boldsymbol{K}_0$;
Set iteration counter i = 0;
while $||\rho^{i+1} - \rho^i||/||\rho^i|| > \delta_{tol}$ **do**
    Compute the initial solution: $\boldsymbol{K}_0 \bar{\boldsymbol{u}}^0 = \boldsymbol{f}_{ext}$;
    Set iteration counter k = 0 (quasi-Newton);
    while $||\bar{\boldsymbol{u}}^{k+1} - \bar{\boldsymbol{u}}^k||/||\bar{\boldsymbol{u}}^k|| > \delta_u$ **do**
        forall *macroscale Gauss points* **do**
            Compute macroscale strain $\boldsymbol{E}(\boldsymbol{x}) = \boldsymbol{B}(\boldsymbol{x})\bar{\boldsymbol{u}}^k$;
            Optimize microstructure configuration $\bar{m}_j^{x,k}$;
        end
        Compute $\boldsymbol{f}_{int}^k = \sum_{j=1}^{N_e} \left[\sum_{x=1}^{N_{gp}} \boldsymbol{B}^T \mathbb{C}(\bar{m}_j^{x,k})\, \boldsymbol{B}\, w_x \right] \bar{\boldsymbol{u}}^k$;
        quasi-Newton update: $\boldsymbol{K}_0 \Delta\bar{\boldsymbol{u}}^k = \boldsymbol{f}_{ext} - \boldsymbol{f}_{int}^k$;
        $\bar{\boldsymbol{u}}^{k+1} = \bar{\boldsymbol{u}}^k + \Delta\bar{\boldsymbol{u}}^k$;
        k++;
    end
    Compute the objective function $f_c(\boldsymbol{\rho})$ and senstivities $\partial f_c/\partial\boldsymbol{\rho}$;
    Update density $\boldsymbol{\rho}^{i+1}$ using the optimal-criteria algorithm; i++;
end

Algorithm 3: Concurrent material and structure optimization framework for multi-phase hierarchical systems with elastic constituents.

tional cost is independent of the number of hierarchical length scales involved. We briefly illustrate this significant advantage via a qualitative analysis of the underlying computational complexity.

With n_{macro} macroscale optimization iterations, n_{itr}^{eq} average quasi-Newton nonlinear equilibrium iterations, and n_{gp} gauss points in the macroscale domain, the overall CPU time scales as:

$$T_{CPU} = T_\mu \times \mathcal{O}(n_{macro}\, n_{itr}^{eq}\, n_{gp}). \tag{5.29}$$

Here, T_μ is the average CPU time required for the solution of one microscale analysis and optimization problem. We note that n_{macro}, n_{itr}^{eq}, and n_{gp} in (5.29) are barely modifiable for a required macroscale spatial discretization. This restriction leaves us with T_μ for reducing T_{CPU}.

With nested computational homogenization in the sense of standard FE^2 type approaches, the computational complexity of T_μ for s microscale levels ($s = 2$ in Fig. 5.1) can be

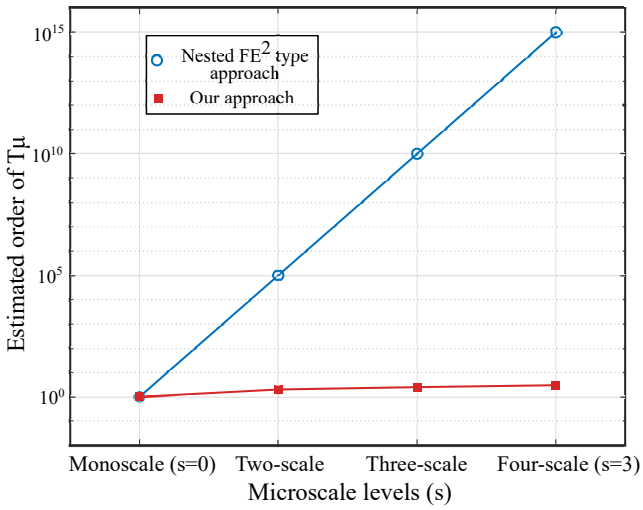

Fig. 5.3: *Computational cost of one microscale optimization problem for different numbers of hierarchical scales.*

approximately written as:

$$T_\mu = \mathcal{O}(n_{micro}^{\mu(1)} n_{gp}^{\mu(1)} \times ... \times n_{micro}^{\mu(s)} n_{gp}^{\mu(s)}) \ , \tag{5.30}$$

where $n_{gp}^{\mu(s)}$ and $n_{micro}^{\mu(s)}$ denote the number of quadrature points in the spatial discretization of the RVE at the s^{th} scale and the number of microstructure optimization iterations required, respectively.

With continuum micromechanics, T_μ is essentially the time to solve the material optimization problem (5.14). As discussed, this can be achieved by solving a straightforward constraint optimization problem that seeks the solution in the microscale design variable space, using fast gradient-based optimization methods [27]. The solution of a material optimization problem is equivalent to solve a set of (n+p) nonlinear equations with (n+p) variables, where n and p are the total number of design variables and the total number of equality constraints, respectively. The addition of another hierarchical scale potentially increases the number of design variables and constraints in the material optimization problem. However, a few additional design variables do not lead to an exponential increase in computational cost required to solve (5.14). We can therefore assume that in our approach, T_μ in (5.29) scales linearly with each scale characterization.

Focusing on the solution of one microscale analysis and optimization problem, Figure 5.3 compares the scaling of the estimated order of the computational cost with increasing number of materials scales in the two approaches discussed. We observe that for computational homogenization, even a simple two-scale ($s = 1$) problem results in the explosion of

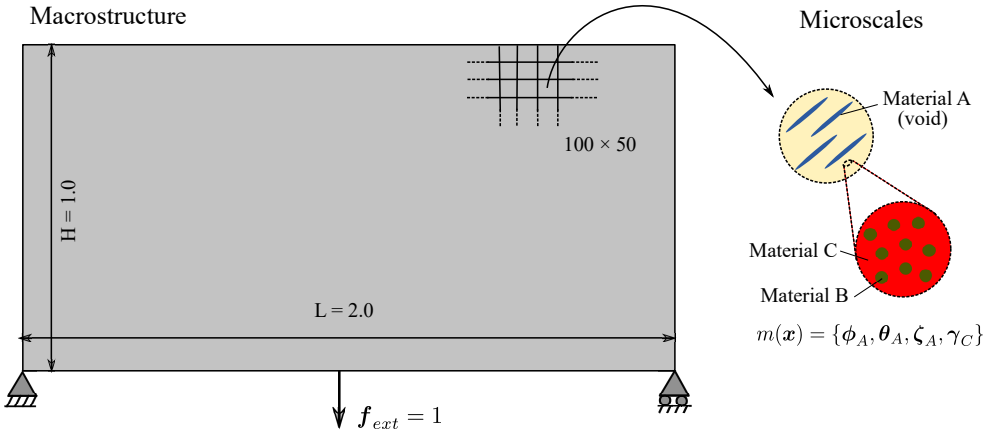

Fig. 5.4: *Multiphase hierarchical system I: the MBB beam.*

the computational expense. For example, given a discretization in each microscale RVE of $n_{gp}^{\mu(1)} \approx 40 \times 40 \times 4$ and an average number of optimization iterations $n_{micro}^{\mu(1)} \approx 20$, the total computational expense T_μ is of order $\sim 10^5$. If we assume the same RVE discretizations and iteration numbers across multiple scales, we observe in Figure 5.3 that the total cost increases exponentially when $s > 1$. In contrast, the computational cost in our approach remains within the same order of magnitude, even when $s > 1$.

5.3 Numerical examples

In this section, we define two test examples with hierarchical systems at the material level that are suitable to illustrate the computational efficiency and validity of our concurrent

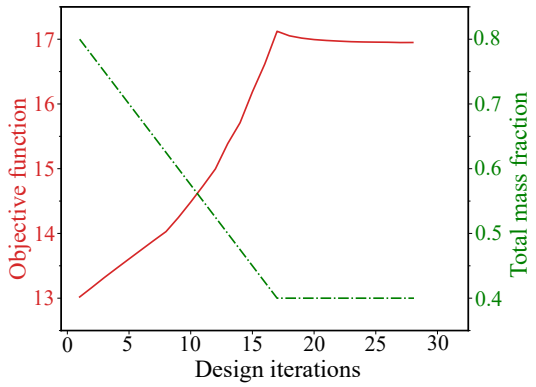

(a) Convergence of compliance and mass fraction with respect to number of macroscale design iterations.

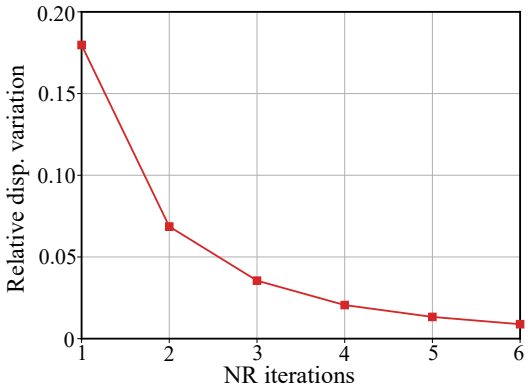

(b) Convergence of the quasi-Newton method in the 19^{th} design iteration.

Fig. 5.5: *Convergence of macroscale and microscale iterative procedures.*

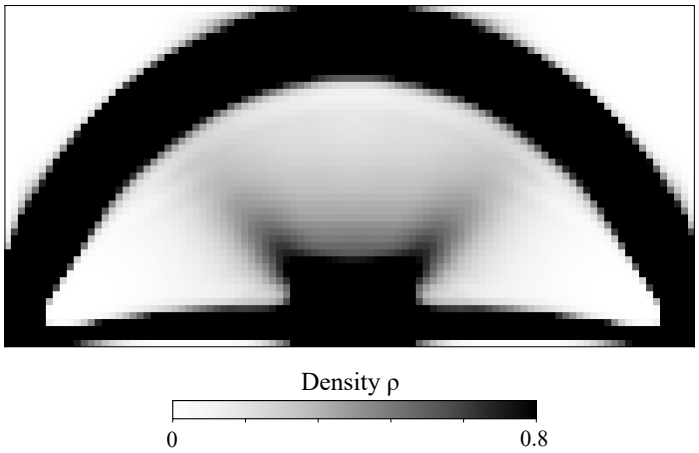

Fig. 5.6: *Optimum density distribution for the MBB problem.*

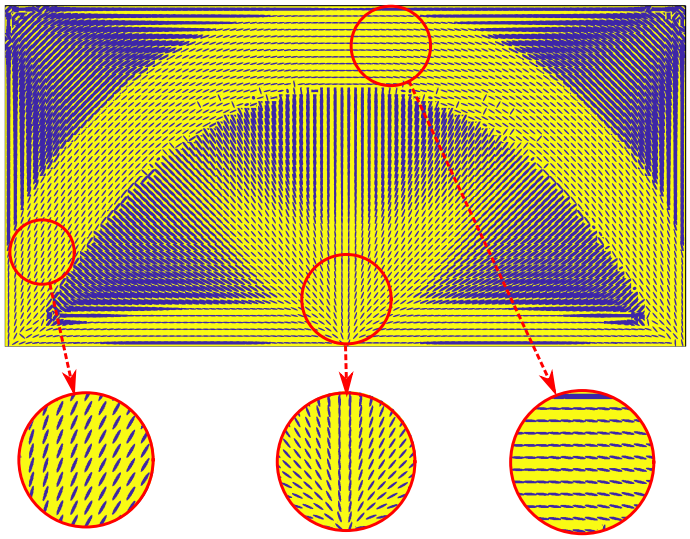

Fig. 5.7: *Optimized microstructure at the mesoscale for the MBB problem.*

material and structure optimization framework.

5.3.1 Messerschmitt-Bölkow-Blohm (MBB) beam

We first consider a standard bridge-type structure that is illustrated in Fig. 5.4. In a structural optimization context, the macroscale configuration is often referred to as Messerschmitt-Bölkow-Blohm (MBB) design problem. The length and height of the macrostructure are 2.0 and 1.0, respectively. The bottom-left end is pinned, and the bottom-right end has a roller support. The structure is loaded with a vertical point load of magnitude one, applied in the middle of the bottom edge of the structure. We discretize the macroscale structure with a 100×50 mesh of 4-node quadrilateral elements, resulting

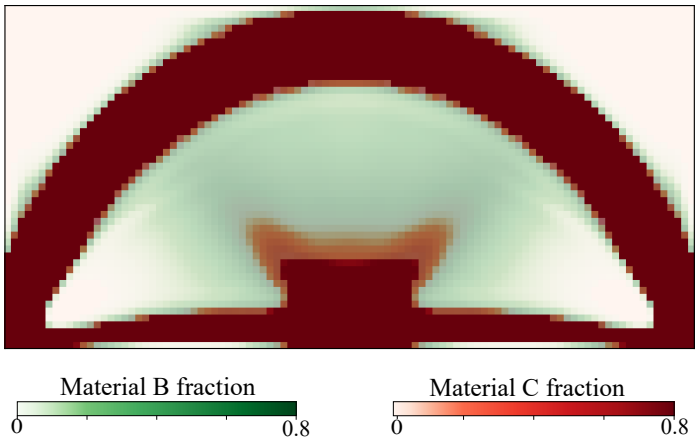

Fig. 5.8: *Optimized volume fractions of Material B and Material C for the MBB problem.*

in $5,000$ macroscale design variables. Each element contains four Gauss points, resulting in $100 \times 50 \times 4 = 20,000$ material optimization problems.

In the scope of this work, we extend the MBB test case at the material level. As illustrated in Fig. 5.4, we consider a hierarchical system that consists of Material A, B, and C at two different length scales. Their densities are $\rho_A = 0$, $\rho_B = 0.5$, and $\rho_C = 1.0$, respectively, their Young's moduli are $E_A = 0.0$, $E_B = 0.5$, and $E_C = 1.0$, respectively, and Poisson's ratio of all constituents is 0.3. For Material A, the elongation ratio of inclusions ranges from $\zeta_A = 1$ to $\zeta_A^{max} = 5$, and its minimum volume fraction is $\phi_A = 0.2$. For Material C, the volume fraction at the lowermost scale is allowed to assume any value between $\gamma_C^{min} = 0$ and $\gamma_C^{max} = 1$. As a consequence, the macroscale density at each point is restricted within the range of $\rho_{min} = 0$ to $\rho_{max} = 0.8$. We conclude that at each Gauss point, the material microstructure is parametrized by the volume fraction $\phi_A^{x,j}$, the orientation $\theta_A^{x,j}$, the elongation $\zeta_A^{x,j}$, and the volume fraction $\gamma_C^{x,j}$, resulting in $80,000$ microscale design variables.

The total amount of material mass available cannot fall below $M_{frac} = 0.4$. As an initial condition at the macroscale, we assume the maximum possible density ρ_{max} in each element. At the material level, we assume an initial microstructure configuration with $\phi_A = 0.1$, $\theta_A = 0.0$, $\zeta_A = 1.0$, and $\gamma_C = 1.0$ at each Gauss point. In each design update, we reduce the target mass fraction by 0.025 until we reach the specified mass fraction $M_{frac} = 0.4$. The move parameter μ and the damping parameter η are set to 0.05 and 0.5. We choose $r_{min} = 0.075$ for the design sensitivity filter (5.25). Given a macroscale density distribution $\boldsymbol{\rho}$, the quasi-Newton scheme uses the initial stiffness matrix $\boldsymbol{K}_0$ for finding the optimum design variables $\bar{\boldsymbol{m}}$ (see Section 5.2.3).

Figures 5.5a and 5.5b show a convergence plot for the macroscale design updates and the

number of quasi-Newton iterations for the macroscale structure problem, respectively. The macroscale design algorithm stops when the relative change in the macroscale density field falls below 0.001. We observe that the algorithm takes 28 density updates to converge to the final design for the MBB problem. The displacement convergence criterion for the quasi-Newton method in each macroscale design iteration is $||\bar{\boldsymbol{u}}^{k+1} - \bar{\boldsymbol{u}}^{k}||/||\bar{\boldsymbol{u}}^{k}|| < 10^{-2}$. For each macroscale density update iteration, it takes 4 to 8 quasi-Newton iterations to reach the macroscale equilibrium solution.

Figures 5.6, 5.7 and 5.8 illustrate the final design of the MBB problem, including the optimized microstructure configurations. The macroscale density plotted in Fig. 5.6 shows a large diffuse gray region that maximizes the compliance by optimally distributing the constituents at different scales. The result resembles natural materials such as bones and plants that often exhibit dense cortical-type regions supported by diffuse softer material.

Figure 5.7 illustrates the details of the optimized morphology at the mesoscale. The yellow color represents the matrix material resulting from homogenization of the lowermost scale. The blue color displays the volume fraction, orientation, and elongation of Material A inclusions. We observe that in the main branches, the inclusions are fully elongated and oriented in the direction of the largest principal stress. In the diffuse regions and joints of the main branches, the morphology is more complex, exhibiting gradual changes in the inclusion characteristics.

The equivalent volume fractions of the three Materials A, B, and C at the macroscale satisfy $\bar{\phi}_A + \bar{\phi}_B + \bar{\phi}_C = 1$ and can thus be computed as follows: $\bar{\phi}_A = \phi_A$, $\bar{\phi}_B = (1 - \phi_A)(1 - \gamma_C)$, and $\bar{\phi}_C = (1 - \phi_A)\gamma_C$. Figure 5.8 displays the equivalent material volume fraction of Material B and Material C at the macroscale, where we use 60% opacity for both. We can identify regions dominated by Material B and C as well as a mixing zone. As expected, the stronger Material C is deposited in the main branches, whereas the softer Material B

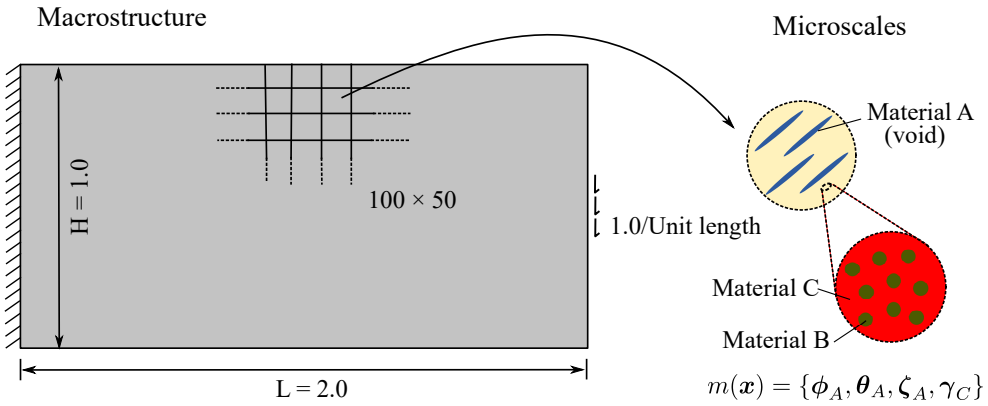

Fig. 5.9: *Multiphase hierarchical system II: the cantilever problem.*

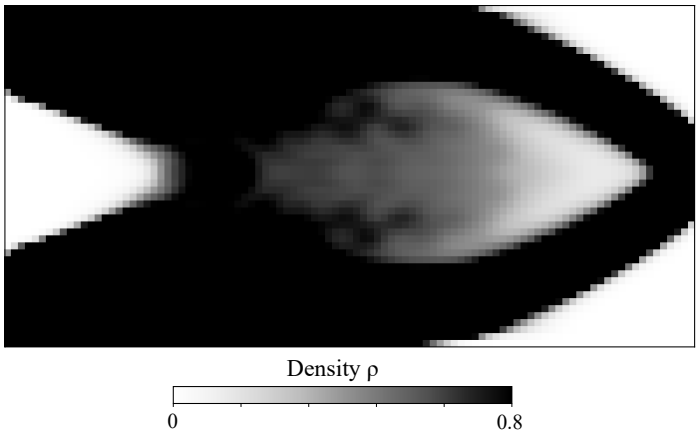

Fig. 5.10: *Optimum density distribution for the cantilever problem.*

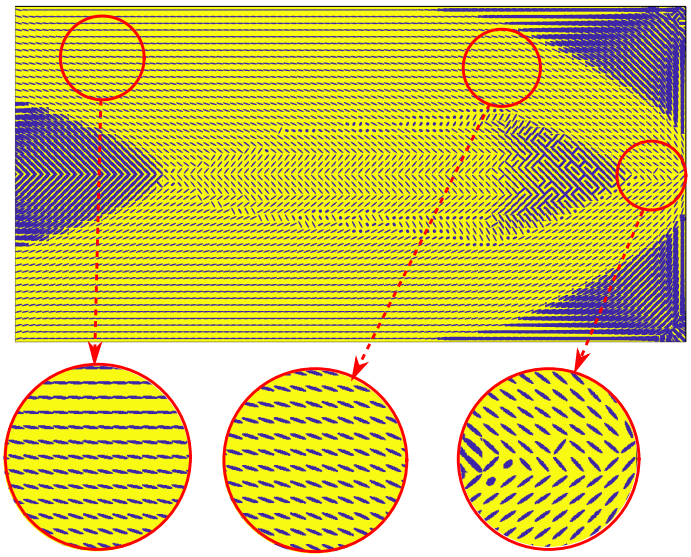

Fig. 5.11: *Optimized microstructure at the mesoscale for the cantilever problem.*

concentrates in the transition zones.

5.3.2 Cantilever beam

As a second test, we define the cantilever design problem illustrated in Fig. 5.9. The length and height of the macrostructure are 2.0 and 1.0, respectively. The right edge is fixed, and the central 4% of the left edge are loaded with a traction of magnitude 1.0 per unit length. We employ the same discretization of the macroscale domain as in the previous example. The total amount of mass available is restricted to $M_{frac} = 0.6$. The move parameter μ, the damping parameter η, and the design sensitivity filter radius r_{min} are 0.05, 0.5, and 0.06, respectively. The rest of the parameters are the same as in the previous example.

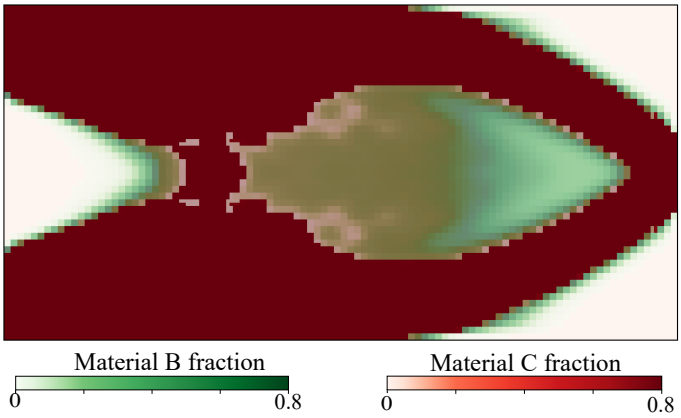

Fig. 5.12: *Optimized volume fractions of Material B and Material C for the cantilever problem.*

We observe in Fig. 5.10 that the optimized density distribution is qualitatively similar to a standard monoscale variable thickness design. An apparent difference, however, is the significant diffused gray region with complex microstructures, resulting from a complex stress-strain distribution throughout the domain, mainly due to the small length to height ratio. This complex distribution drives the microstructure to adapt itself to achieve optimal performance. Figures 5.11 and 5.12 show the morphology of Material A inclusions and the volume fraction distributions of Materials B and C, respectively.

Chapter 6

Structure optimization of elastoplastic multiphase hierarchical systems

Fritzen and co-authors formulated the path-dependent structure (or topology) optimization model with elastoplastic microheterogeneous material definitions [63]. The model considers two scales: the macroscopic structure scale at which the optimization is performed and the microscale that provides homogenized elastoplastic constitutive response via computational homogenization for fixed microstructure definition. The authors employed model order reduction techniques with GPU-based parallelization strategies to claim the computational feasibility. However, the total reported time for standard 2D cantilever benchmark problem with two-scale elastoplastic material definition was approximately one week. This example affirms that the elastoplastic multiphase hierarchical systems are computationally prohibitive even for structure optimization problems with fixed material definition.

In this chapter, we integrate the continuum micromechanics estimates of macroscale elastoplastic properties in the structure optimization formulation to overcome the computational challenge posed by elastoplastic multiphase hierarchical systems. In the context of this formulation, design sensitivities are path-dependent and, therefore, require the entire history of deformation parameterized via internal state variables. Thus, the sensitivity calculations are computationally intensive and demand heavy memory usage compared to the elastic (path-independent) case in the previous chapter. To tackle these challenges, we derive the design sensitivities for the optimization formulation by utilizing the path-dependent adjoint methods following [3, 63]. For the algorithmic completeness, we also summarize the finite element discretization of the weak formulation of the initial boundary value

problem (IBVP), its linearization with the Newton-Raphson method, and the closest point projection algorithm for homogenized elastoplastic material constitutive equations following the excellent presentation given in Simo & Hughes [164]. We will also use these components in the next chapter.

This chapter is structured as follows. Section 6.1 summarizes the homogenized stiffness and flow rule for elasto-plastic multiphase hierarchical materials following the continuum micromechanics principles discussed in Chapter 2. In Section 6.2 and 6.3, we brief the weak formulation of the initial boundary value problem (IBVP) and its discretization via the finite element method, respectively. In Section 6.4, we state the structure optimization model and derive the sensitivity analysis using the adjoint method. Section 6.5 outlines essential algorithmic details and casts all the modules in an algorithmic framework. In Section 6.6, we define benchmark problems with elastoplastic hierarchical material definition to verify our method.

6.1 Continuum micromechanics based constitutive modeling

In this section, we state the homogenized stiffness and flow rule for elastoplastic multiphase hierarchical materials following the continuum micromechanics principles discussed in Chapter 2. We refer to Fig. 6.1 for the macroscale description and representative microscale configuration for illustrating the concepts developed in this chapter.

6.1.1 Local constitutive equations in stress-space

The macroscale strain tensor $\boldsymbol{E}$ can be decomposed into an elastic and plastic part, denoted by $\boldsymbol{E}^e$ and $\boldsymbol{E}^p$, respectively. This relation reads as:

$$\boldsymbol{E} = \boldsymbol{E}^e + \boldsymbol{E}^p. \tag{6.1}$$

For the linearized elasticity, the macroscale stress tensor $\boldsymbol{\Sigma}$ is related with the macroscale strain quantities and the homogenized macroscopic stiffness tensor $\mathbb{C}$ as:

$$\boldsymbol{\Sigma} = \mathbb{C}(m) : (\boldsymbol{E} - \boldsymbol{E}^p), \tag{6.2}$$

where m describes the microstructural heterogeneities. We emphasize that m is given and fixed, and it is not a optimization variable. Next, we introduce the *yield criterion* function

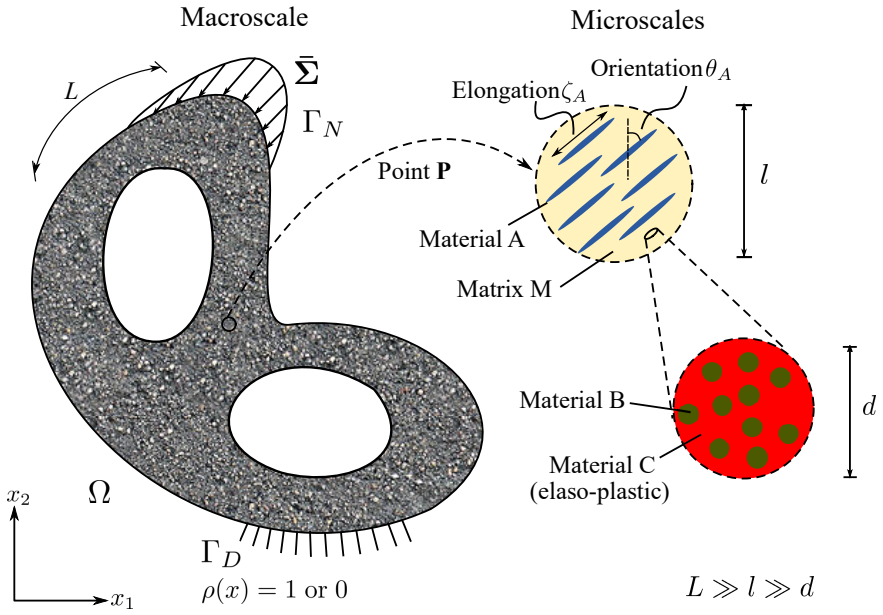

Fig. 6.1: *Sketch of a representative structure optimization problem with given elastoplastic multiphase hierarchical material definition.*

$\mathfrak{F}(\boldsymbol{\Sigma}, m)$ in *stress space* that constrains the admissible stresses to lie in the set $\mathbb{E}_\Sigma$ defined as:

$$\mathbb{E}_\Sigma := \Big\{ \boldsymbol{\Sigma} \in \mathbb{S} \mid \mathfrak{F}(\boldsymbol{\Sigma}, m) \leq 0 \Big\}, \tag{6.3}$$

where $\mathbb{S}$ is the second-order symmetric tensor space.

The essential feature of plastic flow is the notion of *irreversibility*. We built this notion into the formulation by introducing an ideal *associated flow rule* for the evolution of $\boldsymbol{E}^p$ as:

$$\dot{\boldsymbol{E}}^p = \gamma \, \partial_\Sigma \mathfrak{F}(\boldsymbol{\Sigma}, m) \, , \tag{6.4}$$

where $(\dot{\square})$ denotes the rate of change of a quantity, and $\partial_\Sigma \mathfrak{F}$ is the first derivative of $\mathfrak{F}$ with respect to $\boldsymbol{\Sigma}$. The parameter γ is called the *consistency parameter* and obeys the following *Karush-Kuhn-Tucker optimality conditions*:

$$\gamma \geq 0, \;\; \mathfrak{F}(\boldsymbol{\Sigma}, m) \leq 0, \;\; \text{and} \;\; \gamma \, \mathfrak{F}(\boldsymbol{\Sigma}, m) = 0. \tag{6.5}$$

In addition, $\gamma \geq 0$ also satisfies the *consistency requirement*

$$\gamma \, \dot{\mathfrak{F}}(\boldsymbol{\Sigma}, m) = 0. \tag{6.6}$$

Conditions (6.5) and (6.6) are also known as *loading/unloading* and *consistency conditions*, respectively.

6.1.2 Homogenized stiffness and yield criterion

The homogenized macroscopic stiffness tensor $\mathbb{C}$ and the yield criterion $\mathfrak{F}$ remain to be discussed. We summarize the analytical expressions for these homogenized estimates for the multiscale configuration shown in Fig. 6.1 following our discussion in Chapter 2. This material definition is identical to the one shown in Fig. 5.1 of Chapter 5. However, Material C is considered as perfectly elastoplastic material with known yield strength σ_C^Y. The microstructure configuration variables $\phi_A,\ \theta_A,\ \zeta_A$, and γ_C are simply the volume fraction of Material A, the orientation of Material A, the elongation of Material A, and the volume fraction of Material C, respectively. These variables are given for a structure optimization problem.

The expression for the homogenized stiffness tensor $\mathbb{C}$ is derived in Appendix **C**. Please refer (C.1), (C.2), and (C.3) for the detailed derivation and notations. For the completeness of this chapter, we restate the expression as:

$$\begin{aligned}\mathbb{C}_l(\phi_A,\zeta_A,\gamma_C) = \Big\{(1-\phi_A)\ \mathbb{c}_M + \phi_A\ \mathbb{c}_A : [\mathbb{I} + \mathbb{P}^M_{sphrd}(\zeta_A) : (\mathbb{c}_A - \mathbb{c}_M)]^{-1}\Big\} : \\ \Big\{(1-\phi_A)\ \mathbb{I} + \phi_A\ [\mathbb{I}\ + \mathbb{P}^M_{sphrd}(\zeta_A) : (\mathbb{c}_A - \mathbb{c}_M)]^{-1}\Big\}^{-1}\ , \qquad (6.7)\\ \mathbb{C}(m) = \mathbb{C}(\phi_A,\theta_A,\zeta_A,\gamma_C) = \mathbf{T}^{-1}\ \mathbb{C}_l\ \mathbf{T}, \quad \forall\ \boldsymbol{x} \in \Omega\ .\end{aligned}$$

Material C at the microscale is isotropic and perfectly elastoplastic material that follows the von Mises failure criterion expressed as:

$$\mathfrak{f}_C = \sigma_{eq(C)}\ - \sigma_C^Y\ . \qquad (6.8)$$

Following Section 2.3.1 and (6.8), we write the macroscopic yield criterion $\mathfrak{F}$ as:

$$\mathfrak{F}(\boldsymbol{\Sigma},m) = \sqrt{\boldsymbol{\Sigma} : [\mathbb{C}(m)]^{-1} : \frac{\partial\ \mathbb{C}(m)}{\partial\ \mu_C} : [\mathbb{C}(m)]^{-1} : \boldsymbol{\Sigma}}\ -\ \sqrt{\frac{\bar{\phi}_C}{3}}\ \frac{\sigma_C^Y}{\mu_C}, \qquad (6.9)$$

where $\bar{\phi}_C$ is the equivalent volume fraction of Material C computed as $\bar{\phi}_C = (1-\phi_A)\ \gamma_C$, and μ_C is the bulk modulus of Material C. We emphasize again that the multiscale configuration of Fig. 6.1 is used for the purpose of illustration and is easily generalized to cover any other multiphase hierarchical system.

Remark: We note that (6.9) is of the form of $\mathfrak{F} = \sqrt{\boldsymbol{\Sigma} : \mathbb{M} : \boldsymbol{\Sigma}} - R$ that represents the general quadratic form of classical rate-independent plasticity models. With suitable restrictions, one could recover the classical von Mises isotropic yield criterion, the anisotropic criterion of Hill [91], and the Tsai-Wu general anisotropic yield criterion [180]. In the present context, it implies that the elastic domain defined by (6.9) satisfies two critical geometric properties. These properties are (1) the *convexity* of the elastic domain and (2) the *degree-one homogeneity* of the yield criterion. These properties are very important from the mathematical analysis viewpoint for developing solution algorithms for the constitutive equations and for the topology optimization methods.

6.2 The weak formulation of the initial boundary-value problem (IBVP)

We consider a reference domain Ω and restrict our attention to an time interval $[0, T]$ (see Fig. 6.1). The position of a material point in the domain Ω is denoted by $\boldsymbol{x}$. The domain Ω is subjected to traction $\bar{\boldsymbol{\Sigma}}(t)$ at the Neumann boundary Γ_N and the prescribed displacements $\bar{\boldsymbol{u}}^E(t)$ at the Dirichlet boundary Γ_D with a body force $\boldsymbol{b}(\boldsymbol{x}, t)$, where $t \in [0, T]$. Then the macroscale displacement field $\bar{\boldsymbol{u}}(\boldsymbol{x}, t)$ at a material point $\boldsymbol{x}$ and at time $t \in [0, T]$ is a mapping

$$\bar{\boldsymbol{u}} : \Omega \times [0, T] \to \mathcal{R}^3. \tag{6.10}$$

We define the corresponding velocity and strain fields at $(\boldsymbol{x}, t) \in \Omega \times [0, T]$ as:

$$\boldsymbol{v}(\boldsymbol{x}, t) := \frac{\partial\, \bar{\boldsymbol{u}}(\boldsymbol{x}, t)}{\partial\, t} \;\text{ and }\; \boldsymbol{E}(\boldsymbol{x}, t) := \frac{\partial\, \bar{\boldsymbol{u}}(\boldsymbol{x}, t)}{\partial\, \boldsymbol{x}}, \tag{6.11}$$

respectively. We denote the macroscale stress field as $\boldsymbol{\Sigma}(\boldsymbol{x}, t)$. We also assume the compatible initial conditions for the dynamic problems. Then, the balance of momentum about any point along with the stated boundary conditions and initial conditions defines an *initial boundary-value problem* (IBVP) as:

$$\begin{aligned} \rho\, \frac{\partial \boldsymbol{v}(\boldsymbol{x}, t)}{\partial t} - \frac{\partial \boldsymbol{\Sigma}(\boldsymbol{x}, t)}{\partial \boldsymbol{x}} - \boldsymbol{b}(\boldsymbol{x}, t) = 0 \qquad & \forall\, (\boldsymbol{x}, t) \in \Omega \times [0, T], \\ \bar{\boldsymbol{u}} = \bar{\boldsymbol{u}}^E(t) \;\; & \forall (\boldsymbol{x}, t) \in \Gamma_D \times [0, T], \\ \boldsymbol{\Sigma} = \bar{\boldsymbol{\Sigma}}(t) \quad & \forall (\boldsymbol{x}, t) \in \Gamma_N \times [0, T], \end{aligned} \tag{6.12}$$

where ρ is the density at the material point $\boldsymbol{x}$. The constitutive relation between the stress $\boldsymbol{\Sigma}(\boldsymbol{x},t)$ and the displacement field (through the strains $\boldsymbol{E}(\boldsymbol{x},t)$) summarized in the previous section closes this problem. We observe that the state variables in these equations are defined in the rate terms and are subjected to additional constraints imposed by the yield criterion. These complexities of the constitutive equations make the IBVP highly nonlinear and path-dependent.

For the weak formulation of the IBVP, we define the displacement solution space $\mathcal{S}_t$ at time $t \in [0,T]$ as:

$$\mathcal{S}_t = \Big\{ \bar{\boldsymbol{u}}(\cdot,t) : \Omega \to \mathcal{R}^3 \mid \bar{\boldsymbol{u}}(\cdot,t)|_{\Gamma_D} = \bar{\boldsymbol{u}}^E(t) \Big\}. \tag{6.13}$$

Similarly, we define the linear space $\mathcal{V}$ of admissible test functions associated with $\mathcal{S}_t$ satisfying the essential boundary conditions as:

$$\mathcal{V} = \Big\{ \boldsymbol{\eta} : \Omega \to \mathcal{R}^3 \mid \boldsymbol{\eta}|_{\Gamma_D} = \boldsymbol{0} \Big\}. \tag{6.14}$$

With these notations, the weak form of the IBVP (6.12) states: Find a displacement field $\bar{\boldsymbol{u}}(\cdot,t) \in \mathcal{S}_t$ such that:

$$\int_\Omega \rho \, \frac{\partial \boldsymbol{v}}{\partial t} \, \boldsymbol{\eta} \, d\Omega + \int_\Omega \boldsymbol{\Sigma} : \, \frac{\partial \boldsymbol{\eta}}{\partial \boldsymbol{x}} \, d\Omega = \int_\Omega \boldsymbol{b} \cdot \boldsymbol{\eta} \, d\Omega + \int_{\Gamma_N} \bar{\boldsymbol{\Sigma}} \cdot \boldsymbol{\eta} \, ds \;\; \forall \boldsymbol{\eta} \in \mathcal{V} \text{ and } \forall \, t \in [0,T]. \tag{6.15}$$

For the mentioned class of elastoplastic problems, both $\mathcal{S}_t$ for fixed t and $\mathcal{V}$ lie in $\boldsymbol{H}^1(\Omega)$ that is the Sobolov space of functions possessing square integrable derivatives.

6.3 Finite element solution of the elastoplastic initial boundary-value problem

In this section, we outline a generic numerical solution scheme for the elastoplastic IBVP exploiting its weak form (6.15) within the context of the finite element method. The goal is to find the numerical approximation for the displacement solution $\bar{\boldsymbol{u}}(\boldsymbol{x},t)$ to (6.15), where the stress field $\boldsymbol{\Sigma}(\boldsymbol{x},t)$ obeys the local elastoplastic constitutive equations derived in continuum micromechanics framework and stated in Section 6.1. In the subsequent development, we restrict ourselves to quasi-static problems dropping the inertial term that is the first term in (6.15).

First, we arrive at the discretized version of the weak form of the equilibrium equations following standard finite element concepts [99]. Later, we outline an incremental solution procedure for the discretized equilibrium equations. In this description, we use vector-matrix notation to represent the introduced quantities, consistent with standard finite element literature. However, we keep the same symbols for the respective vector-matrix notation.

6.3.1 Spatial discretization

We split the domain Ω into N_e finite elements such that:

$$\Omega = \bigcup_{j=1}^{N_e} \Omega_j, \tag{6.16}$$

where Ω_j denotes the definition of element j, and $\partial\Omega_j$ is its boundary. With the standard definitions of the strain-displacement matrix $\boldsymbol{B}$ and shape function matrix $\boldsymbol{N}$, we arrive at the discrete counterpart of the momentum equation utilizing (6.15). The equations read as:

$$\bar{\boldsymbol{r}}(t) := \boldsymbol{f}^{ext}(t) - \boldsymbol{f}^{int}(\boldsymbol{\Sigma}) = 0 \;\; \forall t \in [0, T], \tag{6.17}$$

$$\boldsymbol{f}^{ext}(t) = \sum_{j=1}^{N_e} \left[\int_{\Omega_j} \boldsymbol{N}^T \boldsymbol{b}(\boldsymbol{x}, t) \; d\Omega_j + \int_{\partial\Omega_j \cap \Gamma_N} \boldsymbol{N}^T \bar{\boldsymbol{\Sigma}}(t) \; ds_j \right], \tag{6.18}$$

$$\boldsymbol{f}^{int}(\boldsymbol{\Sigma}) = \sum_{j=1}^{N_e} \int_{\Omega_j} \boldsymbol{B}^T \boldsymbol{\Sigma}(\boldsymbol{x}, t) \; d\Omega_j. \tag{6.19}$$

$\boldsymbol{f}^{ext}$ and $\boldsymbol{f}^{int}$ are referred as global external force vector and global internal force vector, respectively. Integrals in the above equations are evaluated with standard Gauss quadrature rules. Therefore, from now onwards, we restrict the definition of $\boldsymbol{x}$ to the discrete Gauss points. However, we keep the integral notation in this presentation. The critical step, in this outline, is the evaluation of the stress field $\boldsymbol{\Sigma}(\boldsymbol{x}, t)$ for time $t \in [0, T]$ obeying the local constitutive equations stated in Section 6.1. The incremental procedure outlined in the following section addresses this issue.

6.3.2 Incremental solution procedure

Incremental loading

We partition the considered time interval $[0, T]$ into n_{load} partitions as:

$$[0, T] = \bigcup_{n=0}^{n_{load}-1} [t_n, t_{n+1}] \tag{6.20}$$

and focus on a typical time interval $[t_n, t_{n+1}]$. At time t_n, the state at each macroscale Gauss point $\boldsymbol{x}$ inside element j is given and characterized by $\{\boldsymbol{E}_n, \boldsymbol{\Sigma}_n, \boldsymbol{E}^p_n\}$. We assume that the body is equilibrated at t_n satisfying (6.17) under the body force vector $\boldsymbol{b}_n$ and traction vector $\bar{\boldsymbol{\Sigma}}_n$ with the associated displacement solution field $\bar{\boldsymbol{u}}_n$. With an incremental load $(\Delta\boldsymbol{b}_{n+1}, \Delta\bar{\boldsymbol{\Sigma}}_{n+1})$ in this time step, the loading at $t_{n+1} \in [0, T]$ is

$$\boldsymbol{b}_{n+1} = \boldsymbol{b}_n + \Delta\boldsymbol{b}_{n+1} \text{ and } \bar{\boldsymbol{\Sigma}}_{n+1} = \bar{\boldsymbol{\Sigma}}_n + \Delta\bar{\boldsymbol{\Sigma}}_{n+1} \,. \tag{6.21}$$

This loading entails in the discrete external load vector $\boldsymbol{f}^{ext}_{n+1}$ at time t_{n+1} following (6.18). $\boldsymbol{f}^{ext}_{n+1}$ reads as:

$$\boldsymbol{f}^{ext}_{n+1} = \sum_{j=1}^{N_e} \left[\int_{\Omega_j} \boldsymbol{N}^T \boldsymbol{b}_{n+1} \, d\Omega_j + \int_{\partial\Omega_j \cap \Gamma_N} \boldsymbol{N}^T \bar{\boldsymbol{\Sigma}}_{n+1} \, ds_j \right]. \tag{6.22}$$

Now, the problem at this stage is to update the state variables in a manner consistent with the local constitutive equations to the values $\{\boldsymbol{E}_{n+1}, \boldsymbol{\Sigma}_{n+1}, \boldsymbol{E}^p_{n+1}\}$. The updated state variables and associated displacement field $\bar{\boldsymbol{u}}_{n+1} = \bar{\boldsymbol{u}}_n + \Delta\bar{\boldsymbol{u}}_{n+1}$ must obey the following equilibrium condition:

$$\bar{\boldsymbol{r}}_{n+1} := \boldsymbol{f}^{ext}_{n+1} - \boldsymbol{f}^{int}_{n+1} = 0, \tag{6.23}$$

where

$$\boldsymbol{f}^{int}_{n+1} := \sum_{j=1}^{N_e} \int_{\Omega_j} \boldsymbol{B}^T \boldsymbol{\Sigma}_{n+1} \, d\Omega_j. \tag{6.24}$$

We emphasize that the equilibrium equation (6.23) is generally nonlinear. The source of its nonlinearity is the nonlinear incremental constitutive equations as discussed in the following section. This nonlinearity appears in the equilibrium equation through the global internal

force vector stated in (6.24). The Newton-Raphson algorithm based iterative schemes are used for the solution of such nonlinear incremental equation. We briefly discuss the iterative procedure in Section 6.5.

Incremental form of local constitutive equations

For the solution of local constitutive equations stated in Section 6.1 at each Gauss point $\boldsymbol{x}$, we apply implicit backward-Euler difference scheme to obtain the discrete version of these equations. We assume that the incremental displacement field $\Delta\bar{\boldsymbol{u}}_{n+1}$ is given, which implies that the macroscale strain $\boldsymbol{E}_{n+1}$ at time t_{n+1} is given. The strain is

$$\boldsymbol{E}_{n+1} = \boldsymbol{E}_n + \Delta\boldsymbol{E}_{n+1}, \tag{6.25}$$

where $\Delta\boldsymbol{E}_{n+1} := \nabla^s(\Delta\bar{\boldsymbol{u}}_{n+1})$, and $\nabla^s(\cdot)$ denotes the symmetric gradient. The macroscale stress $\boldsymbol{\Sigma}_{n+1}$ at t_{n+1} follows directly from (6.2) as:

$$\boldsymbol{\Sigma}_{n+1} = \mathbb{C}(m) : (\boldsymbol{E}_{n+1} - \boldsymbol{E}^p_{n+1}). \tag{6.26}$$

With implicit backward-Euler scheme, the discrete version of (6.4) reads as:

$$\boldsymbol{E}^p_{n+1} = \boldsymbol{E}^p_n + \Delta\gamma_{n+1}\, \partial_\Sigma \mathfrak{F}(\boldsymbol{\Sigma}_{n+1}, m), \tag{6.27}$$

where $\Delta\gamma_{n+1} := \gamma_{n+1}\Delta t$, and $\Delta t = t_{n+1} - t_n$. Similarly, the discrete counterpart of the Karush-Kuhn-Tucker conditions stated in (6.5) and (6.5) becomes

$$\Delta\gamma_{n+1} \geq 0, \;\; \mathfrak{F}(\boldsymbol{\Sigma}_{n+1}, m) \leq 0, \;\; \text{and} \;\; \Delta\gamma_{n+1}\, \mathfrak{F}(\boldsymbol{\Sigma}_{n+1}, m) = 0. \tag{6.28}$$

With known $\Delta\bar{\boldsymbol{u}}_{n+1}$, the solution of these coupled nonlinear equations from (6.25) to (6.28) at each gauss point update the state variables $\{\boldsymbol{E}_{n+1}, \boldsymbol{\Sigma}_{n+1}, \boldsymbol{E}^p_{n+1}\}$. Solution strategies of these equations often go by the name of *return-mapping algorithms*. The closest point projection algorithm is a generalization of such return-mapping algorithms to the case of a general yield criterion and flow rule. Algorithmic setup of the closest point algorithm is briefly outlined in Section 6.5.

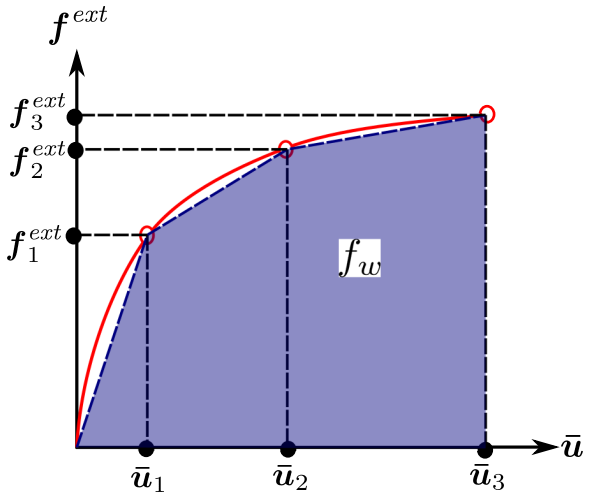

Fig. 6.2: *Total mechanical work f_w in the course of deformation process.*

6.4 Structure optimization model and sensitivity analysis

In this section, we first specify the essential definitions of the structure optimization model used in this chapter. Later, we derive the sensitivity analysis with respect to the structure optimization variables for the macroscale optimization updates.

6.4.1 Model definitions

The reference domain Ω is discretized into N_e finite elements as discussed in (6.16). We assign a structure optimization variable ρ_j to each element j. The N_e dimensional vector of the optimization variables is denoted as $\boldsymbol{\rho} = [\rho_1, \rho_2, \rho_3, ..., \rho_{N_e}]^T$. In the framework of structure or topology optimization, the optimization variables can take values either 0 or 1 denoting void and solid material, respectively. These variables can be interpreted as a generalized material density or indicator parameter.

The macroscale stress $\boldsymbol{\Sigma}$ for the void elements at each time step is set to 0, that is $\boldsymbol{\Sigma} = \boldsymbol{0}$ for $\rho_j = 0$. For the solid elements ($\rho_j = 1$), $\boldsymbol{\Sigma}$ arises from the homogenized constitutive model presented in this chapter. Replacing $\boldsymbol{\Sigma}$ with $\rho_j \boldsymbol{\Sigma}$ in element-wise integrals in (6.19) and (6.24) includes the associated optimization variable ρ_j in the formulation. Then, the discrete equilibrium equation in terms of the structure optimization variables $\boldsymbol{\rho}$ at time t_{n+1} reads as:

$$\bar{\boldsymbol{r}}_{n+1}(\boldsymbol{\rho}, \bar{\boldsymbol{u}}_{n+1}) := \boldsymbol{f}_{n+1}^{ext} - \sum_{j=1}^{N_e} \rho_j \int_{\Omega_j} \boldsymbol{B}^T \boldsymbol{\Sigma}_{n+1} \, d\Omega_j = 0. \tag{6.29}$$

The structure optimization problems involving inelastic material models are potentially ill-posed for a force-controlled setting [35, 98, 126, 160, 171]. Therefore, only displacement-controlled loading is considered, and it is incrementally applied through prescribed displacements $\bar{\boldsymbol{u}}^E(t)$ introduced in Section 6.2. From here onwards, $\boldsymbol{f}^{ext}_{n+1}$ should be read as a discretized form of the loading potential resulting from the non-zero displacement boundary conditions.

In a path-dependent nonlinear structure optimization, a typical objective is to maximize the structural stiffness. It translates as the maximization of the mechanical work expended in the course of the deformation process. With notations introduced in Section 6.3, the total mechanical work f_w is approximated using the trapezoidal rule as:

$$f_w = \frac{1}{2} \sum_{n=0}^{n_{load}-1} (\boldsymbol{f}^{ext}_{n+1} + \boldsymbol{f}^{ext}_{n})^T \, \Delta \bar{\boldsymbol{u}}_{n+1}. \tag{6.30}$$

Figure 6.2 graphically illustrates the definition of f_w. During the optimization, a limit on total available material mass M_{req} is imposed. Then the optimization problem can be formulated as [63]:

$$\begin{aligned} \max_{\boldsymbol{\rho}} :\ & f_w(\boldsymbol{\rho}) \\ \text{s.t.} :\ & \bar{\boldsymbol{r}}_{n+1}(\boldsymbol{\rho}, \bar{\boldsymbol{u}}_{n+1}) = 0 \ \ \forall n = 0, 2, ..., n_{load} - 1 \\ & M(\boldsymbol{\rho}) = \sum_{j=1}^{N_e} \rho_j |\Omega_j| = M_{req} \\ & \rho_j = 0 \text{ or } 1, \ \forall j = 1, 2, ..., N_e \ , \end{aligned} \tag{6.31}$$

where $M(\boldsymbol{\rho})$ is the total mass of the solid elements, and $|\Omega_j|$ is the volume of element j. $\bar{\boldsymbol{u}}_{n+1}$ is the converged displacement solution, and $\bar{\boldsymbol{r}}_{n+1}$ is the equilibrium residual definition at the macroscale at time t_{n+1} that follows from (6.29). Also, the equilibrium state must be satisfied at all time steps.

6.4.2 Sensitivity analysis

The macroscale topology optimization algorithms such as BESO scheme (detailed in Section 6.5) require the sensitivity of the objective function (6.30) with respect to the structure optimization variables $\boldsymbol{\rho}$. Fritzen and co-authors [63, 197] derive the sensitivities using the adjoint method [31, 35], which we summarize here.

The adjoint method begins with the construction of a Lagrangian function f^*_w that enforces the zero residual constraint $\bar{\boldsymbol{r}}_{n+1}$ and $\bar{\boldsymbol{r}}_n$ at time t_{n+1} and t_n for each term of the trapezoidal

rule stated in (6.30). With Lagrangian multipliers $\boldsymbol{\lambda}_{n+1}$ and $\boldsymbol{\mu}_{n+1}$ of the same dimensions as the vector of unknown $\bar{\boldsymbol{u}}$, the Lagrangian function f_w^* reads as:

$$f_w^* = \frac{1}{2} \sum_{n=0}^{n_{load}-1} \Big\{ (\boldsymbol{f}_{n+1}^{ext} + \boldsymbol{f}_n^{ext})^T \, \Delta\bar{\boldsymbol{u}}_{n+1} + (\boldsymbol{\lambda}_{n+1})^T \bar{\boldsymbol{r}}_{n+1} + (\boldsymbol{\mu}_{n+1})^T \bar{\boldsymbol{r}}_n \Big\}. \tag{6.32}$$

Since $\bar{\boldsymbol{r}}_{n+1}$ and $\bar{\boldsymbol{r}}_n$ vanish at the equilibrium solution, the sensitivity of f_w^* is same as that of f_w implying:

$$\frac{\partial f_w}{\partial \rho_j} = \frac{\partial f_w^*}{\partial \rho_j} \, . \tag{6.33}$$

The derivative of f_w^* with respect to the optimization variable ρ_j follows from (6.32) as:

$$\frac{\partial f_w^*}{\partial \rho_j} = \frac{1}{2} \sum_{n=0}^{n_{load}-1} \left\{ \frac{\partial}{\partial \rho_j} \Big((\boldsymbol{f}_{n+1}^{ext} + \boldsymbol{f}_n^{ext})^T \, \Delta\bar{\boldsymbol{u}}_{n+1} \Big) + (\boldsymbol{\lambda}_{n+1})^T \, \frac{\partial \bar{\boldsymbol{r}}_{n+1}}{\partial \rho_j} + (\boldsymbol{\mu}_{n+1})^T \, \frac{\partial \bar{\boldsymbol{r}}_n}{\partial \rho_j} \right\}. \tag{6.34}$$

Given the displacement-controlled loading, the computation of $\partial f_w^* / \partial \rho_j$ leads to certain simplifications with astute choices for the vectors $\boldsymbol{\lambda}_{n+1}$ and $\boldsymbol{\mu}_{n+1}$. To realize these simplifications, we partition all degrees of freedom (DOF) into essential (index E; associated with the Dirichlet boundary conditions) and free (index F; remaining DOFs) DOFs. Then, a generic vector $\boldsymbol{v}$ and matrix $\boldsymbol{M}$ can be represented as:

$$\boldsymbol{v} \sim \begin{bmatrix} \boldsymbol{v}^E \\ \boldsymbol{v}^F \end{bmatrix} \quad \text{and} \quad \boldsymbol{M} \sim \begin{bmatrix} \boldsymbol{M}^{EE} & \boldsymbol{M}^{EF} \\ \boldsymbol{M}^{FE} & \boldsymbol{M}^{FF} \end{bmatrix}, \tag{6.35}$$

respectively. Since the displacements $\bar{\boldsymbol{u}}^E$ on the Dirichlet boundary Γ_D are prescribed, they are independent of the current value of optimization variable $\boldsymbol{\rho}$. It leads to

$$\frac{\partial \Delta\bar{\boldsymbol{u}}_q}{\partial \rho_j} = \frac{\partial}{\partial \rho_j} \begin{bmatrix} \Delta\bar{\boldsymbol{u}}_{\boldsymbol{q}}{}^E \\ \Delta\bar{\boldsymbol{u}}_{\boldsymbol{q}}{}^F \end{bmatrix} = \begin{bmatrix} \boldsymbol{0} \\ \frac{\partial \Delta\bar{\boldsymbol{u}}_{\boldsymbol{q}}{}^F}{\partial \rho_j} \end{bmatrix}, \tag{6.36}$$

which is valid for any arbitrary time step index $q = 0, ..., n_{load} - 1$. With displacement-controlled loading, only possible non-zero entries in the global force vector $\boldsymbol{f}_p^{ext}$ at any time

step index $p = 0, ..., n_{load} - 1$ are the reaction forces $\boldsymbol{f}_p^{ext,E}$. It implies that:

$$\boldsymbol{f}_p^{ext} = \begin{bmatrix} \boldsymbol{f}_p^{ext,E} \\ \mathbf{0} \end{bmatrix}. \tag{6.37}$$

From (6.36) and (6.37), we conclude

$$(\boldsymbol{f}_p^{ext})^T \frac{\partial \Delta \bar{\boldsymbol{u}}_q}{\partial \rho_j} = 0. \tag{6.38}$$

Then the expansion

$$\frac{\partial}{\partial \rho_j}\left((\boldsymbol{f}_p^{ext})^T \, \Delta \bar{\boldsymbol{u}}_q \right) = \left(\frac{\boldsymbol{f}_p^{ext}}{\partial \rho_j} \right)^T \Delta \bar{\boldsymbol{u}}_q + (\boldsymbol{f}_p^{ext})^T \frac{\partial \Delta \bar{\boldsymbol{u}}_q}{\partial \rho_j} \tag{6.39}$$

reduces to

$$\frac{\partial}{\partial \rho_j}\left((\boldsymbol{f}_p^{ext})^T \, \Delta \bar{\boldsymbol{u}}_q \right) = \left(\frac{\boldsymbol{f}_p^{ext}}{\partial \rho_j} \right)^T \Delta \bar{\boldsymbol{u}}_q \, . \tag{6.40}$$

We use this result from (6.40) into (6.34) and arrive at

$$\frac{\partial f_w^*}{\partial \rho_j} = \frac{1}{2} \sum_{n=0}^{n_{load}-1} \left\{ \left(\frac{\boldsymbol{f}_{n+1}^{ext}}{\partial \rho_j} + \frac{\boldsymbol{f}_n^{ext}}{\partial \rho_j} \right)^T \Delta \bar{\boldsymbol{u}}_{n+1} + (\boldsymbol{\lambda}_{n+1})^T \, \frac{\partial \bar{\boldsymbol{r}}_{n+1}}{\partial \rho_j} + (\boldsymbol{\mu}_{n+1})^T \, \frac{\partial \bar{\boldsymbol{r}}_n}{\partial \rho_j} \right\}. \tag{6.41}$$

The derivative of $\bar{\boldsymbol{r}}_{n+1}$ with respect to ρ_j is evaluated following the residual definition in (6.29). The derivative reads as:

$$\frac{\partial \bar{\boldsymbol{r}}_{n+1}}{\partial \rho_j} = \frac{\boldsymbol{f}_{n+1}^{ext}}{\partial \rho_j} - \int_{\Omega_j} \boldsymbol{B}^T \boldsymbol{\Sigma}_{n+1} \, d\Omega_j - \boldsymbol{K}_{n+1}^{tan} \frac{\partial \Delta \bar{\boldsymbol{u}}_{n+1}}{\partial \rho_j} \quad \text{with} \quad \boldsymbol{K}_{n+1}^{tan} = -\frac{\partial \bar{\boldsymbol{r}}_{n+1}}{\partial \bar{\boldsymbol{u}}_{n+1}} \, . \tag{6.42}$$

$\boldsymbol{K}_{n+1}^{tan}$ is the global FE stiffness matrix of the mechanical system at the equilibrium of the $(n+1)^{th}$ load step. We note that the second expression in this equation is augmented with

zeros to keep the dimensional consistency. Using (6.42), we reformulate (6.41) as:

$$\begin{aligned}\frac{\partial f_w^*}{\partial \rho_j} = \frac{1}{2} \sum_{n=0}^{n_{load}-1} \Bigg\{ & \left(\frac{\boldsymbol{f}_{n+1}^{ext}}{\partial \rho_j} \right)^T (\Delta \bar{\boldsymbol{u}}_{n+1} + \boldsymbol{\lambda}_{n+1}) + \left(\frac{\boldsymbol{f}_{n}^{ext}}{\partial \rho_j} \right)^T (\Delta \bar{\boldsymbol{u}}_{n+1} + \boldsymbol{\mu}_{n+1}) \\ & - (\boldsymbol{\lambda}_{n+1})^T \left(\int_{\Omega_j} \boldsymbol{B}^T \boldsymbol{\Sigma}_{n+1} \, d\Omega_j + \boldsymbol{K}_{n+1}^{tan} \frac{\partial \Delta \bar{\boldsymbol{u}}_{n+1}}{\partial \rho_j} \right) \\ & - (\boldsymbol{\mu}_{n+1})^T \left(\int_{\Omega_j} \boldsymbol{B}^T \boldsymbol{\Sigma}_{n} \, d\Omega_j + \boldsymbol{K}_{n}^{tan} \frac{\partial \Delta \bar{\boldsymbol{u}}_{n}}{\partial \rho_j} \right) \Bigg\} . \end{aligned} \tag{6.43}$$

We again emphasize that the objective function value and, therefore, the sensitivities are invariant with respect to the Lagrangian multipliers $\boldsymbol{\lambda}_{n+1}$ and $\boldsymbol{\mu}_{n+1}$. It allows us to chose $\boldsymbol{\lambda}_{n+1}$ and $\boldsymbol{\mu}_{n+1}$ cleverly so that the sensitivity expression (6.43) can be calculated efficiently. Exploiting the definition of $\boldsymbol{f}_{n+1}^{ext}$ from (6.37), we set

$$\boldsymbol{\lambda}_{n+1}^E = -\Delta \bar{\boldsymbol{u}}_{n+1}^E \;\text{ and }\; \boldsymbol{\mu}_{n+1}^E = -\Delta \bar{\boldsymbol{u}}_{n+1}^E \tag{6.44}$$

so that the first two terms in (6.43) are omitted. We further simplify this expression utilizing the definition stated in (6.36) and the symmetry of the global FE stiffness matrix as:

$$\begin{aligned}\frac{\partial f_w^*}{\partial \rho_j} = \frac{1}{2} \sum_{n=0}^{n_{load}-1} \Bigg\{ & - (\boldsymbol{\lambda}_{n+1})^T \int_{\Omega_j} \boldsymbol{B}^T \boldsymbol{\Sigma}_{n+1} \, d\Omega_j - (\boldsymbol{\mu}_{n+1})^T \int_{\Omega_j} \boldsymbol{B}^T \boldsymbol{\Sigma}_{n} \, d\Omega_j \\ & - \left(\boldsymbol{K}_{n+1}^{tan,FE} \boldsymbol{\lambda}_{n+1}^E + \boldsymbol{K}_{n+1}^{tan,FF} \boldsymbol{\lambda}_{n+1}^F \right)^T \frac{\partial \Delta \bar{\boldsymbol{u}}_{n+1}^F}{\partial \rho_j} \\ & - \left(\boldsymbol{K}_{n}^{tan,FE} \boldsymbol{\mu}_{n+1}^E + \boldsymbol{K}_{n}^{tan,FF} \boldsymbol{\mu}_{n+1}^F \right)^T \frac{\partial \Delta \bar{\boldsymbol{u}}_{n}^F}{\partial \rho_j} \Bigg\} . \end{aligned} \tag{6.45}$$

The derivatives of $\bar{\boldsymbol{u}}_{n+1}^F$ and $\bar{\boldsymbol{u}}_{n}^F$ in (6.45) are unknown. They can be eliminated from above equation by solving the following adjoint systems for $\boldsymbol{\lambda}_{n+1}^F$ and $\boldsymbol{\mu}_{n+1}^F$ with prescribed values stated in (6.44) at the essential nodes:

$$\begin{aligned} \boldsymbol{\lambda}_{n+1}^F &= [\boldsymbol{K}_{n+1}^{tan,FF}]^{-1} \, \boldsymbol{K}_{n+1}^{tan,FE} \, \Delta \bar{\boldsymbol{u}}_{n+1}^E, \;\text{ and} \\ \boldsymbol{\mu}_{n+1}^F &= [\boldsymbol{K}_{n}^{tan,FF}]^{-1} \, \boldsymbol{K}_{n}^{tan,FE} \, \Delta \bar{\boldsymbol{u}}_{n+1}^E . \end{aligned} \tag{6.46}$$

Finally the sensitivity $\partial f_w^*/\partial \rho_j$ is calculated as:

$$\frac{\partial f_w^*}{\partial \rho_j} = -\frac{1}{2}\sum_{n=0}^{n_{load}-1}\left\{(\boldsymbol{\lambda}_{n+1})^T\int_{\Omega_j}\boldsymbol{B}^T\boldsymbol{\Sigma}_{n+1}\,d\Omega_j + (\boldsymbol{\mu}_{n+1})^T\int_{\Omega_j}\boldsymbol{B}^T\boldsymbol{\Sigma}_n\,d\Omega_j\right\}, \tag{6.47}$$

where the Lagrangian multipliers $\boldsymbol{\lambda}_{n+1}$ and $\boldsymbol{\mu}_{n+1}$ are completely determined via the relations (6.44) and (6.46).

6.5 Implementation details and algorithmic aspects

In this section, we provide an algorithmic overview of our optimization scheme along with the essential computer implementation details. First, we brief the iterative Newton-Raphson scheme for solving the nonlinear equilibrium equation (6.29) and the closest point projection algorithm to solve the local constitutive equations (6.25) to (6.28) following [47, 164]. For the macroscopic structural optimization, we use the bi-directional evolutionary structural optimization (BESO) algorithm given its robust and efficient performance [98, 197, 198]. Finally, we consolidate all our developments in an algorithmic framework and present them in Algorithm 4.

6.5.1 Newton-Raphson iterative solution procedure

As discussed, the equilibrium equation (6.23) or (6.29) are generally nonlinear due to the nonlinearity of the incremental constitutive equations. The Newton-Raphson method based linearization of (6.29) produces robust and efficient iterative scheme [47]. Denoting $(\bullet)_{n+1}^k$ the value of a variable $(\bullet)$ at the k^{th} iteration during the load step in $[t_n, t_{n+1}]$, we outline the iterative procedure as follows.

We, first, assume the total displacement solution vector $\bar{\boldsymbol{u}}_{n+1}^{(k+1)}$ at the $(k+1)^{th}$ iteration in terms of the incremental displacements $\delta\bar{\boldsymbol{u}}^{(k+1)}$ as:

$$\bar{\boldsymbol{u}}_{n+1}^{(k+1)} = \bar{\boldsymbol{u}}_{n+1}^{(k)} + \delta\bar{\boldsymbol{u}}^{(k+1)}. \tag{6.48}$$

The iteration counter k start from 0 with $\bar{\boldsymbol{u}}_{n+1}^{(0)} = \bar{\boldsymbol{u}}_n$. We again note that the all the state variables at time t_n are known. We linearize the equilibrium equation about the current known state $\bar{\boldsymbol{u}}_{n+1}^{(k)}$ as:

$$\boldsymbol{f}_{n+1}^{ext} - \boldsymbol{f}^{int}(\boldsymbol{\Sigma}_{n+1}^{(k)}) - \frac{\partial \boldsymbol{f}^{int}(\boldsymbol{\Sigma}_{n+1}^{(k)})}{\partial \bar{\boldsymbol{u}}_{n+1}^{(k)}}\,\delta\bar{\boldsymbol{u}}^{(k+1)} = 0, \tag{6.49}$$

Result: Optimized solution vector $\boldsymbol{\rho}$

Initialize $\boldsymbol{\rho}^0$;
Set design iteration counter i = 0;
while $||\rho^{i+1} - \rho^i||/||\rho^i|| > \delta_{tol}$ **do**
  Set up load increments $\Delta\bar{\boldsymbol{u}}_{\boldsymbol{q}}{}^E$ for each loading step index $q = 0, .., n_{load} - 1$;
  Initialize load increment couter $n = 0$;
  Initialize $\bar{\boldsymbol{u}}_0 = \mathbf{0} \implies \boldsymbol{E}_0 = \mathbf{0}$, and $\boldsymbol{E}_0^p = \mathbf{0}$;
  for $n \leq n_{load} - 1$ **do**
    Increment load $\bar{\boldsymbol{u}}_{n+1}^E = \bar{\boldsymbol{u}}_n^E + \Delta\bar{\boldsymbol{u}}_{n+1}^E$;
    Set Newton iteration counter k = 0;
    $\bar{\boldsymbol{u}}_{n+1}^{(0)} = \bar{\boldsymbol{u}}_n$;
    while $||\bar{\boldsymbol{r}}_{n+1}^{(k)}|| < \epsilon_{tol}$ **do**
      forall *macroscale Gauss points* **do**
        Compute the macroscale strain $\boldsymbol{E}_{n+1}^{(k)} = \nabla^s(\bar{\boldsymbol{u}}_{n+1}^{(k)})$;
        Update the state variables $\boldsymbol{\Sigma}_{n+1}^{(k)}$, and $\boldsymbol{E}_{n+1}^{p^{(k)}}$ using closest point algorithm (INPUT: $\boldsymbol{E}_{n+1}^{(k)}, \boldsymbol{E}_n^p$);
        Compute the algorithmic tangent moduli $\partial\boldsymbol{\Sigma}_{n+1}^{(k)}/\partial\boldsymbol{E}_{n+1}^{(k)}$;
      end
      Set up the linear system: $\boldsymbol{K}_{n+1}^{tan,(k)}\ \delta\bar{\boldsymbol{u}}^{(k+1)} = \boldsymbol{f}_{n+1}^{ext} - \boldsymbol{f}^{int}(\boldsymbol{\Sigma}_{n+1}^{(k)}) = \bar{\boldsymbol{r}}_{n+1}^{(k)}$, and solve for $\delta\bar{\boldsymbol{u}}^{(k+1)}$;
      Apply Newton correction to the displacements: $\bar{\boldsymbol{u}}_{n+1}^{(k+1)} = \bar{\boldsymbol{u}}_{n+1}^{(k)} + \delta\bar{\boldsymbol{u}}^{(k+1)}$; k++;
    end
    Calculate and store the Lagrangian multipliers $\boldsymbol{\lambda}_{n+1}$ and $\boldsymbol{\mu}_{n+1}$ for senstivity calculations using the converged state variables;
    n++;
  end
  Compute the objective function $f_w(\boldsymbol{\rho})$ and sensitivities $\partial f_w/\partial\boldsymbol{\rho}$;
  Update density $\boldsymbol{\rho}^{i+1}$ using the BESO algorithm; i++;
end

Algorithm 4: Structure optimization framework for elastoplastic multiphase hierarchical materials.

where, by chain rule,

$$\frac{\partial \boldsymbol{f}^{int}(\boldsymbol{\Sigma}_{n+1}^{(k)})}{\partial \bar{\boldsymbol{u}}_{n+1}^{(k)}} = \sum_{j=1}^{N_e} \rho_j \int_{\Omega_j} \boldsymbol{B}^T\ \frac{\partial \boldsymbol{\Sigma}_{n+1}^{(k)}}{\partial \bar{\boldsymbol{u}}_{n+1}^{(k)}}\ d\Omega_j = \sum_{j=1}^{N_e} \rho_j \int_{\Omega_j} \boldsymbol{B}^T \left[\frac{\partial \boldsymbol{\Sigma}_{n+1}^{(k)}}{\partial \boldsymbol{E}_{n+1}^{(k)}}\right] \frac{\partial \boldsymbol{E}_{n+1}^{(k)}}{\partial \bar{\boldsymbol{u}}_{n+1}^{(k)}} d\Omega_j\ . \tag{6.50}$$

With the definition of strain-displacement matrix $\boldsymbol{B}$, we arrive at

$$\frac{\partial \boldsymbol{f}^{int}(\boldsymbol{\Sigma}_{n+1}^{(k)})}{\partial \bar{\boldsymbol{u}}_{n+1}^{(k)}} = \boldsymbol{K}_{n+1}^{tan,(k)} = \sum_{j=1}^{N_e} \rho_j \int_{\Omega_j} \boldsymbol{B}^T \left[\frac{\partial \boldsymbol{\Sigma}_{n+1}^{(k)}}{\partial \boldsymbol{E}_{n+1}^{(k)}}\right] \boldsymbol{B}\ d\Omega_j, \tag{6.51}$$

where $\boldsymbol{K}_{n+1}^{tan,(k)}$ is the global tangent stiffness matrix at time t_{n+1} and iteration k. $\partial \boldsymbol{\Sigma}_{n+1}^{(k)}/\partial \boldsymbol{E}_{n+1}^{(k)}$ is referred as *the algorithmic tangent moduli*. By rearranging (6.49), we obtain the following linear system of equations:

$$\boldsymbol{K}_{n+1}^{tan,(k)}\ \delta \bar{\boldsymbol{u}}^{(k+1)} = \boldsymbol{f}_{n+1}^{ext} - \boldsymbol{f}^{int}(\boldsymbol{\Sigma}_{n+1}^{(k)}) = \bar{\boldsymbol{r}}_{n+1}^{(k)}, \tag{6.52}$$

that can be solved for the unknown incremental displacements $\delta \bar{\boldsymbol{u}}^{(k+1)}$ for the $(k+1)^{th}$ iteration. The Newton-Raphson iterations are repeated until the specified convergence criterion such as $||\bar{\boldsymbol{r}}_{n+1}^{(k)}|| < \epsilon_{tol}$ is satisfied.

We note that with known $\bar{\boldsymbol{u}}_{n+1}^{(k)}$, the stress $\boldsymbol{\Sigma}_{n+1}^{(k)}$ at each Gauss point can be evaluated following the local constitutive equations stated in Section 6.3.2. Therefore, all the terms in (6.52) are known provided that the algorithmic tangent moduli $\partial \boldsymbol{\Sigma}_{n+1}^{(k)}/\partial \boldsymbol{E}_{n+1}^{(k)}$ can be evaluated at each Gauss point. We outline the stepwise closest point projection algorithm for solving the local constitutive equations and evaluating the algorithmic tangent moduli in the following section.

6.5.2 Closest point projection algorithm for local constitutive equations

The closest point projection is a general algorithm for solving the local constitutive equations stated in (6.25) to (6.28) numerically. This algorithm is a generalization of a typical return map algorithm that is restricted to the von Mises type failure criterion. Broadly speaking, the algorithm is an iterative scheme obtained by the linearization of local constitutive equations. We briefly outline this stepwise procedure in the following BOX. For more details, readers are referred to Chapter 3 in Simo & Hughes [164]. We note that we use tensor notations in solving local constitutive equation, given their direct relation with the micromechanics relations outlined in Chapter 2.

6.5.3 BESO variable updating scheme

The basic idea behind the BESO heuristic algorithm is to reach the optimal structural topology by gradually removing inefficient or redundant material. The target mass in each

Given: $\boldsymbol{E}_{n+1},\ \boldsymbol{E}^p_n, m$, and TOL_1, TOL_2

1. Initialize: $\bar{k} = 0,\ \boldsymbol{E}^{p^{(0)}}_{n+1} = \boldsymbol{E}^p_n,\ \Delta\gamma^{(0)}_{n+1} = 0.$

2. Check the yield criterion $\mathfrak{F}^{(\bar{k})}_{n+1}$ and compute the flow rule residual $\boldsymbol{R}^{(\bar{k})}_{n+1}$ as:

$$\begin{aligned}
\boldsymbol{\Sigma}^{(\bar{k})}_{n+1} &:= \ \mathbb{C}(m) : (\boldsymbol{E}_{n+1} - \boldsymbol{E}^{p^{(\bar{k})}}_{n+1}) \\
\mathfrak{F}^{(\bar{k})}_{n+1} &:= \ \mathfrak{F}(\boldsymbol{\Sigma}^{(\bar{k})}_{n+1}, m) \\
\boldsymbol{R}^{(\bar{k})}_{n+1} &:= -\boldsymbol{E}^{p^{(\bar{k})}}_{n+1} + \boldsymbol{E}^p_n + \Delta\gamma^{(\bar{k})}_{n+1}\ \partial_\Sigma \mathfrak{F}^{(\bar{k})}_{n+1}
\end{aligned}$$

   IF: $\mathfrak{F}^{(\bar{k})}_{n+1} < TOL_1$ and $||\boldsymbol{R}^{(\bar{k})}_{n+1}|| < TOL_2$;
   THEN: $\boldsymbol{\Sigma}_{n+1} = \boldsymbol{\Sigma}^{(\bar{k})}_{n+1};\ \boldsymbol{E}^p_{n+1} = \boldsymbol{E}^{p^{(\bar{k})}}_{n+1},$ EXIT

3. Compute consistent elastic moduli $\mathbb{Z}^{(\bar{k})}_{n+1}$ as:

$$[\mathbb{Z}^{(\bar{k})}_{n+1}]^{-1} := [\mathbb{C}(m)]^{-1} + \Delta\gamma^{(\bar{k})}_{n+1}\ \partial^2_{\Sigma\Sigma}\mathfrak{F}^{(\bar{k})}_{n+1}$$

4. Compute the increment to consistency parameter $\Delta^2\ \gamma^{(\bar{k})}_{n+1}$ as:

$$\Delta^2\ \gamma^{(\bar{k})}_{n+1} := \frac{\mathfrak{F}^{(\bar{k})}_{n+1} - \boldsymbol{R}^{(k)}_{n+1} : \mathbb{Z}^{(\bar{k})}_{n+1} : \partial_\Sigma \mathfrak{F}^{(\bar{k})}_{n+1}}{\partial_\Sigma \mathfrak{F}^{(\bar{k})}_{n+1} : \mathbb{Z}^{(\bar{k})}_{n+1} : \partial_\Sigma \mathfrak{F}^{(\bar{k})}_{n+1}}$$

5. Evaluate the incremental plastic strains $\Delta\boldsymbol{E}^{p^{(\bar{k})}}_{n+1}$ as:

$$\Delta\boldsymbol{E}^{p^{(\bar{k})}}_{n+1} = [\mathbb{C}(m)]^{-1} : \mathbb{Z}^{(\bar{k})}_{n+1} : [\boldsymbol{R}^{(\bar{k})}_{n+1} + \Delta^2\gamma^{(\bar{k})}_{n+1}\ \partial_\Sigma \mathfrak{F}^{(\bar{k})}_{n+1}]$$

6. Update state variables as:

$$\begin{aligned}
\boldsymbol{E}^{p^{(\bar{k}+1)}}_{n+1} &= \boldsymbol{E}^{p^{(\bar{k})}}_{n+1} + \Delta\boldsymbol{E}^{p^{(\bar{k})}}_{n+1} \\
\Delta\gamma^{(\bar{k}+1)}_{n+1} &= \Delta\gamma^{(\bar{k})}_{n+1} + \Delta^2\gamma^{(\bar{k})}_{n+1}
\end{aligned}$$

   Set $\bar{k} \leftarrow \bar{k} + 1$ and GO TO 2.

7. Compute algorithmic elastoplastic tangent moduli as:

$$\begin{aligned}
\left.\frac{\partial\boldsymbol{\Sigma}}{\partial\boldsymbol{E}}\right|_{n+1} &= \mathbb{Z}_{n+1} - \boldsymbol{N}_{n+1} \otimes \boldsymbol{N}_{n+1} \\
\boldsymbol{N}_{n+1} &:= \frac{\mathbb{Z}_{n+1} : \partial_\Sigma \mathfrak{F}(\boldsymbol{\Sigma}_{n+1})}{\sqrt{\partial_\Sigma \mathfrak{F}(\boldsymbol{\Sigma}_{n+1}) : \mathbb{Z}_{n+1} : \partial_\Sigma \mathfrak{F}(\boldsymbol{\Sigma}_{n+1})}}
\end{aligned}$$

design iteration in this evolutionary approach can be expressed as:

$$M^{i+1} = \max\{M_{req}, (1 - c_{er})M^i\}, \tag{6.53}$$

where the evolutionary ratio c_{er} controls the percentage of material removal in each design iteration. M^{i+1} and M^i are the total mass at the $i+1$ and i^{th} design iterations, respectively. M_{req} is the required mass usage.

Sensitivity numbers ranks the element sensitivities that are used to determine the material removal and addition. Following (6.47), the sensitivity number for the considered objective is defined as:

$$\alpha_j = \left(\frac{\partial f_w^*}{\partial \rho_j}\right)^{\eta}, \tag{6.54}$$

where η is a numerical damping coefficient introduced by [197]. η is similar to the damping parameter used in the optimality Criteria method for density-based designs [19]. Damping of sensitivities prevent the instabilities in the structure design evolution process caused by elastoplastic effects.

To avoid mesh dependency and checkerboard patterns, we use the filtering scheme discussed in (5.24), (5.25), and (5.26) in Chapter 5. We rewrite these equations here as:

$$\alpha_j = \frac{\sum_{j'=1}^{N_j} g_{jj'}\ \alpha_j}{\sum_{j'=1}^{N_j} g_{jj'}}, \text{ and } g_{jj'} = \max\{0, r_{min} - \Delta(j, j')\}, \tag{6.55}$$

where N_j is the set of neighboring elements for which center-to-center distance $\Delta(j, j')$ to element j' is smaller than the filter radius r_{min}. To improve convergence, the sensitivity numbers are further averaged with the sensitivity numbers of the previous design iteration as:

$$\alpha_j^{i+1} \to (\alpha_j^{i+1} + \alpha_j^i)/2. \tag{6.56}$$

The optimization variables are updated with the help of two threshold parameters α_{del}^{th} and α_{add}^{th} for material removal and addition, respectively. Essentially, the solid elements are deleted when their sensitivity numbers are less than α_{del}^{th}, and void elements reappear when

their sensitivity numbers are greater than α_{add}^{th}. The scheme reads as:

$$\rho_j^{i+1} = \begin{cases} 0 & \text{if } \alpha_j \leq \alpha_{del}^{th} \text{ and } \rho_j^i = 1 \\ 1 & \text{if } \alpha_{add}^{th} < \alpha_j \text{ and } \rho_j^i = 0 \\ \rho_j^i & \text{otherwise} \end{cases} \tag{6.57}$$

Practically, a small value ρ_{min} is kept for void elements to avoid the singularity in the global stiffness matrix. The parameters α_{del}^{th} and α_{add}^{th} are determined by the following procedure first proposed by [98]:

1. First, assume $\alpha_{add}^{th} = \alpha_{del}^{th} = \alpha^{th}$. Then, α_{th} is determined such that the target material usage M^{i+1} is met at the current iteration.
2. Calculate the admissible ratio c_{ar} defined as the volume of the recovered elements divided by the total number of elements in the current design iteration. If $c_{ar} \leq c_{ar}^{max}$, the maximum admissible ratio, skip the next step. Otherwise, recompute α_{add}^{th} and α_{del}^{th} in the next step.
3. The number of recovered elements is controlled by c_{ar}^{max}. α_{add}^{th} is calculated using the sensitivity numbers of only void elements until $c_{ar} \approx c_{ar}^{max}$. α_{del}^{th} is calculated based on the sensitivity numbers of only solid elements until the target material usage M^{i+1} is met.

6.5.4 General algorithm

We consolidate our developments in an algorithmic framework summarized in Algorithm 4 that mainly consists of three blocks. The outer block represents the macroscale structure

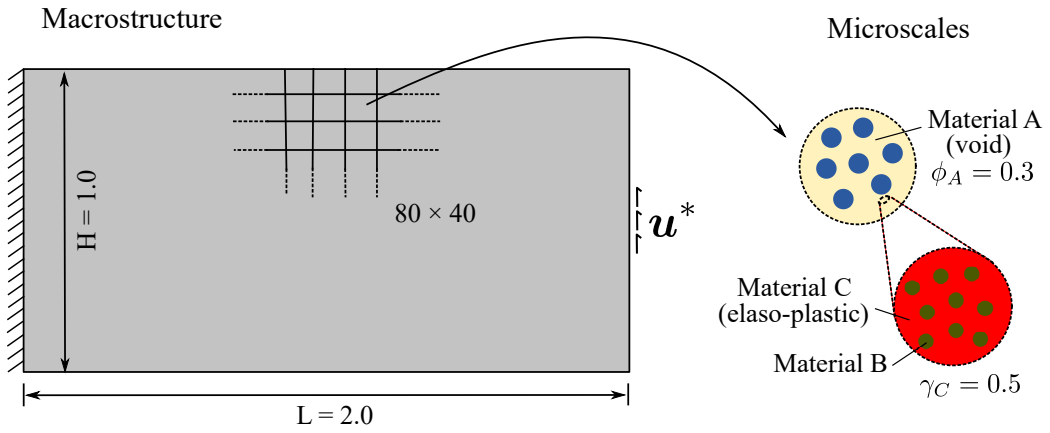

Fig. 6.3: *Cantilever benchmark problem with hierarchical material description.*

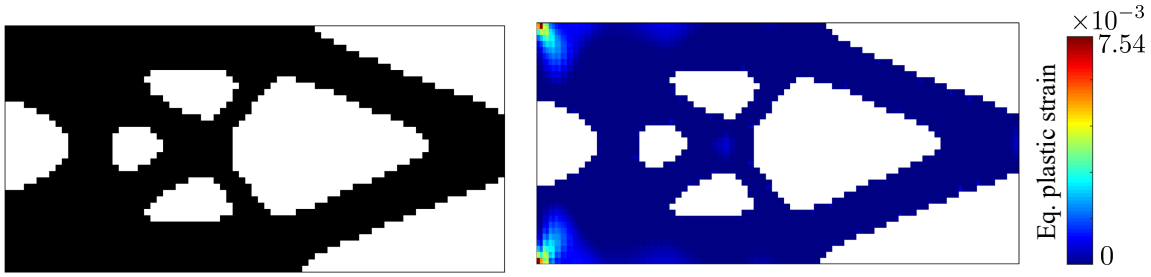

(a) Nonlinear topology design. **(b)** Equivalent plastic strain distribution.

Fig. 6.4: *Final design of the cantilever benchmark problem with equivalent plastic strain distribution for total prescribed displacement load of* $\boldsymbol{u}^* = 10.0$ *mm.*

optimization iterations using the BESO updating scheme. It stops when the macroscale density $\boldsymbol{\rho}$ reaches convergence. The middle block solves the initial boundary value problem for a given macroscale density distribution, following the incremental procedure detailed in Section 6.3.2. The Newton-Raphson solution scheme for each load increment iterates until the residual norm falls below the convergence criterion limit ϵ_{tol}. The inner layer solves the homogenized elastoplastic constitutive equations at each Gauss point with prescribed state variables at this iteration stage, using the closest point projection algorithm summarized in Section 6.5.2.

6.6 Numerical examples

In this section, we define a cantilever design problem with known microscale configuration at the material level as illustrated in Fig. 6.3. The length and height of the macrostructure domain are 2.0 m and 1.0 m, respectively. The left edge is fixed, and the central 10% of

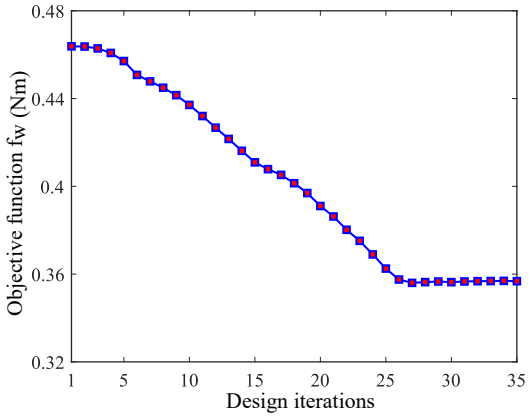

Fig. 6.5: *Convergence of objective function* f_w *with design iterations.*

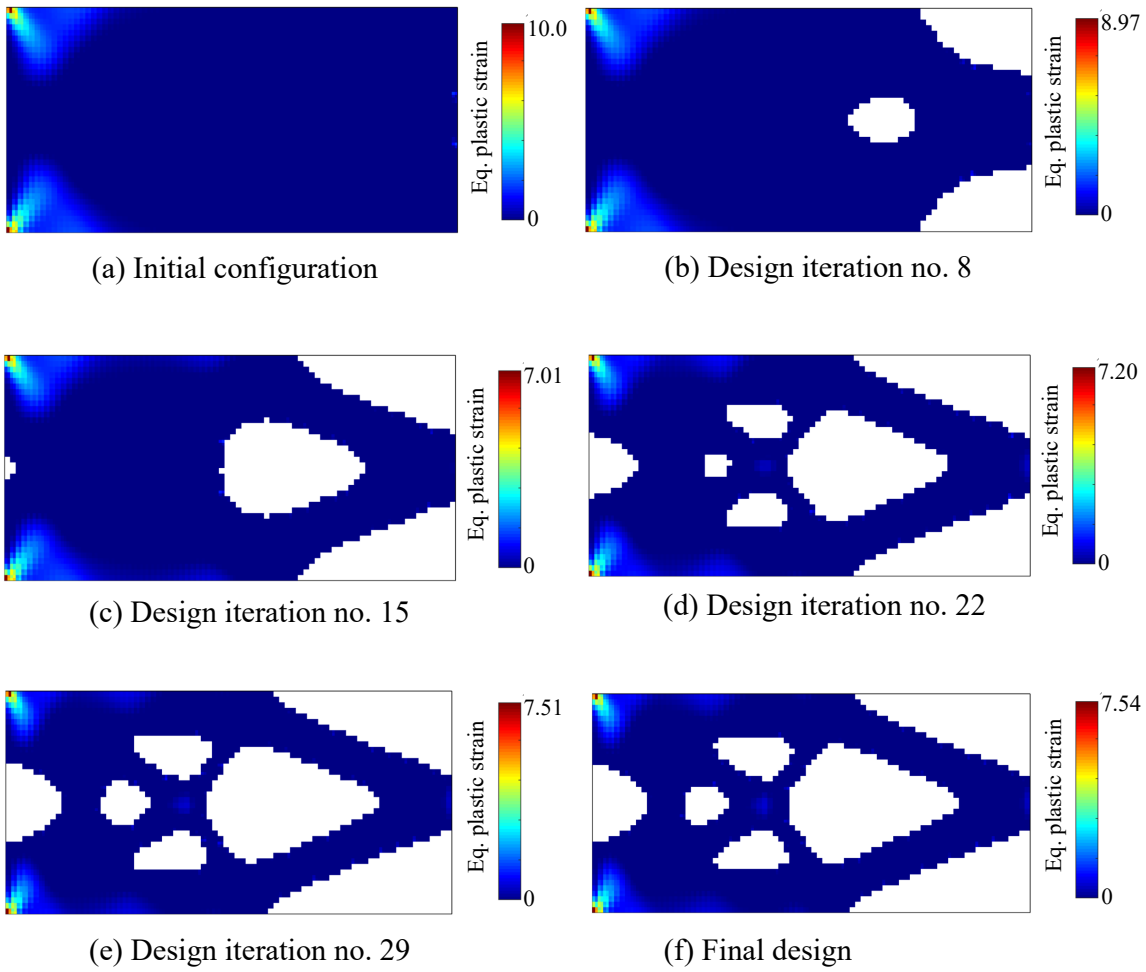

(a) Initial configuration (b) Design iteration no. 8

(c) Design iteration no. 15 (d) Design iteration no. 22

(e) Design iteration no. 29 (f) Final design

Fig. 6.6: *Evolution of topology with equivalent plastic strain (in $\times 10^{-3}$ units) distribution.*

the right edge is prescribed with a displacement loading of $\boldsymbol{u}^* = 10.0$ mm. We discretize the macroscale structure with a 80×40 mesh of 4-node quadrilateral elements, resulting in $l_e = 25$ mm element length. Plain strain conditions are used. The prescribed displacement load $\boldsymbol{u}^* = 10.0$ mm is reached in 8 loading time steps with constant load increments of $\Delta \bar{\boldsymbol{u}}_{\boldsymbol{q}}{}^E = 1.25$ mm. The residual convergence criterion ϵ_{tol} for the Newton iterations is taken as 10^{-5}.

We consider a hierarchical system that consists of Material A, B, and C at two different length scales (see Fig. 6.3). Their Young's moduli (in GPa) are $E_A = 0.0$, $E_B = 0.5$, and $E_C = 1.0$, respectively, and the Poisson's ratio of all constituents is 0.3. Material A forms the spherical inclusions, that is $\zeta_A = 1$, and its volume fraction $\phi_A = 0.3$. For Material C, the volume fraction at the lowermost scale $\gamma_C = 0.5$. The yield strength of Material C is 1 MPa. With this characterization, the homogenized stiffness and yield criterion can be estimated via (6.7) and (6.9).

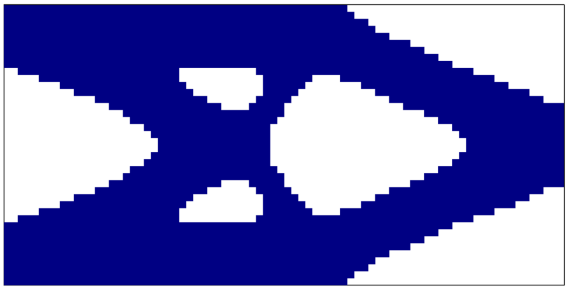

(a) Topology design for linear elastic case.

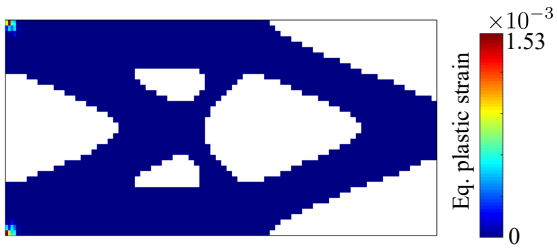

(b) Plastic design with $\boldsymbol{u}^* = 5.0$ mm.

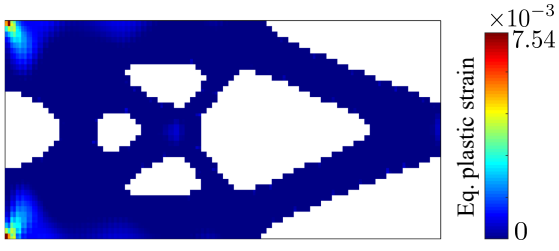

(c) Plastic design with $\boldsymbol{u}^* = 10.0$ mm.

Fig. 6.7: *Comparison of plastic designs corresponding to different load levels with linear elastic case. Equivalent plastic strain distributions are overlaid on the final design layouts for plastic designs.*

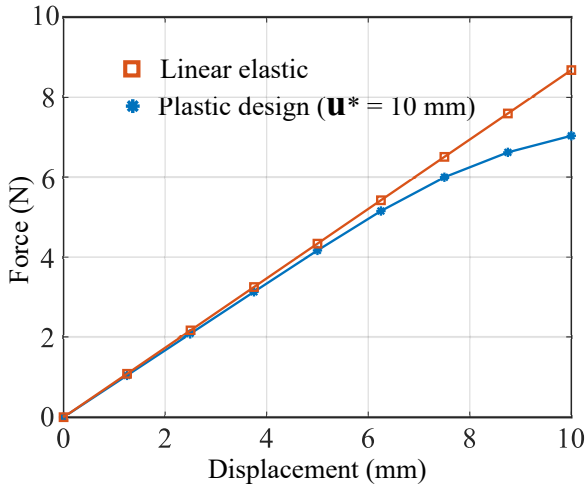

Fig. 6.8: *Comparison of load-displacement curves of final designs corresponding to the linear elastic and plastic designs.*

The total amount of material mass available is restricted to 60% of the maximum possible mass. The evolution rate c_{er} in the BESO algorithm is set to 0.02, and the maximum admissible ratio corresponding to the maximum percentage of recovered material in each design iteration is set to $c_{ar}^{max} = 0.01$. The numerical damping coefficient η in (6.54) to damp the sensitivity numbers is set to 0.5. Following [197], the filter radius r_{min} in the

proposed filtering scheme is reduced linearly from $r_{min} = 20l_e$ to $r_{min} = 4l_e$ with design iterations.

Figures 6.4, 6.5, and 6.6 illustrate the final design for the cantilever problem with the corresponding equivalent plastic strain distribution, a convergence plot for the BESO design iterations, and the design evolution process. As anticipated, the high plastic strains are concentrated at the clamped end, and the frontal end remains elastic. As a consequence, more material is pushed towards the clamped end. The objective value in Fig. 6.5 decreases nearly monotonically as the material is removed in the BESO iterations until the prescribed material usage is achieved. Figure 6.6 details this design evolution process with selected design iterations. It can be observed in these pictures that the design process attempts to attenuate the plastic front. The number of elements with plastic deformation and the magnitude of maximum equivalent plastic strain diminishes with design iterations compared to the initial distribution. In this process, the algorithm pushes more material towards the clamped region and tries to delay the yielding of the material in this region.

Figures 6.7 and 6.8 compare the final designs and the load-displacement curves for the linear elastic design (Material C is considered purely elastic) with the plastic design. We also plot the final structure design with a lower total prescribed displacement load of $\boldsymbol{u}^* = 5.0$ mm for understanding the role of plastic deformations on the final design. From a topological layout perceptive, apparent differences can be observed between the linear elastic and $\boldsymbol{u}^* =$ 10.0 mm loading case. The linear elastic design is a typical layout obtained through the maximization of end compliance type problems. While, the plastic design in Fig. 6.7c places more material towards the clamped region. Moreover, the final design with the prescribed displacement load of $\boldsymbol{u}^* = 5.0$ mm in Fig. 6.7b is closer to the linear elastic design of Fig. 6.7a. At this load level, a very small region experiences plastic deformations, as demonstrated by the equivalent plastic strain distribution plot in Fig. 6.7b. At higher load levels, the mechanical response of the elastoplastic multiphase hierarchical system deviates from the elastic case as shown via the load-displacement curves in Fig. 6.8. The plastic deformations start playing a crucial role and become very important for the optimized design at higher load levels.

Chapter 7

Concurrent material and structure optimization of elastoplastic multiphase hierarchical systems

In this chapter, we establish a novel thermodynamically consistent theoretical foundation of concurrent material and structure optimization for multiphase hierarchical systems with elastoplastic constituents at material scales. We split the formulation into two nested subproblems, one at the macroscale (structure) and the other at the microscale (material). In particular, we reformulate the material optimization problem based on the maximum plastic dissipation principle such that it assumes the format of an elastoplastic constitutive law and can be efficiently solved via modified return mapping algorithms. We integrate the continuum micromechanics based estimates of homogenized stiffness and yield criterion into the formulation that leads to further simplifications and computationally feasible treatment of the material optimization problem.

This chapter is organized as follows: Section 7.1 revisits the thermomechanical formulation of elastoplasticity, which forms the basis of our further developments in this chapter. In Section 7.2, we formulate the path-dependent stiffness maximization problem decomposing material and structure optimization problems for elastoplastic multiphase hierarchical systems. Section 7.3 describes the discrete form of the material and structure optimization subproblems in the finite element framework. In Section 7.4, we develop an algorithmic procedure for the material optimization problem based on the maximum plastic dissipation principle. In Section 7.5, we consolidate all our developments in an algorithmic framework. Finally, we verify our framework with benchmark problems in Section 7.6.

7.1 Thermomechanical formulation of elastoplasticity

We revisit the basic principles of elastoplasticity from a thermodynamics viewpoint. This energy formulation forms the basis of our concurrent structure and material optimization framework for elastoplastic multiphase hierarchical systems. First, we brief the energy form of the initial boundary value problem (IBVP) discussed in the previous chapter. This energy form is also known as the mechanical work identity. Later, we reflect on the principle of maximum plastic dissipation and derive the classical elastoplastic constitutive equations stated in Section 6.1. We follow the excellent presentation given in Simo & Hughes [164] throughout this chapter.

7.1.1 The mechanical work identity

With a specific choice of test function in the weak form (6.15) of the IBVP, we arrive at the basic result known as the mechanical work identity. For fixed otherwise arbitrary time $t \in [0, T]$, the velocity field $\boldsymbol{v}(\boldsymbol{x}, t)$ is an admissible test function, that is $\boldsymbol{v}(\cdot, t) \in \mathcal{V}$. Setting $\boldsymbol{\eta}(\cdot) = \boldsymbol{v}(\cdot, t)$ in (6.15) yields the following fundamental result:

$$\frac{d}{dt}T(\boldsymbol{v}) + P_{int}(\boldsymbol{\Sigma}, \boldsymbol{v}) = P_{ext}(\boldsymbol{v}) \;\; \forall t \in [0, T], \tag{7.1}$$

where

$$\begin{aligned} &\text{kinetic energy} \quad T(\boldsymbol{v}) = \frac{1}{2}\int_\Omega \rho|\boldsymbol{v}|^2 \, d\Omega, \\ &\text{stress power} \quad\;\; P_{int}(\boldsymbol{\Sigma}, \boldsymbol{v}) = \int_\Omega \boldsymbol{\Sigma} : \frac{\partial \boldsymbol{v}}{\partial \boldsymbol{x}} \, d\Omega \\ &\text{external power} \;\; P_{ext}(\boldsymbol{v}) = \int_\Omega \boldsymbol{b}\cdot\boldsymbol{v} \, d\Omega \; + \int_{\Gamma_N} \bar{\boldsymbol{\Sigma}}\cdot\boldsymbol{v} \, ds \; . \end{aligned} \tag{7.2}$$

All the notations are introduced in Chapter 6. This result is essentially the energy conservation principle or the first law of thermodynamics. We note that this form is independent of the specific nature of the local constitutive equation.

We introduce the notion of *internal potential energy* and *dissipation* within the context of elastoplasticity. We define the internal energy of the system as:

$$V_{int} = \int_\Omega \Psi(\boldsymbol{E}^e) \, d\Omega, \tag{7.3}$$

where $\Psi(\boldsymbol{E}^e)$ is the *Helmholtz free energy* density defined in terms of the stored elastic

energy function W and the contribution *hardening* effects. In this presentation, we consider the case of perfect plasticity, which implies that the contribution from hardening is zero and $\Psi = W$. For linear elasticity, W is a quadratic form in the elastic part of the strain tensor $\boldsymbol{E}^e$. With $\mathbb{C}$ as elasticity tensor and $\boldsymbol{E}^e = \boldsymbol{E} - \boldsymbol{E}^p$, the quadratic form reads as:

$$\Psi(\boldsymbol{E}^e) = W(\boldsymbol{E} - \boldsymbol{E}^p) = \frac{1}{2}(\boldsymbol{E} - \boldsymbol{E}^p) : \mathbb{C} : (\boldsymbol{E} - \boldsymbol{E}^p). \tag{7.4}$$

Next, we look at the difference between the stress power $P_{int}(\boldsymbol{\Sigma}, \boldsymbol{v})$ and the rate of change of the internal energy V_{int}, which we denote by $\mathscr{D}^{mech}$. The definition reads as:

$$\mathscr{D}^{mech} := P_{int}(\boldsymbol{\Sigma}, \boldsymbol{v}) - \frac{d}{dt}V_{int} \geq 0 \ \ \forall t \in [0, T]. \tag{7.5}$$

The above identity is nothing but the Clausius-Duhem version of the second law of thermodynamics assuming isothermal conditions [172, 178]. We identify $\mathscr{D}^{mech}$ as the instantaneous *mechanical dissipation* in domain Ω at time $t \in [0, T]$. This inequality is in agreement with the intuitive non-negative notion of the mechanical dissipation $\mathscr{D}^{mech}$.

Inserting the definitions of $P_{int}(\boldsymbol{\Sigma}, \boldsymbol{v})$ and V_{int}, we arrive at:

$$\begin{aligned} \mathscr{D}^{mech} &= \int_\Omega \left[\boldsymbol{\Sigma} : \dot{\boldsymbol{E}} - \frac{\partial \Psi(\boldsymbol{E}^e)}{\partial \boldsymbol{E}^e} : \dot{\boldsymbol{E}}^e \right] d\Omega \geq 0, \\ \mathscr{D}^{mech} &= \int_\Omega \left[\left(\boldsymbol{\Sigma} - \frac{\partial \Psi(\boldsymbol{E}^e)}{\partial \boldsymbol{E}^e} \right) : \dot{\boldsymbol{E}}^e + \boldsymbol{\Sigma} : \dot{\boldsymbol{E}}^p \right] d\Omega \geq 0, \end{aligned} \tag{7.6}$$

where $(\dot{\square})$ denotes the material time derivative of a quantity. The principle of thermodynamic determinism requires that (7.6) remains valid for any kinematic process defined by $\boldsymbol{E}^e$. This implies the following constitutive equations at each material point of domain Ω :

$$\boldsymbol{\Sigma} = \frac{\partial \Psi(\boldsymbol{E}^e)}{\partial \boldsymbol{E}^e} \ \text{ and } \ \mathscr{D}^p := \boldsymbol{\Sigma} : \dot{\boldsymbol{E}}^p \geq 0. \tag{7.7}$$

The first equation is an usual local elastic constitutive relation, where stress is defined as the derivative of the free energy function with respect to the elastic part of the strain tensor. Using the definition of $\Psi(\boldsymbol{E}^e)$ introduced in (7.4) for linear elasticity, we arrive at

$$\boldsymbol{\Sigma} = \mathbb{C} : (\boldsymbol{E} - \boldsymbol{E}^p). \tag{7.8}$$

The second equation in (7.7) defines the elastoplastic constitutive relation that we details in the following section.

7.1.2 The principle of maximum plastic dissipation

The principle of maximum plastic dissipation is a cornerstone to the mathematical formulation of plasticity. In this section, we derive the local constitutive equations for perfect plasticity summarized in Section 6.1.1 from the viewpoint of this principle. Later in the subsequent sections, we exploit this principle for devising the solution strategies for our optimization framework.

For given plastic strains $\boldsymbol{E}^p$, we define the plastic dissipation $\mathscr{D}^p$ at a material point for perfect plasticity as:

$$\mathscr{D}^p[\boldsymbol{\tau}; \dot{\boldsymbol{E}}^p] := \boldsymbol{\tau} : \dot{\boldsymbol{E}}^p, \tag{7.9}$$

where $\boldsymbol{\tau}$ lies in the set of admissible stresses. With the definition of yield criterion function $\mathfrak{F}(\boldsymbol{\tau})$, the admissible stresses lie in the closure of the elastic range defined as:

$$\mathbb{E}_\Sigma := \Big\{ \boldsymbol{\tau} \in \mathbb{S} \mid \mathfrak{F}(\boldsymbol{\tau}) \leq 0 \Big\}. \tag{7.10}$$

In the local form, the principle of maximum plastic dissipation states that, for given plastic strains $\boldsymbol{E}^p$, the plastic dissipation $\mathscr{D}^p$ attains its maximum for actual stress tensor $\boldsymbol{\Sigma}$ among all possible stresses $\boldsymbol{\tau} \in \mathbb{E}_\Sigma$. Mathematically, the principle reads as:

$$\mathscr{D}^p[\boldsymbol{\Sigma}; \dot{\boldsymbol{E}}^p] = \max_{\boldsymbol{\tau} \in \mathbb{E}_\Sigma} \Big\{ \mathscr{D}^p[\boldsymbol{\tau}; \dot{\boldsymbol{E}}^p] \Big\}. \tag{7.11}$$

The classical formulation of plasticity (associative flow rule, loading/unloading conditions) as briefed in Section 6.1.1 directly entails from this principle. To realize this insight, we employ the classical method of Lagrange multipliers for (7.11). We, first, transform the maximization principle into a minimization problem by changing the sign of the objective function. Next, we transform the constraint minimization problem into an unconstrained problem by introducing a Lagrange multiplier $\delta \geq 0$. The corresponding Lagrangian function reads as:

$$\mathscr{L}^p(\boldsymbol{\tau}, \delta; \dot{\boldsymbol{E}}^p) := -\boldsymbol{\tau} : \dot{\boldsymbol{E}}^p + \delta \, \mathfrak{F}(\boldsymbol{\tau}). \tag{7.12}$$

Solution to (7.11) is given by a point $(\boldsymbol{\Sigma}, \gamma)$ satisfying the Karush-Kuhn-Tucker optimality

conditions for the Lagrangian function (7.12). The conditions reads as:

$$\begin{aligned} &\left.\frac{\partial\, \mathcal{L}^p(\boldsymbol{\tau}, \dot{\delta}; \dot{\boldsymbol{E}}^p)}{\partial\, \boldsymbol{\tau}}\right|_{\boldsymbol{\Sigma},\gamma} = -\dot{\boldsymbol{E}}^p + \gamma \left.\frac{\partial \mathfrak{F}(\boldsymbol{\tau})}{\partial \boldsymbol{\tau}}\right|_{\boldsymbol{\Sigma}} = 0, \\ &\gamma \geq 0, \;\; \mathfrak{F}(\boldsymbol{\Sigma}) \leq 0, \;\; \text{and} \;\; \gamma\, \mathfrak{F}(\boldsymbol{\Sigma}) = 0. \end{aligned} \tag{7.13}$$

These statements are precisely the normality of flow rule and loading/unloading conditions stated in (6.4) to (6.6) in the previous chapter.

7.2 Concurrent material and structure optimization formulation

In this section, we formulate the path-dependent stiffness maximization problem for elasto-plastic multiphase hierarchical systems. The objective is to maximize the total mechanical work expended in the course of the deformation process. Later, we decompose the formulation into material and structure optimization sub-problems, exploiting the thermomechanical formulation of elastoplasticity summarized in the previous section. All the material and structure definitions are analogous to Chapter 5 and are summarized in Fig. 7.1.

7.2.1 Setting up the optimization problem with micromechanical design variables

As a simplification, we restricts ourselves to a quasi-static case with no inertial effects. With the definitions introduced in Section 7.1.1, the mechanical work identity (7.1) reduces to:

$$\mathcal{D}^{mech} + \frac{d}{dt} V_{int} = P_{ext}(\boldsymbol{v}). \tag{7.14}$$

The total mechanical work f_w in the considered time interval $[0, T]$ follows directly from (7.14) as:

$$f_w = \int_0^T \Big[\mathcal{D}^{mech} + \frac{d}{dt} V_{int}\Big] dt = \int_0^T P_{ext}(\boldsymbol{v}) dt \; . \tag{7.15}$$

Utilizing the definitions of $\mathcal{D}^{mech}$, V_{int} and $P_{ext}(\boldsymbol{v})$, we arrive at:

$$\begin{aligned} f_w &= \int_0^T \Big[\int_\Omega \Big\{ \mathcal{D}^p[\boldsymbol{\Sigma}; \dot{\boldsymbol{E}}^p] + \dot{\Psi}(\boldsymbol{E}^e) \Big\} d\Omega \Big] \, dt \\ &= \int_0^T \Big[\int_\Omega \boldsymbol{b}(\boldsymbol{x}, t) \cdot \boldsymbol{v} \, d\Omega \, + \int_{\Gamma_N} \bar{\boldsymbol{\Sigma}}(t) \cdot \boldsymbol{v} \, ds \Big] dt. \end{aligned} \tag{7.16}$$

We note that the (pseudo-)time t should be interpreted as a variable representing the loading history.

Next, we introduce the definition of macroscale density $\rho(\boldsymbol{x})$ and microstructural heterogeneities $\boldsymbol{m}(\boldsymbol{x}, t)$ constituting the design vector $[\rho(\boldsymbol{x}), \boldsymbol{m}(\boldsymbol{x}, t)]^T$. We assume that the macroscale density $\rho(\boldsymbol{x})$ is fixed with respect to time. However, $\boldsymbol{m}(\boldsymbol{x}, t)$ is a function of loading history representing a local adaption of microstructure with (pseudo-)time. The set $\boldsymbol{m}(\boldsymbol{x}, t)$ contains the geometric and mechanical characterization of phases that span multiple well-separated microscales, consisting of volume fraction, material properties, shape, and orientation of the different phases in the hierarchical system. The homogenized material constitutive relations $\mathcal{D}^p$ and Ψ in (7.16) depend on the macroscale density $\rho(\boldsymbol{x})$ and the microstructural characterization field $\boldsymbol{m}(\boldsymbol{x}, t)$.

Augmenting the material constitutive definitions $\mathcal{D}^p$ and Ψ with $\rho(\boldsymbol{x})$ and $\boldsymbol{m}(\boldsymbol{x}, t)$, we write the optimization problem from (7.16) as:

$$\begin{aligned} \max_{\substack{\rho(\boldsymbol{x}) \in \mathcal{A}_{ad} \\ \boldsymbol{m}(\boldsymbol{x},t) \in E_{ad}}} f_w &= \max_{\substack{\rho(\boldsymbol{x}) \in \mathcal{A}_{ad} \\ \boldsymbol{m}(\boldsymbol{x},t) \in E_{ad}}} \int_0^T \int_\Omega \Big\{ \mathcal{D}^p[\rho(\boldsymbol{x}), \boldsymbol{m}(\boldsymbol{x}, t), \boldsymbol{\Sigma}; \dot{\boldsymbol{E}}^p] + \dot{\Psi}[\rho(\boldsymbol{x}), \boldsymbol{m}(\boldsymbol{x}, t); \boldsymbol{E}^e] \Big\} d\Omega \, dt \\ &= \max_{\substack{\rho(\boldsymbol{x}) \in \mathcal{A}_{ad} \\ \boldsymbol{m}(\boldsymbol{x},t) \in E_{ad}}} \int_0^T \Big[\int_\Omega \boldsymbol{b}(\boldsymbol{x}, t) \cdot \boldsymbol{v} \, d\Omega \, + \int_{\Gamma_N} \bar{\boldsymbol{\Sigma}}(t) \cdot \boldsymbol{v} \, ds \Big] dt \, . \end{aligned} \tag{7.17}$$

$\mathcal{A}_{ad}$ and E_{ad} define the set of admissible design variables at the macro and microscales, respectively, with possible design constraints. The second part of this equation is the continuous version of the objective function (6.30) defined in the previous chapter. Here, the velocity field $\boldsymbol{v}(\boldsymbol{x}, t)$ and, thus, the displacement field $\bar{\boldsymbol{u}}(\boldsymbol{x}, t)$ implicitly depend on $\rho(\boldsymbol{x})$ and $\boldsymbol{m}(\boldsymbol{x}, t)$. With known macroscale strains $\boldsymbol{E}$ and $\boldsymbol{E}^p$ from the solution of the global equilibrium equations, the first part of (7.17) is an explicit expression in terms of design variables $\rho(\boldsymbol{x})$ and $\boldsymbol{m}(\boldsymbol{x}, t)$. We focus on the first part for the mathematical analysis and development of our optimization formulation.

The definitions of $\mathcal{A}_{ad}$ and E_{ad} are identical to those defined in Chapter 5. The admissible set $\mathcal{A}_{ad}$ seeks a limit on the total material mass M_{req} available for design. Mathematically,

it reads as:

$$\mathcal{A}_{ad} = \Big\{\rho(\boldsymbol{x}) \mid \rho(\boldsymbol{x}) = [\rho_{min}, \rho_{max}],\ \int_{\Omega} \rho(\boldsymbol{x}) d\Omega \leq M_{req},\ \boldsymbol{x} \in \Omega\Big\}, \tag{7.18}$$

where ρ_{min} and ρ_{max} are the bounds on the macroscale material density ρ. The definition of the admissible set E_{ad} is illustrated via the multiscale configuration shown in Fig. 7.1, which identical to the one shown in Fig. 5.1. However, Material C is considered as perfectly elastoplastic. In addition, all the microscale characterization variables such as the volume fraction of Material A, the orientation of Material A, the elongation of Material A, and the volume fraction of Material C are a function of time t too. The microstructure characterization field set $\boldsymbol{m}(\boldsymbol{x}, t)$ is $\{\phi_A(\boldsymbol{x}, t), \theta_A(\boldsymbol{x}, t), \zeta_A(\boldsymbol{x}, t), \gamma_C(\boldsymbol{x}, t)\}$. We write the admissible set E_{ad} as:

$$\begin{aligned} E_{ad} = \Big\{ & \boldsymbol{m}(\boldsymbol{x}, t) \mid \rho(\boldsymbol{x}) = \rho_A \phi_A(\boldsymbol{x}, t) + \rho_M(\boldsymbol{x}, t)(1 - \phi_A(\boldsymbol{x}, t)), \\ & 0 < \phi_A^{min} < \phi_A(\boldsymbol{x}, t) < \phi_A^{max} \leq 1, \\ & \rho_M(\boldsymbol{x}, t) = \rho_B(1 - \boldsymbol{\gamma}_C(\boldsymbol{x}, t)) + \rho_C\ \gamma_C(\boldsymbol{x}, t), \\ & 0 < \gamma_C^{min} < \gamma_C(\boldsymbol{x}, t) < \gamma_C^{max} \leq 1, \\ & \theta_A(\boldsymbol{x}, t) \in [-\pi/2, \pi/2], \\ & \boldsymbol{\zeta}_A(\boldsymbol{x}, t) \in [1, \zeta^{max}],\ \forall (\boldsymbol{x}, t) \in \Omega \times [0, T]\Big\}. \end{aligned} \tag{7.19}$$

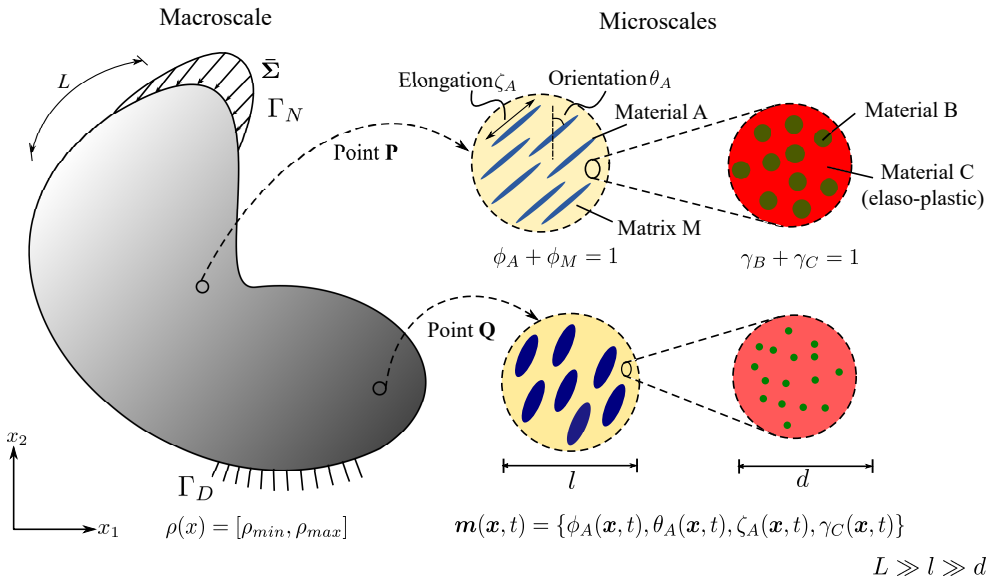

Fig. 7.1: *Sketch of a representative problem for material and structure optimization with elastoplastic multiphase hierarchical system.*

Please refer Section 5.1.1 for the details of notations and relations in (7.19).

7.2.2 Decomposition into material and structure optimization problems

We rewrite the statement (7.17) as:

$$\max_{\rho(\boldsymbol{x})\in\mathcal{A}_{ad}} \max_{\boldsymbol{m}(\boldsymbol{x},t)\in E_{ad}} \int_0^T \Big[\int_\Omega \Big\{ \mathcal{D}^p[\rho(\boldsymbol{x}), \boldsymbol{m}(\boldsymbol{x},t), \boldsymbol{\Sigma}; \dot{\boldsymbol{E}}^p] + \dot{\Psi}[\rho(\boldsymbol{x}), \boldsymbol{m}(\boldsymbol{x},t); \boldsymbol{E}^e] \Big\} d\Omega \Big] \, dt. \tag{7.20}$$

We note that, for a given macroscale density field $\boldsymbol{\rho}(\boldsymbol{x})$, the admissible set E_{ad} is defined pointwise for $(\boldsymbol{x}, t) \in \Omega \times [0, T]$. Thus, we rewrite (7.20) as:

$$\max_{\rho(\boldsymbol{x})\in\mathcal{A}_{ad}} \int_0^T \Big[\int_\Omega \max_{\boldsymbol{m}(\boldsymbol{x},t)\in E_{ad}(\rho)} \Big\{ \mathcal{D}^p[\rho(\boldsymbol{x}), \boldsymbol{m}(\boldsymbol{x},t), \boldsymbol{\Sigma}; \dot{\boldsymbol{E}}^p] + \dot{\Psi}[\rho(\boldsymbol{x}), \boldsymbol{m}(\boldsymbol{x},t); \boldsymbol{E}^e] \Big\} d\Omega \Big] \, dt. \tag{7.21}$$

This statement allows us to decompose the optimization problem (7.17) into two sub-problems. The outer "structure" optimization problem is:

$$\max_{\rho(\boldsymbol{x})\in\mathcal{A}_{ad}} \int_0^T \Big[\int_\Omega \Big\{ \mathcal{D}^p[\rho(\boldsymbol{x}), \bar{\boldsymbol{m}}(\boldsymbol{x},t), \boldsymbol{\Sigma}; \dot{\boldsymbol{E}}^p] + \dot{\Psi}[\rho(\boldsymbol{x}), \bar{\boldsymbol{m}}(\boldsymbol{x},t); \boldsymbol{E}^e] \Big\} d\Omega \Big] \, dt, \tag{7.22}$$

where $\bar{\boldsymbol{m}}(\boldsymbol{x}, t)$ optimizes the following sub-problem or "material" optimization problem:

$$\max_{\boldsymbol{m}(\boldsymbol{x},t)\in E_{ad}(\rho)} \Big\{ \mathcal{D}^p[\boldsymbol{m}(\boldsymbol{x},t), \boldsymbol{\Sigma}; \dot{\boldsymbol{E}}^p] + \dot{\Psi}[\boldsymbol{m}(\boldsymbol{x},t); \boldsymbol{E}^e] \Big\} \;\; \forall (\boldsymbol{x}, t) \in \Omega \times [0, T]. \tag{7.23}$$

A combination of (7.22) and (7.23) constitutes the concurrent material and structure optimization formulation.

We note that the macroscale strains $\boldsymbol{E}$ and $\boldsymbol{E}^p$, and the density distribution $\rho(\boldsymbol{x})$ are given for this material optimization problem. $\rho(\boldsymbol{x})$ dictate the construction of admissible space E_{ad} for the problem, and, therefore, we take it out from $\mathcal{D}^p$ and Ψ definitions in (7.23) and consider it into E_{ad}. We modify the material constitutive equations (7.4), (7.8), (7.10), and (7.11) including the definitions of $\rho(\boldsymbol{x})$ and $\boldsymbol{m}(\boldsymbol{x}, t)$. With $\boldsymbol{m}(\boldsymbol{x}, t) \in E_{ad}(\rho)$, the free energy density relation (7.4) and the stress-strain relation (7.8) for linearized elasticity reads as:

$$\Psi[\boldsymbol{m}(\boldsymbol{x},t); \boldsymbol{E}^e] = \frac{1}{2}(\boldsymbol{E} - \boldsymbol{E}^p) : \mathbb{C}(\boldsymbol{m}(\boldsymbol{x},t)) : (\boldsymbol{E} - \boldsymbol{E}^p), \tag{7.24}$$

and

$$\boldsymbol{\Sigma} = \mathbb{C}(\boldsymbol{m}(\boldsymbol{x},t)) : (\boldsymbol{E} - \boldsymbol{E}^p). \tag{7.25}$$

Similarly, the elastoplastic material constitutive equations through (7.10) and (7.11) are augmented to include $\rho(\boldsymbol{x})$ and $\boldsymbol{m}(\boldsymbol{x},t)$ as:

$$\mathscr{D}^p[\boldsymbol{m}(\boldsymbol{x},t), \boldsymbol{\Sigma}; \dot{\boldsymbol{E}}^p] = \max_{\boldsymbol{\tau}\in\mathbb{E}_\Sigma} \left\{ \boldsymbol{\tau} : \dot{\boldsymbol{E}}^p \right\}, \tag{7.26}$$

and

$$\mathbb{E}_\Sigma := \left\{ \boldsymbol{\tau} \in \mathbb{S} \mid \boldsymbol{m}(\boldsymbol{x},t) \in E_{ad}(\rho),\ \mathfrak{F}(\boldsymbol{\tau}, \boldsymbol{m}(\boldsymbol{x},t)) \leq 0 \right\}. \tag{7.27}$$

Micromechanics principles outlined in Chapter 2 estimate the homogenized stiffness $\mathbb{C}(\boldsymbol{m}(\boldsymbol{x},t))$ and the homogenized yield criterion $\mathfrak{F}(\boldsymbol{\tau}, \boldsymbol{m}(\boldsymbol{x},t))$ as a function of microstructural variables.

One can interpret the material optimization problem as a reformulated elastoplastic constitutive law that provides the locally optimal material response against the external loading history. Therefore, the microstructure variable $\boldsymbol{m}(\boldsymbol{x},t)$ can be thought of as an "internal state variable" analogous to any path-dependent history variable encountered in the elastoplasticity formulations. This notion of $\boldsymbol{m}(\boldsymbol{x},t)$ is also consistent with the structure of the modified relations (7.26) and (7.27). This interpretation will be used later in devising the optimization algorithm for the material optimization problem.

7.3 Finite element discretization

In this section, we focus on the finite element discretization of the concurrent material and structure optimization formulation. In the previous chapter, we detailed the incremental solution procedure using the finite element method for the elastoplastic initial boundary value problem (IBVP). We exploit all the developments of the previous chapter for the implementation of our optimization formulation. We again emphasize that we use vector-matrix notation to represent the introduced quantities in the macroscale governing equations, consistent with standard finite element literature with the same symbols for the respective vector-matrix notation.

7.3.1 Model definitions in discrete setting

Following Section 6.3, we partition the considered time interval $[0, T]$ into n_{load} partitions and split the domain Ω into N_e finite elements as:

$$[0,T] = \bigcup_{n=0}^{n_{load}-1} [t_n, t_{n+1}] \;\text{ and }\; \Omega = \bigcup_{j=1}^{N_e} \Omega_j, \tag{7.28}$$

where each element has N_{gp} Gauss quadrature points. In this discrete setting, the design variables $[\rho(\boldsymbol{x}), \boldsymbol{m}(\boldsymbol{x}, t)]^T$ for our example material in Fig. 7.1 can now be defined elementwise as:

$$\begin{aligned}
\boldsymbol{\rho} &= [\rho_1, \rho_2, \rho_3, ..., \rho_{N_e}], \\
\boldsymbol{m} &= [\boldsymbol{m}_0, \boldsymbol{m}_1, ..., \boldsymbol{m}_{n+1}, ..\boldsymbol{m}_{n_{load}-1}], \\
\boldsymbol{m}_{n+1} &= [(m_{n+1}^{1,1}, .., m_{n+1}^{N_{gp},1}), ..., (m_{n+1}^{1,N_e}, .., m_{n+1}^{N_{gp},N_e})], \\
m_{n+1}^{x,j} &= [\phi_{A,n+1}^{x,j}, \theta_{A,n+1}^{x,j}, \zeta_{A,n+1}^{x,j}, \gamma_{C,n+1}^{x,j}], \quad x = 1, ..., N_{gp},\ j = 1, ..., N_e.
\end{aligned} \tag{7.29}$$

The macroscale density ρ_j is assumed to be constant in each element and load increment, with j being the element index. The microstructure design variable set $\boldsymbol{m}$ is defined at each (macroscale) Gauss point and time increment. The microstructure configuration $m_{n+1}^{x,j}$ consists of volume fraction $\phi_{A,n+1}^{x,j}$, orientation $\theta_{A,n+1}^{x,j}$ elongation $\zeta_{A,n+1}^{x,j}$ for Material A, and volume fraction $\gamma_{C,n+1}^{x,j}$ of Material C. Subscript index $(n+1)$ denotes the time increment, and superscript index (x, j) denote the Gauss point index x in element j.

With these definitions in hand, the discrete version of optimization problem (7.17) follows as:

$$\begin{aligned}
\max_{\boldsymbol{\rho},\boldsymbol{m}} f_w = \max_{\boldsymbol{\rho},\boldsymbol{m}} \sum_{n=0}^{n_{load}-1} \sum_{j=1}^{N_e} \Bigg[\sum_{x=1}^{N_{gp}} \Big\{ \boldsymbol{\Sigma}_{n+1}^T (\boldsymbol{E}_{n+1}^p - \boldsymbol{E}_n^p) + \Psi(\boldsymbol{E}_{n+1} - \boldsymbol{E}_{n+1}^p) \\
- \Psi(\boldsymbol{E}_n - \boldsymbol{E}_n^p) \Big\} w_x \Bigg] \qquad (7.30) \\
= \max_{\boldsymbol{\rho},\boldsymbol{m}} \frac{1}{2} \sum_{n=0}^{n_{load}-1} (\boldsymbol{f}_{n+1}^{ext} + \boldsymbol{f}_n^{ext})^T \, \Delta \bar{\boldsymbol{u}}_{n+1}.
\end{aligned}$$

The quantities in (7.30) require further explanation: $\boldsymbol{\Sigma}_{n+1}$, $\boldsymbol{E}_{n+1}$, and $\boldsymbol{E}_{n+1}^p$ are the macroscale stress, macroscale strain, and the plastic part of macroscale strain at at $(n+1)_{th}$ load increment. Similarly, $\boldsymbol{f}_{n+1}^{ext}$ is the external force vector, and $\bar{\boldsymbol{u}}_{n+1}$ is the converged macroscale displacement solution vector at $(n+1)^{th}$ load increment. w_x contains the Gauss

point weight and the determinant of the Jacobian matrix for element j. All the quantities at n^{th} load increment are known.

With the equivalent discretized definitions of $\mathcal{A}_{ad}$ and E_{ad} from (7.18) and (7.19), the optimization statement reads as:

$$
\begin{aligned}
\max_{\boldsymbol{\rho},\boldsymbol{m}} :\ & f_w(\boldsymbol{\rho},\boldsymbol{m}) \\
\text{s.t.} :\ & \bar{\boldsymbol{r}}_{n+1}(\boldsymbol{\rho},\boldsymbol{m}_{n+1},\bar{\boldsymbol{u}}_{n+1}) = 0 \ \ \forall n = 0,1,...,n_{load}-1 \\
& M(\boldsymbol{\rho}) = \sum_{j=1}^{N_e} \rho_j |\Omega_j| = M_{req} = M_{frac} \times \rho_C \times |\Omega| \\
& \rho_j \in [\rho_{min},\rho_{max}],\ \forall j = 1,2,...,N_e \\
& \rho_j = \rho_A \phi_{A,n+1}^{x,j} + \rho_M (1-\phi_{A,n+1}^{x,j});\ \ \rho_M = \rho_B (1-\gamma_{C,n+1}^{x,j}) + \rho_C \gamma_{C,n+1}^{x,j} \\
& \phi_{A,n+1}^{x,j} \in [\phi_A^{min},\phi_A^{max}];\ \ \theta_{A,n+1}^{x,j} \in [-\pi/2,\pi/2];\ \zeta_{A,n+1}^{x,j} \in [1,\zeta^{max}] \\
& \gamma_{C,n+1}^{x,j} \in [\gamma_C^{min},\gamma_C^{max}] \ \ \forall x = 1,...,N_{gp},\ j = 1,...,N_e.
\end{aligned}
\tag{7.31}
$$

.

Here, $\bar{\boldsymbol{r}}_{n+1}$ is the force residual at the macroscale, which we define later. ρ_j and $|\Omega_j|$ are the density and volume of element j. The total available mass M_{req} can be expressed in terms of fraction M_{frac} with respect to the mass when the densest material occupies the complete domain. The fourth, fifth, and sixth lines in (7.31) directly result from $\boldsymbol{m}_{n+1}$ and E_{ad} definitions. One can observe a large number of macro and microscale design variables with humongous nonlinear equality-inequality constraints in (7.31). This inconvenient definition of constraints makes the sensitivity analysis computationally cumbersome that precludes leveraging the established gradient-based optimization algorithms. Therefore, the material-structure decomposition of this problem is an essential step to make this formulation computationally tractable.

7.3.2 Discrete form of the material and structure optimization subproblems

Denoting $\bar{\boldsymbol{m}}$ as optimized microstructure configuration set, we write the discrete version of structure optimization problem (7.22) as:

$$\begin{aligned}
\max_{\boldsymbol{\rho}}: \; & f_w = \frac{1}{2} \sum_{n=0}^{n_{load}-1} (\boldsymbol{f}_{n+1}^{ext} + \boldsymbol{f}_{n}^{ext})^T \, \Delta \bar{\boldsymbol{u}}_{n+1} \\
\text{s.t.}: \; & \bar{\boldsymbol{r}}_{n+1}(\boldsymbol{\rho}, \bar{\boldsymbol{m}}_{n+1}, \bar{\boldsymbol{u}}_{n+1}) = 0 \;\; \forall n = 0, 1, ..., n_{load} - 1 \\
& M(\boldsymbol{\rho}) = \sum_{j=1}^{N_e} \rho_j |\Omega_j| = M_{req} = M_{frac} \times \rho_C \times |\Omega|; \;\; \forall n = 1, 2, ..., n_{load} - 1 \\
& \rho_j \in [\rho_{min}, \rho_{max}], \; \forall j = 1, 2, ..., N_e.
\end{aligned} \tag{7.32}$$

The force residual $\bar{\boldsymbol{r}}_{n+1}(\boldsymbol{\rho}, \bar{\boldsymbol{m}}_{n+1}, \bar{\boldsymbol{u}}_{n+1})$ at $(n+1)^{th}$ load increment is defined as:

$$\bar{\boldsymbol{r}}_{n+1}(\boldsymbol{\rho}, \bar{\boldsymbol{m}}_{n+1}, \bar{\boldsymbol{u}}_{n+1}) = \boldsymbol{f}_{n+1}^{ext} - \sum_{j=1}^{N_e} \left[\sum_{x=1}^{N_{gp}} \boldsymbol{B}^T \boldsymbol{\Sigma}_{n+1} \, w_x \right], \tag{7.33}$$

where $\boldsymbol{B}$ is the strain-displacement matrix and $\boldsymbol{\Sigma}_{n+1}$ is the macroscale stress at a Gauss point $\boldsymbol{x}$ inside element j.

Following (7.25) and (7.27), $\boldsymbol{\Sigma}_{n+1}$ can be written in terms of microstructure configuration $\bar{m}_{n+1}^{x,j}$ that solves the material optimization problem (detailed later in (7.36)) as:

$$\boldsymbol{\Sigma}_{n+1} = \mathbb{C}(\bar{m}_{n+1}^{x,j})(\boldsymbol{E}_{n+1} - \boldsymbol{E}_{n+1}^{p}), \tag{7.34}$$

where $\boldsymbol{\Sigma}_{n+1}$ must lie in the following stress admissible set:

$$\mathbb{E}_{\Sigma_{n+1}} := \Big\{ \boldsymbol{\tau} \in \mathbb{S} \mid \bar{m}_{n+1}^{x,j} \in E_{ad}(\rho_j), \; \mathfrak{F}(\boldsymbol{\tau}, \bar{m}_{n+1}^{x,j}) \leq 0 \Big\}. \tag{7.35}$$

We note that the macroscale strain $\boldsymbol{E}_{n+1}$ at each Gauss point can be queried using the displacement solution $\bar{\boldsymbol{u}}_{n+1}$. Equation (7.33) is constitutively nonlinear and solved through the Newton-Raphson iterative solution procedure summarized in Section 6.5.1. We observe that the microstructure design variables $\boldsymbol{m}$ are implicitly accounted for by $\bar{\boldsymbol{r}}_1, \bar{\boldsymbol{r}}_2, ..., \bar{\boldsymbol{r}}_{n+1}$.

For a given material distribution $\boldsymbol{\rho}$ and macroscale strain $\boldsymbol{E}_{n+1}$ the material optimization problem for Gauss point $\boldsymbol{x}$ inside element j for $(n+1)^{th}$ load increment follows from (7.23)

as:

$$\bar{m}_{n+1}^{x,j} = \underset{m_{n+1}^{x,j}(\rho_j)}{\arg\max} \Big\{ \boldsymbol{\Sigma}_{n+1} : (\boldsymbol{E}_{n+1}^p - \boldsymbol{E}_n^p) + \Psi(\boldsymbol{E}_{n+1} - \boldsymbol{E}_{n+1}^p) - \Psi(\boldsymbol{E}_n - \boldsymbol{E}_n^p) \Big\}$$

$$\begin{aligned}
\text{s.t. : } & \boldsymbol{\Sigma}_{n+1} = \mathbb{C}(m_{n+1}^{x,j}) : (\boldsymbol{E}_{n+1} - \boldsymbol{E}_{n+1}^p) \\
& \mathfrak{F}(\boldsymbol{\Sigma}_{n+1}, m_{n+1}^{x,j}) \leq 0 \\
& \Psi(\boldsymbol{E}_{n+1} - \boldsymbol{E}_{n+1}^p) = \frac{1}{2}(\boldsymbol{E}_{n+1} - \boldsymbol{E}_{n+1}^p) : \mathbb{C}(m_{n+1}^{x,j}) : (\boldsymbol{E}_{n+1} - \boldsymbol{E}_{n+1}^p) \\
& \rho_j = \rho_A \phi_{A,n+1}^{x,j} + \rho_M (1 - \phi_{A,n+1}^{x,j});\ \rho_M = \rho_B (1 - \gamma_{C,n+1}^{x,j}) + \rho_C \gamma_{C,n+1}^{x,j} \\
& \phi_{A,n+1}^{x,j} \in [\phi_A^{min}, \phi_A^{max}];\ \ \theta_{A,n+1}^{x,j} \in [-\pi/2, \pi/2];\ \zeta_{A,n+1}^{x,j} \in [1, \zeta^{max}] \\
& \gamma_{C,n+1}^{x,j} \in [\gamma_C^{min}, \gamma_C^{max}] \ . \\
& .
\end{aligned} \tag{7.36}$$

The first part of this equation directly comes from the incremental form of the principle of maximum plastic dissipation principle outlined in Section 7.1.2. Similarly, the second part is the incremental form of the Helmholtz free energy rate defined in (7.23). We note that all the quantities at the n^{th} load increment are known, and, therefore, $\Psi(\boldsymbol{E}_n - \boldsymbol{E}_n^p)$ does not play any role in this maximization problem. The first and second line in the constraint definition is the result of microscale design variable $m_{n+1}^{x,j}$ dependent stress-strain relation and yield criterion as described in (7.34). The third line is the definition of the Helmholtz free energy for the perfect plasticity with a quadratic form of stored elastic energy function coming from (7.24). The rest of the constraints are straightforward from E_{ad} definition, also described in (7.31). We again emphasize that we write this problem in tensor notation, given its direct relation with continuum micromechanics based material models outlined in Chapter 2.

7.4 Treatment of the material optimization problem

The crucial step in this formulation is the solution to the material optimization problem. In contrast to the strain energy maximization problem in Chapter 5, solution to (7.36) is not straightforward. The material optimization problem (7.36) can be interpreted as a constitutive law at each material point that provides locally optimal mechanical response to the loading history. Intuitively, it maximizes the area under the homogenized elastoplastic stress-strain curve for each material point. Multiple stress-strain curves are available at each loading increment, defined by the the microscale design variable $m_{n+1}^{x,j}$. This inter-

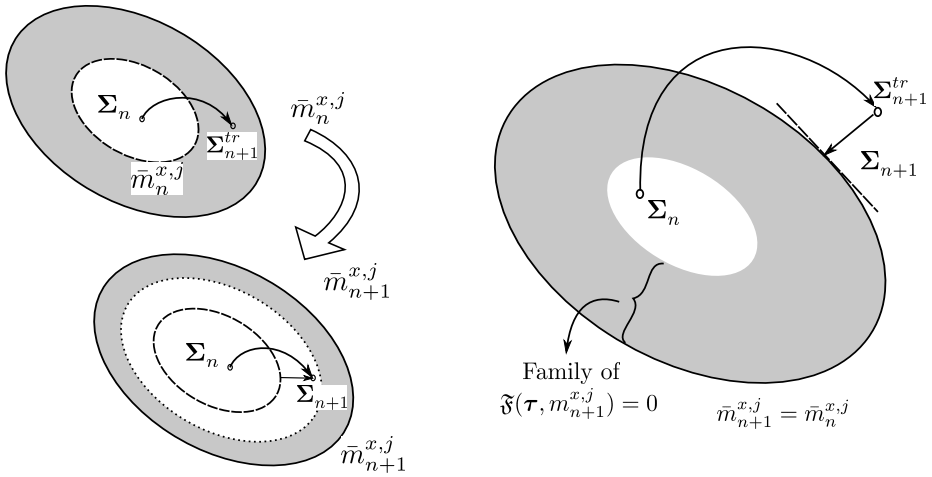

Fig. 7.2: *Geometric illustration of solution strategy of the material optimization problem.*

dependency couples the history variable $\boldsymbol{E}^p_{n+1}$ with $m^{x,j}_{n+1}$ for this maximization problem.

A few ideas can be explored in devising a solution strategy for this slave problem. One idea is to postulate a relevant potential that treats the variable $m^{x,j}_{n+1}$ as a hardening-like state variable. It will result in a modified flow rule (potentially non-associative) that contains the microscale design variable $m^{x,j}_{n+1}$ information as elastic compliance type constitutive modulus [108]. The other idea is to explore the outer approximation method for nonlinear programming problems [77]. From the formulation viewpoint, these approaches are general and without any assumptions on the microscale material behavior. However, from the implementation perspective, we can not leverage the well-established structure of the return-mapping type algorithm outlined in Section 6.5.2 for this reformulated elasto-plastic constitutive law.

Within the context of our application, we focus on the homogenized elastoplastic constitutive relations, derived in Chapter 2 and reiterates in Section 6.1 in the previous chapter. This special case leads to significant simplifications to this problem, which we define later in this section. First, we employ the maximum plastic dissipation principle for insights into the material optimization problem. Following the insights, we devise an algorithmic procedure combining the closest point projection algorithm (see Section 6.5.2) to handle the material optimization problem. Finally, we restraint ourselves to the continuum micromechanics based homogenized elastoplastic constitutive relations and outline further simplifications.

7.4.1 The principle of maximum plastic dissipation perspective

For devising a solution strategy for the material optimization problem, we return to our discussion on the principle of maximum plastic dissipation in Section 7.1.2. As discussed, the first part of the material optimization problem (7.36) is the incremental statement of the maximum plastic dissipation principle. We focus on this part and rewrite it using (7.11) as:

$$\hat{m}_{n+1}^{x,j} = \underset{m_{n+1}^{x,j} \in E_{ad}(\rho_j)}{\arg\max} \Big\{ \max_{\boldsymbol{\tau} \in \mathbb{E}_{\Sigma_{n+1}}} \boldsymbol{\tau} : (\boldsymbol{E}_{n+1}^{p} - \boldsymbol{E}_{n}^{p}) \Big\}, \text{ and} \tag{7.37a}$$

$$\mathbb{E}_{\Sigma_{n+1}} := \Big\{ \boldsymbol{\tau} \in \mathbb{S} \mid m_{n+1}^{x,j} \in E_{ad}(\rho_j),\ \mathfrak{F}(\boldsymbol{\tau}, m_{n+1}^{x,j}) \leq 0 \Big\}. \tag{7.37b}$$

$\mathbb{E}_{\Sigma_{n+1}}$ define the set of admissible stresses reflected in the constraint definition of (7.36). $\hat{m}_{n+1}^{x,j}$ defines the solutions of this problem that restricts the search space for the solution $\bar{m}_{n+1}^{x,j}$ of the original problem (7.36).

Next, we combine both maximum statements in (7.37a) to a single maximum statement that looks for the actual macroscale stress tensor $\boldsymbol{\Sigma}_{n+1}$ and solution $\hat{m}_{n+1}^{x,j}$ within the modified admissible space definition $\mathbb{E}_{\Sigma_{n+1}}$. The reformulated statements read as:

$$\{\boldsymbol{\Sigma}_{n+1}, \hat{m}_{n+1}^{x,j}\} = \underset{(\boldsymbol{\tau}, m_{n+1}^{x,j}) \in \mathbb{E}_{\Sigma_{n+1}}}{\arg\max} \Big\{ \boldsymbol{\tau} : (\boldsymbol{E}_{n+1}^{p} - \boldsymbol{E}_{n}^{p}) \Big\}, \text{ and} \tag{7.38a}$$

$$\mathbb{E}_{\Sigma_{n+1}} := \Big\{ \boldsymbol{\tau} \in \mathbb{S},\ \ m_{n+1}^{x,j} \in E_{ad}(\rho_j) \mid \mathfrak{F}(\boldsymbol{\tau}, m_{n+1}^{x,j}) \leq 0 \Big\}. \tag{7.38b}$$

We note that the interpretation of microscale design variable $m_{n+1}^{x,j}$ as internal state variable naturally comes from these statements. Likewise (7.12), we define a Lagrangian function that converts the constraint optimization problem (7.38a) into an unconstrained problem. The Lagrangian function reads as:

$$\mathcal{L}_{n+1}(\boldsymbol{\tau}, m_{n+1}^{x,j}, \delta) := -\boldsymbol{\tau} : (\boldsymbol{E}_{n+1}^{p} - \boldsymbol{E}_{n}^{p}) + \delta\, \mathfrak{F}(\boldsymbol{\tau}, m_{n+1}^{x,j}), \tag{7.39}$$

where δ is a Lagrangian multiplier such that $\delta \geq 0$. Solution to (7.38a) is given by a point $(\boldsymbol{\Sigma}_{n+1}, \hat{m}_{n+1}^{x,j}, \Delta\gamma_{n+1})$ satisfying Karush-Kuhn-Tucker optimality conditions for the

Lagrangian function (7.39). The conditions entail:

$$\begin{aligned}
&\left.\frac{\partial\, \mathcal{L}_{n+1}}{\partial\, \boldsymbol{\tau}}\right|_{\boldsymbol{\Sigma}_{n+1},\hat{m}^{x,j}_{n+1},\Delta\gamma_{n+1}} = -(\boldsymbol{E}^p_{n+1} - \boldsymbol{E}^p_n) + \Delta\gamma_{n+1}\ \left.\frac{\partial \mathfrak{F}(\boldsymbol{\tau}, m^{x,j}_{n+1})}{\partial \boldsymbol{\tau}}\right|_{\boldsymbol{\Sigma}_{n+1},\hat{m}^{x,j}_{n+1}} = 0,\\
&\left.\frac{\partial\, \mathcal{L}_{n+1}}{\partial\, m^{x,j}_{n+1}}\right|_{\boldsymbol{\Sigma}_{n+1},\hat{m}^{x,j}_{n+1},\Delta\gamma_{n+1}} = \Delta\gamma_{n+1}\ \left.\frac{\partial \mathfrak{F}(\boldsymbol{\tau}, m^{x,j}_{n+1})}{\partial m^{x,j}_{n+1}}\right|_{\boldsymbol{\Sigma}_{n+1},\hat{m}^{x,j}_{n+1}} = 0,\\
&\Delta\gamma_{n+1} \geq 0,\ \ \mathfrak{F}(\boldsymbol{\Sigma}_{n+1}, \hat{m}^{x,j}_{n+1}) \leq 0,\ \ \text{and}\ \ \Delta\gamma_{n+1}\, \mathfrak{F}(\boldsymbol{\Sigma}_{n+1}, \hat{m}^{x,j}_{n+1}) = 0.
\end{aligned} \tag{7.40}$$

The general structure of (7.40) is similar to the typical local constitutive equations for plasticity (flow rule, loading/unloading conditions). Equation $(7.40)_2$ represents the evolution of microstructure in a particular load increment n+1. From an algorithmic development perspective, we define the following elastic trial state with known optimal material configuration $\bar{m}^{x,j}_n$ from previous load increment as:

$$\begin{aligned}
&\boldsymbol{E}^p_{n+1} := \boldsymbol{E}^p_n \implies \boldsymbol{E}^{e,tr}_{n+1} = \boldsymbol{E}_{n+1} - \boldsymbol{E}^p_n\\
&\boldsymbol{\Sigma}^{tr}_{n+1} := \mathbb{C}(\bar{m}^{x,j}_n) : (\boldsymbol{E}_{n+1} - \boldsymbol{E}^p_n)\\
&\mathfrak{F}^{tr}_{n+1} := \mathfrak{F}(\boldsymbol{\Sigma}^{tr}_{n+1}, \bar{m}^{x,j}_n)
\end{aligned} \tag{7.41}$$

Further, we assume that the homogenized yield criterion $\mathfrak{F}$ is convex. This convexity assumption led to the following important property:

$$\mathfrak{F}^{tr}_{n+1} \geq \mathfrak{F}_{n+1},\ \ \text{and}\ \ \mathfrak{F}_{n+1} = \mathfrak{F}(\boldsymbol{\Sigma}_{n+1}, \bar{m}^{x,j}_{n+1}). \tag{7.42}$$

For a formal proof of this property, readers are referred to Chapter 3 in [164]. In the context of continuum micromechanics based homogenized yield criterion, we comment on the convexity in the next section.

This trial state in combination with (7.40) leads to three cases that provides important insights for solving the material optimization problem. Figure 7.2 geometrically presents two non-trivial cases in a typical return-mapping interpretation. We discuss these cases here.

↪ **Case 1:** If $\mathfrak{F}^{tr}_{n+1} < 0$, then by property (7.42) it follows that $\mathfrak{F}_{n+1} < 0$. Then the discrete KKT condition $\Delta\gamma_{n+1}\, \mathfrak{F}_{n+1} = 0$ in (7.40) implying $\Delta\gamma_{n+1} = 0$. This means that it is a **purely elastic step**, and $\boldsymbol{E}^p_{n+1} = \boldsymbol{E}^p_n$ from $(7.40)_1$. With $\Delta\gamma_{n+1} = 0$, $(7.40)_2$ is automatically satisfied with no restrictions on the evolution of microstructure

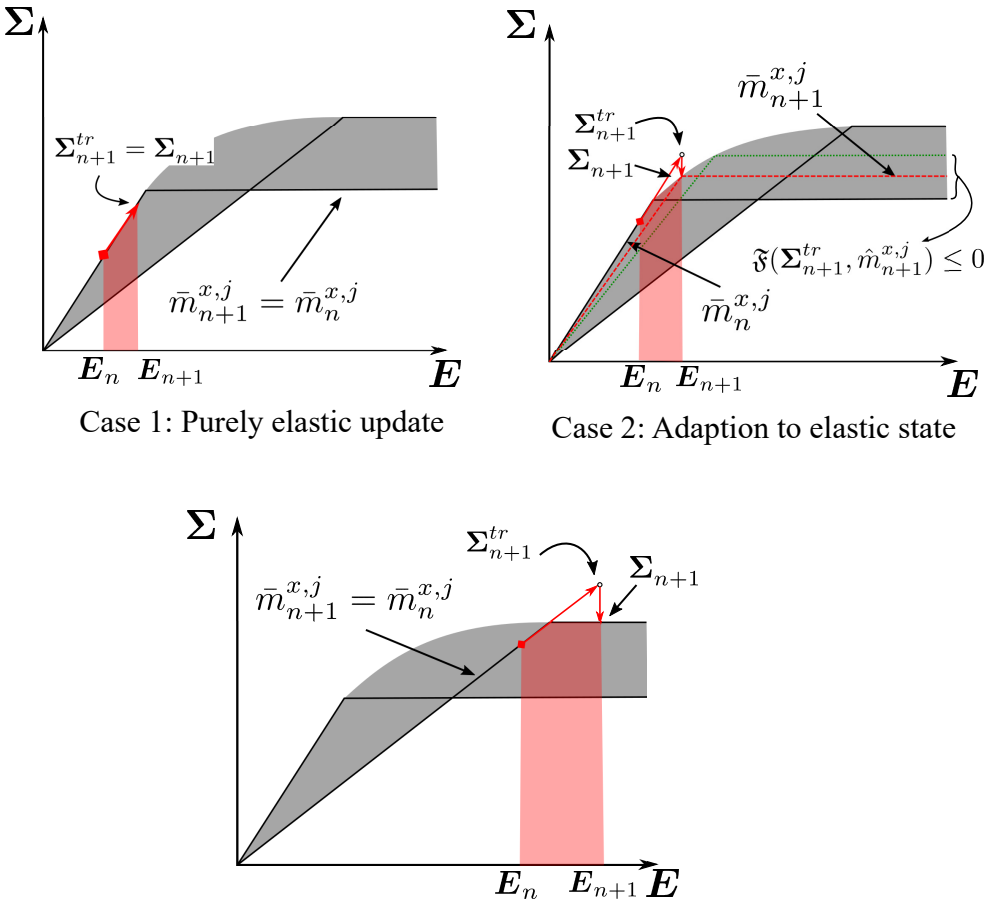

Fig. 7.3: *Graphical solution of a material optimization problem in one dimensional case for different possible cases.*

configuration $m^{x,j}_{n+1}$. Therefore, the solution $\bar{m}^{x,j}_{n+1}$ of the material optimization problem reduces to the strain energy maximization that follows from (7.36) as:

$$\bar{m}^{x,j}_{n+1} = \underset{m^{x,j}_{n+1} \in E_{ad}(\rho_j)}{\arg\max} \frac{1}{2}(\boldsymbol{E}_{n+1} - \boldsymbol{E}^p_{n+1}) : \mathbb{C}(m^{x,j}_{n+1}) : (\boldsymbol{E}_{n+1} - \boldsymbol{E}^p_{n+1}). \tag{7.43}$$

↪ **Case 2:** If $\mathfrak{F}^{tr}_{n+1} > 0$, and if it is possible to find solutions of $\mathfrak{F}^{tr(2)}_{n+1} := \mathfrak{F}(\boldsymbol{\Sigma}^{tr}_{n+1}, \hat{m}^{x,j}_{n+1}) \leq 0$ for $\hat{m}^{x,j}_{n+1} \in E_{ad}(\rho_j)$. Then, property (7.42) indicates that $\mathfrak{F}_{n+1} < 0$ solution is possible via the evolution of microstructure (see Fig 7.2). Again, equation (7.40) leads to $\boldsymbol{E}^p_{n+1} = \boldsymbol{E}^p_n$ and $\Delta\gamma_{n+1} = 0$. We call this case as **adaption to elastic state through**

microstructure evolution. The solution $\bar{m}^{x,j}_{n+1}$ in this case follows as:

$$\bar{m}^{x,j}_{n+1} = \underset{\mathfrak{F}(\boldsymbol{E}^e_{n+1}, m^{x,j}_{n+1}) < \mathfrak{F}^{tr(2)}_{n+1}}{\arg\max} \frac{1}{2}(\boldsymbol{E}_{n+1} - \boldsymbol{E}^p_{n+1}) : \mathbb{C}(m^{x,j}_{n+1}) : (\boldsymbol{E}_{n+1} - \boldsymbol{E}^p_{n+1}). \quad (7.44)$$

The constraint in this problem ensures that the state remains elastic and can be interpreted as a restrictions on the search space for $m^{x,j}_{n+1}$ posed by (7.38a). We write $\mathfrak{F}$ in strain space to emphasize that the strain state is known and problem (7.44) is a function of $m^{x,j}_{n+1}$ only.

↪ **Case 3:** If $\mathfrak{F}^{tr}_{n+1} > 0$, and $\mathfrak{F}^{tr(2)}_{n+1} := \mathfrak{F}(\boldsymbol{\Sigma}^{tr}_{n+1}, \hat{m}^{x,j}_{n+1}) = 0$ does not have any solution. It implies that only a **plastic update** is feasible, and $\boldsymbol{E}^p_{n+1} \neq \boldsymbol{E}^p_n$. It requires $\Delta\gamma_{n+1} > 0$, and the condition $\Delta\gamma_{n+1}\, \mathfrak{F}_{n+1} = 0$ implies $\mathfrak{F}_{n+1} = 0$. Then from $(7.40)_2$, we conclude $\partial\mathfrak{F}/\partial m^{x,j}_{n+1} = 0$. Consequently, the material configuration remains unchanged, that is, $\bar{m}^{x,j}_{n+1} = \bar{m}^{x,j}_n$. It means that the solution to the material optimization problem in this load increment is trivial. Rest of the relations in (7.40) reduces to typical elastoplastic constitutive equations with known stiffness and yield criterion, which can be solved with the closest point projection algorithm outlined in Section 6.5.2 of previous chapter. We geometrically illustrate this case in Fig. 7.2.

Figure 7.3 depicts a representative graphical solution of the material optimization problem in all these case for one-dimensional linear elastic perfectly plastic material models. The gray region in these graphs represents the family of stress-strain curves for different microstructure design configurations $m^{x,j}_{n+1}$. The material state (stress, strain, microscale configuration) at n^{th} load level is known, and the macroscale strain $\boldsymbol{E}_{n+1}$ at the $(n+1)^{th}$ increment is given. Typical strain increments are infinitesimal, and large increments are shown for illustration purpose only. The next material state from the material optimization problem warrants that the area increment (red shaded region in graphs) is maximized. In the first case, the purely elastic state leads to a trivial solution for linear-elastic perfectly plastic models with the same microstructure configuration, that is $\bar{m}^{x,j}_{n+1} = \bar{m}^{x,j}_n$. Case 2 is of particular interest. The trial stress $\boldsymbol{\Sigma}^{tr}_{n+1}$ predicts a plastic update. However, it is possible to find material configurations $\hat{m}^{x,j}_{n+1}$ such that $\mathfrak{F}(\boldsymbol{\Sigma}^{tr}_{n+1}, \hat{m}^{x,j}_{n+1}) \leq 0$. The material adapts to elastic state through updated microscale configuration $\bar{m}^{x,j}_{n+1}$ (denoted with red dashed line) obtained via (7.44). In case 3, no material configuration allows an elastic state for the trial stress $\boldsymbol{\Sigma}^{tr}_{n+1}$. Therefore, the material configuration remains unchanged, and the stress-strain state is updated through a return-mapping/closest point projection algorithm. We summarized these insights into an algorithmic form in the following BOX.

1. Given: $\boldsymbol{E}_{n+1},\ \boldsymbol{E}_n,\ \boldsymbol{E}^p_n,\ \bar{m}^{x,j}_n,\ \rho_j$
2. Compute elastic trial stress $\boldsymbol{\Sigma}^{tr}_{n+1}$

$$\boldsymbol{\Sigma}^{tr}_{n+1} := \mathbb{C}(\bar{m}^{x,j}_n) : (\boldsymbol{E}_{n+1} - \boldsymbol{E}^p_n)$$

3. Check yield criterion $\mathfrak{F}^{tr}_{n+1} := \mathfrak{F}(\boldsymbol{\Sigma}^{tr}_{n+1}, \bar{m}^{x,j}_n)$

   IF: $\mathfrak{F}^{tr}_{n+1} < 0$
   CASE 1: Elastic update $\Delta\gamma_{n+1} = 0; \boldsymbol{E}^p_{n+1} = \boldsymbol{E}^p_n$
   Microscale design $\bar{m}^{x,j}_{n+1}$ update through straightforward strain energy maximization:

$$\underset{m^{x,j}_{n+1} \in E_{ad}(\rho_j)}{\arg\max} \frac{1}{2}(\boldsymbol{E}_{n+1} - \boldsymbol{E}^p_{n+1}) : \mathbb{C}(m^{x,j}_{n+1}) : (\boldsymbol{E}_{n+1} - \boldsymbol{E}^p_{n+1})$$

   ELSE IF: $\mathfrak{F}^{tr}_{n+1} > 0$
   CHECK IF: $\mathfrak{F}^{tr(2)}_{n+1} := \mathfrak{F}(\boldsymbol{\Sigma}^{tr}_{n+1}, \hat{m}^{x,j}_{n+1}) \leq 0;$ for $\hat{m}^{x,j}_{n+1} \in E_{ad}(\rho_j)$
   CASE 2: Evolve microscale design ensuring elastic material behavior
   $\Delta\gamma_{n+1} = 0;\ \boldsymbol{E}^p_{n+1} = \boldsymbol{E}^p_n; \bar{m}^{x,j}_{n+1}$ is solution of

$$\underset{\mathfrak{f}(\boldsymbol{E}^e_{n+1}, m^{x,j}_{n+1}) < \mathfrak{F}^{tr(2)}_{n+1}}{\arg\max} \frac{1}{2}(\boldsymbol{E}_{n+1} - \boldsymbol{E}^p_{n+1}) : \mathbb{C}(m^{x,j}_{n+1}) : (\boldsymbol{E}_{n+1} - \boldsymbol{E}^p_{n+1})$$

   ELSE:
   CASE 3: Only plastic update possible $\implies \Delta\gamma_{n+1} > 0;\ \bar{m}^{x,j}_{n+1} = \bar{m}^{x,j}_n$
   Update $\boldsymbol{E}^p_{n+1}$ through closest point projection algorithm.
4. Output: $\bar{m}^{x,j}_{n+1}, \boldsymbol{E}^p_{n+1}$, and $\boldsymbol{\Sigma}_{n+1} = \mathbb{C}(\bar{m}^{x,j}_{n+1}) : (\boldsymbol{E}_{n+1} - \boldsymbol{E}^p_{n+1})$.

7.4.2 A special case: continuum micromechanics based homogenization

Figure 7.4 geometrically represents the continuum micromechanics based homogenized stress-strain response (in one-dimensional case) and homogenized yield surfaces in π plane. Key properties, detailed in this section, explain these responses and lead to further simplifications in the material optimization solution procedure. We drop (x, j) superscript for the clarity of presentation. We restate the homogenized yield criterion (6.7) for the reference

to this section as (all the notation are described in the previous chapter):

$$\mathfrak{F}(\boldsymbol{\tau}, m_{n+1}) = \sqrt{\boldsymbol{\tau} : [\mathbb{C}(m_{n+1})]^{-1} : \frac{\partial\, \mathbb{C}(m_{n+1})}{\partial\, \mu_C} : [\mathbb{C}(m_{n+1})]^{-1} : \boldsymbol{\tau}} \; - \; \sqrt{\frac{\bar{\phi}_C}{3}}\, \frac{\sigma_C^Y}{\mu_C}. \quad (7.45)$$

Property 1: An important conclusion from the previous section's discussion is that the microscale design update is possible in an elastic step only. In the elastic step, the material optimization problem is essentially a strain energy maximization. We know that the maximum strain energy is obtained for a general orthotropic material by aligning the material axis with the principal strain axes for the elastic strains [103, 143]. Therefore, the elastic part of macroscale strain $\boldsymbol{E}^e_{n+1} := \boldsymbol{E}_{n+1} - \boldsymbol{E}^p_{n+1}$ at each Gauss point entails the optimal material orientation $\bar{\theta}_{A,n+1}$ for $(n+1)^{th}$ load increment.

Property 2: The optimal material orientation $\bar{\theta}_{A,n+1}$ is the only microscale variable that may change in each load increment. We denote the set of remaining microscale design variables as $m^l_{n+1} = [\phi_{A,n+1}, \zeta_{A,n+1}, \gamma_{C,n+1}]$. The optimal configuration $\bar{m}^l_{n+1}$ for m^l_{n+1} remains unchanged throughout the loading history, that is $\bar{m}^l_{n+1} = \bar{m}^l_n \;\; \forall n = 1, 2, ..., n_{load} - 1$.

Proof: To prove this property, we write the strain energy maximization expressions appeared in the previous section in index notation. First, we denote the orthonormal basis corresponds to the global coordinate system with indices as $\{\boldsymbol{e}_p\}$. Problem (7.43) or (7.44)

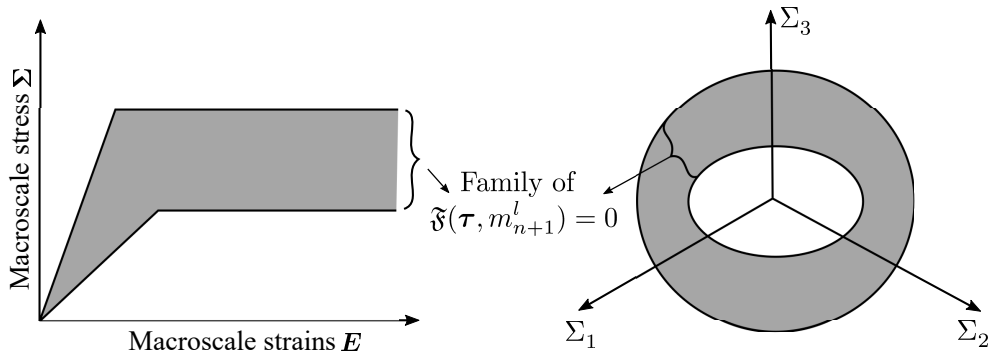

Fig. 7.4: *Geometric illustration of representative continuum micromechanics based homogenized material response with microscale design variable set m^l_{n+1}. (a) Stress-strain response in one dimensional representation, (b) Homogenized yield surfaces in π plane representation.*

at n^{th} load increment with $\boldsymbol{E}^e_n := \boldsymbol{E}_n - \boldsymbol{E}^p_n$ can be rewritten in index notation as:

$$\max_{m_n} \frac{1}{2}\boldsymbol{E}^e_n : \mathbb{C}(m_n) : \boldsymbol{E}^e_n = \max_{m_n} \frac{1}{2} E^e_{pq(n)} \boldsymbol{e}_p \otimes \boldsymbol{e}_q : C_{pqrs}(m_n) \boldsymbol{e}_p \otimes \boldsymbol{e}_q \otimes \boldsymbol{e}_r \otimes \boldsymbol{e}_s : E^e_{rs(n)} \boldsymbol{e}_r \otimes \boldsymbol{e}_s$$
$$= \max_{m_n} \frac{1}{2} E^e_{pq(n)}\ C_{pqrs}(m_n)\ E^e_{rs(n)}. \tag{7.46}$$

The coordinate system co-linear with principal strain directions is denoted with Roman indexed basis $\{\hat{\boldsymbol{e}}_i\}$. The transformation matrix Q_{pi} between both systems depends on $\bar{\theta}_{A,n}$. Utilizing Q_{pi} and its orthogonal property, we define the following tensor component transformations:

$$\hat{\boldsymbol{e}}_i = Q_{pi}\boldsymbol{e}_p;\ \ \hat{E}^e_{ij(n)} = Q_{pi}Q_{qj}E^e_{pq(n)};\ \ C_{pqrs} = Q_{pi}Q_{qj}Q_{rk}Q_{sl}\hat{C}_{ijkl}, \tag{7.47}$$

where $\hat{E}^e_{pq(n)}$ are the components of the elastic part of the macroscale strain tensor $E^e_{pq(n)}$ in the principle coordinate system. Also, $\hat{E}^e_{ij(n)} = 0$ if $i \neq j$ and diagonal components $(i = j)$ are the principle strain values for $E^e_{pq(n)}$. Similarly, $\hat{C}_{ijkl}$ are the components of the stiffness tensor in the principal coordinate system. Using (7.47), we reformulate the maximization problem (7.46) in terms of $m^l_n = [\phi_{A,n}, \zeta_{A,n}, \gamma_{C,n}]$ as:

$$\max_{m^l_n} \frac{1}{2} \hat{E}^e_{ij(n)}\ \hat{C}_{ijkl}(m^l_n)\ \hat{E}^e_{kl(n)}. \tag{7.48}$$

With $\bar{m}^l_n$ as the solution to this maximization problem, we can rewrite (7.48) as:

$$\hat{E}^e_{ij(n)}\ \hat{C}_{ijkl}(\bar{m}^l_n)\ \hat{E}^e_{kl(n)} \geq \hat{E}^e_{ij(n)}\ \hat{C}_{ijkl}(m^l_n)\ \hat{E}^e_{kl(n)}. \tag{7.49}$$

We assume that the macroscale loading increases monotonically. Therefore, the elastic part of macroscale tensor at $(n+1)^{th}$ load increment $\hat{E}^e_{ij(n+1)}$ in principle coordinate system can be written in terms of $\hat{E}^e_{ij(n)}$ components with appropriate scaling. Exploiting the definition of Kronecker delta δ, we write $\hat{E}^e_{ij(n+1)}$ in terms of scaling components $a_{i\alpha}$ as:

$$\hat{E}^e_{ij(n+1)} = a_{i\alpha}\delta_{j\alpha}\hat{E}^e_{ij(n)} \ \text{ and } \ a_{i\alpha} \geq 0. \tag{7.50}$$

As the scaling components are non-negative, we augment the expression (7.49) and arrive

at:

$$\begin{aligned} a_{i\alpha}\delta_{j\alpha}\hat{E}^e_{ij(n)}\,\hat{C}_{ijkl}(\bar{m}^l_n)\,a_{k\beta}\delta_{l\beta}\hat{E}^e_{kl(n)} \geq a_{i\alpha}\delta_{j\alpha}\hat{E}^e_{ij(n)}\,\hat{C}_{ijkl}(m^l_n)\,a_{k\beta}\delta_{l\beta}\hat{E}^e_{kl(n)} \\ \implies \hat{E}^e_{ij(n+1)}\,\hat{C}_{ijkl}(\bar{m}^l_n)\,\hat{E}^e_{kl(n+1)} \geq \hat{E}^e_{ij(n+1)}\,\hat{C}_{ijkl}(m^l_n)\,\hat{E}^e_{kl(n+1)}. \end{aligned} \tag{7.51}$$

This is the expression for the strain energy maximization problem at $(n+1)^{th}$ load increment analogous to (7.48) or (7.49). We emphasize that our definition of admissible set E_{ad} depends only on the macroscale density distribution and, therefore, remains unchanged throughout the loading history. It implies that the admissible microstructure solutions m^l_{n+1} at $(n+1)^{th}$ increment are equal to m^l_n, that is $m^l_{n+1} = m^l_n$. With the assumption of linearized elasticity, we straightforwardly arrive at:

$$\hat{E}^e_{ij(n+1)}\,\hat{C}_{ijkl}(\bar{m}^l_n)\,\hat{E}^e_{kl(n+1)} \geq \hat{E}^e_{ij(n+1)}\,\hat{C}_{ijkl}(m^l_{n+1})\,\hat{E}^e_{kl(n+1)} \implies \bar{m}^l_{n+1} = \bar{m}^l_n. \tag{7.52}$$

Property 3: The homogenized yield criterion $\mathfrak{F}(\boldsymbol{\tau}, m^l_{n+1})$ is convex. As discussed in Section 6.1.2, the yield criterion is of the form of general quadratic form that satisfies two important properties, (1) convexity and (2) degree-one homogeneity. Another intuitive interpretation is based on the convexity of elastic strain energy in the terms of principal strain component for the elastic part of the macroscale strain tensor [103, 117]. The yield criterion is essentially driven by the quadratic average of elastic strain energy and, therefore, is convex.

Property 4: The microscale configuration $\bar{m}^l_{n+1}$ corresponding to the maximum stiffness (maximum strain energy density) also results in the maximum strength properties for the homogenized response. Figure 7.4 graphically represent this property for one dimensional case with family of possible stress-strain curves. The stress-strain curve corresponds to the configuration $\bar{m}^l_{n+1}$ acts as a upper bound for all possible stress-strain curves. Mathematically, we write this property as:

$$\begin{aligned} \hat{E}^e_{ij(n+1)}\,\hat{C}_{ijkl}(\bar{m}^l_{n+1})\,\hat{E}^e_{kl(n+1)} \geq \hat{E}^e_{ij(n+1)}\,\hat{C}_{ijkl}(m^l_{n+1})\,\hat{E}^e_{kl(n+1)} \\ \implies \mathfrak{F}(\boldsymbol{\tau}, \bar{m}^l_{n+1}) \leq \mathfrak{F}(\boldsymbol{\tau}, m^l_{n+1}). \end{aligned} \tag{7.53}$$

A proof of this property can be written exploiting the upper and lower bound definitions via Voigt and Reuss mixture rules for continuum micromechanics based homogenization schemes. This property holds true if the stiffer base constituent in the hierarchical system exhibits higher yield strength. In our case, it implies that if $E_C > E_B \implies \sigma^Y_C > \sigma^Y_B$, where E_C & E_B are the Young's modulus, and σ^Y_C & σ^Y_B are the yield strength of Material

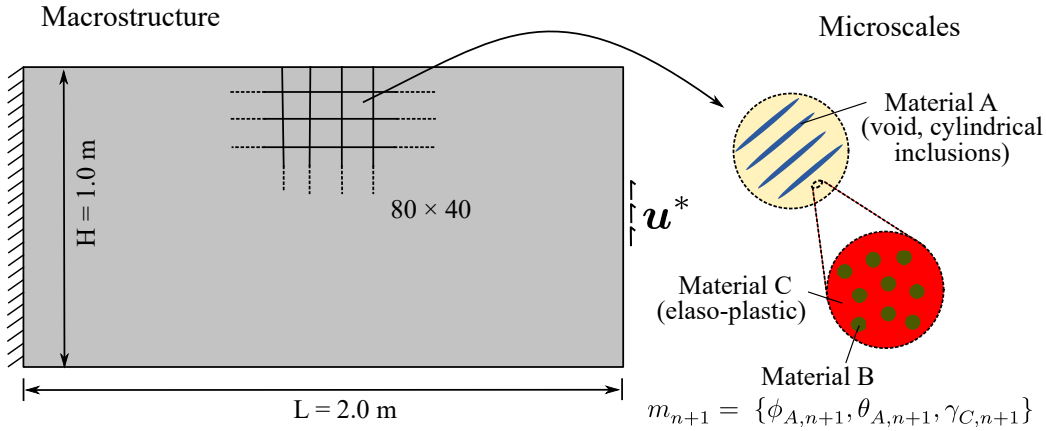

Fig. 7.5: *Cantilever benchmark problem description for material and structure optimization problem with elastoplastic multiphase hierarchical material definition.*

C and Material B. In our case, only Material C is considered as elastoplastic, and (7.53) holds true for all $\bar{\phi}_C > 0$ in (7.45).

These properties lead to two important simplifications to the algorithmic procedure for the material optimization problem discussed in the previous section. The first simplification comes from Property 4, which implies that Case 2 is inconceivable in our case. This can also be concluded by comparing Fig. 7.4 with Fig. 7.3. Besides, Property 1 & 2 suggest that the material optimization problem should be solved once for the first increment. Later, only the material orientation changes, which is straightforward from the elastic part of the macroscale strain tensor. From a computational viewpoint, these simplifications result in an enormous reduction in computational efforts.

7.5 Implementation details and algorithmic aspects

Algorithm 5 consolidates all the developments presented in this chapter into an algorithmic framework. The structure of the algorithm is similar to Algorithms 3 & 4 presented in the previous chapters. The algorithm mainly consists of three blocks. The outer block represents the macroscale structure optimization iterations using the optimality criteria method detailed in (5.28) of Chapter 5. It stops when the macroscale density $\boldsymbol{\rho}$ reaches convergence. The middle block solves the initial boundary value problem for given macroscale density distribution, following the Newton-Raphson incremental procedure detailed in Section 6.3.2 and Section 6.5.2. The inner layer solves the material optimization problem following Section 7.4 at each Gauss point with prescribed state variables at this iteration stage for each load increment.

Result: Optimized solution vector $[\boldsymbol{\rho}, \bar{\boldsymbol{m}}]^T$

Initialize $\boldsymbol{\rho}^0, \boldsymbol{m}^0$;
Set design iteration counter i = 0;
while $||\rho^{i+1} - \rho^i||/||\rho^i|| > \delta_{tol}$ **do**
  Set up load increments $\Delta\bar{\boldsymbol{u}}_{\boldsymbol{q}}{}^E$ for each loading step index $q = 0, .., n_{load} - 1$;
  Initialize load increment couter $n = 0$;
  Initialize $\bar{\boldsymbol{u}}_0 = \boldsymbol{0} \implies \boldsymbol{E}_0 = \boldsymbol{0}$, and $\boldsymbol{E}_0^p = \boldsymbol{0}$;
  for $n \leq n_{load} - 1$ **do**
    Increment load $\bar{\boldsymbol{u}}_{n+1}^E = \bar{\boldsymbol{u}}_n^E + \Delta\bar{\boldsymbol{u}}_{n+1}^E$;
    Set Newton iteration counter k = 0;
    $\bar{\boldsymbol{u}}_{n+1}^{(0)} = \bar{\boldsymbol{u}}_n$;
    while $||\bar{\boldsymbol{r}}_{n+1}^{(k)}|| < \epsilon_{tol}$ **do**
      forall *macroscale Gauss points* **do**
        Compute the macroscale strain $\boldsymbol{E}_{n+1}^{(k)} = \nabla^s(\bar{\boldsymbol{u}}_{n+1}^{(k)})$;
        Update the state variables $\boldsymbol{\Sigma}_{n+1}^{(k)}$, $\boldsymbol{E}_{n+1}^{p^{(k)}}$, and $\bar{m}_{n+1}^{x,j}$ by solving the material optimization problem;
      end
      Set up the linear system: $\boldsymbol{K}_{n+1}^{tan,(k)}\ \delta\bar{\boldsymbol{u}}^{(k+1)} = \boldsymbol{f}_{n+1}^{ext} - \boldsymbol{f}^{int}(\boldsymbol{\Sigma}_{n+1}^{(k)}) = \bar{\boldsymbol{r}}_{n+1}^{(k)}$, and solve for $\delta\bar{\boldsymbol{u}}^{(k+1)}$;
      Apply Newton correction to the displacements: $\bar{\boldsymbol{u}}_{n+1}^{(k+1)} = \bar{\boldsymbol{u}}_{n+1}^{(k)} + \delta\bar{\boldsymbol{u}}^{(k+1)}$; k++;
    end
    Calculate and store Lagrangian multipliers $\boldsymbol{\lambda}_{n+1}$ and $\boldsymbol{\mu}_{n+1}$ for senstivity calculations using converged state variables;
    n++;
  end
  Compute the objective function $f_w(\boldsymbol{\rho})$ and sensitivities $\partial f_w/\partial\boldsymbol{\rho}$;
  Update density $\boldsymbol{\rho}^{i+1}$ using the optimality criteria algorithm; i++;
end

Algorithm 5: Concurrent structure and material optimization framework for elasto-plastic structures with multiphase hierarchical materials.

The sensitivity analysis in this equation is remained to be discussed. In the previous chapter, we applied the adjoint method to derive sensitivities for the macroscale structure optimization problem. The layout of the structure optimization problem (7.32) is similar to the problem (6.31) in the previous chapter. Moreover, we consider only the displacement-controlled loading scenario considering the ill-posed nature of force-controlled boundary value problems involving inelastic material models [35, 98, 126, 160, 171]. With the similar procedure, we arrive that the following sensitivity expression:

$$\frac{\partial f_w^*}{\partial \rho_j} = -\frac{1}{2}\sum_{n=0}^{n_{load}-1}\left\{(\boldsymbol{\lambda}_{n+1})^T\sum_{x=1}^{N_{gp}}\left[\boldsymbol{B}^T\frac{\partial\boldsymbol{\Sigma}_{n+1}}{\partial\rho_j}w_x\right] + (\boldsymbol{\mu}_{n+1})^T\sum_{x=1}^{N_{gp}}\left[\boldsymbol{B}^T\frac{\partial\boldsymbol{\Sigma}_n}{\partial\rho_j}\ w_x\right]\right\}. \quad (7.54)$$

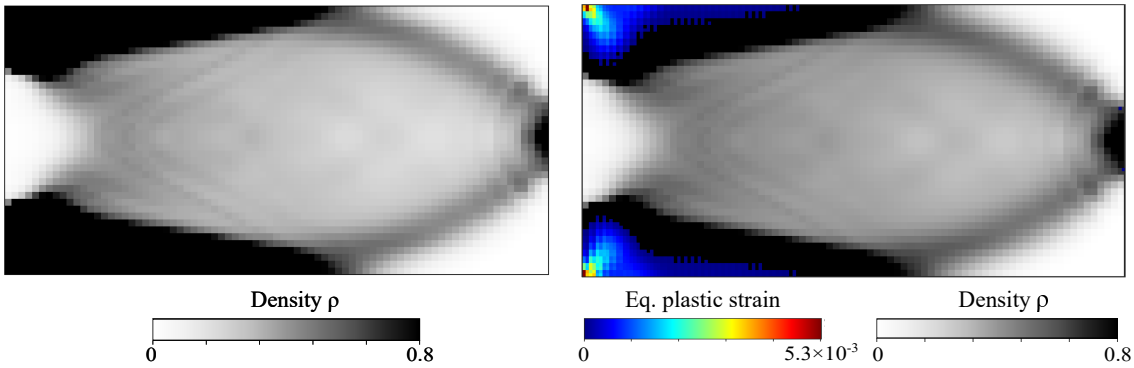

(a) Optimum desity distribution. **(b)** Equivalent plastic strain distribution.

Fig. 7.6: *Final design of the cantilever benchmark problem with equivalent plastic strain distribution for total prescribed displacement load of* $\boldsymbol{u}^* = 7.5$ *mm.*

With the definition of macroscale stress $\boldsymbol{\Sigma}_{n+1}$ from (7.34), this equation reads as:

$$\frac{\partial f_w^*}{\partial \rho_j} = -\frac{1}{2} \sum_{n=0}^{n_{load}-1} \left\{ (\boldsymbol{\lambda}_{n+1})^T \sum_{x=1}^{N_{gp}} \left[\boldsymbol{B}^T \frac{\partial \mathbb{C}(\bar{m}_{n+1}^{x,j})}{\partial \rho_j} (\boldsymbol{E}_{n+1} - \boldsymbol{E}_{n+1}^p) w_x \right] \right. \\ \left. + (\boldsymbol{\mu}_{n+1})^T \sum_{x=1}^{N_{gp}} \left[\boldsymbol{B}^T \frac{\partial \mathbb{C}(\bar{m}_n^{x,j})}{\partial \rho_j} (\boldsymbol{E}_n - \boldsymbol{E}_n^p) w_x \right] \right\}. \tag{7.55}$$

We note that the history of kinematic state variables $\boldsymbol{E}$ and $\boldsymbol{E}^p$ are known. The derivative of homogenized stiffness $\mathbb{C}$ with respect to the element density ρ_j can be evaluated with chain rule, as demonstrated in Section 5.2.4. The Lagrangian multipliers $\boldsymbol{\lambda}_{n+1}$ and $\boldsymbol{\mu}_{n+1}$ are determined via the following relations that arise from (6.44) and (6.46):

$$\boldsymbol{\lambda}_{n+1}^E = -\Delta \bar{\boldsymbol{u}}_{n+1}^E \;\text{ and }\; \boldsymbol{\lambda}_{n+1}^F = \; [\boldsymbol{K}_{n+1}^{tan,FF}]^{-1} \; \boldsymbol{K}_{n+1}^{tan,FE} \; \Delta \bar{\boldsymbol{u}}_{n+1}^E, \tag{7.56a}$$

$$\boldsymbol{\mu}_{n+1}^E = -\Delta \bar{\boldsymbol{u}}_{n+1}^E \;\text{ and }\; \boldsymbol{\mu}_{n+1}^F = \; [\boldsymbol{K}_{n}^{tan,FF}]^{-1} \; \boldsymbol{K}_{n}^{tan,FE} \; \Delta \bar{\boldsymbol{u}}_{n+1}^E \; . \tag{7.56b}$$

Index E and F denote essential (Dirichlet) boundary condition degree of freedoms (DOFs) and the remaining free DOFs. $\Delta \bar{\boldsymbol{u}}_{n+1}^E$ is the displacement load increment, and $\boldsymbol{K}_{n+1}^{tan}$ is the global FE stiffness matrix of the mechanical system at the equilibrium of the $(n+1)^{th}$ load step.

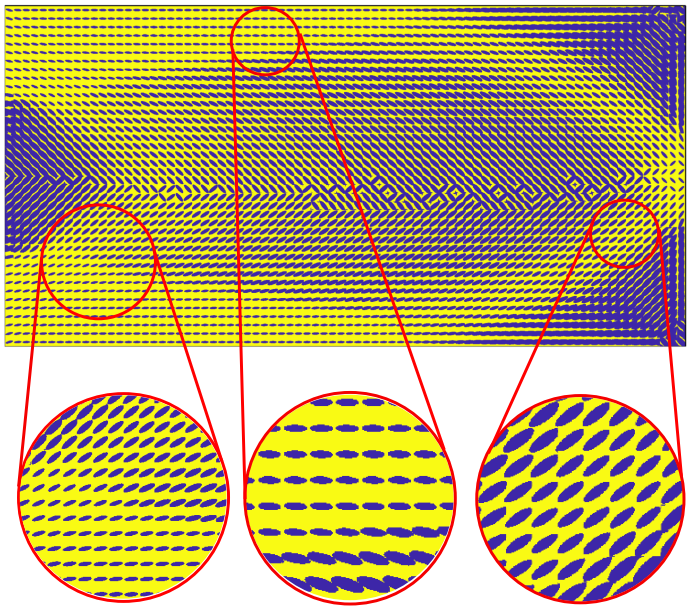

(a) Optimal microstructure at mesoscale.

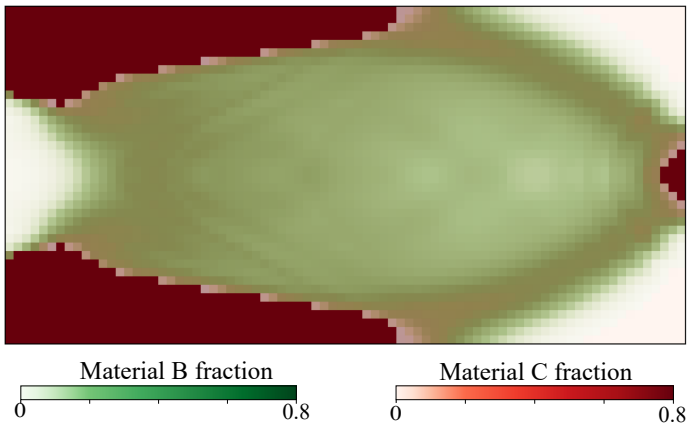

(b) Optimized equivalent volume fractions of Material B and Material C.

Fig. 7.7: *Optimal material configuration for total prescribed displacement load of* $\boldsymbol{u}^* = 7.5$ *mm.*

7.6 Numerical examples

To demonstrate the developed concepts, we modify the definition of the cantilever design problem illustrated in the previous chapters (see Fig. 7.5). The length and height of the macrostructure are 2.0 m and 1.0 m, respectively. The left edge is fixed, and the central 10% of the right edge is prescribed with displacement loading of $\boldsymbol{u}^* = 7.5$ mm. Plane strain conditions are considered. The prescribed displacement load $\boldsymbol{u}^* = 7.5$ mm is reached in 6

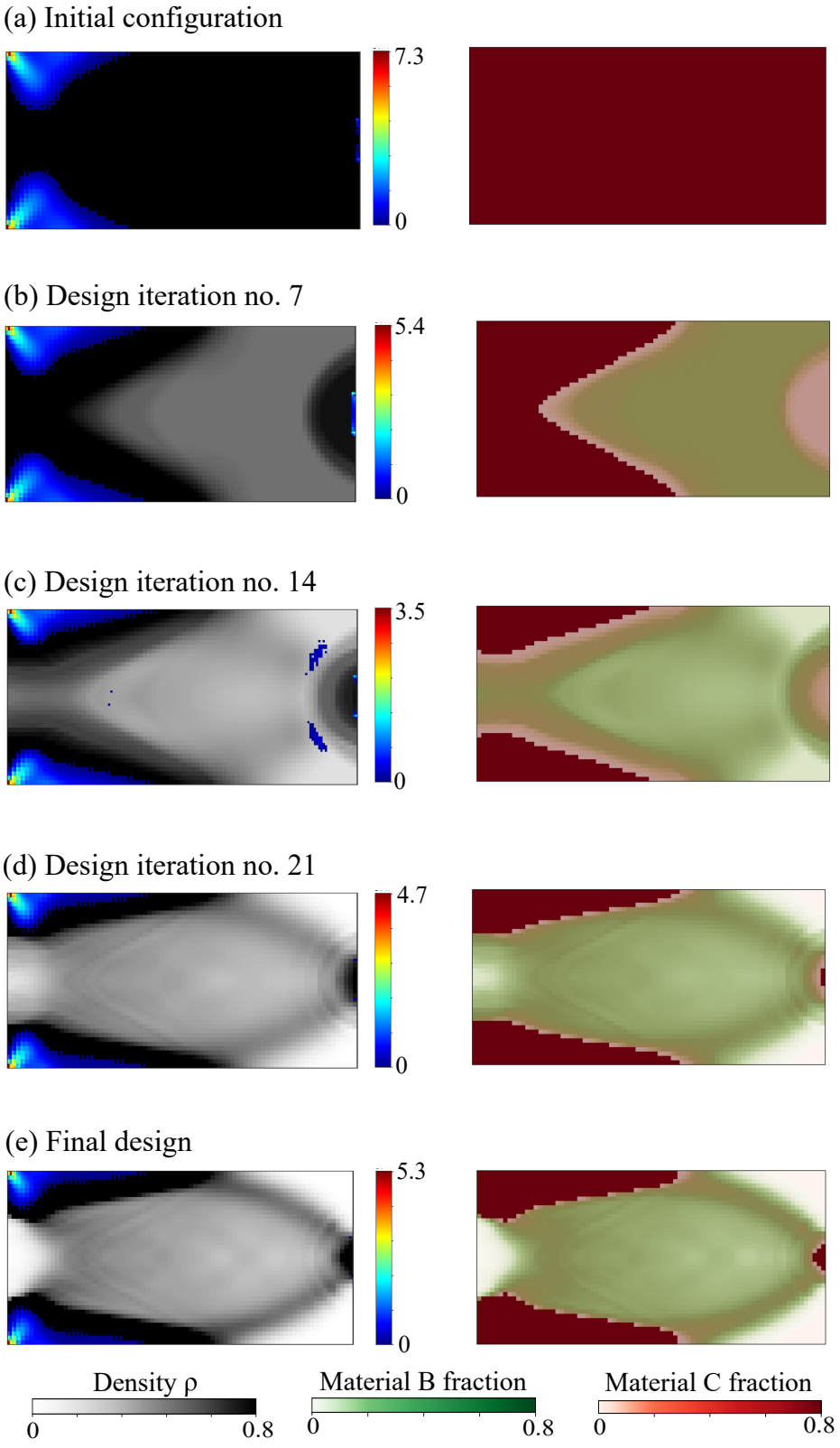

Fig. 7.8: *The evolution of macroscale density configuration with design iterations with equivalent plastic strains in $\times 10^{-3}$ units (overlaid on corresponding density distribution in rainbow colormap) and equivalent volume fractions of Material B and C plots.*

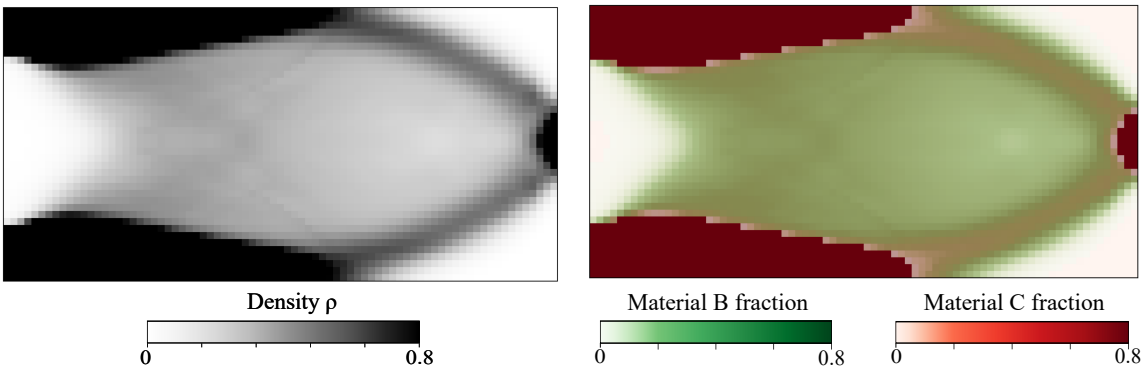

(a) Optimum desity distribution.

(b) Optimized equivalent volume fractions of Material B and Material C.

Fig. 7.9: *Final design of the cantilever benchmark problem for linear elastic case (Material C is considered purely elastic).*

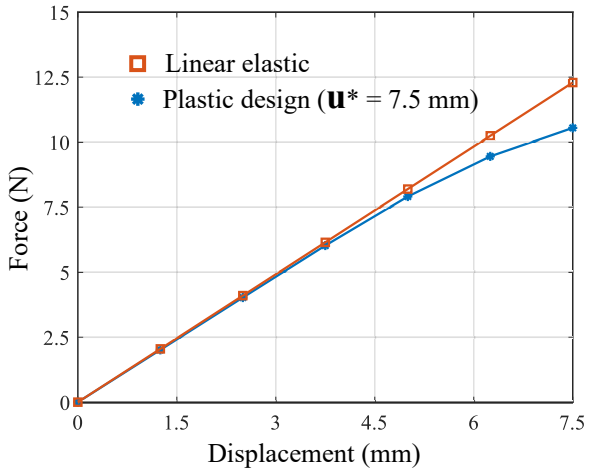

Fig. 7.10: *Comparison of load vs displacement curves of final designs corresponding to the linear elastic and plastic designs.*

loading time steps with constant load increments of $\Delta\bar{\boldsymbol{u}}^E = 1.25$ mm. We discretize the macroscale structure with an 80×40 mesh of 4-node quadrilateral elements, resulting in $l_e = 25$ mm element length and $3,200$ macroscale design variables. Each element contains four Gauss points, resulting in $80 \times 40 \times 4 = 12,800$ material optimization problems in each load step.

In this example, as illustrated in Fig. 7.5, we consider a hierarchical system that consists of Material A, B, and C at two different length scales. Their densities (in Kg/m^3) are $\rho_A = 0$, $\rho_B = 0.5$, and $\rho_C = 1.0$, respectively, their Young's moduli (in GPa) are $E_A = 0.0$, $E_B = 0.5$, and $E_C = 1.0$, respectively, and Poisson's ratio of all constituents is 0.3. Material C is elastoplastic with the yield strength of 1 MPa. We assume that the elongation ratio of

Material A inclusions is fix and equal to 5. Thus, it is not included in the microscale design variable set $\boldsymbol{m}$. At each Gauss point, the material microstructure is parametrized by the volume fraction $\phi^{x,j}_{A,n+1}$, the orientation $\theta^{x,j}_{A,n+1}$, and the volume fraction $\gamma^{x,j}_{C,n+1}$ for $(n+1)^{th}$ load step resulting in $38,400$ microscale design variables at each load step. The minimum volume fraction of Material A is set to $\phi^{min}_A = 0.2$. The existence of the homogenized yield criterion $\mathfrak{F}$ in (7.45) requires $\bar{\phi}_C = (1-\phi_A)\,\gamma_C > 0$. It implies that the bounds $\phi^{max}_A < 1-h$ and $\gamma^{min}_C > h$, where h is a small positive number. Restricting ρ_{min} to 0.001 and ρ_{max} to 0.799 satisfy these requirements.

The total amount of material mass available is restricted to 40% of the maximum possible mass. As an initial condition at the macroscale, we assume the maximum possible density ρ_{max} in each element. At the material level, we assume an initial microstructure configuration with $\phi_A = 0.0$, $\theta_A = 0.0$, and $\gamma_C = 1.0$ at each Gauss point. In each design update, we reduce the target mass fraction by 0.025 until we reach the specified mass fraction $M_{frac} = 0.4$. The move parameter μ and the damping parameter η are set to 0.05 and 0.5. The filter radius r_{min} is reduced linearly from $r_{min} = 20l_e$ to $r_{min} = 4l_e$ as proposed in Section 6.6.

Figure 7.6 illustrates the final design for the cantilever problem with equivalent plastic strain distribution. The macroscale design algorithm takes 34 density updates to converge to the final design. Figure 7.6a and b plot the optimized macroscale density and equivalent plastic strains overlaid on the density plot, respectively. The plastic strains are concentrated at the boundaries of the clamped end, which, as a consequence, push material towards these regions. We emphasize that the plastic front plays a key role in the optimal density distribution. This observation is demonstrated in Fig. 7.6b, where the sharp features near the clamped end mimic the plastic front.

Figure 7.7 displays the details of the optimized morphology at the mesoscale and the equivalent volume fraction of Material B and Material C. The color schemes and the definitions of the equivalent volume fractions are same as described in Section 5.3.1. As anticipated, the inclusions follow the direction of the largest principal stress optimizing the elastoplastic response of the cantilever. The stiffer Material C is deposited in the regions that are anticipated to yield first. We can also identify the diffuse regions with complex morphology and mixing of Material C and B.

Figure 7.8 details the evolution of the optimization process outlining selected design iterations with equivalent plastic strains overlaid on the corresponding density distribution and Material B and C volume fraction plots. The evolution of the macroscale density and equivalent plastic strains shows that the design process attempts to attenuate the plastic front. In this process, the algorithm pushes more material towards the clamped region, delaying the yielding in this region. The evolution of the equivalent Material C fraction

is particularly interesting. Material C is the stiffest material among the constituents and shows elastoplastic behavior. Its evolution is heavily influenced by the plastic front, which eventually reflects in the macroscale density configuration with sharp features.

We compare the optimal configurations from this example with the results of an equivalent linear elastic design that assumes purely elastic properties of Material C. Figure 7.9 plots the optimized density and the equivalent volume fraction of Material B and C. Comparing these plots with Fig. 7.6 and 7.7b, apparent differences can be observed in the optimized layouts. The plastic design places more material towards the clamped region with clear features imitating the plastic front, whereas this is missing in the linear elastic design. We also plot the load-displacement curves for both cases in Fig. 7.10. At the higher load levels, the load-displacement curves start deviating, and plasticity starts playing a crucial role in the optimal configurations. We conclude that the linear elastic designs and plastic design are functionally different, and it is important to consider plastic effects originating from different scales in biological systems that are expected to develop dissipation-based energy absorption mechanisms against external impacts.

Summary and conclusions

In this part, for the first time, we presented novel approaches integrating continuum micromechanics estimates that can tackle the concurrent material and structure optimization problems for multiphase hierarchical systems with practically available computing resources. First, we established the decomposed material and structure optimization sub-problems for end-compliance minimization problems with an overall elastic response at both the material and structure levels. Continuum micromechanics estimates rendered the material optimization as a series of inexpensive "discretization-free" constraint optimization problems, whose computational cost is independent of the number of hierarchical scales involved. We also demonstrated a computationally feasible extension for the macroscale structure optimization problems with a given elastoplastic hierarchical material definition. Finally, we derived a non-trivial extension of the concurrent optimization framework to account for elastoplastic behavior at the material level, building on the thermomechanical formulation of elastoplasticity. We extensively verified the validity and efficiency of our approaches with newly defined benchmark problems that, for the first time, become computationally feasible via our framework.

PART III

Towards simulation supported genetic tailoring of cereals

Introduction

In this part, we transfer the developed concepts in the context of biomechanical tailoring applications involving multiphase plant hierarchical materials. We mainly focus on improving breeding decisions to target lodging-resistant cereals. Lodging, the failure of a plant to fully recover after bending, occurs when an extreme force from wind or rain is applied to the plant. There are two major classifications of lodging. The first is root lodging, which occurs when the roots fail to be anchored to the soil substrate by either root slippage or root breakage. The second is stem breakage, which constitutes buckling along any point on the stem. Lodging is particularly detrimental to the cultivation of cool-season cereals such as *Avena sativa* L. (oat) and *Triticum aestivum* L. (wheat) by causing substantial yield reductions in the range of 30-90% [22, 189].

Conventional breeding methods are based on identifying traits that strongly correlate with lodging, mainly through visual inspections on a large number of genetic lines in the field. Typically, plant breeders identify a basket of potential traits, also called *phenotypes*, based on historical data and their experiences. The sufficient variability of these phenotypes is assumed to exist in the available genetic lines or *cultivars* of targeted cereal. These traits are extensively measured and correlated with the field-based visual severity ratings with suitable statistical tests. Table 7.1 is an example summary of one such experimental study to breed lodging-resistant oats, conducted by our collaborators **D. Jo Heuschele**, **Kevin P. Smith** and their colleagues from the Department of Agronomy and Plant Genetics, the University of Minnesota. It is anticipated that a superior combination of traits or *ideotype* for lodging-resistant oat can be identified from these correlations. Every entry in this table is a result of several repetitive measurements on plants that were grown in field at various location. It is important to note the humongous time and labor costs of such lodging studies.

Often such conventional breeding studies tend to be unreliable and inconclusive in correlating traits with lodging behavior. Reasons include the complex anatomy and morphology of crops at multiple length scales, the complicated interaction of the traits contributing to lodging, and environmental factors. This conundrum was summarized by [68] almost 100 years ago as " *lodging in cereals is dependent on so many factors of unequal value in the*

Table 7.1: *Example phenotypic correlation matrix for lodging experimental studies (Courtesy: D. Jo Heuschele & Kevin P. Smith).*

Phenotypes	**1.**	**2.**	**3.**	**4.**	**5.**	**6.**	**7.**	**8.**	**9.**	**10.**	**11.**	**12.**	**13.**
1. Plant height													
2. Internode (no. 1) dia.	0.18												
3. Internode (no. 2) dia.	-0.22	0.35											
4. Severity score	0.34	-0.04	**-0.52**										
5. Stem biomass	**0.57**	**0.74**	0.45	0.35									
6. Flag leaf sheath	**0.57**	0.35	-0.31	**0.66**	0.50								
7. Leaf sheath (node 2)	0.48	0.02	-0.22	**0.53**	0.30	**0.86**							
8. Leaf sheath (node 3)	0.19	0.12	-0.35	**0.71**	0.15	**0.73**	**0.78**						
9. Node (no. 4) dia.	0.46	**0.55**	**0.59**	0.05	**0.74**	0.20	0.17	-0.22					
10. Internode (no. 1) length	0.35	**0.63**	0.46	0.42	**0.73**	0.27	0.25	0.21	**0.63**				
11. Node (no. 1) dia.	**0.54**	**0.50**	0.18	0.49	**0.69**	**0.66**	**0.63**	0.35	**0.64**	**0.77**			
12. Wall thickness	0.16	0.37	0.38	0.32	**0.50**	**0.50**	**0.58**	**0.50**	0.38	**0.59**	**0.61**		
13. Root plate	-0.07	-0.19	0.22	-0.46	-0.14	-0.45	-0.42	**-0.52**	-0.09	**-0.55**	**-0.61**	-0.37	

The values in bold show the significant correlations.

different sorts that no one factor seems to be correlated closely enough with lodging to be of much value as a selection index." Therefore, all these traits and their interactions must be considered for an accurate investigation of lodging resistance. This factor limits the extent of experimental research, as adding each trait in the experimental basket exponentially increases the time and labor cost.

In contrast to experiments, computer simulations or so-called *in silico* experiments have apparent advantages of the fast and cheap realization of trait parameters on the consequences of lodging behavior [59]. Typically, such simulation models require massive simplification to represent nature's complexities into mathematical formulations. Thus, often these models are phenomenological and demand massive parametric tuning. We have developed rigorous and computationally feasible multiscale analysis and optimization tools in previous parts that are free from such shortcomings. These tools can potentially form the rigorous basis of simulation frameworks to support breeding decisions to maximize the lodging resistance of cereals.

This part mainly focuses on two objectives. First, we work together with plant scientists to quantify the lodging behavior of wheat and oat from experiment and simulation viewpoints. Our goal is to establish that the integration of our multiscale material model based simulations reveals the multiscale origin of failure mechanisms leading to lodging that would not have been possible with purely experimental approach. Second, we set up optimization models to understand the self-optimizing mechanisms in plants, building on the concepts developed in Part II. Our rationale behind this approach is based on the fact that the biological materials and structures have attained a certain degree of optimality through evolutionary selection. Therefore, optimized material and structure configurations via our framework will point towards an ideal crop variety given an evidence supported assessment of mechanical, physiological, biological, and phylogenetic constraints. In future, these results will help plant geneticists in searching for more complex combinations of traits to breed lodging-resistant cereals.

This part is structured as follows. In Chapter 8, we briefly discuss the controlled wind tunnel experiments with key conclusions to quantify the stem bending behavior of oat and wheat stems. Later, we demonstrate that our multiscale material model helps understanding the causal relationship of the observed stem behavior with the physical traits at different length scales. Reflecting on the mechanistic perspective on the self-adaption, Chapter 9 outlines the potential of our optimization framework for engineering applications by reproducing self-optimizing mechanisms in plant structures with an example of bamboo and oat stems.

Chapter 8

Multiscale material-model-based predictive simulations to support breeding lodging-resistant cereals

We outline a unique opportunity presented by collaborative efforts of researchers from mechanics and simulation backgrounds with plant scientists in a broader context of breeding lodging-resistant cereals. Our collaborators **Alexander Q. Susko**, **D. Jo Heuschele**, **Kevin P. Smith**, and **Michele Guala** ran comprehensive wind tunnel experiments to investigate the stem bending behavior of cereals under known aerodynamic forces. However, a rigorous causal relationship of the observed behavior with the physical traits of the plants could not be established. We demonstrate that the evidence-supported simulations can greatly help interpret the experimental results and design future experimental studies with extensively reduced labor and resource costs.

This chapter is organized as follows: Section 8.1 briefly summarizes the wind tunnel experimental setup and key conclusions to quantify the stem bending and failure behavior of oat and wheat plants. In Section 8.2, we build and validate a finite element simulation framework integrating the multiscale material modeling approach developed in Part I to predict the stem strength behavior of single oat and wheat stems. Finally, in Section 8.3, we utilize the framework for understanding the causal relationship of the observed stem behavior in the wind tunnel with the physical traits at different length scales that could confer lodging resistance for these major cereal crops.

8.1 Quantification of wheat and oat stem bending behavior through wind tunnel measurements

Wind tunnel testing of cereal crops offers the opportunity to obtain detailed phenotypes relevant to lodging resistance that cannot be quantified under typical field conditions. Wind tunnel testing serves to isolate two aspects of the complicated problem of lodging in cereals: the estimation of wind-induced forces on the plant that causes stem bending, and the response of the stems under a known drag force. Controlled wind tunnel testing supported by advanced video analysis methods quantifies the aerodynamic and bending behavior of cereal stems with the help of metrics such as plant drag coefficients and the stem deformation profile. We brief the essential setup and measurement details with key conclusions of the conducted experimental study. For more details, please refer to the thesis by **Alexander Q. Susko** [168].

8.1.1 Details of experimental setup

Four commercial varieties of oat – Gopher, IL078721, ND021052, Reins – and four varieties of wheat – Linkert, MN113946, Rollag, Shelly – were selected for testing based on their morphological variability and lodging resistance in field trials. Plants were grown in a greenhouse until approximately 18 days after all completed heading of the plants.

First, several measurements of plant morphological traits were taken. The *heading date* was recorded in the greenhouse as the number of days since planting to time when 50% of the first panicle or spike emerged. The plant *stem strength* was estimated using a load cell mounted to an aluminum bar, measuring the force F required to bend all stems at the half-height point in one pot to an approximate 50° angle with respect to the ground [190]. The *plant height*, defined from the base of plant stems to the tip of the tallest panicle or spike, was measured. For the estimation of leaf and stem *biomass*, each plant sample was cleared of its panicles and spikes after the experiment, kept in a dryer at 60°C, and weighed.

Each plant pot was subjected to controlled air flows in the atmospheric wind tunnel of the St. Anthony Falls Laboratory at the University of Minnesota Twin-Cities. The wind tunnel is equipped with a 149 kW fan, is a 37.5 m long closed-loop, with a test section of 16 m in length and 1.7 m $\times$ 1.7 m in cross-sectional area. Wind tunnel mean velocity was measured at a fixed height of 60 cm above the wind tunnel floor using a Pitot tube recording dynamic pressure and a thermocouple recording air temperature, required for air density estimate. Each plant was exposed to constant wind velocities of 4, 8, and 12 m/s at consecutive 50 s intervals. The wind tunnel testing protocol consisted of an uninterrupted video of plant

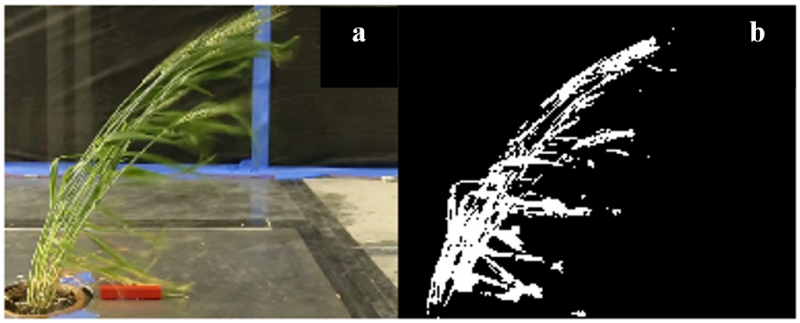

Fig. 8.1: *(a) A snapshot frame of wheat plant under the wind tunnel and (b) masked frame after applying image processing operations for estimating phenotypes.*

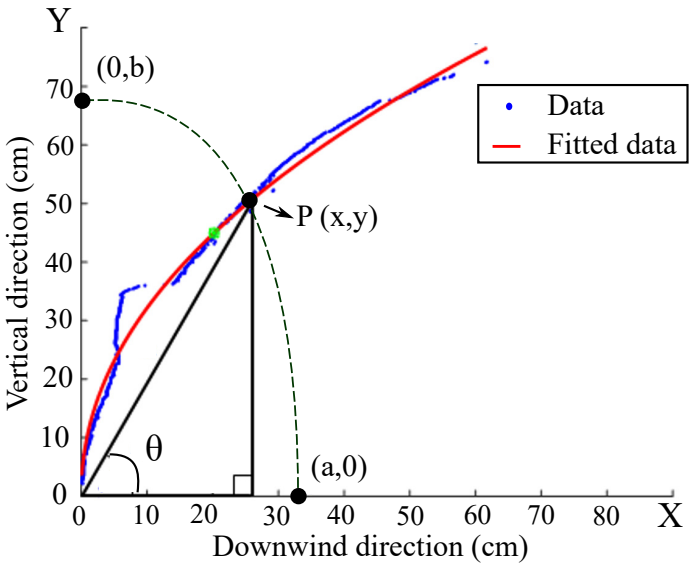

Fig. 8.2: *Windward edge profile from masked frame for particular snapshot of recorded video of wind tunnel experiment. Green dashed line approximates the ellipsoidal trajectory of point P, initially located at (0,b) where b is half of the total height of plant.*

bending and covering the entire sequence of mean velocity variation. Data were averaged over a one-second window and used to calculate the wind velocity at every second of the video. Figure 8.1 shows an example of a snapshot of a wheat plant under the wind tunnel with a masked frame after applying standard image processing operations.

From the captured video, various phenotypes defining the plant bending behavior are measured. Each frame of the video is masked and points on the windward edge of the plant are plotted (see Fig. 8.2). These points are fitted to a power-law curve ($y = cx^d$) that approximates the deformation profile of the stem. This fitted curve avails the bending angle θ at any instant during the test, as defined in Fig. 8.2. The bending angle at the maximum wind velocity during the test is denoted as $\theta_{\max}$. The stem bending resistance

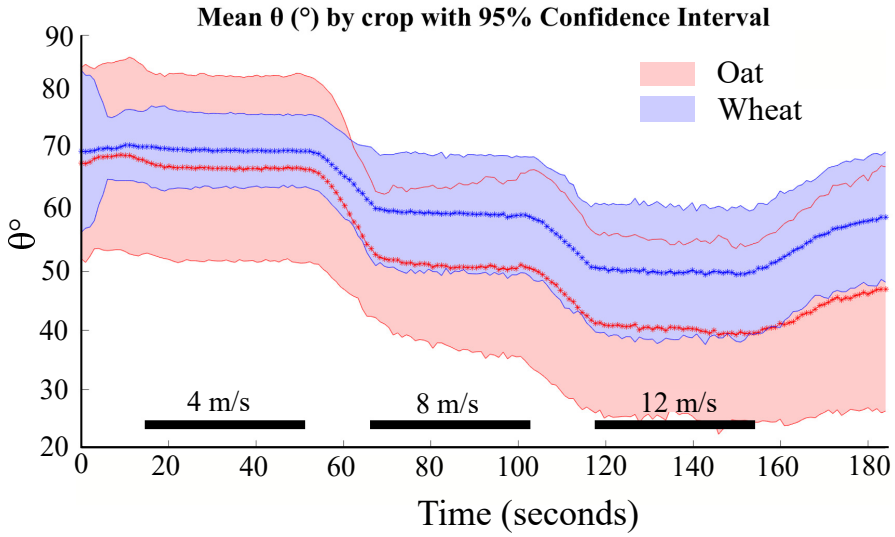

Fig. 8.3: *Stem bending angle values θ averaged for wheat and oat at each second over the course of the wind tunnel testing regime. Shaded areas represent 95% confidence intervals around the mean θ value for each crop at a given second.*

under the action of wind drag force is quantified using the coefficient of lodging resistance CL_r introduced by [75]. Previous studies have found a positive correlation between CL_r and the lodging severity observed in the field for different oat varieties [60, 75]. Therefore, it is anticipated that higher CL_r will correspond to the improved lodging resistance of cereals. CL_r is a proportional measure of the amount of torque resisted by a cereal stem during bending under a known force F. It is calculated as $CL_r = aF/bx$, where a, b and x in Fig. 8.2 are calculated when $\theta = 50°$ corresponding to the reference deformation associated with the measured force F. Similarly, to capture the aerodynamic behavior of stems, the drag coefficient C_d is calculated as $C_d = 2F/\rho_{\text{air}} v_w^2 A$, where ρ_{air} and v_w are the density and velocity of air, and A is the effective frontal area at the reference deformation ($\theta = 50°$) estimated using video data.

Tables 8.1 and 8.2 summarize the statistical results of this study. The crops, cultivar nested within crop, and block (position on the greenhouse bench) effects were analyzed using the analysis of variance (ANOVA) on C_d, $\theta_{\max}$, d, and CL_r response values using a typical linear regression model. For crop effects, we present the mean separations according to the least significant difference (LSD) test with a threshold value for $p < 0.05$. We calculated Pearson correlation coefficients among the linear relationships of the physical and video-derived plant phenotypes using the cultivar averaged values.

Table 8.1: *Mean separation for video estimated parameters between wheat and oat.*

Crop	Mean C_d	Mean CL_r	Mean d	Mean $\theta_{\max}$ (°)	Mean Recovery θ (°)
Oat	0.76	0.06*	0.63	45.9*	4.3
Wheat	0.68	0.13	0.59	53.8	5.19

* Asterisk indicates significant differences ($p < 0.05$) between means in the same column.

8.1.2 Results and conclusions from wind tunnel experiments

The crucial conclusions from these experiments in the light of lodging resistance of cereals are (1) the individual plant differences dictate the aerodynamic behavior of the cereal crops instead of the aggregate crop differences, (2) stem bending behavior quantified by CL_r and $\theta_{\max}$ is significantly stiffer for the wheat samples than the oat samples, (3) the ability to recover the original configuration after the wind exposure is better in the wheat plants as compared to the oat plants, and (4) the stem strength and CL_r are negatively correlated with the plant height and biomass in this experiment. We detail these conclusions in the following discussion.

The statistical test results for the drag coefficients (C_d) implies that the individual plant differences dictate the aerodynamic behavior of the cereal crops instead the aggregate crop differences. As assessed in this set of experiments at the reference deformation, the cereal drag coefficients (C_d) do not vary aerodynamically at the crop (p = 0.79), block (p = 0.71), or cultivar nested within a crop level (p = 0.66) in the ANOVA test. We note that $p < 0.05$ indicates a statistically significant difference among data sets. The LSD test results demonstrates high variability of C_d values within the crops without significantly different means (see Table 8.1). The mean reported C_d for the wheat samples is 0.68 with 95% confidence intervals of 0.41 and 0.96. While, C_d for the oat samples is 0.76 with 0.2 and 1.33 as 95% confidence intervals.

The coefficient of lodging resistance CL_r representing the stem bending behavior is significantly higher in the wheat than the oat plants. CL_r value at the reference deformation ($\theta = 50°$) vary significantly among the crops with p = 0.004. However, it does not vary among blocks (p = 0.26) or among cultivars nested within crops (p = 0.32). The wheat has a significantly higher mean CL_r than the oat according to the LSD test as summarized in Table 8.1. Stem bending curvature is represented by the power-law coefficient d, and this is not found to be significantly different between the crops ($p = 0.66$), blocks ($p = 0.4$) or cultivars nested within crops ($p = 0.12$). Similarly, in the LSD test, mean d coefficients among the crops are not significantly different at the reference deformation (see Table 8.1).

The bending angle at the maximum wind velocity $\theta_{\max}$ and the recovery angle after the

shutting of the wind tunnel fan relate with the response of the cereals stems in extreme storm events. The oat samples reach a significantly lower $\theta_{\max}$ and do not recover compared to the wheat samples. $\theta_{\max}$ varies significantly between the crops ($p = 0.008$), while the block ($p = 0.4$) and cultivar nested within crop ($p = 0.11$) effects are insignificant. Also, the wheat demonstrates a significantly higher mean $\theta_{\max}$ than the oat in the LSD test. Figure 8.3 plots the average bending profiles for the oat and wheat samples with the bending angle θ at every second of the test. The wheat shows a significantly greater θ, especially during the 12 m/s velocity regime in the wind tunnel in comparison to the oat that indicates a stiffer response of the wheat. The recovery angle does not vary significantly among the crops ($p = 0.11$) or cultivars nested within crops ($p = 0.08$), but does vary significantly among the blocks ($p = 0.03$). The mean recovery angle is higher in the wheat than the oat, though it does not differ significantly according to the LSD test. Moreover, the recovery angle is notably higher in the wheat following the cessation of the 12 m/s velocity regime in the wind tunnel (Fig. 8.3).

Table 8.2: *Phenotypic correlation matrix of Pearson correlation coefficients.*

	1.	2.	3.	4.	5.	6.	7.	8.
1. C_d								
2. CL_r	0.37							
3. $\theta_{\max}$	0.13	0.52*						
4. d	0.08	-0.24	-0.02					
5. Heading date	0.13	-0.20	-0.31	-0.52*				
6. Stem strength	0.46*	0.94***	0.39	-0.23	-0.01			
7. Plant height	0.19	-0.64***	-0.57**	0.11	0.31	-0.44		
8. Biomass	0.13	-0.44	-0.37	0.01	0.58**	-0.27	0.75***	

Significance codes: '***' 0.001, '**' 0.01, '*' 0.05.

Next, we present the correlations across cultivars of the major video derived phenotypes (CL_r, C_d , $\theta_{\max}$, and d) with the plant physical traits, including the stem strength, height and biomass in Table 8.2. The positive correlation of stem strength with both C_d and $\theta_{\max}$ implies that a higher wind velocity and drag force is required to achieve the reference deformation. Stronger cereal stems demonstrates a stiffer response and remain upright under increased wind drag force [21], which explains the positive correlation between the stem strength and drag coefficient.

Parameters quantifying stem bending such as CL_r and $\theta_{\max}$ reveals both significant differences among the crops and their physiological dependencies. CL_r and the stem strength are strongly correlated, as CL_r is essentially a scaled stem strength value with respect to the deformation profile characteristics. The positive relationship between the increased $\theta_{\max}$ and CL_r is also apparent as upright plants resist a greater proportion of the drag force

on the stems. The stem strength and CL_r are also negatively correlated with the plant height and biomass in this experiment. As anticipated, the plant height and biomass are positively correlated. Taller plants with higher biomass result in higher moments and shear forces experienced by the bottom internode sections, which lowers the stem strength.

8.2 Multiscale material-model-based finite element simulations of oat and wheat stems

Conclusions from the wind tunnel experiments lead us to the fact that the wheat stems response is stiffer than the oat, which eventually results in relatively better lodging resistance of the former. Beyond these conclusions, we can not confidently determine the causal relationship of this observed behavior with the physical traits of the plants such as chemical composition (lignin, hemicellulose, and cellulose content), tissue characteristics (volume fractions and cell structure of parenchyma, bundles etc.) and plant morphology (internode height, cross-section details). Adding each trait in the experimental study will lead to exorbitant labor and resource costs. In contrast, our multiscale material model for plants developed in Part I presents an opportunity for a physics-based understanding of the origin of experimentally observed behavior and its quantitative relation with physical traits at different length scales.

We, first, summarize the essential modeling details of integrating the multiscale material model into the finite element framework to simulate the single stem behavior of wheat and oat under the given wind conditions. Later, we validate the simulated deformation profile and failure behavior with the wind tunnel measurements. This work is done in collaboration with **Svetlana Baranova**.

8.2.1 Modeling details

Figure 8.4 outlines the conceptual overview of the multiscale material-model-based finite element simulation framework of single cereal stems under given wind conditions. In this figure, the green box summarizes all the input data required for the simulations. This data comprehensively characterize the single stem physiology that consists of (1) the constituent materials' chemical composition, (2) cellular structure and tissue characterization, and (3) plant morphology, including node, internode, and panicle characteristics. The blue box contains the prepossessing steps required for the finite element simulations, including (1) the generation of geometric model and mesh, (2) macroscale stiffness and strength properties, and (3) applied external wind drag force. Combining all these inputs, we build a finite

element model for wheat and oat stem in the commercial software ABAQUS (red box). Later, the simulation results (black box) are analyzed in conjunction with the wind tunnel experiment results for insights on the multiscale origin of lodging resistance in cereals. All the data are compiled in Appendix **D**. Multiscale material model is discussed in detail in Chapter 4 of Part I. We briefly discuss the other essential components of this framework.

Figure 8.5 illustrates a typical cereal plant anatomy and its schematic description with the measured plant morphology data, including the length of internodes, cross-sectional characteristics, and panicle characteristics. The data is compiled in Tables D.3 and D.4 in Appendix **D**. To create a geometric model for finite element simulations, we only include two lowermost internodes, given that stem failures have been generally observed in this region (see Fig. 8.5c). Node morphology in the model is derived from μ-CT data detailed in Section 4.1.1. We further assume that the oat and wheat internodes cross-sections are hollow cylinders with an outer radius as an average radius of the corresponding section.

The rest of the upper plant exerts an external gravitational force equal to its weight W_{u}, which is calculated as:

$$W_{\mathrm{u}} = g\left(m_{\mathrm{p}} + \rho\pi \sum_{i=3}^{4} L_i t_i \left(2r_i - t_i\right)\right), \tag{8.1}$$

where g is the gravity acceleration, m_p is the measured mass of panicle, ρ is the density of stem and assumed to be equal to 3×10^{-4} g/mm^3 for both oat and wheat, L_i t_i, and r_i are the length, thickness, and average cross-section outer radius of the corresponding section i, respectively (see Appendix **D**). In addition, the weight of the modeled part is introduced as a body force $G = \rho g$. To estimate the wind-induced drag force on the plant, we assume that only the panicle area contributes significantly and neglect the stem area for the calculations. This force is approximated via force F_{w} and moment M_{w} defined as:

$$F_{\mathrm{w}} = \frac{1}{2}\,\rho_{\mathrm{a}}\,A_{\mathrm{p}}\,C_{d,p}\,v_{\mathrm{w}}^2 \tag{8.2}$$

and

$$M_{\mathrm{w}} = F_{\mathrm{w}}\left(L_3 + L_4 + \frac{1}{2}h_p\right). \tag{8.3}$$

The symbols in these equations need further explanation: ρ_a is the air density as 1.225×10^{-6} g/mm^3, A_p is the panicle area, $C_{d,p}$ is the drag coefficient characterizing the aerodynamic characteristic of the panicle, v_w is the wind velocity, L_3 and L_4 are lengths of third and fourth internodes, and h_p is the panicle height. The bracket term in (8.3) is essentially the

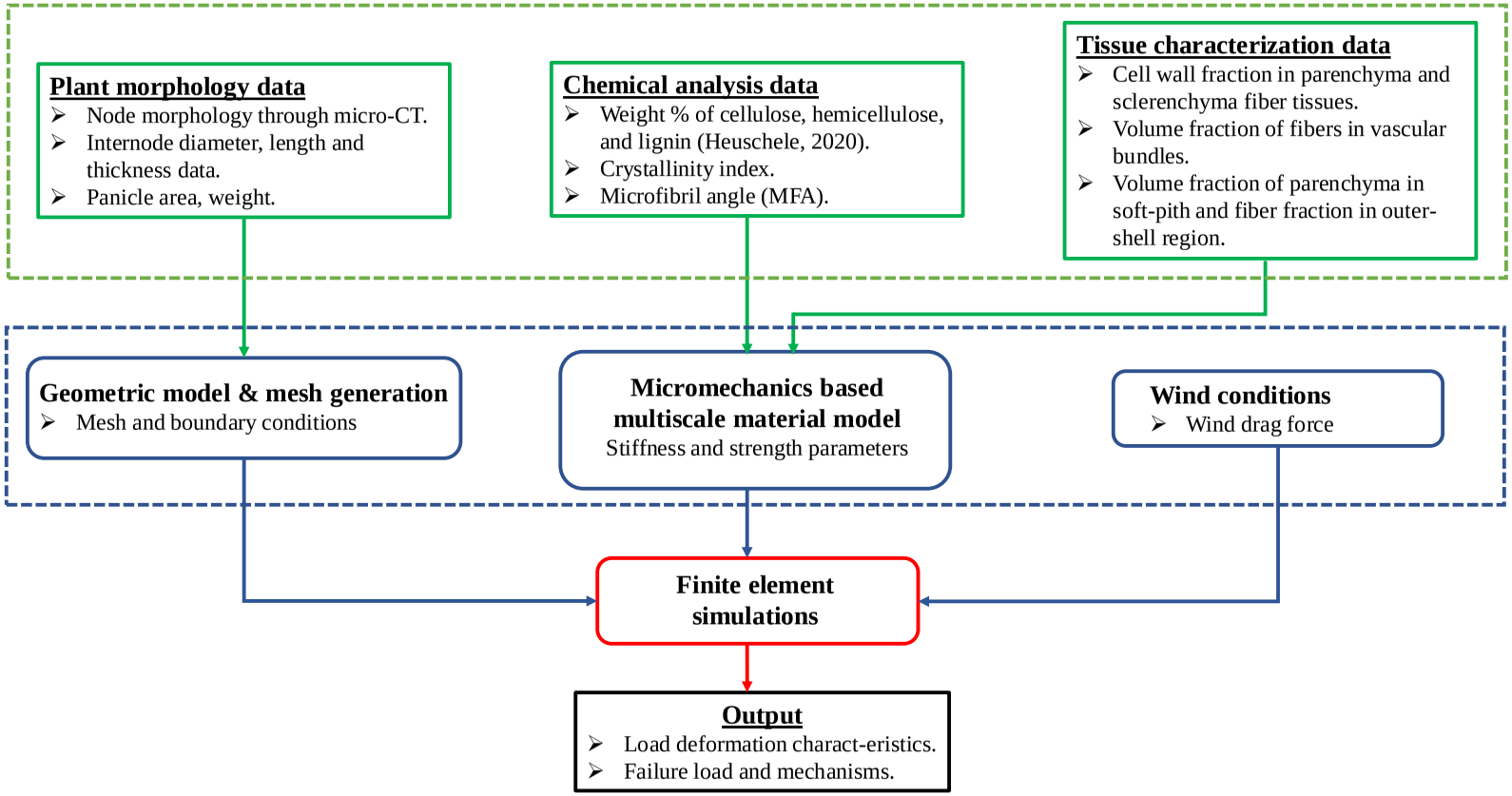

Fig. 8.4: *Conceptual overview of multiscale material-model-based finite element simulation framework.The green boxes indicate input data required for the model. Blue boxes denote the existing essential tools required to generate material and geometric properties for simulations with external applied wind drag force. Outputs are outlined in black.*

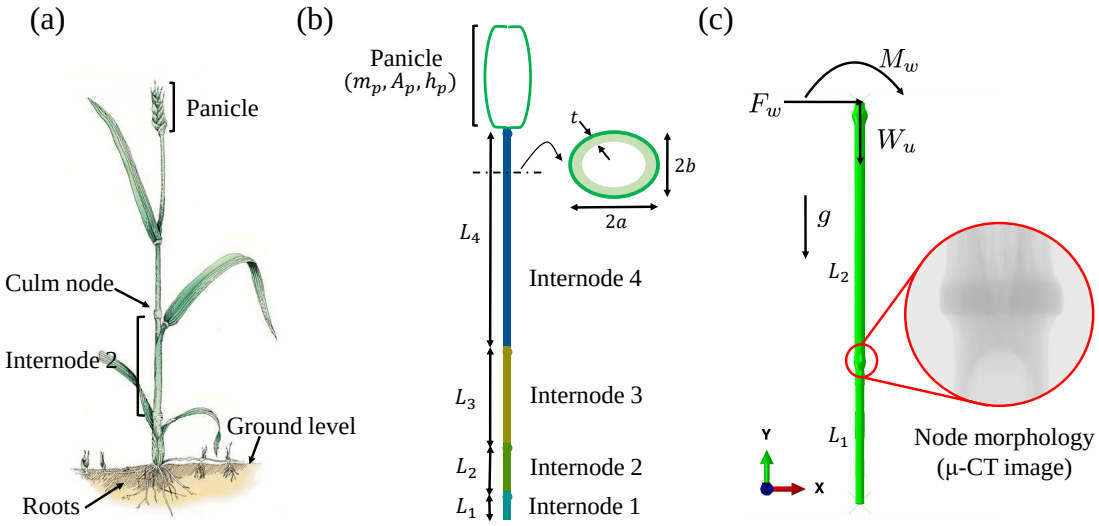

Fig. 8.5: *(a) Typical anatomy of a cereal plant, (b) Macroscale geometry of the plant denoting measured plant morphology traits, and (c) Geometric model utilizing node morphology from μ-CT data for finite element simulations with applied external forces.*

lever-arm of force F_{w} causing moment M_{w}.

We build a finite element model for each wheat and oat stem in the commercial software ABAQUS, discretizing the inner solid core region with twenty-node brick elements (C3D20R) and the outer shell region with eight-node shell elements (S8R), respectively. Since the basis functions of the shell conform with those of the solids at the coupling surface, surface locking between the shell and solid elements is prevented [158]. We assign the calculated macroscopic elastic stiffness moduli and strength properties for both the solid-pith and shell region. The bottom nodes of the model are fixed. Load conditions include body force G, applied through the whole model, and external forces F_{w}, W_{u} and moment M_{w}, applied to the upper node located at the center of the upper cross-section of the model. We perform nonlinear finite element analysis using the static-general algorithm in ABAQUS. The model deformation is computed in two steps: in *the loading step*, wind force F_{w} and moment M_{w} are gradually increased, simulating loading due to the wind condition. In *the unloading step*, they are gradually decreased, simulating the unloading process after wind conditions. The force W_{u} remains the same during all two steps.

8.2.2 Model validation with wind tunnel experiment results

We validate our framework by comparing the simulated deformation profile with the experimentally observed one in the wind tunnel (see Fig. 8.6). We extract the deformation profile from wind tunnel frames in the time interval when the flow velocity was stable at 8

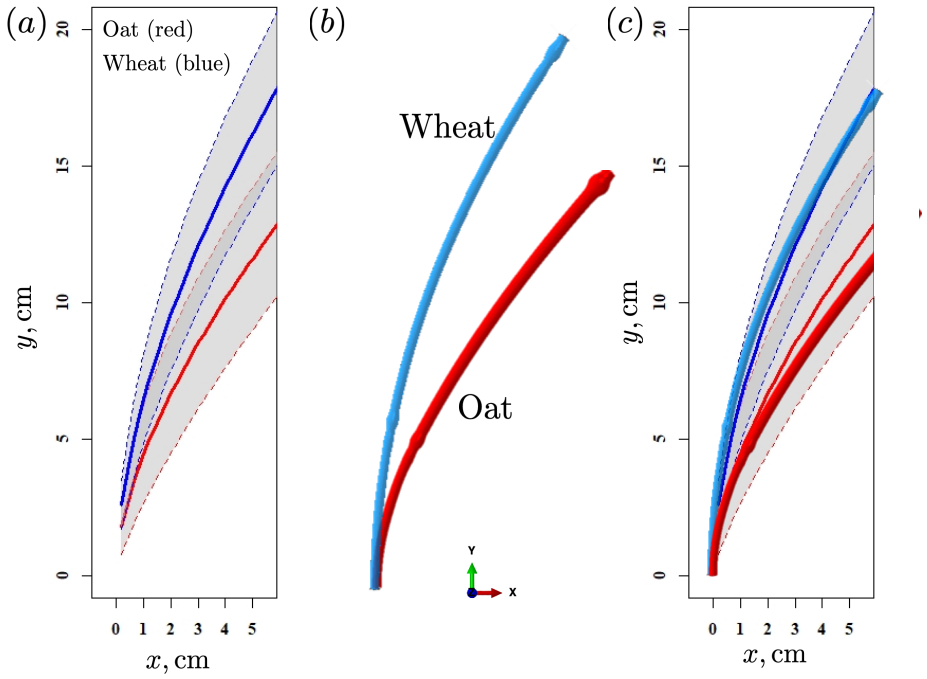

Fig. 8.6: *(a) Observed stem deformation in wind tunnel under wind velocity $v_w = 8$ m/s, (b) predicted stem deformation from simulations for $v_w = 8$ m/s, (c) superposition of (a) and (b).*

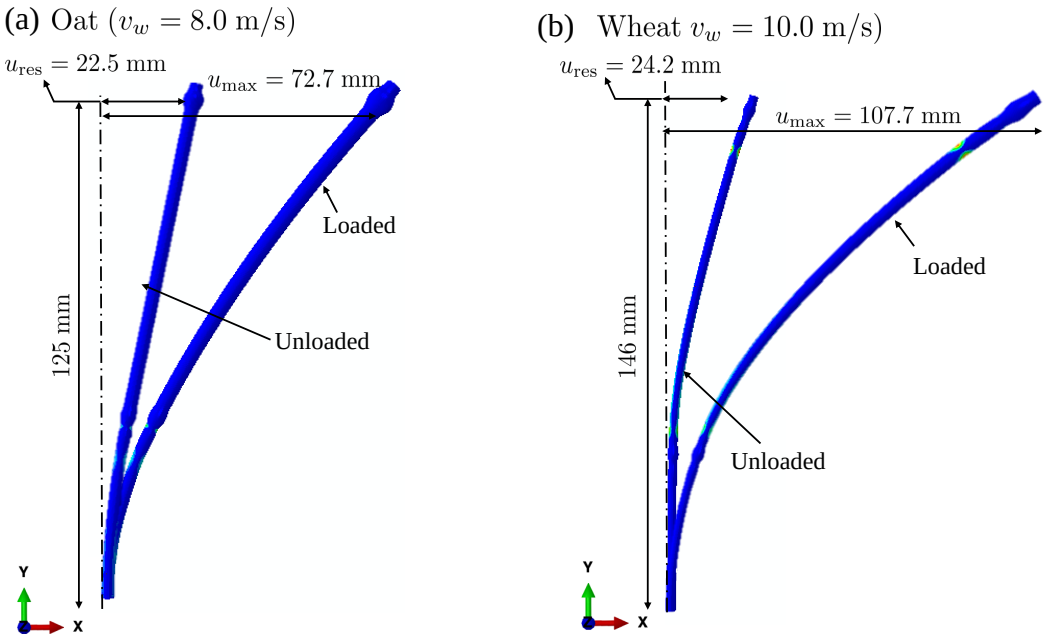

Fig. 8.7: *Deformed profiles for both (a) oat and (b) wheat after loading/unloading steps at limiting wind velocity levels 8.0 m/s and 10.0 m/s, respectively.*

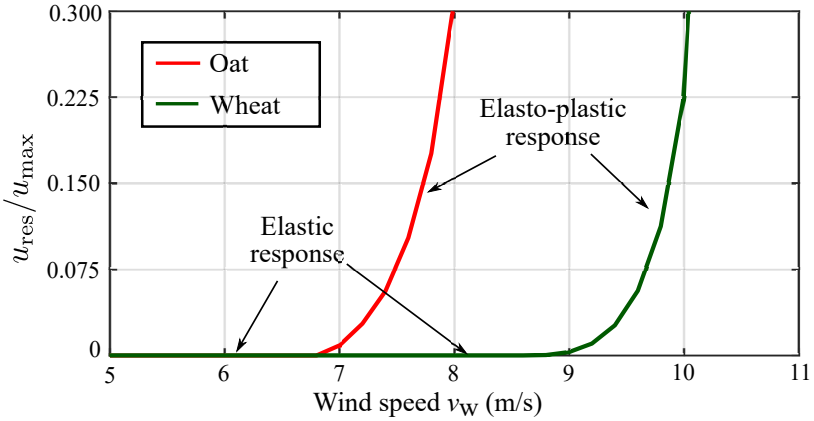

Fig. 8.8: *Residual ratio u_{res}/u_{max} vs. wind velocity v_w for oat and wheat models with distinct elastic and elastoplastic regions.*

m/s for all oat and wheat cultivar/rep combinations. We convert this data into the mean deformation profiles with 95% confidence intervals for both cereals (see Fig. 8.6a). All the required parameters for simulating deformation profile under given wind velocity are listed in Appendix **D** except the drag coefficient for panicle $C_{d,p}$ in (8.2). In general, the drag coefficient is not an absolute constant for a given body. It varies with the wind velocity and transient shape characteristics. We assume $C_{d,p} = 0.5$ close to the drag coefficient of a vertical cylinder in crossflow for simplification. The simulated deformation profile for the wind velocity $v_w = 8$ m/s is superimposed on the observed deformation profiles in Fig. 8.6c. The comparison demonstrates that the simulations sufficiently predict the observed deformation profiles under the given wind conditions.

Next, we investigate the failure behavior of both wheat and oat stems. We simulate multiple scenarios for wind-induced drag force levels corresponding to the wind velocity v_w experienced in the wind tunnel. As mentioned, the simulations are performed in two steps: the *loading step* and *unloading step*. Variables u_{max} and u_{res} are introduced as maximum absolute values of displacement of the upper nodes of models after loading and unloading steps, respectively. If the stem recovers to its initial position, that is $u_{res} = 0$, the stem remains in the elastic range with no material damage or plastification for this wind velocity level. Whereas, a nonzero residual displacement after unloading ($u_{res} \neq 0$) implies the elastoplastic behavior of the stem with permanent material damage.

Figures 8.7 and 8.8 illustrate the relative differences in the failure behavior of wheat and oat stems. We define a residual ratio corresponding to wind velocity v_w as u_{res} scaled with respect to u_{max}, that is, u_{res}/u_{max}. We simulate both stems for wind velocity levels until the residual ratio u_{res}/u_{max} reaches 0.3, which we define as the maximum wind-induced drag force endured by them stems before failure. This limiting wind velocity level is 8.0 m/s for

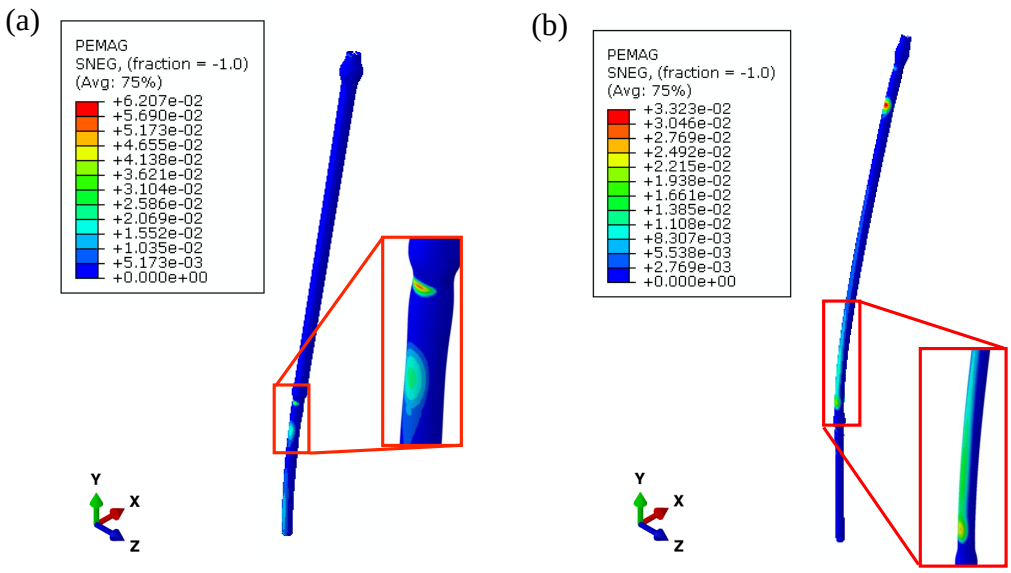

Fig. 8.9: *Distribution of plastic strain (PEMAG) among (a) oat's stem after unloading step ($v_w = 8.0$ m/s) and (b) wheat's stem after unloading step ($v_w = 10.0$ m/s).*

oat and 10.0 m/s for wheat. Figure 8.7 shows the deformation profiles for both cereals after loading/unloading steps for these wind velocity levels with u_{res} and u_{max} values. Figure 8.8 plots the residual ratio $u_{\text{res}}/u_{\text{max}}$, with applied wind velocities v_{w}. The figure also points to two distinct regions denoting the elastic and elastoplastic response of stems against the applied wind load. This plot can also be interpreted as a representative load-displacement curve, where the residual ratio is the characteristic displacement and the wind-induced drag is the characteristic force.

It is clear from these figures that the wheat stem fails at a higher wind velocity level as compared to the oat stem. Moreover, the recovery at the same level of wind velocity is better for wheat than the oat. These graphs also agree with the experimental results summarized in Fig. 8.3. The oat samples experienced permanent damage during the 8 m/s wind velocity regime with little recovery after the wind tunnel was switched off. The simulated limited value 8.0 m/s falls within this velocity regime. While, the wheat samples did not show any visible damage and exhibited better recovery after withstanding maximum wind velocity of 12 m/s. Our simulations successfully predict these differences.

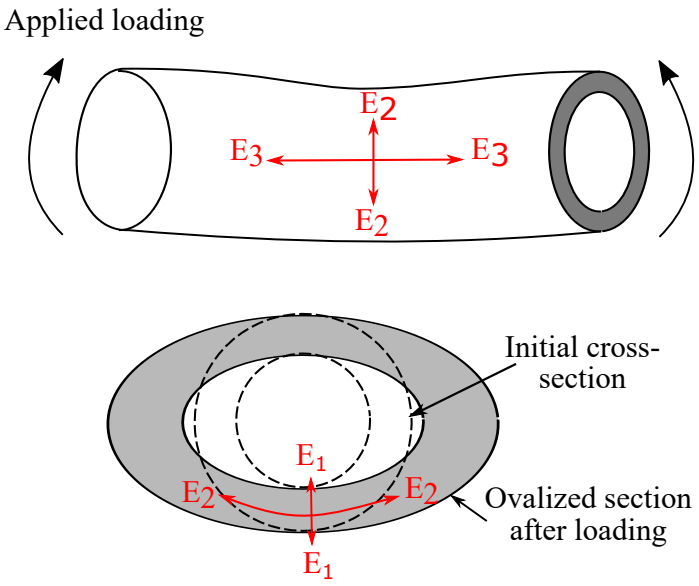

Fig. 8.10: *Ovalization of cross-section with associated stiffness parameters.*

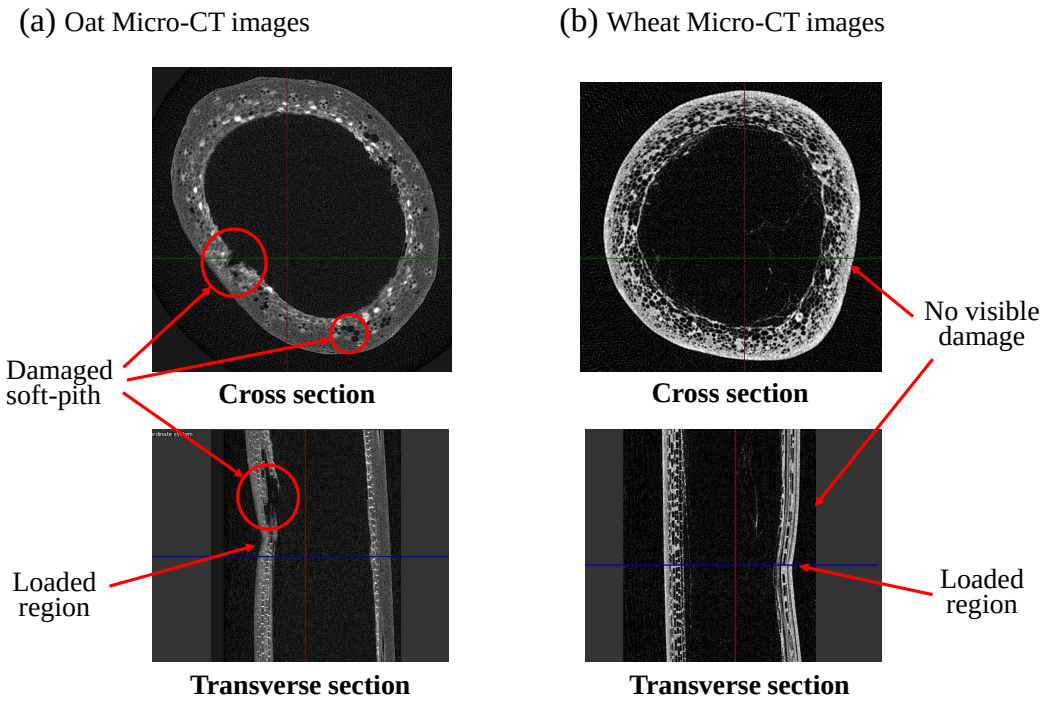

Fig. 8.11: *Micro-CT investigations into the (a) oat and (b) wheat samples after loading/unloading process, demonstrating evident cross-section ovalization and material damage in oat, as compared to wheat.*

8.3 Simulations driven insights into the origin of stem deformation and failure behavior

The integrated multiscale material model presents an opportunity to explain the origin of the overall stiffer response of wheat that leads to its lodging resistance. A careful investigation of parameters characterizing the hierarchical structure of oat and wheat reveals two important differences: (1) the lignin percentage in the cell wall material in wheat is higher than the oat (see Table D.1), and (2) the cell wall fraction in parenchyma tissues of the wheat stem is higher than that of oats (see Table D.2). These differences lead to the stiffer and stronger soft-pith region in wheat compared to oat, which is evident from the calculated stiffness and strength parameters. In particular, the transverse stiffness and strength (E_1, E_2 and σ_{11}, σ_{22}) are significantly higher in wheat than oat. The other important distinction in the plant morphology of both cereals is that the first internode cross-section in wheat is almost solid with no hollow space (see Table D.3). The shear forces and moments generated by external forces are higher in the lower part of the plant and, therefore, require a stiffer response. The plant morphology characteristics and the stronger solid-pith in wheat ensured this stiffer response.

The recovery of cereals to the original position following wind exposure is crucial from a lodging resistance perspective. The amount of recovery relates to the extent of material damage at the tissue level. Cereals can heal the tissues after the damage. Therefore, if the material damage is limited, the stem heals to the original strength, contributing to its lodging resistance. Plastic strain profiles in Fig. 8.9 represent the extent of material damage in both wheat and oat. The nodal region near the first internode is particularly important. The plastic strains are concentrated in the region just below the first node in the oat stem, which encompasses the local material damage. All the oat samples in the wind tunnel report such damage in the first internode. In the wheat stems, however, the plastic strains are distributed along the first internode region, avoiding any significant localized material damage. This optimal distribution in wheat results in better recovery and, hence, better lodging resistance than the oat.

The origin of these distinct mechanisms in oat and wheat lies in the underlying physics at different length scales in their hierarchical organization. The strength of both soft-pith and outer-shell regions results from the yielding of lignin in the cell wall material. Higher parenchyma cell wall fraction and lignin percentage in wheat result in the transverse stiffness and strength parameters three times compared to oats. The localized material damage is initiated by the ovalization of a plant's cross-section. Figure 8.10 visually explains this ovalization process of stem cross-section with the associated stiffness parameters. With

comparable axial stiffness E_3, the solid-pith's transverse stiffness ($E_1 = E_2$) dictates the ovalization induced material damage. Thus, the reduced transverse stiffness and strength of the soft-pith region in oat facilitate the ovalization with limited prevention of local material damage compared to wheat.

The Micro-CT investigations also support these insights into the stem samples after the loading/unloading process (see Fig. 8.11). Oat and wheat internode samples were subjected to displacement-controlled loading using a universal testing frame (MTS Instron 858 Mini Bionix II) with a 500 N load cell. Once the specimen lost its structural integrity, the force began to decrease. Thereafter, we unloaded the specimen and imaged the loaded area using a Micro-CT machine. Figure 8.11a shows a clear ovalization of the oat cross-section as compared to wheat. A closer look at these images reveals the ruptured tissues in the oat cross and transverse section views at multiple places. However, the wheat images show an intact cross-section with no visible damage to the soft-pith material. This visual evidence strongly supports our model-driven insights into the failure behavior of both cereals.

Chapter 9

Predicting self-adapting mechanisms through concurrent material and structure optimization concepts

In the previous chapter, we substantiated the benefits of multiscale material-model-based simulations in interpreting the experimental results for improved breeding of lodging-resistant cereals. The multiscale analysis enables us to understand the origin of existing observed failure mechanisms that help future breeding decisions. However, predicting an ideal lodging resistant variety, in a brute-force sense, requires testing all possible combinations of traits or design variables. This leads to computationally prohibitive costs since the number of design variables is exorbitant for this application. Therefore, a rational design strategy is required for predicting complex combinations of traits that could lead to an ideal lodging-resistant variety.

In this chapter, we demonstrate the potential of our optimization framework to overcome the mentioned challenges and in reproducing the naturally existing self-adapting mechanisms in plants. Conceptually, we start from the fact that biological materials and structures have attained a certain degree of optimality through evolutionary selection. The optimized configurations from our framework should point towards the ideal plant configuration for intended applications. We introduce two prototype examples, involving bamboo and cereal stems, as a template to rationally understand the adaptive mechanisms utilizing the optimization framework developed in Part II.

This chapter is organized as follows: Section 9.1 is a perspective note that examines self-

adaption and growth from a mechanical optimization viewpoint. In Section 9.2, we set up an end-compliance type problem for the hierarchical optimization of bamboo. Section 9.3 works towards finding traits for lodging resistant cereals by reproducing dissipation mechanisms in the node regions via our optimization framework.

9.1 "Newtonian" perspective on self-adaption of biological systems

A mechanical perspective of growth or self-adaption in biological materials, in the case of bone, can be traced back to Wolff to almost 130 years back in 1892 [192]. Wolff took inspiration out of Culmann's, a civil engineer, graphical statics [42] and compared the alignment of the cancellous tissue of the human femur with the stress trajectories of a curved crane-like beam. He concluded that the similarity in patterns could not be coincidental, and the mechanical load applied to living bone influences the structure of bone tissue. He himself nicely summarized this argument as (from the translation [193] of the original paper [192]): *"Thus the law of bone remodeling is the law according to which alterations of the internal architecture clearly observed and following mathematical rules, as well as secondary alterations of the external form of the bone following the same mathematical rules, occur as a consequence of primary changes in the shape and stressing or in the stressing of the bones."* This statement of Wolff or often stated as "Wolff's law" has formed the foundation of research in paleontology, bio-archaeology, and bone remodeling to this date [154]. Similar mechanical, or say *"Newtonian,"* principles have been the starting point for studying growth/self-adaption in other biological systems, including tumor tissues, cardiovascular systems, and plants [8]. We emphasize the striking parallels of Wolff's statement with overarching goals of our concurrent material (*internal architecture*) and structure (*external form*) optimization of multiphase hierarchical systems.

Several studies, however, in recent decades have criticized and questioned Wolff's premises of mathematical (or mechanical) treatment of self-adaption and remodeling [23, 41, 43, 142]. These criticisms have started vigorous debates on approaching growth and self-adaption research, and biologists and mechanists happen to differ substantially. These different viewpoints are well reflected in the articles titled *"The 'Law of bone transformation': A case of crying Wolff?"* by Bertram & Swartz [23] and *"The law of adaptive bone remodeling : A case for crying Newton?"* by Huiskes [100] arguing from biology and mechanics perspective, respectively. These articles are captivative reads, as the titles suggest, to understand both the viewpoints. In summary, broad criticisms by biologists are (1) the Wolff law is an oversimplification to understand adaption and growth, (2) it does not offer

any explanation on the biological mechanisms behind adaption, and (3) the growth and adaption can be explained by other non-mechanical causes. Mechanists counter argue that if the consistent set of assumptions or "Algorithm" led to useful predictions or answers, even the intrinsic validity of assumptions are not well understood with the current state of knowledge, Algorithm holds a substantial value.

We delve into more details on the key concerns of biologists on this issue following [44]. The reason for divergences in the observed growth behavior from purely mechanics-based predictions is that the living biological system has to satisfy many *non-mechanical and phylogenetic constraints* while optimizing its mechanical response. These constraints could be so overwhelming that the observed morphology may be far from the mechanically "ideal" configuration. The *non-mechanical constraints* include reproductive, food, functional, and physiological demands of the biological system. These demands essentially reflect in the chemical reactions happening at the cellular and molecular levels. These reactions happen close to the chemical equilibrium. This requirement essentially limits the rate of change of material characteristics from an energetic perspective. This also explains the often used rate of strain energy (or strain) based phenomenological models in the growth literature.

Evolutionary history or *"phylogeny"* of a biological system constrains the extent of possibilities for mechanical optimization of the system. Natural selection works step-by-step, and every modification must be immediately better to the existing system; otherwise, it will not survive (*survival of the fittest*). In the mechanistic language, if a system is currently at some point in a fitness hyperspace defined in terms of possible genetic variables, the natural selection in the next step will push the current state up the steepest possible slope in this hyperspace. It implies that the biological systems seek the immediate local optimum in each natural selection step and can not moves towards a global optimum from these local optimum states. Therefore, the current state of a biological system is achieved by a series of humongous local optimization problems, which does not necessarily lead to a global optimum. This restriction explains why biological systems are not mechanically "ideal."

Keeping both perspectives in mind, we insist on the relevance of a broader "Newtonian" or mechanistic view in the study of adaption mechanisms in biological materials. However, we emphasize the importance of considering the non-mechanical and phylogenetic constraints in the representative predictions of growth and adaption. We have examined the energetic perspectives of these constraints and believe that our optimization framework in current form or with relevant changes can rationally integrate them, given the evidence-based quantification of these constraints. For instance, the non-mechanical constraints can be quantified in terms of the tissue material fraction satisfying its intended biological purpose and can be integrated as bounds in material optimization problems. Similarly, phylogenetic constraints can be reflected in the choice of optimization methods that force the design

variables to reach the nearest local optimum. We emphasize that the collaborative efforts by the experimental biologist and computational mechanists will improve the understanding of growth, and both viewpoints will eventually converge.

In this chapter, we introduce two prototype examples involving bamboo and cereal stems as a first step to outline a broader approach to understand self-adaption mechanisms at multiple length scales in plants utilizing our optimization framework. In addition to incorporating discussed constraints, the computationally tractable multiscale analysis represents a main challenge for any optimization framework to approach these problems [36, 149, 153]. We have established that our optimization framework is capable of handling these computational challenges. We believe that our framework presents a promising opportunity to study growth and adaption and especially their relationship with the lower length scales, which is currently missing in the literature. We note that we, by no means, claim to answer all the raised concerns in this chapter. However, these examples can be work as a template on which detailed models can be built in the future.

9.2 Hierarchical optimization of bamboo culm

In this section, we demonstrate the potential of our end-compliance based optimization framework developed in Chapter 5 to explore the self-adapting mechanisms for bamboo materials. Bamboo does not show secondary growth of tissues and therefore heavily relies on microstructure optimization at the material level [7, 116]. Figure 9.1 illustrates that microimaging results confirm the functional optimization in bamboo materials at different length scales [49, 121]. In Chapter 3, we have developed and validated a multiscale material model of bamboo culm material. Here, we integrate this material model in our optimization

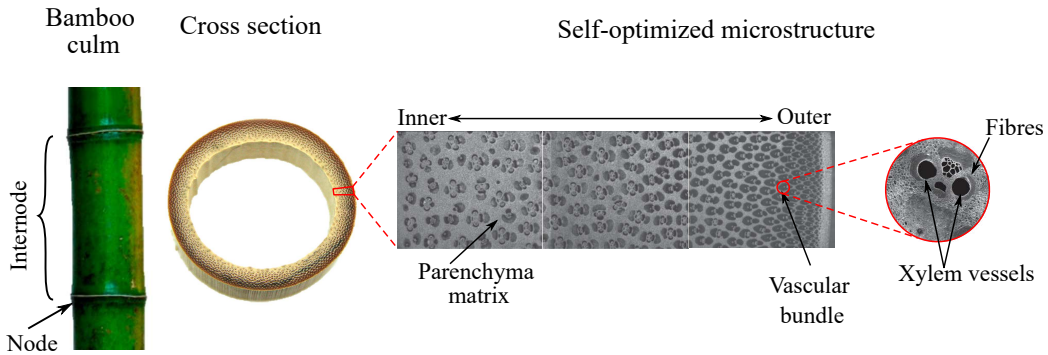

Fig. 9.1: *Macroscale anatomy of bamboo with microstructure details through scanning electron microscopy images. The images are reported by* Mannan, Knox *and* Basu *[121] and reproduced with kind permission from Royal Society Publishing.*

framework to reproduce the self-optimizing mechanisms in the natural hierarchical system of the bamboo culm. Please refer to Chapter 5 for the detailed meaning of each symbol.

Figure 9.2 summarizes the resulting hierarchical optimization problem. We assume that bamboo culm adapts itself to optimally resist bending caused by lateral wind loads. We model one quadrant of the bamboo cross-section under symmetry boundary conditions and apply linearly varying radially symmetric axial strains. The outer and inner radius of the quadrant are 90 mm and 72 mm. This strain distribution is equivalent to the combination of pure bending caused by lateral wind from each direction. With known axial strains and zero out-of-plane shear strains, the problem can be reduced dimensionally such that only in-plane displacements and strains are unknown. Thus, the quadrant is discretized with a 90×13 mesh of 4-node quadrilateral generalized plane strain elements, where the aspect ratio of each element is as close to one as possible.

We refer to Section 3.3 for further details on the multiscale characterization and homogenization of the elastic properties of bamboo culm. In the current model, we assume that the cell wall fraction $\phi_{wall}^{par(x,j)}$ in the parenchyma tissues, the fiber fraction $\phi_{fib}^{x,j}$ in the vascular bundles, and the vascular bundle fraction $\phi_{vb}^{x,j}$ at the cross-section scale are the microstructure design variables at each Gauss point in the domain. Bamboo is a transversely isotropic material, being isotropic in the cross-sectional plane. The macroscale homogenized stiffness tensor in (3.9) as a function of the microscale design variables can be rewritten as:

$$\mathbb{C}_{sec}(\mathbb{C}_{par}(\phi_{wall}^{par(x,j)}),\mathbb{C}_{vb}(\phi_{fib}^{x,j}),\phi_{vb}^{x,j}) = \Big\{(1-\phi_{vb}^{x,j})\,\mathbb{C}_{par} + \phi_{vb}^{x,j}\mathbb{C}_{vb} : [\mathbb{I} + \mathbb{P}_{cyl}^{par} : (\mathbb{C}_{vb} - \mathbb{C}_{par})]^{-1}\Big\} : \Big\{(1-\phi_{vb}^{x,j})\,\mathbb{I} + \phi_{vb}^{x,j}[\mathbb{I} + \mathbb{P}_{cyl}^{par} : (\mathbb{C}_{vb} - \mathbb{C}_{par})]^{-1}\Big\}^{-1}. \tag{9.1}$$

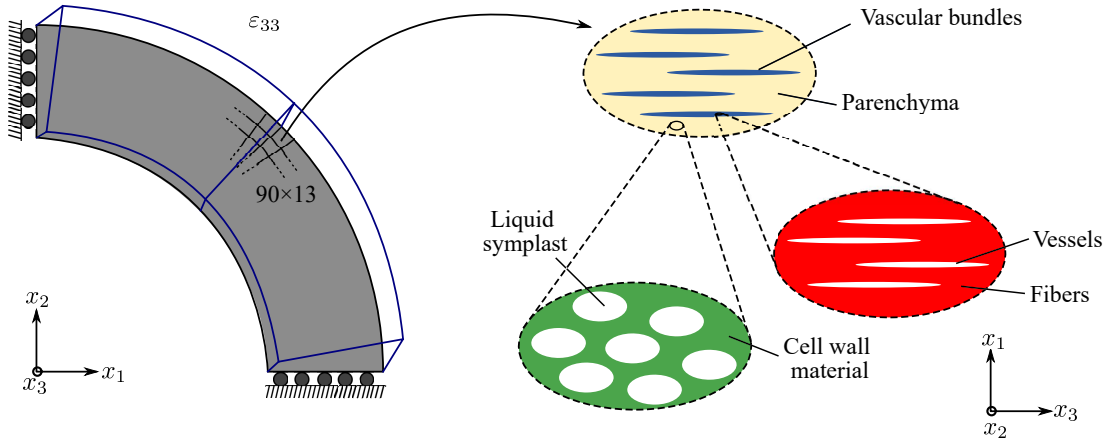

Fig. 9.2: *Model problem for the hierarchical optimization of bamboo culm.*

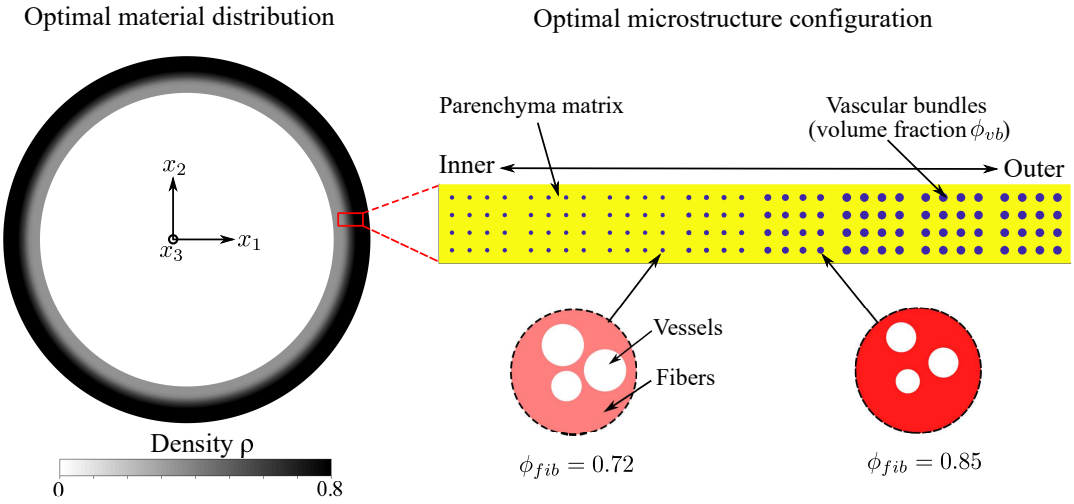

Fig. 9.3: *Optimized material distribution and microstructure configuration for the bamboo culm example.*

Here, $\mathbb{C}_{par}$ and $\mathbb{C}_{vb}$ are the homogenized stiffness tensors of parenchyma tissues and vascular bundle tissues, calculated following (3.6) and (3.8).

We write the discretized optimization statement of the material optimization sub-problems for the bamboo example following (5.14):

$$\begin{aligned} \bar{m}_j^x = \underset{\phi_{wall}^{par},\phi_{fib},\phi_{vb}}{\arg\max} \; : \; & \frac{1}{2}\boldsymbol{E} : \mathbb{C}_{sec}(\phi_{wall}^{par}, \phi_{fib}, \phi_{vb}) : \boldsymbol{E} \\ \text{s.t.} : \; & \rho = \rho_{wall}\phi_{wall}^{par}(1-\phi_{vb}) + \rho_{fib}\phi_{fib}\phi_{vb} \\ & \phi_{wall}^{par,min} \le \phi_{wall}^{par} \le \phi_{wall}^{par,max} \\ & \phi_{fib}^{min} \le \phi_{fib} \le \phi_{fib}^{max} \\ & \phi_{vb}^{min} \le \phi_{vb} \le \phi_{fib}^{max}, \end{aligned} \tag{9.2}$$

where ρ is the given macroscale dry density for the relevant finite element. ρ_{wall} and ρ_{fib} are the density of cell wall materials and sclerenchyma fibers. The first statement in the constraints simply connects ρ with the microscale design variables through the rule of mixture. This optimization problem is a constraint optimization problem with nonlinear equality constraint. We utilize the Sequential Least Squares Programming (SLSQP) method implemented in the SciPy library to solve this problem.

The bounds on the design variable in (9.2) reflect non-mechanical constraints. In bamboo plants, parenchyma tissues and xylem-phloem vessels are responsible for food storage and nutrient-water transport, respectively, and are therefore required to be built in for functional reasons. We incorporate this biological constraint by adopting the bounds on these volume

fractions that are experimentally reported in [49] in the material optimization problem. These bounds for ϕ^{par}_{wall}, ϕ_{fib}, and ϕ_{vb} are $[0.18, 0.22]$, $[0.70, 0.95]$, and $[0.15, 0.60]$, respectively.

The structure optimization problem to obtain the optimal material density distribution is rewritten following (5.11) as:

$$
\begin{aligned}
&\min_{\boldsymbol{\rho}} : f_c(\boldsymbol{\rho}) = \bar{\boldsymbol{u}}^T \boldsymbol{K}_{opt} \bar{\boldsymbol{u}} \\
&\text{s.t.} : \bar{\boldsymbol{r}} = \boldsymbol{f}^T_{ext} - \sum_{j=1}^{N_e} \left[\sum_{x=1}^{N_{gp}} \boldsymbol{B}^T \, \mathbb{C}_{sec}(\bar{m}^x_j) \, \boldsymbol{B} \, w_x \right] \bar{\boldsymbol{u}}_j = 0 \\
&\qquad M(\boldsymbol{\rho}) = \sum_{j=1}^{N_e} \rho_j |\Omega_j| = M_{req} = \rho_{avg} \times |\Omega| \\
&\qquad \rho_j \in [\rho_{min}, \rho_{max}], \ \forall j = 1, 2, ..., N_e \ .
\end{aligned}
\tag{9.3}
$$

At the structure scale, the total amount of material is restricted by the reported average density ρ_{avg}. We interpret this constraint as the limitation posed by the available biological energy required in the synthesis of biomass per unit volume in the bamboo plant. The sensitivity analysis for the macroscale design update follows from Section 5.2.4. The first derivative of $\mathbb{C}_{sec}$ with respect to density ρ_j is replaced with

$$
\frac{\partial \, \mathbb{C}_{sec}(\bar{m}^x_j)}{\partial \rho_j} = \frac{\partial \, \mathbb{C}_{sec}}{\partial \phi^{par}_{wall}} \frac{\partial \, \phi^{par}_{wall}}{\partial \rho_j} + \frac{\partial \, \mathbb{C}_{sec}}{\partial \phi_{fib}} \frac{\partial \phi_{fib}}{\partial \rho_j} + \frac{\partial \, \mathbb{C}_{sec}}{\partial \phi_{vb}} \frac{\partial \phi_{vb}}{\partial \rho_j} \ . \tag{9.4}
$$

The derivative of $\mathbb{C}_{sec}$ with respect to microscale design variables at the material level is evaluated using finite difference approximations. The move parameter μ, the damping parameter η, and the design sensitivity filter radius r_{min} for macroscale design update are 0.02, 0.5, and 0.01.

Figure 9.3 illustrates the optimized material distribution at the structure scale and the optimized material microstructure configuration, both obtained with our framework. The optimum density distribution exhibits a strong gradient towards the outer part of the cross section, which is in agreement with the engineering intuition and consistent with experimental observations. Figure 9.3 also plots the optimized mesoscale morphology along a radial strip of eight 4-node elements. The yellow color represents the parenchyma matrix, and the area of blue circles represents the optimized volume fraction ϕ_{vb} of vascular bundles at a particular location. We also plot the optimized vascular bundle morphology at two locations, showing different fiber volume fractions ϕ_{fib}. The obtained radial trends for the microscale design variables follow the trends experimentally reported in [49]. We, therefore, conclude that our framework can quantitatively predict the functional organization and self-adapting mechanism for this natural hierarchical system.

9.3 Treating genetic tailoring of cereals as an optimization problem

In this section, we approach the problem of finding suitable traits to breed lodging-resistant cereals from a concurrent material and structure optimization viewpoint. In the last chapter, we observed that the node regions are of particular interest from a macroscale mechanical behavior perspective. The plant stems are slender and susceptible to local buckling. From the structure mechanics standpoint, these nodes act as shear stiffeners in a cereal stem structure and increase the resistance to local buckling substantially. However, the nodes become a preferred region for stress concentrations resulting in the macroscopic failure initiated by elastoplastic material damage near node regions, as concluded in the previous chapter. We investigate the self-adaptive dissipation mechanisms in cereal nodes utilizing our optimization framework presented in Chapter 7.

We summarize the model prototype problem for the hierarchical optimization of a cereal node region in Fig. 9.4. We take the length and height of the macrostructure domain as 10 mm and 5 mm, typical to a node dimensions. The left edge is completely fixed, and the right edge is controlled to ensure that the displacement in the X direction is fixed. The prescribed displacement loading in the Y direction on the right edge at all the nodes on the boundary is equal to $\boldsymbol{u}^* = 0.4$ mm. The displacement load $\boldsymbol{u}^* = 0.4$ mm is reached in four loading time steps with constant load increments of $\Delta\bar{\boldsymbol{u}}^E = 0.1$ mm. We discretize the macroscale structure with a 60×30 mesh of 4-node quadrilateral elements. This macrostructure model definition is equivalent to a cereal node cross-section that undergoes combined shear and

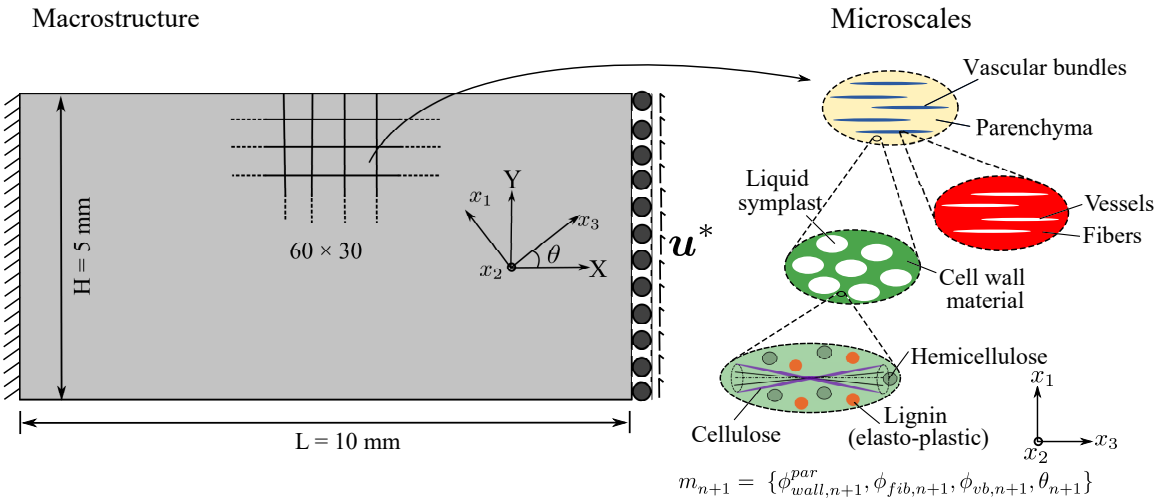

Fig. 9.4: *Model problem for the hierarchical optimization of cereal node region.*

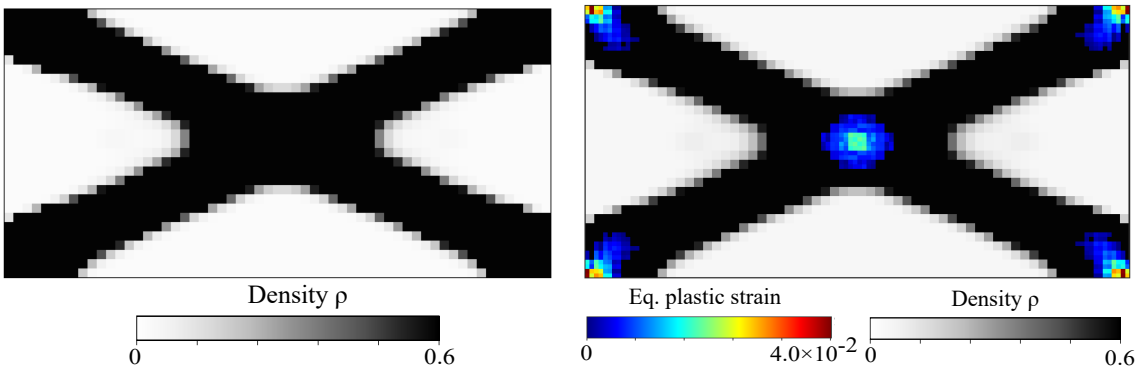

(a) Optimum desity distribution. **(b)** Equivalent plastic strain distribution.

Fig. 9.5: *Final design of the cereal node region with equivalent plastic strain distribution for total prescribed displacement load of* $\boldsymbol{u}^* = 0.4$ *mm.*

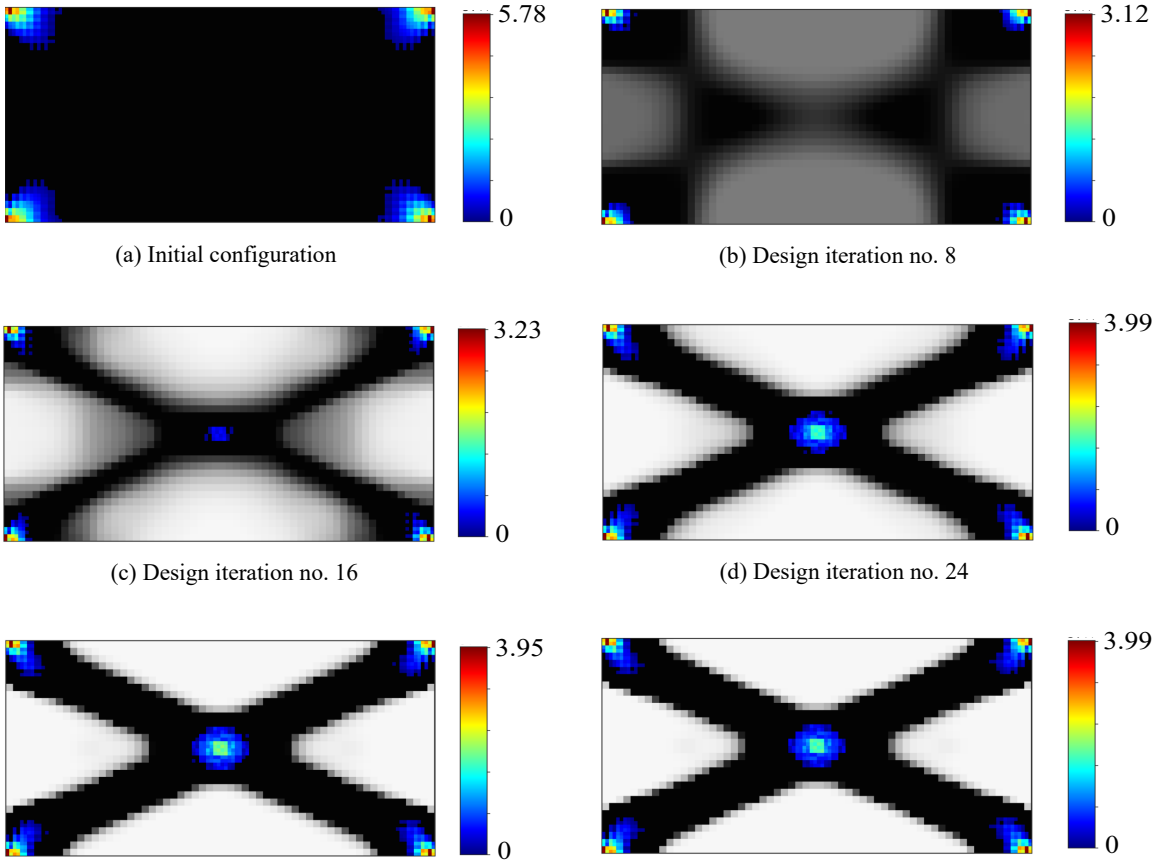

(a) Initial configuration (b) Design iteration no. 8

(c) Design iteration no. 16 (d) Design iteration no. 24

(c) Design iteration no. 32 (f) Final design

Fig. 9.6: *The evolution of macroscale density configuration with design iterations with equivalent plastic strains in* $\times 10^{-2}$ *units (overlaid on corresponding density distribution in rainbow colormap).*

bending loads.

We integrate the multiscale material model for homogenized elastic and limit state properties of cereal stems developed in Chapter 4. The dense epidermal layers or outer-shell primarily perform various non-mechanical biological functions such as protecting against the insects, regulating gas exchanges, and metabolism. Thus, it is not included in the current model and only solid-pith is considered for the hierarchical optimization. The microstructure design variable $m_{n+1}^{x,j}$ consists of the cell wall fraction $\phi_{wall,n+1}^{par(x,j)}$ in the parenchyma, the fiber fraction $\phi_{fib}^{x,j}$ in the vascular bundles, the vascular bundle fraction $\phi_{vb}^{x,j}$ in the solid pith, and the orientation $\theta_{n+1}^{x,j}$ of the anisotropy axis of the solid-pith from global X direction (see Fig. 9.4). We again note that the subscript index $(n+1)$ denotes the time increment, and superscript index (x,j) denote the Gauss point index x in element j.

The macroscale homogenized stiffness tensor $\mathbb{C}$ in global co-ordinate system as a function of the microscale design variables $m_{n+1}^{x,j}$ can be written following (4.7) as:

$$\mathbb{C}_{pith}(\mathbb{C}_{par}(\phi_{wall,n+1}^{par(x,j)}),\, \mathbb{C}_{vb}(\phi_{fib,n+1}^{x,j}),\, \phi_{vb,n+1}^{x,j}) = \Big\{(1-\phi_{vb,n+1}^{x,j})\,\mathbb{C}_{par} + \phi_{vb,n+1}^{x,j}\mathbb{C}_{vb} : [\mathbb{I} + \mathbb{P}_{cyl}^{par} : (\mathbb{C}_{vb} - \mathbb{C}_{par})]^{-1}\Big\} : \Big\{(1-\phi_{vb,n+1}^{x,j})\,\mathbb{I} + \phi_{vb,n+1}^{x,j}[\mathbb{I} + \mathbb{P}_{cyl}^{par} : (\mathbb{C}_{vb} - \mathbb{C}_{par})]^{-1}\Big\}^{-1}, \tag{9.5a}$$

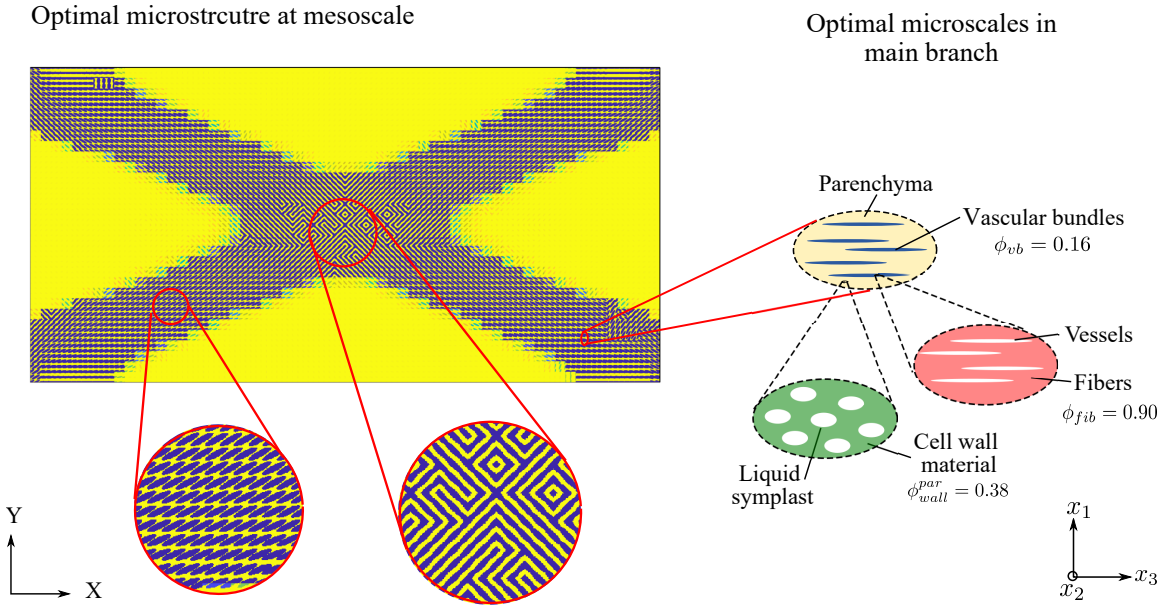

Fig. 9.7: *Optimal microstructure configuration at different scales for total prescribed displacement load of* $\boldsymbol{u}^* = 0.4$ *mm.*

$$\mathbb{C}(m_{n+1}^{x,j}) = [\mathbf{T}(\theta_{n+1}^{x,j})]^{-1}\ \mathbb{C}_{pith}\ [\mathbf{T}(\theta_{n+1}^{x,j})]\ . \tag{9.5b}$$

Here, $\mathbb{C}_{par}$ and $\mathbb{C}_{vb}$ are the homogenized stiffness tensors of parenchyma tissues and vascular bundle tissues in the solid-pith region, calculated following (4.4) and (4.6). Composition of all other RVEs in the multiscale material model of cereal stems is considered constant, and model parameters corresponding to Gopher oat variety are used in this example. $\mathbf{T}$ is a standard rotation matrix used for tensor transformations.

Lignin exhibits elastoplastic material behavior at the constituent level, and the macroscale limit state point corresponds to the yielding of lignin. For the solid pith, both parenchyma and vascular bundle branches have lignin at the lowermost cell wall material levels. Therefore, the yielding of lignin within any one of parenchyma or vascular bundle tissues determines the elastic limit state of the soft-pith material (see Section 4.2.3). However, the resulting macroscale yield criterion loses the general quadratic form, and the simplifications outlined in Section 7.4.2 are not valid. In this prototype model, we assume that only lignin in parenchyma cell wall material is elastoplastic (see Fig. 9.4). In this case, the macroscale homogenized yield criterion reads as:

$$\mathfrak{F}(\boldsymbol{\tau}, m_{n+1}^{x,j}) = \sqrt{\boldsymbol{\tau} : [\mathbb{C}(m_{n+1}^{x,j})]^{-1} : \frac{\partial\, \mathbb{C}(m_{n+1}^{x,j})}{\partial\, \mu_{lig,par}} : [\mathbb{C}(m_{n+1}^{x,j})]^{-1} : \boldsymbol{\tau}}\ -\ \sqrt{\frac{\overline{\phi}_{lig,par}}{3}}\ \frac{\sigma_{lig}^{y}}{\mu_{lig}} \tag{9.6}$$

With these definitions in hand, we write the material optimization problem for Gauss point $\boldsymbol{x}$ inside element j for $(n+1)^{th}$ load increment following (7.36) as:

$$\begin{aligned}
\bar{m}_{n+1}^{x,j} = \underset{m_{n+1}^{x,j}(\rho_j)}{\arg\max} \Big\{ & \boldsymbol{\Sigma}_{n+1} : (\boldsymbol{E}_{n+1}^{p} - \boldsymbol{E}_{n}^{p}) + \Psi(\boldsymbol{E}_{n+1} - \boldsymbol{E}_{n+1}^{p}) - \Psi(\boldsymbol{E}_{n} - \boldsymbol{E}_{n}^{p}) \Big\} \\
\text{s.t. :}\ & \boldsymbol{\Sigma}_{n+1} = \mathbb{C}(m_{n+1}^{x,j}) : (\boldsymbol{E}_{n+1} - \boldsymbol{E}_{n+1}^{p}) \\
& \mathfrak{F}(\boldsymbol{\Sigma}_{n+1}, m_{n+1}^{x,j}) \leq 0 \\
& \rho_j = \rho_{wall}\ \phi_{wall,n+1}^{par(x,j)}(1 - \phi_{vb,n+1}^{x,j}) + \rho_{fib}\ \phi_{fib,n+1}^{x,j}\ \phi_{vb,n+1}^{x,j} \\
& \phi_{wall}^{par,min} \leq \phi_{wall,n+1}^{par(x,j)} \leq \phi_{wall}^{par,max};\ \ \phi_{fib}^{min} \leq \phi_{fib,n+1}^{x,j} \leq \phi_{fib}^{max} \\
& \phi_{vb}^{min} \leq \phi_{vb,n+1}^{x,j} \leq \phi_{fib}^{max};\ \ -\pi/2 \leq \theta_{n+1}^{x,j} \leq \pi/2,
\end{aligned} \tag{9.7}$$

where ρ_j is the given macroscale dry density for the finite element with index j. The first two lines in the constraints definition define the microstructure dependent constitutive

equations. The rest of the constraints' definitions are identical to (9.2). We adopt bounds for $\phi^{par(x,j)}_{wall,n+1}$, $\phi^{x,j}_{fib,n+1}$, and $\phi^{x,j}_{vb,n+1}$ are $[0.01, 0.38]$, $[0.75, 0.90]$, and $[0.01, 0.16]$, respectively. The upper bound reflects the measured microscale parameters reported in Table B.1 and D.2. We note that the bounds remain constant with time increment, which implies that the definition of admissible set E_{ad} remains unchanged throughout loading history. This is an important condition for the discussed simplifications in Section 7.4.2. Please refer Section 7.4 for the algorithmic treatment of the material problem.

The structure optimization problem maximizing mechanical work expended during the course of deformation follows from (7.32) as:

$$\begin{aligned}
\max_{\boldsymbol{\rho}} :\ & f_w(\boldsymbol{\rho}, \bar{\boldsymbol{m}}) = \frac{1}{2} \sum_{n=0}^{n_{load}-1} (\boldsymbol{f}^{ext}_{n+1} + \boldsymbol{f}^{ext}_{n})^T \, \Delta \bar{\boldsymbol{u}}_{n+1} \\
\text{s.t.} :\ & \bar{\boldsymbol{r}}_{n+1}(\boldsymbol{\rho}, \bar{\boldsymbol{m}}_{n+1}, \bar{\boldsymbol{u}}_{n+1}) = 0 \ \ \forall n = 0, 1, ..., n_{load} - 1 \\
& M(\boldsymbol{\rho}) = \sum_{j=1}^{N_e} \rho_j |\Omega_j| = M_{req} = \rho_{avg} \times |\Omega|; \ \ \forall n = 1, 2, ..., n_{load} - 1 \\
& \rho_j \in [\rho_{min}, \rho_{max}], \ \forall j = 1, 2, ..., N_e.
\end{aligned} \tag{9.8}$$

The symbols and definitions in this equation are analogous to (7.32). The total amount of material is restricted by the reported average density $\rho_{avg} = 0.30$. Readers are advised to follow Section 7.5 and Algorithm 5 for details of sensitivity analysis and implementation. The move parameter μ and the damping parameter η are set to 0.02 and 0.5. The filter radius r_{min} is reduced linearly from $r_{min} = 15l_e$ to $r_{min} = 4l_e$ following Section 7.6.

Figures 9.5 and 9.6 illustrate the final macroscale density with the equivalent plastic strains and the evolution of optimization process. The macroscale design algorithm takes 38 density updates to converge to the final design. In the optimal layout, the branches from the left internode converge into the central node region and the branches of the right internode emerges. Similar node morphology has been observed in micro-CT images reported and discussed in Section 4.1.1. Moreover, [70] reported such observations from microimages for wheat nodes too. The plastic strains are concentrated in the ends and middle region due to the anticipated high shear deformations. The optimal density layout puts material in areas to attenuate plastic fronts, which can also be observed in the design evolution history in Fig. 9.7. This again emphasizes the role of plastic front in the optimal structural layout.

Figure 9.7 plots the optimal microstructure configuration at different scales at the final load level. At the mesoscale, the material orientation aligns with the largest principal stress direction. The material orientation follows the stress flow direction in the main branches, while the morphology is more complex in the central node region. We also plot the optimal

configurations at lower material scales in the main branches. These results indicate the choice of a stronger solid-pith material for the optimal mechanical response, which we concluded in the previous chapter.

These optimized hierarchical configurations can be interpreted as "ideal" cereal node morphology and support the search for physical traits that could improve lodging response. The biological materials have attained a certain degree of optimality through evolution, and the resistant varieties will point towards this configuration. For instance, the varieties, which are closer to the optimal configuration $\phi_{wall}^{par} = 0.38, \phi_{fib} = 0.90$ and $\phi_{vb} = 0.16$, are anticipated to be lodging resistant. We can observe this fact in our comparison of wheat and oat stem in the previous chapter, where the wheat stems with a higher cell wall fraction in the parenchyma section lead to a stiffer and stronger solid-pith conferring better lodging resistance. We note that, at this moment, we do not have hard experimental evidence for accurately quantifying the non-mechanical constraints, which calls for a collaborative effort with plant scientists. However, we establish that the study of self-adaptive mechanisms in the context of biotailoring applications with hierarchical plant materials is computationally feasible with our optimization framework.

Summary and conclusions

This part outlined the potential of our multiscale analysis and optimization methods in approaching a real-world application in the particular context of improving breeding decisions to target lodging-resistant cereals. We established that the multiscale-model-based finite element simulations combined with the controlled wind tunnel experiments provide important insights on the lodging behavior and its relation with the physical traits of the plant. The experimental observations support the conclusion that the wheat stems response is stiffer than the oat, based on the measured phenotypes. These conclusions were in agreement with the relatively better lodging resistance of wheat as compared to oat. However, these observations do not in themselves establish causal relationships of this observed behavior with the physical traits of the plants. In future, the validated finite element simulation framework can be extended for

Conventional lodging studies, for instance the wind tunnel experiments in this case, only focused on statistically relating lodging behavior with a limited number of easily measurable traits. On the contrary, our simulation framework comprehensively includes chemical composition (lignin, hemicellulose, and cellulose content), tissue characteristics (volume fractions and cell structure of parenchyma, bundles), and plant morphology (internode height, cross-section details). This feature of our simulation framework directed us to conclude that the distinct physiological differences in the hierarchical organization of wheat and oat stems resulted in their wide differences in lodging resistance. In future, the validated finite element simulation framework can be extended for *"a-priori"* predictions of certain traits, enabling a full simulation of plant-wind interactions *in silico* from genetic sequences to aid in the selection of lodging resistance in cereals and other crops. The gained insight from these simulations will help in devising breeding strategies for lodging-resistant cereals reducing time and labor costs.

Reflecting on the mechanical perspective on self-adaption, we applied our optimization framework to simulate self-adapting mechanisms in plant structures with a focus on bamboo and oat stems. To this end, we integrated our multiscale material models within our concurrent material and structure optimization approaches. We also emphasized that our

framework can incorporate the non-mechanical constraints as bounds on in the material optimization problem. We demonstrated that the resulting optimum design identified by our framework corresponds to material configurations at different scales that are observed in nature. We believe that our analysis and optimization framework provides an opportunity for collaborative efforts among experimental biologist and computational mechanists to unravel self-adaption mechanisms in plants. These insights could offer input to breeding efforts to find more complex combinations of traits that are important for improving lodging resistance, but have not been identified yet.

Chapter 10

Thesis conclusion and outlook

This thesis has presented the computationally feasible and accurate multiscale analysis and optimization methods that form a rigorous foundation for the study of multiphase hierarchical systems. Broadly speaking, the thesis has developed evidence-supported multiscale material models for plants, established rigorous foundations of the efficient concurrent material and structure optimization framework, and applied these concepts for real-world application to support the breeding of lodging-resistant cereals. Part I, II, and III dealt with these objectives, and key conclusions are reported at the end of each part. Here, we summarize these developments in a broader perspective of multiphase hierarchical systems.

The key feature of our multiscale approach is that all the model inputs have a strong physiological basis in the hierarchical organization of plants, and the model is free from empirical parameter tuning. This feature has enabled us to quantitatively understand the multiscale origin of macroscale properties, which otherwise would have been not possible. We have also outlined the experimental characterization for mining these model inputs with an example of oat stems using chemical analysis and advanced microimaging techniques such as transmission electron microscopy, scanning electron microscopy, light microscopy, and micro-CT scans. Given the fast progress in microimaging techniques, this multiscale approach can serve as a template to characterize and model other multiphase hierarchical materials, including bones, organs, rocks, and concrete.

The computational cost of our concurrent material and structure optimization framework does not explode exponentially with the number of hierarchical scales. For the first time, this property has enabled us to optimize multiphase hierarchical systems with several material scales. The framework is developed to understand the self-optimizing mechanisms

in biological materials and promises excellent potential in this line by reproducing these mechanisms in plants. However, the framework is general and can be seamlessly transferred to other applications involving multiphase hierarchical materials, for instance 3D printing of civil structures using concrete[80, 135].

This thesis also instantiates unique opportunities presented by collaborative efforts of researchers from computational mechanics backgrounds with life sciences to address important applications involving biological materials. In particular, this work helps rationalize decision-making in the breeding efforts of lodging-resistant cereals that can reduce labor and resource costs. Broadly speaking, this work establishes the importance of integrating simulations with conventional experimental approaches to address complex biological systems for a broad class of applications. We believe that this line of research could open up new possibilities for other bioengineering applications such as the efficient conversion of crop residues to biofuel, paper, and textile, biomedical applications through multiscale bone remodeling simulations, and fabrication of bioinspired engineering materials.

We think that the methods developed in this thesis are stepping stones towards the rigorous and rational studies of multiphase hierarchical systems. However, many questions are yet to be answered, and this work opens a number of opportunities for future research. Here, we discuss few directions and some initial thoughts.

↪ The multiscale material models developed in Part I are mainly valid for a small strain tensor assumption. We have successfully extended our formulation to account for the small strain-based elastoplastic effects originating from microscales for macroscale properties. However, continuum micromechanics can not include highly nonlinear phenomenons such as fracture and finite strain plasticity effects happening at the microscales. One possible solution is to solve the relevant RVE within the computational homogenization paradigm while remaining RVEs continue to be homogenized using continuum micromechanics. Such a hybrid approach can enable us to include these highly nonlinear effects without compromising computational feasibility.

↪ The current development of the material and structure optimization framework in Chapter 7 only includes a general quadratic form of macroscale failure criterion, which led to the series of simplifications in the material optimization problem from an implementation viewpoint. The quadratic form is the result of assuming von Mises failure criterion at the constituent level. In many multiphase hierarchical systems, inelastic effects originating from microscale may be well captured by other failure criteria. Moreover, current development considers the macroscopic response as ideal elastoplastic with no hardening. Both hardening effects and general failure criterion at microscales can be accounted for

within the continuum micromechanics. The transformation field analysis summarized in Chapter 1 is particularly promising in this context. Our optimization framework is general, and these aspects can be incorporated with proper modifications in the solution strategy of the material optimization problem.

↪ For the target application of lodging-resistant cereals, the proposed optimization framework needs further theoretical and implementation developments. From a modeling perspective, the cereal stems are anticipated to check the stability failure at the structure level. This requirement can be achieved by adding a constraint on the buckling load factor in the structure optimization problem of our framework. The buckling load factor can be computed using linearized buckling analysis [56, 201]. Despite the computational advantages achieved through continuum micromechanics, high computational cost remains a potential bottleneck for three-dimensional path-dependent optimization problems such as for our intended application. In our framework, the material optimization problem at each Gauss point and the sensitivity analysis in each element are fully decoupled, therefore, enabling straightforward parallelization on a GPU or multi-threaded CPU architecture. The macroscale structure problem can be handled via efficient data structures, fast iterative solvers, and preconditioners to solve the resulting linearized algebraic equations, provided through the open-source library PETSc. We plan to exploit these properties in transferring our developments to an efficient high-performance computational setting with proper parallelization and memory usage.

↪ We reflect on the mechanical or "Newtonian" perspective on the functional adaption and growth of biological systems in Chapter 9. We emphasize an encouraging and natural fit of our optimization framework with the energetic descriptions of experienced mechanical, non-mechanical and phylogenetic constraints. A possible close connection between the computational growth and adaption approaches and structure optimization has been outlined in the past [8, 144]. However, this connection has not been explored rigorously to date. We think that the overall structure of our framework is suitable for building a growth and adaption framework in a material and structure optimization paradigm. An apparent advantage is the possible seamless connection of the macroscale constitutive and growth evolution equations with the underlying microscales.

List of journal publications

The journal publications submitted and/or published by the author of this dissertation during his time at the University of Minnesota are listed here:

↪ **T. Gangwar**, A.Q. Susko, S. Baranova, M. Guala, K.P. Smith, D.J. Heuschele. Wheat and oat stem bending differences validated through multiscale analysis to inform lodging resistance. *Journal of Experimental Botany*, submitted, 2021.

↪ **T. Gangwar**, D. Schillinger. Concurrent material and structure optimization of multi-phase hierarchical systems within a continuum micromechanics framework. *Structural and Multidisciplinary Optimization*, doi: 10.1007/s00158-021-02907-1, 2021.

↪ **T. Gangwar**, D.J. Heuschele, K.P. Smith, A. Fok, G. Annor, D. Schillinger. Multiscale characterization and micromechanical modeling of crop stem materials. *Biomechanics and Modeling in Mechanobiology*, 20:69–91, 2021.

↪ **T. Gangwar**, D. Schillinger. Microimaging-informed continuum micromechanics accurately predicts macroscopic stiffness and strength properties of hierarchical plant culm materials. *Mechanics of Materials*, 130:39-57, 2019.

↪ **T. Gangwar**, J. Calder, T. Takahashi, J.E. Bechtold, D. Schillinger. Robust variational segmentation of 3D bone CT data with thin cartilage interfaces. *Medical Image Analysis*, 47:95-110, 2018.

↪ D. Schillinger, **T. Gangwar**, A. Gilmanov, D.J. Heuschele, H.K. Stolarski. Embedded shell finite elements: solid-shell interaction, surface locking, and application to image-based bio-structures. *Computer Methods in Applied Mechanics and Engineering*, 335:298-326, 2018.

References

[1] Abasolo, W., Eder, M., Yamauchi, K., Obel, N., Reinecke, A., Neumetzler, L., Dunlop, J. W., Mouille, G., Pauly, M., Höfte, H., et al. (2009). Pectin may hinder the unfolding of xyloglucan chains during cell deformation: implications of the mechanical performance of arabidopsis hypocotyls with pectin alterations. *Molecular Plant*, 2(5):990–999.

[2] Abe, K. and Yano, H. (2010). Comparison of the characteristics of cellulose microfibril aggregates isolated from fiber and parenchyma cells of Moso bamboo (Phyllostachys pubescens). *Cellulose*, 17(2):271–277.

[3] Alberdi, R., Zhang, G., Li, L., and Khandelwal, K. (2018). A unified framework for nonlinear path-dependent sensitivity analysis in topology optimization. *International Journal for Numerical Methods in Engineering*, 115(1):1–56.

[4] Aldaeus, F., Schweinebarth, H., Törngren, P., and Jacobs, A. (2011). Simplified determination of total lignin content in kraft lignin samples and black liquors. *Holzforschung*, 65(4):601–604.

[5] Allaire, G. and Aubry, S. (1999). On optimal microstructures for a plane shape optimization problem. *Structural Optimization*, 17(2-3):86–94.

[6] Allaire, G., Jouve, F., and Toader, A.-M. (2004). Structural optimization using sensitivity analysis and a level-set method. *Journal of Computational Physics*, 194(1):363–393.

[7] Amada, S., Munekata, T., Nagase, Y., Ichikawa, Y., Kirigai, A., and Zhifei, Y. (1996). The mechanical structures of bamboos in viewpoint of functionally gradient and composite materials. *Journal of Composite Materials*, 30(7):800–819.

[8] Ambrosi, D., Ateshian, G. A., Arruda, E. M., Cowin, S., Dumais, J., Goriely, A., Holzapfel, G. A., Humphrey, J. D., Kemkemer, R., Kuhl, E., et al. (2011). Perspectives on biological growth and remodeling. *Journal of the Mechanics and Physics of Solids*, 59(4):863–883.

[9] Anderson, N. (2016). Cell wall-bound p-coumaric and ferulic acid analysis. *Bio-protocol*, 6(19):e1955.

[10] Anderson, N. A., Bonawitz, N. D., Nyffeler, K., and Chapple, C. (2015). Loss of ferulate 5-hydroxylase leads to mediator-dependent inhibition of soluble phenylpropanoid biosynthesis in arabidopsis. *Plant Physiology*, 169(3):1557–1567.

[11] Bader, T. K., Hofstetter, K., Hellmich, C., and Eberhardsteiner, J. (2010). Poromechanical scale transitions of failure stresses in wood: from the lignin to the spruce level. *ZAMM-Journal of Applied Mathematics and Mechanics/Zeitschrift für Angewandte Mathematik und Mechanik*, 90(10-11):750–767.

[12] Bader, T. K., Hofstetter, K., Hellmich, C., and Eberhardsteiner, J. (2011). The poroelastic role of water in cell walls of the hierarchical composite softwood. *Acta Mechanica*, 217(1-2):75–100.

[13] Bao, M. (2005). *Analysis and design principles of MEMS devices*. Elsevier.

[14] Barnett, J. R. and Bonham, V. A. (2004). Cellulose microfibril angle in the cell wall of wood fibres. *Biological Reviews*, 79(2):461–472.

[15] Baucher, M., Halpin, C., Petit-Conil, M., and Boerjan, W. (2003). Lignin: genetic engineering and impact on pulping. *Critical Reviews in Biochemistry and Molecular Biology*, 38(4):305–350.

[16] Bendsøe, M. P. (1989). Optimal shape design as a material distribution problem. *Structural Optimization*, 1(4):193–202.

[17] Bendsøe, M. P. and Kikuchi, N. (1988). Generating optimal topologies in structural design using a homogenization method. *Computer Methods in Applied Mechanics and Engineering*, 71(2):197 – 224.

[18] Bendsøe, M. P. and Sigmund, O. (1999). Material interpolation schemes in topology optimization. *Archive of Applied Mechanics*, 69(9-10):635–654.

[19] Bendsøe, M. P. and Sigmund, O. (2013). *Topology optimization: theory, methods, and applications*. Springer Science & Business Media.

[20] Bergander, A. and Salmén, L. (2002). Cell wall properties and their effects on the mechanical properties of fibers. *Journal of Materials Science*, 37(1):151–156.

[21] Berry, P., Spink, J., Gay, A. P., and Craigon, J. (2003). A comparison of root and stem lodging risks among winter wheat cultivars. *The Journal of Agricultural Science*, 141(2):191–202.

[22] Berry, P., Sterling, M., Spink, J., Baker, C., Sylvester-Bradley, R., Mooney, S., Tams, A., and Ennos, A. (2004). Understanding and reducing lodging in cereals. *Advances in Agronomy*, 84(04):215–269.

[23] Bertram, J. E. and Swartz, S. M. (1991). The 'law of bone transformation': a case of crying wolff? *Biological Reviews*, 66(3):245–273.

[24] Bessa, M., Bostanabad, R., Liu, Z., Hu, A., Apley, D. W., Brinson, C., Chen, W., and Liu, W. K. (2017). A framework for data-driven analysis of materials under uncertainty: Countering the curse of dimensionality. *Computer Methods in Applied Mechanics and Engineering*, 320:633–667.

[25] Bhushan, B. (2009). Biomimetics: lessons from nature–an overview. *Philosophical Transactions of the Royal Society A: Mathematical, Physical and Engineering Sciences*, 367(1893):1445–1486.

[26] Blanchard, R., Morin, C., Malandrino, A., Vella, A., Sant, Z., and Hellmich, C. (2016). Patient-specific fracture risk assessment of vertebrae: A multiscale approach coupling x-ray physics and continuum micromechanics. *International Journal for Numerical Methods in Biomedical Engineering*, 32(9):e02760.

[27] Boyd, S., Boyd, S. P., and Vandenberghe, L. (2004). *Convex optimization*. Cambridge university press.

[28] Braidwood, L., Breuer, C., and Sugimoto, K. (2014). My body is a cage: mechanisms and modulation of plant cell growth. *New Phytologist*, 201(2):388–402.

[29] Brulé, V., Rafsanjani, A., Pasini, D., and Western, T. L. (2016). Hierarchies of plant stiffness. *Plant Science*, 250:79–96.

[30] Buehler, M. J. (2007). Molecular nanomechanics of nascent bone: fibrillar toughening by mineralization. *Nanotechnology*, 18(29):295102.

[31] Buhl, T., Pedersen, C. B., and Sigmund, O. (2000). Stiffness design of geometrically nonlinear structures using topology optimization. *Structural and Multidisciplinary Optimization*, 19(2):93–104.

[32] Burgert, I. and Dunlop, J. W. (2011). Micromechanics of cell walls. In *Mechanical integration of plant cells and plants*, pages 27–52. Springer.

[33] Cadman, J. E., Zhou, S., Chen, Y., and Li, Q. (2013). On design of multi-functional microstructural materials. *Journal of Materials Science*, 48(1):51–66.

[34] Cavalier, D. M., Lerouxel, O., Neumetzler, L., Yamauchi, K., Reinecke, A., Freshour, G., Zabotina, O. A., Hahn, M. G., Burgert, I., Pauly, M., et al. (2008). Disrupting two arabidopsis thaliana xylosyltransferase genes results in plants deficient in xyloglucan, a major primary cell wall component. *The Plant Cell*, 20(6):1519–1537.

[35] Cho, S. and Jung, H.-S. (2003). Design sensitivity analysis and topology optimization of displacement–loaded non-linear structures. *Computer Methods in Applied Mechanics and Engineering*, 192(22-24):2539–2553.

[36] Coelho, P., Fernandes, P., Rodrigues, H., Cardoso, J., and Guedes, J. (2009). Numerical modeling of bone tissue adaptation - a hierarchical approach for bone apparent density and trabecular structure. *Journal of Biomechanics*, 42(7):830–837.

[37] Coelho, P. G., Fernandes, P. R., Guedes, J. M., and Rodrigues, H. C. (2008). A hierarchical model for concurrent material and topology optimisation of three-dimensional structures. *Structural and Multidisciplinary Optimization*, 35(2):107–115.

[38] Cosgrove, D. J. (2015). Plant cell wall extensibility: connecting plant cell growth with cell wall structure, mechanics, and the action of wall-modifying enzymes. *Journal of Experimental Botany*, 67(2):463–476.

[39] Cousins, W. (1976). Elastic modulus of lignin as related to moisture content. *Wood Science and Technology*, 10(1):9–17.

[40] Cousins, W. (1978). Young's modulus of hemicellulose as related to moisture content. *Wood Science and Technology*, 12(3):161–167.

[41] Cowin, S. (2001). The false premis in wolff's law. In *Bone biomechanics handbook*, pages 30–1–32–5. Boca Raton: CRC Press.

[42] Culmann, C. (1866). *Die graphische Statik.*. Zurich.

[43] Currey, J. D. (1995). The validation of algorithms used to explain adaptive remodeling in bone. In *A. Odgaard and H. Weinans (Eds.), Bone structure and remodeling*, pages 9–13. World Scientific.

[44] Currey, J. D. (1999). Why aren't skeletal tissues perfect? In *IUTAM Symposium on Synthesis in Bio Solid Mechanics*, pages 93–102. Springer.

[45] Da, D. (2019). *Topology optimization design of heterogeneous materials and structures*. John Wiley & Sons.

[46] de Borst, K. and Bader, T. K. (2014). Structure–function relationships in hardwood–insight from micromechanical modelling. *Journal of Theoretical Biology*, 345:78–91.

[47] de Souza Neto, E. A., Peric, D., and Owen, D. R. (2011). *Computational methods for plasticity: theory and applications*. John Wiley & Sons.

[48] Deaton, J. D. and Grandhi, R. V. (2014). A survey of structural and multidisciplinary continuum topology optimization: post 2000. *Structural and Multidisciplinary Optimization*, 49(1):1–38.

[49] Dixon, P. G. and Gibson, L. J. (2014). The structure and mechanics of moso bamboo material. *Journal of the Royal Society Interface*, 11(99):20140321.

[50] Dvorak, G. J. (1992). Transformation field analysis of inelastic composite materials. *Proceedings of The Royal Society London A*, 437(1900):311–327.

[51] Dvorak, G. J. and Benveniste, Y. (1992). On transformation strains and uniform fields in multiphase elastic media. *Proceedings of The Royal Society London A*, 437(1900):291–310.

[52] Efendiev, Y., Galvis, J., and Hou, T. Y. (2013). Generalized multiscale finite element methods (gmsfem). *Journal of Computational Physics*, 251:116–135.

[53] Egan, P., Sinko, R., LeDuc, P. R., and Keten, S. (2015). The role of mechanics in biological and bio-inspired systems. *Nature Communications*, 6(1):1–12.

[54] Elices, M. (2000). *Structural biological materials: design and structure-property relationships*. Elsevier.

[55] Espinosa, E., Sánchez, R., Otero, R., Domínguez-Robles, J., and Rodríguez, A. (2017). A comparative study of the suitability of different cereal straws for lignocellulose nanofibers isolation. *International Journal of Biological Macromolecules*, 103:990–999.

[56] Ferrari, F. and Sigmund, O. (2019). Revisiting topology optimization with buckling constraints. *Structural and Multidisciplinary Optimization*, 59(5):1401–1415.

[57] Feyel, F. and Chaboche, J.-L. (2000). Fe2 multiscale approach for modelling the elasto-viscoplastic behaviour of long fibre sic/ti composite materials. *Computer methods in applied mechanics and engineering*, 183(3-4):309–330.

[58] Fish, J. (2013). *Practical multiscaling*. John Wiley & Sons.

[59] Fratzl, P. and Weinkamer, R. (2007). Nature's hierarchical materials. *Progress in materials Science*, 52(8):1263–1334.

[60] Frey, K. J. and Norden, A. (1959). Lodging resistance studies in oats. ii. inheritance and heritability 1. *Agronomy Journal*, 51(9):535–537.

[61] Fritsch, A. and Hellmich, C. (2007). Universal microstructural patterns in cortical and trabecular, extracellular and extravascular bone materials: micromechanics-based prediction of anisotropic elasticity. *Journal of Theoretical Biology*, 244(4):597–620.

[62] Fritsch, A., Hellmich, C., and Dormieux, L. (2009). Ductile sliding between mineral crystals followed by rupture of collagen crosslinks: experimentally supported micromechanical explanation of bone strength. *Journal of Theoretical Biology*, 260(2):230–252.

[63] Fritzen, F., Xia, L., Leuschner, M., and Breitkopf, P. (2016). Topology optimization of multiscale elastoviscoplastic structures. *International Journal for Numerical Methods in Engineering*, 106(6):430–453.

[64] Fuqua, M. A., Huo, S., and Ulven, C. A. (2012). Natural fiber reinforced composites. *Polymer Reviews*, 52(3):259–320.

[65] Gangwar, T. and Schillinger, D. (2019). Microimaging-informed continuum micromechanics accurately predicts macroscopic stiffness and strength properties of hierarchical plant culm materials. *Mechanics of Materials*, 130:39–57.

[66] Gao, H., Ji, B., Jäger, I. L., Arzt, E., and Fratzl, P. (2003). Materials become insensitive to flaws at nanoscale: lessons from nature. *Proceedings of the National Academy of Sciences*, 100(10):5597–5600.

[67] Gao, J., Luo, Z., Li, H., and Gao, L. (2019). Topology optimization for multiscale design of porous composites with multi-domain microstructures. *Computer Methods in Applied Mechanics and Engineering*, 344:451–476.

[68] Garber, R. and Olson, P. (1919). A study of the relation of some morphological characters to lodging in cereals 1. *Agronomy Journal*, 11(5):173–186.

[69] Geers, M. G., Kouznetsova, V. G., Matouš, K., and Yvonnet, J. (2017). Homogenization methods and multiscale modeling: nonlinear problems. *Encyclopedia of Computational Mechanics Second Edition*, pages 1–34.

[70] Ghaffar, S. H. and Fan, M. (2015). Revealing the morphology and chemical distribution of nodes in wheat straw. *Biomass and Bioenergy*, 77:123–134.

[71] Gibson, L. J. (2005). Biomechanics of cellular solids. *Journal of Biomechanics*, 38(3):377–399.

[72] Gibson, L. J. (2012). The hierarchical structure and mechanics of plant materials. *Journal of The Royal Society Interface*, 9(76):2749–2766.

[73] Gibson, L. J. and Ashby, M. F. (1999). *Cellular solids: structure and properties*. Cambridge University Press.

[74] Gibson, L. J., Ashby, M. F., and Harley, B. A. (2010). *Cellular materials in nature and medicine*. Cambridge University Press.

[75] Grafius, J. and Brown, H. (1954). Lodging resistance in oats 1. *Agronomy Journal*, 46(9):414–418.

[76] Gritsch, C. S. and Murphy, R. J. (2005). Ultrastructure of fibre and parenchyma cell walls during early stages of culm development in dendrocalamus asper. *Annals of botany*, 95(4):619–629.

[77] Grossmann, I. E. (2009). *MINLP: outer approximation algorithmMINLP: Outer Approximation Algorithm*, pages 2179–2183. Springer US, Boston, MA.

[78] Grun, T., von Scheven, M., Bischoff, M., and Nebelsick, J. (2018). Structural stress response of segmented natural shells: a numerical case study on the clypeasteroid echinoid echinocyamus pusillus. *Journal of The Royal Society Interface*, 15(143):20180164.

[79] Habibi, M. K., Samaei, A. T., Gheshlaghi, B., Lu, J., and Lu, Y. (2015). Asymmetric flexural behavior from bamboo's functionally graded hierarchical structure: underlying mechanisms. *Acta Biomaterialia*, 16:178–186.

[80] Hager, I., Golonka, A., and Putanowicz, R. (2016). 3d printing of buildings and building components as the future of sustainable construction? *Procedia Engineering*, 151:292–299.

[81] Hamed, E., Jasiuk, I., Yoo, A., Lee, Y., and Liszka, T. (2012). Multi-scale modelling of elastic moduli of trabecular bone. *Journal of The Royal Society Interface*, 9(72):1654–1673.

[82] Hamed, E., Lee, Y., and Jasiuk, I. (2010). Multiscale modeling of elastic properties of cortical bone. *Acta Mechanica*, 213(1-2):131–154.

[83] Harrington, J., Astley, R., and Booker, R. (1998). Modelling the elastic properties of softwood. *Holz als Roh- und Werkstoff*, 56(1):37–41.

[84] Hellmich, C., Barthélémy, J.-F., and Dormieux, L. (2004a). Mineral–collagen interactions in elasticity of bone ultrastructure–a continuum micromechanics approach. *European Journal of Mechanics-A/Solids*, 23(5):783–810.

[85] Hellmich, C. and Ulm, F.-J. (2002). Micromechanical model for ultrastructural stiffness of mineralized tissues. *Journal of Engineering Mechanics*, 128(8):898–908.

[86] Hellmich, C., Ulm, F.-J., and Dormieux, L. (2004b). Can the diverse elastic properties of trabecular and cortical bone be attributed to only a few tissue-independent phase properties and their interactions? *Biomechanics and Modeling in Mechanobiology*, 2(4):219–238.

[87] Hettich, T., Hund, A., and Ramm, E. (2008). Modeling of failure in composites by x-fem and level sets within a multiscale framework. *Computer Methods in Applied Mechanics and Engineering*, 197(5):414–424.

[88] Heuschele, J. D., Smith, K. P., and Annor, G. A. (2020). Variation in lignin, cell wall-bound p-coumaric, and ferulic acid in the nodes and internodes of cereals and their impact on lodging. *Journal of agricultural and food chemistry*, 68(45):12569–12576.

[89] Hill, R. (1948). A theory of the yielding and plastic flow of anisotropic metals. *Proceedings of the Royal Society of London A: Mathematical, Physical and Engineering Sciences*, 193(1033):281–297.

[90] Hill, R. (1963). Elastic properties of reinforced solids: some theoretical principles. *Journal of the Mechanics and Physics of Solids*, 11(5):357–372.

[91] Hill, R. (1998). *The mathematical theory of plasticity*, volume 11. Oxford university press.

[92] Hofstetter, K., Hellmich, C., and Eberhardsteiner, J. (2005). Development and experimental validation of a continuum micromechanics model for the elasticity of wood. *European Journal of Mechanics-A/Solids*, 24(6):1030–1053.

[93] Hofstetter, K., Hellmich, C., and Eberhardsteiner, J. (2006). The influence of the microfibril angle on wood stiffness: a continuum micromechanics approach. *Computer Assisted Mechanics and Engineering Sciences*, Vol. 13, No. 4:523–536.

[94] Hofstetter, K., Hellmich, C., Eberhardsteiner, J., and Mang, H. A. (2008). Micromechanical estimates for elastic limit states in wood materials, revealing nanostructural failure mechanisms. *Mechanics of Advanced Materials and Structures*, 15(6-7):474–484.

[95] Holstov, A., Bridgens, B., and Farmer, G. (2015). Hygromorphic materials for sustainable responsive architecture. *Construction and Building Materials*, 98:570–582.

[96] Horvath, L., Peszlen, I., Peralta, P., Kasal, B., and Li, L. (2010). Mechanical properties of genetically engineered young aspen with modified lignin content and/or structure. *Wood and Fiber Science*, 42(3):310–317.

[97] Huang, X. and Xie, M. (2010). *Evolutionary topology optimization of continuum structures: methods and applications*. John Wiley & Sons.

[98] Huang, X. and Xie, Y. (2008). Optimal design of periodic structures using evolutionary topology optimization. *Structural and Multidisciplinary Optimization*, 36(6):597–606.

[99] Hughes, T. J. (2000). *The finite element method: linear static and dynamic finite element analysis*. Dover Publications.

[100] Huiskes, R. (1995). The law of adaptive bone remodeling : a case for crying newton? In *A. Odgaard and H. Weinans (Eds.), Bone structure and remodeling*, Recent advances in human biology: Vol. 2, pages 15–23. World Scientific.

[101] Janssen, J. J. (1981). *Bamboo in building structures*. PhD thesis, Technische Hogeschool Eindhoven.

[102] Janssen, J. J. (2012). *Mechanical properties of bamboo*, volume 37. Springer Science & Business Media.

[103] Jog, C. S., Haber, R. B., and Bendsøe, M. P. (1994). Topology design with optimized, self-adaptive materials. *International Journal for Numerical Methods in Engineering*, 37(8):1323–1350.

[104] Jones, L., Ennos, A. R., and Turner, S. R. (2001). Cloning and characterization of irregular xylem4 (irx4): a severely lignin-deficient mutant of arabidopsis. *The Plant Journal*, 26(2):205–216.

[105] Koehler, L. and Telewski, F. W. (2006). Biomechanics and transgenic wood. *American Journal of Botany*, 93(10):1433–1438.

[106] Köhler, L. and Spatz, H.-C. (2002). Micromechanics of plant tissues beyond the linear-elastic range. *Planta*, 215(1):33–40.

[107] Komuraiah, A., Kumar, N. S., and Prasad, B. D. (2017). The study of relationship between fracture angles of natural fiber with its micro fibril angle. *Procedia Engineering*, 173:1198 – 1202.

[108] Krabbenhøft, K. (2009). A variational principle of elastoplasticity and its application to the modeling of frictional materials. *International Journal of Solids and Structures*, 46(3-4):464–479.

[109] Kröner, E. (1958). Computation of the elastic constants of polycrystals from constants of single crystals. *Zeitschrift für Physik*, 151:504–518.

[110] Kröner, E. (1961). Zur plastischen Verformung des Vielkristalls. *Acta Metallurgica*, 9(2):155–161.

[111] Kumar, T. and Suresh, K. (2019). A density-and-strain-based K-clustering approach to microstructural topology optimization. *Structural and Multidisciplinary Optimization*, pages 1–17.

[112] Laws, N. (1977). A note on interaction energies associated with cracks in anisotropic solids. *Philosophical magazine*, 36(2):367–372.

[113] Laws, N. (1985). A note on penny-shaped cracks in transversely isotropic materials. *Mechanics of Materials*, 4(2):209–212.

[114] Le, B., Yvonnet, J., and He, Q.-C. (2015). Computational homogenization of nonlinear elastic materials using neural networks. *International Journal for Numerical Methods in Engineering*, 104(12):1061–1084.

[115] Lee, C., Zhong, R., Richardson, E. A., Himmelsbach, D. S., McPhail, B. T., and Ye, Z.-H. (2007). The parvus gene is expressed in cells undergoing secondary wall thickening and is essential for glucuronoxylan biosynthesis. *Plant and Cell Physiology*, 48(12):1659–1672.

[116] Liese, W. and Weiner, G. (1996). Ageing of bamboo culms. A review. *Wood Science and Technology*, 30(2):77–89.

[117] Lipton, R. (1994). A saddle-point theorem with application to structural optimization. *Journal of Optimization Theory and Applications*, 81(3):549–568.

[118] Liu, J., Gaynor, A. T., Chen, S., Kang, Z., Suresh, K., Takezawa, A., Li, L., Kato, J., Tang, J., Wang, C. C., et al. (2018). Current and future trends in topology optimization for additive manufacturing. *Structural and Multidisciplinary Optimization*, 57(6):2457–2483.

[119] Liu, Z., Bessa, M., and Liu, W. K. (2016). Self-consistent clustering analysis: an efficient multi-scale scheme for inelastic heterogeneous materials. *Computer Methods in Applied Mechanics and Engineering*, 306:319–341.

[120] Loehnert, S. and Belytschko, T. (2007). A multiscale projection method for macro/microcrack simulations. *International Journal for Numerical Methods in Engineering*, 71(12):1466–1482.

[121] Mannan, S., Knox, J. P., and Basu, S. (2017). Correlations between axial stiffness and microstructure of a species of bamboo. *Royal Society Open Science*, 4(1):160412.

[122] Mannan, S., Zaffar, M., Pradhan, A., and Basu, S. (2016). Measurement of microfibril angles in bamboo using Mueller matrix imaging. *Applied Optics*, 55(32):8971–8978.

[123] Mark, R. (1967). *Cell Wall Mechanics of Tracheids*. Yale University Press.

[124] Masson, R. (2008). New explicit expressions of the Hill polarization tensor for general anisotropic elastic solids. *International Journal of Solids and Structures*, 45(3-4):757–769.

[125] Matsuo, M., Sawatari, C., Iwai, Y., and Ozaki, F. (1990). Effect of orientation distribution and crystallinity on the measurement by x-ray diffraction of the crystal lattice moduli of cellulose i and ii. *Macromolecules*, 23(13):3266–3275.

[126] Maute, K., Schwarz, S., and Ramm, E. (1998). Adaptive topology optimization of elastoplastic structures. *Structural optimization*, 15(2):81–91.

[127] McCann, M. C., Buckeridge, M. S., and Carpita, N. C. (2014). *Plants and bioenergy*. Springer.

[128] Mishnaevsky Jr, L. and Qing, H. (2008). Micromechanical modelling of mechanical behaviour and strength of wood: State-of-the-art review. *Computational Materials Science*, 44(2):363–370.

[129] Mitch, D. R. (2009). *Splitting capacity characterization of bamboo culms*. PhD thesis, University of Pittsburgh.

[130] Mohmod, A. L., Ariffin, W. T. W., and Ahmad, F. (1990). Anatomical features and mechanical properties of three malaysian bamboos. *Journal of Tropical Forest Science*, pages 227–234.

[131] Mori, T. and Tanaka, K. (1973). Average stress in matrix and average elastic energy of materials with misfitting inclusions. *Acta Metallurgica*, 21(5):571–574.

[132] Morin, C., Vass, V., and Hellmich, C. (2017). Micromechanics of elastoplastic porous polycrystals: theory, algorithm, and application to osteonal bone. *International Journal of Plasticity*, 91:238–267.

[133] Nakshatrala, P. B., Tortorelli, D. A., and Nakshatrala, K. (2013). Nonlinear structural design using multiscale topology optimization. part I: Static formulation. *Computer Methods in Applied Mechanics and Engineering*, 261:167–176.

[134] Nemat-Nasser, S. and Hori, M. (2013). *Micromechanics: overall properties of heterogeneous materials*, volume 37. Elsevier.

[135] Ngo, T. D., Kashani, A., Imbalzano, G., Nguyen, K. T., and Hui, D. (2018). Additive manufacturing (3d printing): A review of materials, methods, applications and challenges. *Composites Part B: Engineering*, 143:172–196.

[136] Nguyen, L. and Schillinger, D. (2018). A multiscale predictor/corrector scheme for efficient elastoplastic voxel finite element analysis, with application to ct-based bone strength prediction. *Computer Methods in Applied Mechanics and Engineering*, 330:598 – 628.

[137] Nguyen, L., Stoter, S., Baum, T., Kirschke, J., Ruess, M., Yosibash, Z., and Schillinger, D. (2017). Phase-field boundary conditions for the voxel finite cell method: Surface-free stress analysis of CT-based bone structures. *International Journal for Numerical Methods in Biomedical Engineering*, doi:10.1002/cnm.2880.

[138] Nguyen, L. H. and Schillinger, D. (2019a). The multiscale finite element method for nonlinear continuum localization problems at full fine-scale fidelity, illustrated through phase-field fracture and plasticity. *Journal of Computational Physics*, 396:129–160.

[139] Nguyen, L. H. and Schillinger, D. (2019b). A residual-driven local iterative corrector scheme for the multiscale finite element method. *Journal of Computational Physics*, 377:60–88.

[140] Nishino, T., Takano, K., and Nakamae, K. (1995). Elastic modulus of the crystalline regions of cellulose polymorphs. *Journal of Polymer Science Part B: Polymer Physics*, 33(11):1647–1651.

[141] Park, Y. B. and Cosgrove, D. J. (2015). Xyloglucan and its interactions with other components of the growing cell wall. *Plant and Cell Physiology*, 56(2):180–194.

[142] Pearson, O. M. and Lieberman, D. E. (2004). The aging of wolff's "law": ontogeny and responses to mechanical loading in cortical bone. *American Journal of Physical Anthropology*, 125(S39):63–99.

[143] Pedersen, P. (1989). On optimal orientation of orthotropic materials. *Structural Optimization*, 1(2):101–106.

[144] Pedersen, P. and Bendsøe, M. P. (1999). *IUTAM Symposium on Synthesis in Bio Solid Mechanics*, volume 69. Kluwer, Dordrecht.

[145] Peña, M. J., Zhong, R., Zhou, G.-K., Richardson, E. A., O'Neill, M. A., Darvill, A. G., York, W. S., and Ye, Z.-H. (2007). Arabidopsis irregular xylem8 and irregular xylem9: implications for the complexity of glucuronoxylan biosynthesis. *The Plant Cell*, 19(2):549–563.

[146] Persson, K. (2000). *Micromechanical modelling of wood and fibre properties*, volume 1013. Division of Structural Mechanics, Lund Institute of Technology.

[147] Pichler, B. and Hellmich, C. (2011). Upscaling quasi-brittle strength of cement paste and mortar: A multi-scale engineering mechanics model. *Cement and Concrete Research*, 41(5):467–476.

[148] Pichler, B., Scheiner, S., and Hellmich, C. (2008). From micron-sized needle-shaped hydrates to meter-sized shotcrete tunnel shells: micromechanical upscaling of stiffness and strength of hydrating shotcrete. *Acta Geotechnica*, 3(4):273.

[149] Radman, A., Huang, X., and Xie, Y. (2013). Topology optimization of functionally graded cellular materials. *Journal of Materials Science*, 48(4):1503–1510.

[150] Ray, A. K., Mondal, S., Das, S. K., and Ramachandrarao, P. (2005). Bamboo - A functionally graded composite-correlation between microstructure and mechanical strength. *Journal of Materials Science*, 40(19):5249–5253.

[151] Ritchie, R. O., Buehler, M. J., and Hansma, P. (2009). Plasticity and toughness in bone. *Physics Today*, 62(6):41.

[152] Rodrigues, H. C., Guedes, J. M., and Bendsoe, M. P. (2002). Hierarchical optimization of material and structure. *Structural and Multidisciplinary Optimization*, 24(1):1–10.

[153] Rodrigues, H. C., Jacobs, C., Guedes, J. M., and Bendsøe, M. P. (1999). Global and local material optimization models applied to anisotropic bone adaptation. In Pedersen, P. and Bendsøe, M. P., editors, *IUTAM Symposium on Synthesis in Bio Solid Mechanics*, pages 209–220, Dordrecht. Springer Netherlands.

[154] Ruff, C., Holt, B., and Trinkaus, E. (2006). Who's afraid of the big bad wolff?:"wolff's law" and bone functional adaptation. *American Journal of Physical Anthropology*, 129(4):484–498.

[155] Ryden, P., Sugimoto-Shirasu, K., Smith, A. C., Findlay, K., Reiter, W.-D., and McCann, M. C. (2003). Tensile properties of arabidopsis cell walls depend on both a xyloglucan cross-linked microfibrillar network and rhamnogalacturonan ii-borate complexes. *Plant Physiology*, 132(2):1033–1040.

[156] Salençon, J. (2012). *Handbook of continuum mechanics: General concepts thermoelasticity*. Springer Science & Business Media.

[157] Sato, T. (1968). A modified method for lead staining of thin sections. *Microscopy*, 17(2):158–159.

[158] Schillinger, D., Gangwar, T., Gilmanov, A., Heuschele, J. D., and Stolarski, H. K. (2018). Embedded shell finite elements: Solid–shell interaction, surface locking, and

application to image-based bio-structures. *Computer Methods in Applied Mechanics and Engineering*, 335:298–326.

[159] Schulgasser, K. and Witztum, A. (1992). On the strength, stiffness and stability of tubular plant stems and leaves. *Journal of Theoretical Biology*, 155(4):497–515.

[160] Schwarz, S., Maute, K., and Ramm, E. (2001). Topology and shape optimization for elastoplastic structural response. *Computer Methods in Applied Mechanics and Engineering*, 190(15-17):2135–2155.

[161] Sethian, J. A. and Wiegmann, A. (2000). Structural boundary design via level set and immersed interface methods. *Journal of computational physics*, 163(2):489–528.

[162] Sigmund, O. (2001). A 99 line topology optimization code written in Matlab. *Structural and Multidisciplinary Optimization*, 21(2):120–127.

[163] Sigmund, O. and Maute, K. (2013). Topology optimization approaches. *Structural and Multidisciplinary Optimization*, 48(6):1031–1055.

[164] Simo, J. C. and Hughes, T. J. (2006). *Computational inelasticity*, volume 7. Springer Science & Business Media.

[165] Suquet, P. (1995). Overall properties of nonlinear composites: a modified secant moduli theory and its link with ponte castañeda's nonlinear variational procedure. *Comptes rendus de l'Académie des sciences. Série II, Mécanique, physique, chimie, astronomie*, 320(11):563–571.

[166] Suquet, P. (1997). Effective properties of nonlinear composites. In *Continuum micromechanics*, pages 197–264. Springer.

[167] Suquet, P. (2014). *Continuum micromechanics*, volume 377. Springer.

[168] Susko, A. (2019). *Deciphering lodging resistance in oat and other cereal crops*. PhD thesis, University of Minnesota.

[169] Suzuki, K. and Itoh, T. (2001). The changes in cell wall architecture during lignification of bamboo, Phyllostachys aurea Carr. *Trees*, 15(3):137–147.

[170] Swan, C. C. and Kosaka, I. (1997a). Voigt–Reuss topology optimization for structures with linear elastic material behaviours. *International Journal for Numerical Methods in Engineering*, 40(16):3033–3057.

[171] Swan, C. C. and Kosaka, I. (1997b). Voigt–Reuss topology optimization for structures with nonlinear material behaviors. *International Journal for Numerical Methods in Engineering*, 40(20):3785–3814.

[172] Tadmor, E. B., Miller, R. E., and Elliott, R. S. (2012). *Continuum mechanics and thermodynamics: from fundamental concepts to governing equations*. Cambridge University Press.

[173] Tashiro, K. and Kobayashi, M. (1996). Molecular theoretical study of the intimate relationships between structure and mechanical properties of polymer crystals. *Polymer*, 37(10):1775–1786.

[174] Theocaris, P. S. and Stavroulakis, G. E. (1999). Optimal material design in composites: An iterative approach based on homogenized cells. *Computer Methods in Applied Mechanics and Engineering*, 169(1-2):31–42.

[175] Thompson, D. W. (1942). On growth and form. *On growth and form*.

[176] Timothy, J. J. and Meschke, G. (2016). A cascade continuum micromechanics model for the effective elastic properties of porous materials. *International Journal of Solids and Structures*, 83:1–12.

[177] Timothy, J. J. and Meschke, G. (2017). Cascade continuum micromechanics model for the effective permeability of solids with distributed microcracks: Self-similar mean-field homogenization and image analysis. *Mechanics of Materials*, 104:60–72.

[178] Truesdell, C. and Noll, W. (2004). The non-linear field theories of mechanics. In *The non-linear field theories of mechanics*, pages 1–579. Springer.

[179] Trujillo, D. and Lopez, L. (2016). Bamboo material characterisation. In *Nonconventional and Vernacular Construction Materials*, pages 365–392. Elsevier.

[180] Tsai, S. W. and Wu, E. M. (1971). A general theory of strength for anisotropic materials. *Journal of composite materials*, 5(1):58–80.

[181] Turner, S. R. and Somerville, C. R. (1997). Collapsed xylem phenotype of arabidopsis identifies mutants deficient in cellulose deposition in the secondary cell wall. *The plant Cell*, 9(5):689–701.

[182] Voelker, S. L., Lachenbruch, B., Meinzer, F. C., Kitin, P., and Strauss, S. H. (2011). Transgenic poplars with reduced lignin show impaired xylem conductivity, growth efficiency and survival. *Plant, cell & environment*, 34(4):655–668.

[183] Vogel, S. (2013). *Comparative biomechanics: life's physical world*. Princeton University Press.

[184] Wainwright, S. A. (1982). *Mechanical design in organisms*. Princeton University Press.

[185] Wakashima, K. and Tsukamoto, H. (1991). Mean-field micromechanics model and its application to the analysis of thermomechanical behaviour of composite materials. *Materials Science and Engineering: A*, 146(1-2):291–316.

[186] Wang, M. Y. and Wang, X. (2004). "color" level sets: a multi-phase method for structural topology optimization with multiple materials. *Computer Methods in Applied Mechanics and Engineering*, 193(6-8):469–496.

[187] Wang, M. Y., Wang, X., and Guo, D. (2003). A level set method for structural topology optimization. *Computer Methods in Applied Mechanics and Engineering*, 192(1-2):227–246.

[188] Wegst, U. G., Bai, H., Saiz, E., Tomsia, A. P., and Ritchie, R. O. (2015). Bioinspired structural materials. *Nature Materials*, 14(1):23.

[189] Weibel, R. and Pendleton, J. (1964). Effect of artificial lodging on winter wheat grain yield and quality 1. *Agronomy Journal*, 56(5):487–488.

[190] Wiersma, J. J., Dai, J., and Durgan, B. R. (2011). Optimum timing and rate of trinexapac-ethyl to reduce lodging in spring wheat. *Agronomy Journal*, 103(3):864–870.

[191] Willis, J. (1977). Bounds and self-consistent estimates for the overall properties of anisotropic composites. *Journal of the Mechanics and Physics of Solids*, 25(3):185–202.

[192] Wolff, J. (1892). *Das Gesetz der Transformation der Knochen*. Berlin, A. Hirchwild.

[193] Wolff, J. (1986). *The law of bone remodelling (Das Gesetz der Transformation der Knocken)*. Springer, Berlin.

[194] Xia, L. and Breitkopf, P. (2014). Concurrent topology optimization design of material and structure within FE2 nonlinear multiscale analysis framework. *Computer Methods in Applied Mechanics and Engineering*, 278:524–542.

[195] Xia, L. and Breitkopf, P. (2015). Multiscale structural topology optimization with an approximate constitutive model for local material microstructure. *Computer Methods in Applied Mechanics and Engineering*, 286:147–167.

[196] Xia, L. and Breitkopf, P. (2017). Recent advances on topology optimization of multiscale nonlinear structures. *Archives of Computational Methods in Engineering*, 24(2):227–249.

[197] Xia, L., Fritzen, F., and Breitkopf, P. (2017). Evolutionary topology optimization of elastoplastic structures. *Structural and Multidisciplinary Optimization*, 55(2):569–581.

[198] Xia, L., Xia, Q., Huang, X., and Xie, Y. M. (2018). Bi-directional evolutionary structural optimization on advanced structures and materials: a comprehensive review. *Archives of Computational Methods in Engineering*, 25(2):437–478.

[199] Yeats, T., Vellosillo, T., Sorek, N., Ibáñez, A. B., and Bauer, S. (2016a). Rapid determination of cellulose, neutral sugars, and uronic acids from plant cell walls by one-step two-step hydrolysis and hpaec-pad. *Plant Physiology*, 6(20):e1978.

[200] Yeats, T. H., Sorek, H., Wemmer, D. E., and Somerville, C. R. (2016b). Cellulose deficiency is enhanced on hyper accumulation of sucrose by a h+-coupled sucrose symporter. *Plant Physiology*, 171(1):110–124.

[201] Yi, B., Zhou, Y., Yoon, G. H., and Saitou, K. (2019). Topology optimization of functionally-graded lattice structures with buckling constraints. *Computer Methods in Applied Mechanics and Engineering*, 354:593–619.

[202] Yosibash, Z., Trabelsi, N., and Milgrom, C. (2007). Reliable simulations of the human proximal femur by high-order finite element analysis validated by experimental observations. *Journal of Biomechanics*, 40(16):3688–3699.

[203] Yuan, Z. and Fish, J. (2009). Multiple scale eigendeformation-based reduced order homogenization. *Computer Methods in Applied Mechanics and Engineering*, 198(21-26):2016–2038.

[204] Zaoui, A. (2002). Continuum micromechanics: survey. *Journal of Engineering Mechanics*, 128(8):808–816.

[205] Zhang, X., Li, J., Yu, Z., Yu, Y., and Wang, H. (2017). Compressive failure mechanism and buckling analysis of the graded hierarchical bamboo structure. *Journal of Materials Science*, 52(12):6999–7007.

[206] Zheng, X., Lee, H., Weisgraber, T. H., Shusteff, M., DeOtte, J., Duoss, E. B., Kuntz, J. D., Biener, M. M., Ge, Q., Jackson, J. A., et al. (2014). Ultralight, ultrastiff mechanical metamaterials. *Science*, 344(6190):1373–1377.

[207] Zhong, R., Peña, M. J., Zhou, G.-K., Nairn, C. J., Wood-Jones, A., Richardson, E. A., Morrison, W. H., Darvill, A. G., York, W. S., and Ye, Z.-H. (2005). Arabidopsis fragile fiber8, which encodes a putative glucuronyltransferase, is essential for normal secondary wall synthesis. *The Plant Cell*, 17(12):3390–3408.

[208] Zhong, R., Taylor, J. J., and Ye, Z.-H. (1997). Disruption of interfascicular fiber differentiation in an arabidopsis mutant. *The Plant Cell*, 9(12):2159–2170.

[209] Zhong, R. and Ye, Z.-H. (2004). Amphivasal vascular bundle 1, a gain-of-function mutation of the ifl1/rev gene, is associated with alterations in the polarity of leaves, stems and carpels. *Plant and Cell Physiology*, 45(4):369–385.

[210] Zhu, J.-H., Zhang, W.-H., and Xia, L. (2016). Topology optimization in aircraft and aerospace structures design. *Archives of Computational Methods in Engineering*, 23(4):595–622.

[211] Zohdi, T. I. (2017). Homogenization methods and multiscale modeling. *Encyclopedia of Computational Mechanics Second Edition*, pages 1–24.

Appendices

A Complete data sets to compare modeling and experimental results for bamboo culms

In the following, we report additional data for comparison of experimental stiffness and strength results with model predictions, along with measured and model parameters. Please see Section 3.5.1 for further details.

Table A.1: *Axial stiffness modulus: experimental results E_{exp} versus model predictions $E_{est} = 1/\mathbb{C}^{-1}_{sec,33}$, along with measured and model parameters.*

r/a	**Density (g/cm3)**	$\mathbf{V_{vb}}$	$\mathbf{S_f}$	$\mathbf{E_{exp}}$ **(GPa)**	ϕ_{vb}	ϕ^{vb}_{fib}	ϕ^{fib}_{wall}	$\mathbf{E_{est}}$ **(GPa)**
Internode number 5								
0.08	0.421	0.10	0.73	3.78	0.10	0.73	0.36	4.88
0.12	0.427	0.11	0.74	6.47	0.11	0.74	0.36	5.01
0.14	0.432	0.11	0.74	3.82	0.11	0.74	0.36	5.01
0.30	0.468	0.15	0.78	4.33	0.15	0.78	0.36	6.36
0.35	0.484	0.16	0.79	5.00	0.16	0.79	0.36	5.72
0.35	0.492	0.17	0.80	5.08	0.17	0.80	0.36	5.88
0.55	0.553	0.22	0.83	6.72	0.22	0.83	0.48	7.84
0.58	0.566	0.23	0.84	6.33	0.23	0.84	0.48	8.08
0.60	0.577	0.24	0.85	6.95	0.24	0.85	0.48	8.33
0.75	0.659	0.31	0.88	10.62	0.31	0.88	0.75	13.93
0.80	0.694	0.34	0.89	12.18	0.34	0.89	0.75	15.03
0.85	0.726	0.36	0.90	15.30	0.36	0.90	0.75	15.83
Internode number 11								
0.14	0.435	0.12	0.74	5.57	0.12	0.74	0.36	5.12
0.15	0.438	0.12	0.74	4.68	0.12	0.74	0.36	5.12
0.15	0.440	0.12	0.74	5.34	0.12	0.74	0.36	5.12
0.37	0.506	0.18	0.79	7.84	0.18	0.79	0.48	6.92
0.39	0.515	0.19	0.80	7.65	0.19	0.80	0.48	7.14
0.40	0.521	0.20	0.80	6.60	0.20	0.80	0.48	7.31
0.57	0.604	0.27	0.84	9.68	0.27	0.84	0.48	8.82
0.59	0.619	0.28	0.84	10.34	0.28	0.84	0.48	9.01
0.64	0.654	0.31	0.86	11.94	0.31	0.86	0.48	9.73
0.82	0.813	0.44	0.90	17.48	0.44	0.90	0.75	18.45
0.83	0.814	0.45	0.90	18.02	0.45	0.90	0.75	18.78
0.85	0.844	0.47	0.90	20.24	0.47	0.90	0.75	19.43
Internode number 14								
0.11	0.432	0.11	0.74	5.92	0.11	0.74	0.36	5.01
0.13	0.435	0.12	0.74	5.30	0.12	0.74	0.36	5.12
0.16	0.445	0.13	0.75	5.15	0.13	0.75	0.36	5.26
0.33	0.502	0.18	0.78	5.58	0.18	0.78	0.36	5.93
0.36	0.515	0.19	0.79	6.87	0.19	0.79	0.48	7.09
0.42	0.541	0.22	0.80	7.26	0.22	0.80	0.48	7.67
0.56	0.627	0.29	0.84	8.04	0.29	0.84	0.48	9.19
0.62	0.670	0.33	0.85	9.10	0.33	0.85	0.48	10.02
0.61	0.669	0.33	0.85	11.78	0.33	0.85	0.48	10.02
0.83	0.894	0.52	0.90	16.82	0.52	0.90	0.75	21.06
0.83	0.897	0.52	0.90	17.59	0.52	0.90	0.75	21.06
0.82	0.883	0.51	0.90	19.74	0.51	0.90	0.75	20.74

Table A.2: *Ultimate axial strength: experimental results $\Sigma_{exp}^{ult,c}$ versus micromechanics model predictions $\Sigma_{est}^{ult,c}$, along with measured model parameters and estimated elastic limit points $\Sigma_{est}^{el,c}$.*

r/a	**Density (g/cm3)**	$\mathbf{V_{vb}}$	$\mathbf{S_f}$	$\mathbf{\Sigma_{exp}^{ult,c}}$ **(MPa)**	ϕ_{vb}	ϕ_{fib}^{vb}	ϕ_{wall}^{fib}	$\mathbf{\Sigma_{est}^{el,c}}$ **(MPa)**	$\mathbf{\Sigma_{est}^{ult,c}}$ **(MPa)**
0.24	0.536	0.14	0.73	56	0.14	0.73	0.36	23	42
0.24	0.535	0.14	0.73	51	0.14	0.73	0.36	23	42
0.25	0.533	0.15	0.73	51	0.15	0.73	0.36	23	43
0.44	0.544	0.21	0.76	61	0.21	0.76	0.48	32	58
0.47	0.553	0.22	0.76	69	0.22	0.76	0.48	32	59
0.48	0.557	0.23	0.76	68	0.23	0.76	0.48	33	60
0.51	0.572	0.24	0.77	67	0.24	0.77	0.48	34	62
0.74	0.764	0.38	0.84	101	0.38	0.84	0.75	69	123
0.75	0.776	0.39	0.85	106	0.39	0.85	0.75	71	127
0.75	0.770	0.38	0.85	107	0.38	0.85	0.75	70	125
0.74	0.760	0.37	0.84	108	0.37	0.84	0.75	67	121
0.24	0.459	0.14	0.79	52	0.14	0.79	0.36	24	44
0.24	0.461	0.14	0.79	58	0.14	0.79	0.36	24	44
0.25	0.464	0.14	0.79	55	0.14	0.79	0.36	24	44
0.26	0.466	0.15	0.79	52	0.15	0.79	0.36	24	45
0.46	0.538	0.21	0.79	61	0.21	0.79	0.48	32	59
0.47	0.542	0.21	0.79	59	0.21	0.79	0.48	32	59
0.49	0.551	0.22	0.79	65	0.22	0.79	0.48	33	60
0.49	0.552	0.22	0.80	59	0.22	0.80	0.48	33	61
0.51	0.558	0.23	0.80	59	0.23	0.80	0.48	34	62
0.74	0.705	0.35	0.84	100	0.35	0.84	0.75	65	116
0.75	0.707	0.35	0.84	102	0.35	0.84	0.75	65	116
0.74	0.701	0.35	0.84	104	0.35	0.84	0.75	65	116
0.76	0.719	0.36	0.85	106	0.36	0.85	0.75	66	118

B Compilation of experimental data for oats

Details on model input data for oats

The "universal" mechanical properties of base materials cellulose, hemicellulose and lignin, are listed in Table 3.1. COUSINS found that the stiffness of lignin and hemicellulose decreases with increasing moisture content [39, 40], and reported the relations with the relative humidity. The graphs read 67% reduction in Young's modulus of both lignin and hemicellulose at the relative humidity of 70%, the average relative humidity in St.Paul. The crystallinity index (CI), which quantifies the fraction of crystalline cellulose in relation to the volume of the whole cellulose, has been predicted experimentally using X-ray diffraction for oats as $CI = 0.44$ [55].

The volume fraction of the constituents in the cell wall material RVEs in Fig. 4.4 can easily be calculated from chemical composition data listed in Table 4.1 following Section 3.5.1. The volume fractions of phases in all other RVEs in Fig. 4.4 are the other required inputs for the model. We derive the volume fractions with the help of microimages reported in Section 4.1. The data are reported in Table B.1.

Table B.1: *Measured model parameters phases.*

Variety	ϕ_{wall}^{par}	$\phi_{wall}^{fib^*}$	ϕ_{fib}	ϕ_{vb}	$\phi_{wall}^{shell^*}$	t/t_{shell}
Gopher	0.18	0.50	0.82	0.16	0.40	0.14
Reins	0.15	0.50	0.85	0.13	0.40	0.15
ND021052	0.17	0.50	0.80	0.11	0.40	0.16
IL07-8721	0.20	0.50	0.90	0.13	0.40	0.15

*Measured from TEM images of oats of the Gopher variety. In absence of imaging data, we assume that other varieties share the same volume fractions.

Four-point bending test results for oat specimens

In Table B.2, we also summarize the geometric measurements, the linear-elastic slope $(\Delta P/\Delta\delta)_{exp}$, and the failure load P_{exp}^{max} for each four-point bending test specimen. Please see Section 4 for further details.

Table B.2: *Linear-elastic slope and failure load: four-point bending test results vs model predictions along with geometric measurements.*

Variety	**a (mm)**	**b (mm)**	**t (mm)**	$(\Delta P/\Delta\delta)_{exp}$	P_{exp}^{max}	$(\Delta P/\Delta\delta)_{est}$	P_{est}^{max}
Gopher	1.77	1.60	0.36	6.5	5.7	5.0	5.4
Gopher	1.52	1.31	0.38	4.8	5.8	3.8	4.8
Gopher	1.45	1.42	0.60	7.3	5.9	6.2	8.5
Gopher	1.75	1.56	0.31	4.5	4.9	3.7	3.9
Gopher	1.66	1.52	0.30	5.6	4.6	3.5	3.6
Gopher	1.54	1.50	0.43	6.5	5.2	5.5	6.7
Reins	2.12	1.96	0.60	6.3	10.3	8.7	11.2
Reins	2.04	1.89	0.44	8.7	8.6	5.9	6.9
Reins	1.67	1.51	0.64	8.4	8.9	6.0	8.4
Reins	1.74	1.63	0.39	8.5	7.6	4.0	4.6
Reins	1.97	1.86	0.58	8.4	11.3	7.9	10.1
Reins	1.76	1.74	0.46	6.7	6.6	5.4	6.6
ND021052	1.35	1.34	0.41	5.9	5.8	2.7	4.2
ND021052	1.83	1.79	0.40	4.9	5.1	3.9	5.3
ND021052	1.67	1.56	0.51	6.5	6.1	4.4	6.6
ND021052	1.93	1.86	0.35	4.7	5.2	3.7	4.8
ND021052	1.83	1.71	0.88	7.5	11.7	8.4	14.7
ND021052	1.80	1.70	0.39	2.8	3.7	3.7	4.8
IL07-8721	1.50	1.47	0.57	11.2	11.3	5.5	8.1
IL07-8721	1.79	1.56	0.98	15.8	16.7	10.1	15.8
IL07-8721	1.68	1.54	0.83	8.4	11.1	8.3	12.5
IL07-8721	1.74	1.71	0.46	8.0	7.2	6.3	7.7
IL07-8721	1.84	1.74	0.46	5.9	6.5	6.4	7.8
IL07-8721	1.79	1.69	0.45	5.5	5.8	6.1	7.6

Refer Fig. 4.5a for the meaning of **a**, **b**, and **t**.

C Homogenized stiffness through continuum micromechanics for benchmark problems

We state the analytical expression for the macroscale homogenized stiffness $\mathbb{C}$ at a material point $\boldsymbol{x}$ in the domain Ω (see Fig. 5.1). The expression at each scale is based on (2.21). The microstructure characterization variables $\{\boldsymbol{\phi}_A(\boldsymbol{x}), \boldsymbol{\theta}_A(\boldsymbol{x}), \boldsymbol{\zeta}_A(\boldsymbol{x}), \boldsymbol{\gamma}_C(\boldsymbol{x})\}$ are defined in Fig. 5.1. We drop $(\boldsymbol{x})$ from these variables for conciseness of presentation in the following expressions.

At the lowermost scale RVE, Material B forms spherical inclusions in the matrix of Material C. The stiffness tensors for Material B and C are $\mathbb{c}_B$ and $\mathbb{c}_C$, respectively. The volume fraction of Material B and C at the lowermost scale are γ_B and γ_C such that $\gamma_B + \gamma_C = 1$. The RVE can be suitably modeled by the Mori-Tanaka scheme. Hence, we assume that $\mathbb{C}^0 = \mathbb{c}_C$ and the Hill tensor $\mathbb{P}_r^0 = \mathbb{P}_{sph}^C$, which corresponds to spherical inclusions in the isotropic matrix of Material C. Following (2.21), we arrive at the homogenized stiffness tensor $\mathbb{c}_M$ of the RVE:

$$\begin{aligned}\mathbb{c}_M(\gamma_C) = \Big\{\gamma_C\, \mathbb{c}_C + (1-\gamma_C)\, \mathbb{c}_B : [\mathbb{I} + \mathbb{P}_{sph}^C : (\mathbb{c}_B - \mathbb{c}_C)]^{-1}\Big\} : \\ \Big\{\gamma_C\, \mathbb{I} + (1-\gamma_C)\, [\mathbb{I}\ + \mathbb{P}_{sph}^C : (\mathbb{c}_B - \mathbb{c}_C)]^{-1}\Big\}^{-1}.\end{aligned} \tag{C.1}$$

This homogenized material matrix M hosts the inclusions of Material A with stiffness $\mathbb{c}_A$. The orientation and elongation ratio of these inclusions are θ_A and ζ_A, respectively. We estimate the homogenized stiffness of this RVE with the Mori-Tanaka scheme. We assume that $\mathbb{C}^0 = \mathbb{c}_M$ and the Hill tensor $\mathbb{P}_r^0 = \mathbb{P}_{sphrd}^M(\zeta_A)$, which corresponds to spheroidal inclusions with the elongation ratio ζ_A in the isotropic matrix of material M. We write the macroscale homogenized stiffness $\mathbb{C}_l$ in the co-ordinate system aligned with the inclusion elongation direction following (2.21). The expression is:

$$\begin{aligned}\mathbb{C}_l(\phi_A, \zeta_A, \gamma_C) = \Big\{(1-\phi_A)\, \mathbb{c}_M + \phi_A\, \mathbb{c}_A : [\mathbb{I} + \mathbb{P}_{sphrd}^M(\zeta_A) : (\mathbb{c}_A - \mathbb{c}_M)]^{-1}\Big\} : \\ \Big\{(1-\phi_A)\, \mathbb{I} + \phi_A\, [\mathbb{I}\ + \mathbb{P}_{sphrd}^M(\zeta_A) : (\mathbb{c}_A - \mathbb{c}_M)]^{-1}\Big\}^{-1}.\end{aligned} \tag{C.2}$$

The macroscale stiffness tensor $\mathbb{C}$ in the global co-ordinate system is obtained with the help of the standard tensor transformation matrix $\mathbf{T}$ as:

$$\mathbb{C}(\phi_A, \theta_A, \zeta_A, \gamma_C) = \mathbf{T}^{-1}\, \mathbb{C}_l\, \mathbf{T}, \quad \forall\, \boldsymbol{x} \in \Omega. \tag{C.3}$$

The expressions for the Hill tensors $\mathbb{P}^{C}_{sph}$ and $\mathbb{P}^{M}_{sphrd}(\zeta_A)$ are given in [124].

Now, we can rewrite the optimization statement (5.14):

$$\max_{\phi_A,\theta_A,\zeta_A,\gamma_C} \frac{1}{2}\boldsymbol{E} : \mathbb{C}(\phi_A,\theta_A,\zeta_A,\gamma_C) : \boldsymbol{E}. \tag{C.4}$$

where we omit the constraints posed in (5.14) for clarity of notation. The equation (C.4) can be simplified further by eliminating θ_A [103, 143]. We know that for a general orthotropic material, the maximum strain energy is obtained by aligning the material axis with the principle strain axes. Therefore, the macroscale strain at each Gauss point entails the optimal material orientation $\bar{\theta}_A$ at the particular Gauss point. This further helps us simplify problem (C.4) to:

$$\begin{aligned}\max_{\phi_A,\zeta_A,\gamma_C} \max_{\theta_A} \frac{1}{2}\boldsymbol{E} : \mathbb{C}(\phi_A,\theta_A,\zeta_A,\gamma_C) : \boldsymbol{E} \\ \max_{\phi_A,\zeta_A,\gamma_C} \frac{1}{2}\boldsymbol{E} : \mathbb{C}(\phi_A,\bar{\theta}_A,\zeta_A,\gamma_C) : \boldsymbol{E}.\end{aligned} \tag{C.5}$$

This reduced problem can be solved by standard gradient-based fast optimization algorithms. We use the standard SciPy library available in python.

D Required input data for multiscale material model based simulations of oat and wheat stems

We compile all the required input data for the simulation of oat and wheat stems. Table D.1 sums up the chemical analysis data including the chemical composition of lignin, hemicellulose and cellulose, and crystallinty index of oat and wheat [88]. The other required input are volume fractions of phases at different hierarchical levels such as cell wall fraction in parenchyma tissues, sclerenchyma fibers and shell fibers, fiber fraction in vascular bundles, and vascular bundle fraction in soft-pith. These parameters are retrieved from microimages such as light microscopy, transmission electron microscopy and scanning electron microscopy. Following Chapter 4, we compile this input data in Table D.2 for wheat and oat. Remaining plant morphology data such as cross sectional and panicle characteristics are compiled in Table D.3 and D.4. This data is used for building geometric model of cereal stem and calculating wind drag force.

Table D.1: *Chemical analysis data for oat and wheat.*

Crop	**Lignin %**	**Hemicellulose %**	**Cellulose %**	**Crystallinity index**
Oat	50.69	18.80	30.51	0.44
Wheat	59.96	16.50	23.54	0.45

Table D.2: *Measured model parameters from microimages for tissue characterization.*

Crop	ϕ_{wall}^{par}	ϕ_{wall}^{fib}	ϕ_{fib}	ϕ_{vb}	ϕ_{wall}^{shell}	t_{shell}/t
Oat	0.18	0.50	0.82	0.16	0.40	0.14
Wheat	0.38	0.50	0.75	0.12	0.40	0.15

Table D.3: *Plant morphology data.*

		Length L (mm)	**Max diameter 2a (mm)**	**Min diameter 2b (mm)**	**Thickness t (mm)**
Oat	Internode 1	47	3.12	2.75	0.94
	Internode 2	78	3.56	2.98	0.60
	Internode 3	169	3.30	2.86	0.34
	Internode 4	377	3.30	2.86	0.34
Wheat	Internode 1	46	2.54	2.44	–
	Internode 2	100	2.73	2.33	0.28
	Internode 3	163	3.54	3.17	0.37
	Internode 4	346	3.54	3.17	0.37

Wheat's first internode is completely filled.

Table D.4: *Panicle characteristics to calculate wind drag force.*

Crop	**Mass (g)**	**Height (mm)**	**Area (mm^2)**
Oat	2.44	173	3562
Wheat	1.05	106	996